Katrin Niegelhell, Dipl.-Ing.

Interactions at Polysaccharide Surfaces

DOCTORAL THESIS

to achieve the university degree of

Doktorin der technischen Wissenschaften

submitted to

Graz University of Technology

Supervisor

Em.Univ.-Prof. Dipl.-Ing. Dr.techn. Franz Stelzer

Institute for Chemistry and Technology of Materials

Ass.Prof. Mag.rer.nat. Dr.rer.nat. Stefan Spirk
Institute for Paper-, Pulp- and Fiber Technology

Graz, September 2017

AFFIDAVIT

I declare that I have authored this thesis independently, that I have not used other than the declared sources/resources, and that I have explicitly indicated all material which has been quoted either literally or by content from the sources used. The text document uploaded to TUGRAZonline is identical to the present doctoral thesis.

1. 9. 2017
_____
Date

_____
Signature

-God made the bulk; surfaces were invented by the devil-

Wolfgang Pauli

Acknowledgements

Abstract

This thesis reports on interactions occurring at polysaccharide surfaces. On the one hand, the interactions between proteins and polysaccharide surfaces were explored in order to gain better insight into the processes and to enable tuning of such. In the first part of the thesis, protein adsorption onto various cellulosic blends, cellulose thin films derived from different precursors and tissue engineering biopolymers was investigated. The results thereof enable the development of smart materials composed of renewable polymers, such as anti-fouling coatings or substrates for sensing devices. Secondly, interactions between polysaccharides and polysaccharide surfaces were examined. For instance, the adsorption behavior of cationic starches employed in paper industry was elucidated and crucial factors governing this behavior were determined, which are useful for new developments in papermaking. Moreover, a method allowing the monitoring of surface regions and bulk material of a thin film separately was developed. This analysis approach will serve as a tool in surface and interface science to get a better insight into processes at interfaces such as adsorption, surface modification and water interaction.

In summary, all of the topics covered in this thesis aim at the understanding of adsorption phenomena at polysaccharide surfaces, leading to the development of new materials and applications of biopolymers, thereby supporting the replacement of fossil-based polymers by ones derived from renewable resources.

Zusammenfassung

Diese Doktorarbeit beschäftigt sich mit Wechselwirkungen an Polysaccharid-Oberflächen. Zum einen wurden Wechselwirkungen zwischen Proteinen und Polysacchariden erforscht um einen besseren Einblick in diese Prozesse zu erlangen und sie zu kontrollieren. Im ersten Teil der These wurden verschiedene Cellulose-Mischungen, aus unterschiedlichen Vorstufen hergestellte Cellulose-Dünnschichtfilme und Gewebetechnik Biopolymere untersucht. Die Resultate davon ermöglichen die Entwicklung von neuen Materialien aus erneuerbaren Rohstoffen, wie schmutzabweisende Beschichtungen oder Substrate für Sensoren. Des Weiteren wurden Wechselwirkungen zwischen Polysacchariden und Polysaccharid-Oberflächen getestet. Beispielsweise wurden die entscheidenden Faktoren für das Adsorptionverhalten von kationischen Stärken, welche in der Papierindustrie eingesetzt werden, bestimmt, was als Grundlage für neue Entwicklungen im Prozess der Papierherstellung dienen kann. Darüber hinaus wurde eine Methode zur separaten Beobachtung von Oberflächenregionen und dem Bulkmaterial einer Probe entwickelt. Diese Art von Analyse kann helfen, Prozesse wie Adsorption, Oberflächenmodifikation oder Quellung im Bereich von Oberflächen bzw. Grenzflächen, besser zu verstehen.

Die Themen dieser Arbeit zielen auf ein grundlegendes Verständnis von Adsorptionsphänomenen an Polysaccharid-Oberflächen ab, was zur Entwicklung von neuen Materialien und Anwendungen von Biopolymeren beitragen soll und in weiterer Folge die Ersetzung von fossilen Rohstoffen durch erneuerbare Polymere unterstützt.

Table of Contents

Aim and Motivation

The work presented in this thesis is mainly focused on the investigation of polysaccharide-polysaccharide and protein-polysaccharide interactions. The studies described in this thesis make use of surface sensitive techniques that are able to monitor adsorption in real-time, such as multi-parameter surface plasmon resonance spectroscopy or quartz crystal microbalance. These techniques help to elucidate fundamental events at the example of model thin films. The research is aimed at a deeper understanding of these phenomena to assist the development of new materials and to find new applications for renewable polymers, such as cellulose. However, the ultimate goal is the substitution of fossil based polymers by biopolymers, which is one of the main challenges of our time.

The thesis is divided into 3 parts. The first part focuses on the adsorption of proteins onto polysaccharide or biopolymers to understand the principles of interactions and find ways to tune those for applications. The second part deals with interactions of polysaccharides with polysaccharide surfaces, in order to modify those surfaces. The third part comprises a method which enables a closer look at processes occurring at surfaces by monitoring the surface regions and the bulk material separately, by combining atomic force microscopy and multi-parameter surface plasmon resonance spectroscopy. The last part includes the papers and corresponding supporting information which are collated in this thesis.

The following manuscripts are summarized in this cumulative thesis. I am first author or shared first author (#2) of all papers, except for paper #4, #6 and #8. Only results where I contributed are included from those papers.

1) Niegelhell, K.; Süßenbacher, M.; Sattelkow, J.; Plank, H.; Zhang, K.; Spirk, S. Bound vs Free Fatty Acids in Cellulose – How Bound and Free Fatty Acids in Cellulose Influence Nonspecific Protein Adsorption, *intended for submission to Biomacromolecules*.

2) Strasser, S.; Niegelhell, K.; Kaschowitz, M.; Markus, S.; Kargl, R.; Stana-Kleinschek, K.; Slugovc, C.; Mohan, T.; Spirk, S. Exploring Nonspecific Protein Adsorption on Lignocellulosic Amphiphilic Bicomponent Films, *Biomacromolecules* **2016**, *17* (3), 1083–1092.

3) Niegelhell, K.; Süßenbacher, M.; Jammernegg, K.; Ganner, T.; Schwendenwein, D.; Schwab, H.; Stelzer, F.; Plank, H.; Spirk, S. Enzymes as Biodevelopers for Nano- and Micropatterned Bicomponent Biopolymer Thin Films, *Biomacromolecules* **2016**, *17* (11), 3743–3749.

4) Mohan, T.; Niegelhell, K.; Nagaraj, C.; Reishofer, D.; Spirk, S.; Olschewski, A.; Stana Kleinschek, K.; Kargl, R. J. Interaction of Tissue Engineering Substrates with Serum Proteins and Ist Influenec on Human Primary Endothelial Cells, *Biomacromolecules* **2017**, *18* (2), 413–421.

5) Niegelhell, K; Ganner, T.; Payerl, C.; Plank, H.; Jantscher-Krenn, E.; Spirk S. Adsorption Behavior of Lectins – A MP-SPR Study, *working version*.

6) Weissl, M.; Niegelhell, K.; Reishofer, D.; Zankl, A.; Innerlohinger, J.; Spirk, S. Homogenous Cellulose Thin Films by Regeneration of Cellulose Xanthate – Properties and Characterization, *submitted to Cellulose* (**July 2017**).

7) Niegelhell, K.; Chemelli, A.; Hobisch, J.; Griesser, T.; Reiter, H.; Hirn, U.; Spirk, S. Interaction of Industrially Relevant Cationic Starches with Cellulose, *submitted to Carbohydrate Polymers* (**July 2017**).

8) Ganser, C.; Niegelhell, K.; Czibula, C.; Chemelli, A.; Teichert, C.; Schennach, R.; Spirk, S. Topography Effects in AFM Force Mapping Experiments in Xylan-Decorated Cellulose Thin Films, *Holzforschung* **2016**, *70* (12), 1115–1123.

9) Niegelhell, K; Kontturi, K; Hirn, U.; Spirk S. Multilayer Density Analysis of Thin Films, *submitted to Langmuir* (**September 2017**).

The following papers published during my masters (#10) and doctoral studies (#11) are not included in this thesis.

10) Mohan, T.; Niegelhell, K.; Zarth, C. S. P.; Kargl, R.; Köstler, S.; Ribitsch, V.; Heinze, T.; Spirk, S.; Stana-Kleinschek, K. Triggering Protein Adsorption on Tailored Cationic Cellulose Surfaces, *Biomacromolecules* **2014**, 15 (11), 3931–3941.

11) Niegelhell, K.; Leimgruber, S.; Grießer, T.; Brandl, C.; Chernev, B.; Schennach, R.; Trimmel, G.; Spirk, S. Adsorption Studies of Organophosphonic Acids on Differently Activated Gold Surfaces, *Langmuir* **2016**, 32 (6), 1550–1559.

Theoretical Background

I - Protein Adsorption

"Protein adsorption at solid surfaces is a common and often studied but very complex phenomenon."[1] The vast number of parameters influencing the interactions of proteins with solid surfaces is discussed in the following chapter. The importance of protein adsorption is presented by the innumerous applications in various fields, such as biology, medicine or food industry, which are covered by this chapter.[1]

Parameters Controlling Protein Adsorption

The complex phenomenon of protein adsorption on surfaces is influenced by various factors including external parameters and properties of the protein or the surfaces themselves. The main external parameters are temperature, ionic strength and pH value. Temperature affects the equilibrium state and the kinetics of protein adsorption. In general, higher amounts of adsorbed protein are found at elevated temperatures, due to increased diffusivity of the adsorbing species towards the substrate.[1,2] Ionic strength influences the electrostatic interactions between charged entities by screening effects. High ionic strength either impedes adsorption of charged proteins to oppositely charged surfaces or enhances adsorption to substrates with the same charge. Additionally, high ionic strength may lead to aggregation of the proteins, the so-called 'salting out' effect.[3,4] The pH value determines the electrostatic state of a protein. Proteins are positively charged at pH values below the isoelectric point (IEP), whereas they are negatively charged at pH values above the IEP. When the pH value equals the IEP, the protein has a net charge of zero, not meaning that there are no charges at all present at the protein surface. At the IEP, adsorbed protein amounts are usually maximized because of lowered solubility and lowered electrostatic repulsion between the proteins leading to denser packing of the adsorbed layer.[5–7]

Besides the external parameters, intrinsic protein properties, such as size, structural stability and composition, determine the adsorption behavior. Proteins can be divided into 'soft' and 'hard' proteins, showing high or little tendency to structural changes upon adsorption, respectively. 'Soft' proteins are usually of intermediate size or high molecular weight (more than 50 kDa, e.g., β- casein, α-lactoalbumin, haemoglobin), whereas 'hard' proteins are small and rigid (ca. 20 kDa, e.g., lysozyme, β-lactoglobulin).[2] The size defines the contact area, which is decisive for the adsorption ability of a protein. The so-called 'Vroman' effect describes preferential adsorption of larger molecules compared to smaller ones in protein mixtures caused by stronger binding due to larger contact area.[8]

Furthermore, the properties of the substrate, such as surface free energy, morphology, charge and polarity have to be considered when discussing protein adsorption phenomena.[9,10] Those properties are modifiable by e.g., coating a substrate with polymers, the build-up of self-assembled monolayers or deposition of Langmuir-Blodgett films.[10–12] The tendency of proteins to adsorb rather on apolar than polar surfaces is explained by the fact that such surfaces destabilize the structure of the protein and change its conformation, resulting in stronger inter-protein and protein-surface interactions.[13] Upon the release of water molecules from apolar parts of adsorbent and sorbent, the Gibb's free energy decreases, i.e. the entropy increases, which is the main driving force for adsorption of proteins onto hydrophobic substrates. Conformational changes occur prior to adsorption enabling/optimizing interactions between the hydrophobic parts of the protein and the hydrophobic surface.[14]

The Behavior of Proteins at Surfaces

The behavior of proteins at interfaces is considered to be affected by the individual behavior of the molecule including its conformation and orientation and the ensemble behavior of several proteins regarding inter-protein interactions as well.

Individual Behavior of Proteins at Surfaces

The main parameters describing the individual behavior of proteins are orientation and conformation. Different types of proteins display various shapes, such as heart-like shaped (e.g., BSA), rod-like (e.g., fibrinogen), or Y-shaped (e.g. IgG). The favored orientation of a protein after adsorption onto a surface is determined by the free energy minimum resulting from entropy gain (via release of solvent molecules or counter ions), van-der-Waals interactions, coulomb forces and hydrogens bonds. Proteins exhibit extremely complex structures providing hydrophobic, hydrophilic and charged domains, therefore, the affinity to a substrate varies within the molecule. Depending on the nature of the substrates, suitable protein domains are exposed in order to adsorb. Structurally stable, i.e. 'hard', proteins can either adsorb in 'end-on' or 'side-on' orientation, meaning preferential attachment to the surface with the short or the long axis of the molecules. In contrast, 'soft' proteins undergo conformational changes to optimize the free energy minimum upon adsorption. The re-organization of the protein results in a gain of free energy and an increase of the contact-area leading to stronger bonding.[15] The changes in orientation and conformation induced by adsorption can influence the biological function of the protein.[2]

Ensemble Behavior of Proteins at Surfaces

The adsorption behavior of proteins is influenced by many factors, including protein-protein interactions. Those interactions determine whether the proteins adsorb in a multilayer, monolayer or sub-monolayer fashion. Multilayers are seldomly observed and can be traced back to protein

aggregation under special conditions such as high electrolyte concentrations repressing inter-protein repulsion.[5] Monolayers are formed when inter-protein attraction is weak or alike-charged proteins repel each other.[16] Electrostatic repulsion between adsorbed proteins leads to loosely packed monolayers, whereas densely packed layers are built from neutral proteins.[5,7] In general, the interactions between adsorbing proteins, the so-called lateral effects, determine the structure of the adsorbed layer as well as the amount of adsorbed molecules. Less repulsion leads to denser packing and therefore to a higher extent of protein deposition. This can be achieved by, for instance, adding electrolytes to the adsorbent solution thereby screening the charges of the proteins.[3] The mediation of adsorption by already adsorbed proteins is called cooperative effect. This effect is linked to the electrostatic field in the circumference of the pre-adsorbed proteins. Proteins are vertically attracted by the surface and horizontally repelled by the neighboring proteins simultaneously leading to enhanced adsorption near pre-adsorbed proteins.[17]

In terms of the ensemble behavior of proteins influencing adsorption kinetics, overshoot effects need to be discussed. Overshoot effects refer to adsorption kinetics displaying a local maximum instead of a monotonically growing curve before the saturation (equilibrium of adsorption and desorption) of the surface is reached. There are 3 different explanations for this effect. The first proposes that the surface is temporarily oversaturated due to a time-delay of desorption. The amount of adsorbed proteins is reduced when desorption starts.[2] The second explanation is based on the so-called 'Vroman' effect, where a small protein rapidly adsorbs but is then replaced by a larger one showing higher affinity to the surface.[8] The third theory proposes that the overshoot effect is induced by orientation changes of the protein. The protein initially adsorbs in 'end-on' orientation, which allows more molecules to adsorb, and is then replaced by molecules adsorbing in energetically preferred 'side-on' orientation leading to less adsorbed amount than before.[18]

Another parameter affecting adsorption kinetics is the aggregation or clustering of proteins. Strong protein-protein interactions induce the aggregation/clustering in most cases directly on the surface. Proteins show a high affinity to protein aggregates existing at a surface. Larger aggregates induce higher affinity than smaller ones, therefore adsorption kinetics are accelerated upon growth of surface coverage. The formation of protein clusters upon adsorption is assigned to cooperative effects.[19,20]

Applications of Protein Adsorption

Describing the vast number of applications of protein adsorption would go beyond the scope of this thesis. Nevertheless, this sub-chapter gives an overview on the applications concerning renewable polymer systems, where protein adsorption was exploited to improve material properties.

One approach to make use of protein adsorption is the development of matrices for controlled protein deposition, which is the first step in the development of sensor devices. The controlled protein adsorption on polysaccharide surfaces can be achieved by modification with other substances. For instance, protein adsorption properties of cellulosic materials can be tuned by depositing polysaccharides, such as cationic cellulose derivatives, cationic chitosan derivatives, non-modified chitosan or carboxymethyl cellulose.[21–24]

The inverse principle was shown by Taajamaa et al.[25] who reported on the site-specific deposition of gold nanoparticles on pre-adsorbed protein patches. The 2-D assembly of gold nanoparticles was achieved by preferential adsorption of a protein onto parts of a phase separated polymer film and subsequent electrostatically driven deposition of the nanoparticles.

The controlled deposition of proteins plays an important role in regenerative medicine as well. Surfaces treated with certain proteins or growth factors mediate the adhesion and growth of

specific cells, which are then harvested for the production of tissue. Additionally, the proteins present at an implants surface may decide whether inflammation takes place or not.[26,27]

The interaction of polysaccharides with proteins represents a key parameter in the development of drug delivery systems. Polysaccharide nanoparticles are promising systems that can either entrap drugs or vaccines, or adsorb them onto their surfaces. Potential systems are initially tested with cheap and easy available proteins as model drugs very often.[28]

Moreover, protein adsorption can also be utilized to study the function of enzymes. For instance, insights into the degradation process of enzymes can be gained by studying the interaction of the degrading enzyme with poly-3-hydroxybutyrate and similar polyester and aliphatic surfaces.[29] Model systems made from cellulose and lignin were employed to study the influence of lignin in cellulosic biomass on biodegradation process by examining the preferential adsorption and activity of monocomponent cellulases.[30]

Furthermore, the investigation of protein adsorption is of high importance for anti-fouling materials. Anti-fouling surfaces are applied in medical devices, food and packaging industry, marine and industrial equipment, water purification systems and paper industry, for instance. By inhibition of protein adsorption, the attachment of bacteria, fungi or algae and the subsequent formation of a biofilm is prevented.[31,32] Surfaces showing low nonspecific protein adsorption are potential materials for anti-fouling coatings, therefore basic adsorption studies are necessary. Cellulose derivatives, as well as other polysaccharides, are tested for protein repellent behavior leading to some applications of superhydrophobic surfaces, for example for the coating of paper.[33–35]

II - Polyelectrolyte Adsorption

Polyelectrolytes, such as polysaccharides, lignin sulfonates or polypeptides and proteins, are polymers carrying ionizable groups. Depending on the type of group, polyelectrolytes are classified as polycation/polybase or polyanion/polyacid. Some polyelectrolytes show a constant charge at all pH conditions, the so-called 'hard' polyelectrolytes, whereas 'soft' polyelectrolytes display a dependence of charge and pH value.[36]

As mentioned before, the deposition of polysaccharides is often employed to influence the interaction capacity of a material with proteins. Therefore, this chapter elucidates the behavior of polyelectrolytes in solution and during adsorption.

Polyelectrolytes in Solution

In dilute solutions of polyelectrolytes, the inter-chain interactions are negligible. Under these circumstances, lowly charged polyelectrolytes behave as a random coil, similar to uncharged polymers. For polyelectrolytes featuring higher charge density, electrostatic repulsion inside the chain results in a stretched molecule. The coiling of the polyelectrolyte chain can be induced by the addition of salt, which screens the charged present at the polymer. This leads to molecules comprising stretched and coiled areas. The distance between the coiled parts of the polyelectrolyte is called persistence length.[36]

In semidilute solutions, where the distance between two individual polyelectrolyte molecules is in the order of their size, polyelectrolytes start to overlap. The overlap concentration depending on the number of monomers and the chain size in salt-free solutions refers to as the concentration at which overlap begins. When the concentration of the polyelectrolyte is above the overlap concentration, the correlation length refers to as the average mesh size of the polyelectrolyte in solution. Within the correlation volume (correlation length cubed), each charged monomer is

electrostatically repelled by the other monomers bearing a charge, whereas it is attracted to the counterions present. The interaction between correlation volumes can be ignored, however evaluation of the interactions inside the correlation volume is useful for the determination of coil size and stretching. Different mathematical models are able to estimate these interactions. In semidilute polyelectrolyte solutions, the persistence length is proportional to the correlation length suggesting the existence of only a single scale length. The concentration dependence of the correlation length at semidilute conditions upon salt addition is comparable to that in solutions of uncharged polymers.[37]

Parameters Controlling Polyelectrolyte Adsorption

The adsorption behavior of polyelectrolytes is influenced by various parameters, such as concentration of the polyelectrolyte, type of solvent, pH value or ionic strength. An increase in polyelectrolyte concentration is often accompanied by faster adsorption kinetics and a higher extent of adsorption, which is relates to conformation changes. Hydrogen bonding and electrostatic interactions are the main driving forces for polyelectrolyte adsorption. A charged surface provides an electrostatic field that is screened by counterions and electrolytes decaying with increasing distance. This electrostatic field attracts the oppositely charged polyelectrolyte to a certain extent, depending on the ionic strength of the ambient medium. At low ionic strength, the attractive forces are less screened compared to high ionic strength. In addition, ions present screen the charges of the polyelectrolyte, which then acts as a neutral polymer, and influences its conformation. Coiling of the polyelectrolyte is induced by adding salt, resulting in less repulsion of adsorbed molecules and denser packing. Upon adsorption, a coiled polymer requires less space on the surface compared to a stretched one, thus leading to increased adsorbed amounts. For 'soft' polyelectrolytes, the pH value determines the charge density and thereby the conformation. Therefore, adsorption is

governed by the pH value for those molecules, whereas for 'hard' polyelectrolytes, e.g., polymers comprising quaternary ammonium groups, the pH value is insignificant.[37]

Adsorbed polyelectrolyte molecules are divided into three parts; 'tails', 'loops' and 'trains'. 'Trains' are the parts of the polyelectrolyte sticking to the surfaces. 'Tails' are the ends of the polymers chains pointing towards the solvent. 'Loops' are connecting the 'trains' but are not in contact with the sorbent. The layer thickness of adsorbed polyelectrolyte depends on the conformation of the 'loops' as well as on the type of sorbent surface. The roughness of the sorbent and its charge density are decisive factors as well. High roughness leads to larger contact area and an increased number of charges present at the surface resulting in more attachment sites for the oppositely charged polymer. Additionally, the electrolyte can be trapped inside the adsorbed polyelectrolyte layer to some extent, which influences the conformation and thickness as well.[36]

III - Techniques to Monitor Adsorption Phenomena

A variety of techniques are capable of monitoring adsorption phenomena, thus giving insights into adsorption kinetics and isotherms, adsorbent-sorbent and adsorbent-adsorbent interactions, adsorbed layer thickness and density, etc. In most cases, only the combination of complementary techniques provides enough information to unravel a specific phenomenon.[2]

The following chapter provides an overview of techniques employed in the investigation of adsorption phenomena. A more detailed description is given for the analysis techniques used within this thesis.

Label-free Techniques

The detection of unlabeled molecules during adsorption can be accomplished by several techniques. Adsorption kinetics and isotherms are studied best with optical techniques, such as ellipsometry[38], surface plasmon resonance (SPR) spectroscopy[39,40] or optical waveguide lightmode spectroscopy (OWLS)[41]. Attenuated total reflection infrared (ATR-IR)[42,43] and circular dichroism spectroscopy[44] enable the investigation of conformational changes occurring upon adsorption. Quartz crystal microbalance with dissipation (QCM-D)[45] detects the adsorbed mass including coupled water. The water content of an adsorbed layer can be determined by combining QCM-D with SPR spectroscopy (yielding the adsorbed dry mass). Moreover, the viscoelastic properties of the adsorbed layer are determined. A powerful tool to study the layer thickness is neutron and x-ray reflectivity with a resolution down to sub-nanometer size. Imaging techniques, such as atomic force microscopy (AFM)[46] and scanning tunneling microscopy (STM)[47] enable the observation of a surface prior, during and after adsorption with a lateral resolution on the atomic level.

Surface Plasmon Resonance Spectroscopy (SPR)

SPR spectroscopy is an extremely important tool for the study of interaction and adsorption processes and is applied in various research areas ranging from basic material characterization to the development of high-end sensor devices. SPR spectroscopy is an optical technique based on the resonance of surface plasmon waves resulting from fluctuations in the dielectric field of the freely moving electron gas at the surface of a metal. The surface plasmon waves can be excited to resonance, meaning that they oscillate with the same frequency, under certain conditions. These resonance conditions are met when the propagation vector of the incoming light equals the propagation vector of the surface plasmons.[48]

$$\frac{\omega}{c} \sqrt{\varepsilon_0} \, \sin(\theta_c) = \frac{\omega}{c} \sqrt{\frac{\varepsilon_1 \, \varepsilon_2}{\varepsilon_1 + \varepsilon_2}} \tag{1}$$

where ω is the angular frequency of light in vacuum, c is the velocity of light in vacuum, ε_0 is the dielectric constant of the prism, Θ_c is the angle of incident light, ε_1 is the dielectric constant of the metal and ε_2 is the dielectric constant of the medium.

In order to induce surface plasmon resonance, a *p*-polarized laser light source is directed at a metal surface under total reflection conditions (**Figure 1**). Usually, a thin metal film deposited on a glass substrate is employed. The metal can be coated with various materials leading to a variety of experimental possibilities. The incident light is reflected from the metal surface and the intensity of reflected light is recorded by the photodetector. A minimum of reflected light intensity occurs when a part of the incoming light is taken up by the plasmons leading to the SPR resonance. Modern SPR devices, so-called multi-parameter SPR (MP-SPR) spectrometers, attain spectra in dependence of the incident angle of the incoming light, enabling the measurement in air as well as in liquid media (by application of a flow cell). Additionally, MP-SPR spectrometers are equipped

with more than one wavelength allowing the determination of the thickness and the refractive index of an adsorbed layer simultaneously.[49]
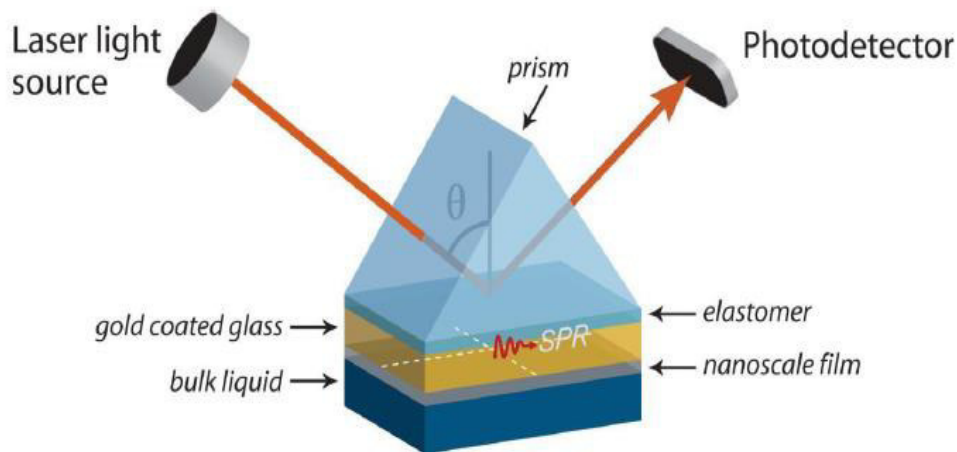
Figure 1. Set-up of a MP-SPR spectrometer.[bionavis.com]

In MP-SPR spectra, the intensity of the reflected light is plotted versus the incident angle of the incoming light. The angle at which the minimum occurs is called SPR angle. The SPR angle, as mentioned in the resonance conditions, is dependent on the chemical environment of the metal surface. In adsorption experiments, the SPR angle changes due to adsorbed material deposited on the surface. By plotting the SPR angle in dependence of time during an adsorption experiment, a sensogram is obtained (**Figure 2**). At the beginning of an adsorption experiment, the surface is equilibrated with liquid until a stable signal is detected. Then, the adsorption solution is injected into the flow cell. After the adsorption, the surface is rinsed with pure liquid again to remove loosely bound material.
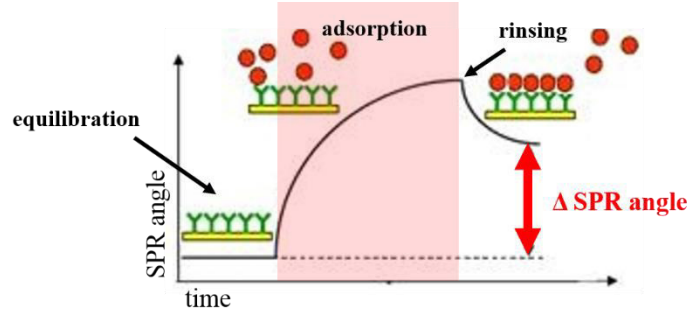
Figure 2. Schematic sensogram of an adsorption experiment.

The evaluation of SPR data provides either the adsorbed mass without coupled water or the thickness and refractive index of the adsorbed layer. The amount of adsorbed mass is calculated from the change in SPR angle upon adsorption according to the deFeijter equation (2).[38]

$$\Gamma = \frac{\Delta\theta \times k \times d_p}{dn/dc} \tag{2}$$

where Γ is the surface concentration, $\Delta\Theta$ is the change in SPR angle, κ is the sensitivity factor obtained from calibration of the instrument, d_p is the thickness of the sample (approximated to be 100 nm) and dn/dc is the refractive index increment of the adsorbed material.

The determination of the thickness and the refractive index of an adsorbed layer is achieved by simulation of the SPR spectra via a multilayer model. The simulations are based on Fresnel equations and the applied models comprise the thickness and refractive index of each layer present in the sample (glass, metal, sample, adsorbed layer). The simulation at a single wavelength provides a refractive index (n) – thickness (d) continuum without a unique solution. In order to determine a unique solution, measurements at two wavelengths resulting in two different sets of $n - d$ continua are required. The refractive index is dependent on the wavelength, therefore, the $n - d$ continuum measured at one wavelength can be shifted to the other wavelength via the chromatic dispersion ($dn/d\lambda$). The $n - d$ curves obtained at both wavelengths are plotted in the

same graph. The *n − d* curve of one wavelength is shifted by the *dn/dλ* value of the corresponding material. The resulting intersection point provides the unique solution. In special cases, the investigated layer consists of more than one material. Then, the curves can be shifted with the *dn/dλ* values of those substances leading to more intersections. The composition of the studied film is calculated from the resulting refractive indices. A re-estimation of the *dn/dλ* value for the film with known composition is performed and the original curve is shifted with the new *dn/dλ* value yielding the unique solution.[50]

The second method for the evaluation of thickness and refractive index of a sample is the 2-media approach. It is similar to the 2-wavelength method, however, spectra are attained in two media instead of measuring at two wavelengths. The intersection of the *n − d* continua of both media provides the unique solution for the adsorbed layer. It has to be noted that a difference in refractive index of the two media is required to obtain reliable results from this approach.[51]

Quartz Crystal Microbalance and Dissipation (QCM-D)

QCM-D measures the change in frequency (*Δf*) and dissipation (*ΔD*) of an oscillating piezoelectric quartz crystal upon increase/decrease of mass at the surface, making it a useful tool in the investigation of adsorption processes.[52] The change in mass (*Δm*) is calculated according to the Sauerbrey equation (3).

$$\Delta m = \frac{\Delta f}{n} \tag{3}$$

where *C* is the Sauerbrey constant (-0.177 mg·Hz^{-1}·m^{-2} for a 5 MHz crystal) and *n* is the overtone number.[53]

The Sauerbrey equation is applicable for rigid, inelastic layers coupled to the oscillation of the crystal. Viscoelastic films, which are not completely coupled to the crystal's oscillation, lose

energy during oscillation, thus making the introduction of another parameter – the dissipation – necessary. The dissipation is defined as follows.

$$\Delta D = \frac{E_{diss}}{2 \pi E_{stor}} \tag{4}$$

where E_{diss} is the energy dissipated and E_{stor} is the total energy stored during one oscillation cycle.

The dissipation is high for soft films, whereas rigid layers display small dissipation values. The ΔD vs. Δf plot can be utilized to determine the type of film. A constant slope indicates a rigid film, while deviations in the slope are found for viscoelastic layers. The mass change for viscoelastic films can be determined by viscoelastic modelling, e.g. Voight modelling.[54,55]

Atomic Force Microscopy (AFM)

Atomic force microscopy has gained high importance in the field of surface science since it was first reported in 1986.[46] The method enables the investigation of the surface structure on the atomic scale. Surface imaging is accomplished by simply scanning the surface with a sharp tip fixed on a cantilever while it is maintained at constant force or constant height above the sample. As the tip moves along the features of the surface, the cantilever is deflected. This deflection is monitored by a beam of laser light reflected from the cantilever onto a photodiode. Then, either the height deviation (in constant force mode) or the deflection force on the sample (in constant height mode) is recorded, generating an image. Besides imaging a surface, AFM is able to determine, for instance, the mechanical properties, such as hardness and elasticity, of a surface. Furthermore, the observation of surfaces in liquid is possible. The most recent advance in AFM technology are so-called 'fast scan' instruments capable of monitoring surfaces in real-time, for example, during enzymatic degradation or adsorption.[56–58]

Zeta-Potential Determination

The zeta potential is the electric potential at the shear plane of the interfacial electric double layer. It describes the potential difference between the medium and a stationary layer of fluid attached to a particle or a surface. Detailed chemistry and ion distributions at the liquid-solid interface affect the zeta potential. The determination of the zeta potential is achieved by indirect measurement.[59,60] One option to determine the zeta potential is via the streaming (oscillation) potential. The streaming potential generated by a pressure-driven flow through a channel is measured, and the zeta potential (ζ) is calculated from the following equation according to Smoluchkowski (5).

$$\zeta = \frac{dU}{dp} \times \frac{\eta}{\varepsilon_r \times \varepsilon_0} \times \kappa \tag{5}$$

where U is the streaming potential, p is the pressure, η is the viscosity of the fluid, ε_r is the relative permittivity of the fluid, ε_0 is the dielectric constant of vacuum and κ is the conductivity of the fluid.[61]

State of the art electro kinetic analyzers enable the real-time observation of adsorption processes at various surfaces.

X-Ray Photoelectron Spectroscopy (XPS)

The basic principle of XPS can be described as follows. X-ray radiation is directed at a sample where the incident X-ray photon interacts with an electron present in a certain shell of an atom leading to the emission of a photoelectron. An electron from a higher level shell fills the vacancy resulting in either X-ray fluorescence or radiation-free Auger emission. The kinetic energy of the outgoing photoelectron is measured and related to the electron binding energy. Thereby, the element and atomic level of which the photoelectron was emitted is determined.[62,63] Since the measurements are done under ultra high vacuum ($< 10^{-9}$ mbar), XPS cannot be used for liquid

samples.[64] Besides the elemental composition, XPS allows for gaining information about the chemistry of the surface as well. Therefore, it is frequently applied to corroborate the results of SPR, QCM-D or other techniques that indirectly measure the adsorption of a compound.

Fluorescence Detection Techniques

The application of fluorescence labelling in order to detect molecules during adsorption has gained a lot of significance over the past decades. Fluorescence detection techniques provide astonishing sensitivity (down to a single molecule), user-friendly handling and versatility. There are two classes of instruments, namely sensing and imaging devices. Sensing devices focus on a fixed spot on the sample, whereas imaging techniques visualize a certain area. Techniques capable of imaging and sensing are, for instance, total internal reflection fluorescence (TIRF)[65] and supercritical angle fluorescence (SAF) detection[66]. Fluorescence correlation spectroscopy (FCS)[67] and Förster resonance energy transfer (FRET)[68] are able to monitor aggregation and folding processes. Near-field scanning optical microscopy (NSOM)[69] even overcomes the Abbe-limit of resolution by combining the scanning mechanism of AFM and near-field optics. Promising developments in the area of fluorescence detection are, for instance, stimulated emission depletion (STED) microscopy[70], saturated pattern excitation microscopy (SPEM)[71], photoactivated localization microscopy (PALM)[72] and stochastic optical reconstruction microscopy (STORM)[73]. Disadvantages of fluorescent detections techniques include the labelling of the investigated molecules, since its influence on the adsorption cannot be excluded. Another problem is the effect of varying local conditions on the emission intensity of fluorophores, which influences the experimental results.[2]

PART I – Protein-Polysaccharide Interactions

Contents

1) Niegelhell, K.; Süßenbacher, M.; Sattelkow, J.; Plank, H.; Zhang, K.; Spirk, S. Bound vs Free Fatty Acids in Cellulose – How Bound and Free Fatty Acids in Cellulose Influence Nonspecific Protein Adsorption, *submitted to Biomacromolecules* (**August 2017**).

2) Strasser, S.; Niegelhell, K.; Kaschowitz, M.; Markus, S.; Kargl, R.; Stana-Kleinschek, K.; Slugovc, C.; Mohan, T.; Spirk, S. Exploring Nonspecific Protein Adsorption on Lignocellulosic Amphiphilic Bicomponent Films, *Biomacromolecules* **2016**, *17* (3), 1083–1092.

3) Niegelhell, K.; Süßenbacher, M.; Jammernegg, K.; Ganner, T.; Schwendenwein, D.; Schwab, H.; Stelzer, F.; Plank, H.; Spirk, S. Enzymes as Biodevelopers for Nano- and Micropatterned Bicomponent Biopolymer Thin Films, *Biomacromolecules* **2016**, *17* (11), 3743–3749.

4) Mohan, T.; Niegelhell, K.; Nagaraj, C.; Reishofer, D.; Spirk, S.; Olschewski, A.; Stana Kleinschek, K.; Kargl, R. J. Interaction of Tissue Engineering Substrates with Serum Proteins and Ist Influenec on Human Primary Endothelial Cells, *Biomacromolecules* **2017**, *18* (2), 413–421.

5) Niegelhell, K; Ganner, T.; Payerl, C.; Plank, H.; Jantscher-Krenn, E.; Spirk S. Adsorption Behavior of Lectins – A MP-SPR Study, *working version*.

6) Weissl, M.; Niegelhell, K.; Reishofer, D.; Zankl, A.; Innerlohinger, J.; Spirk, S. Homogenous Cellulose Thin Films by Regeneration of Cellulose Xanthate – Properties and Characterization, *submitted to Cellulose* (**July 2017**).
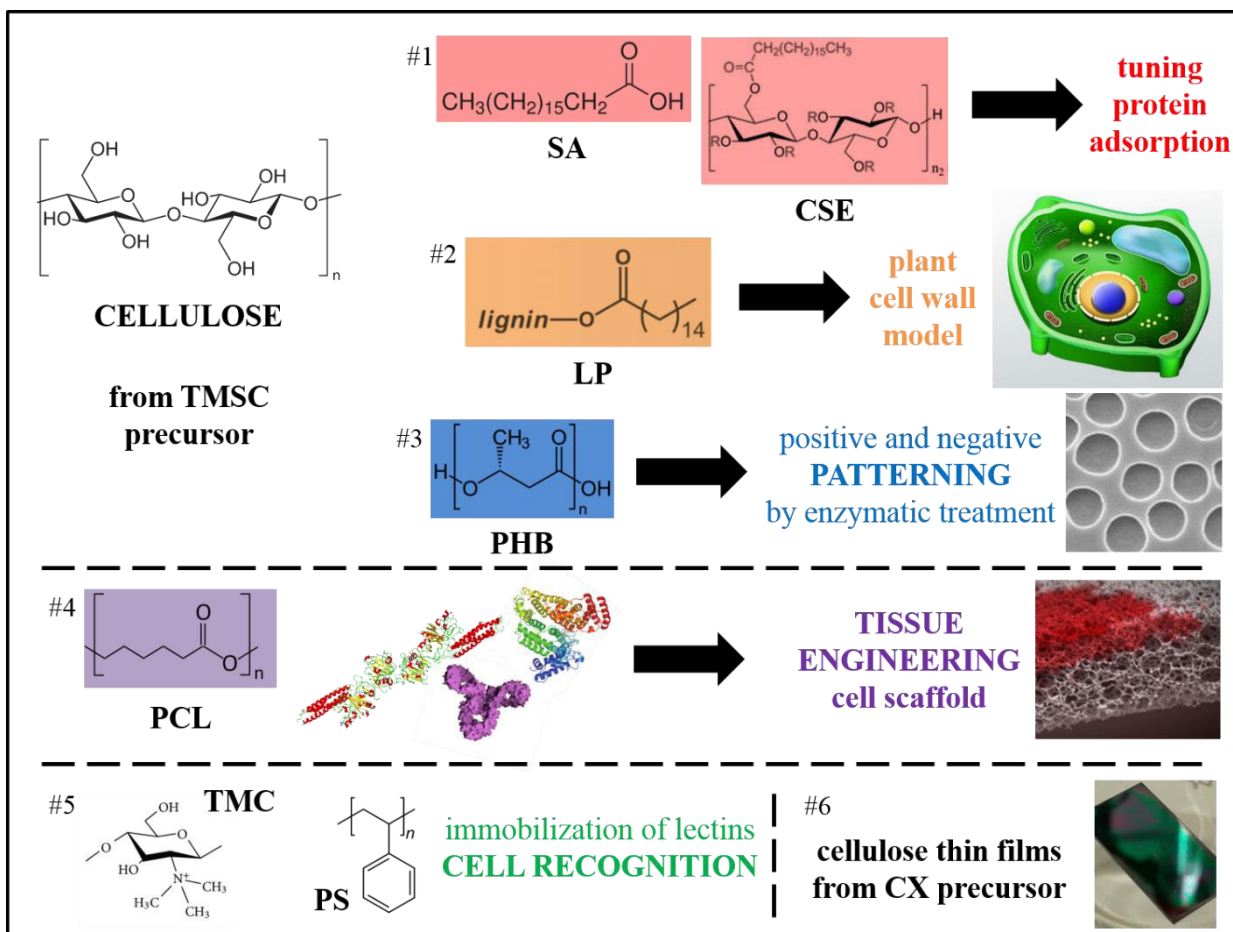
Protein-Polysaccharide Interactions

The interactions of proteins with polysaccharide surfaces are relevant in many fields of applications, such as anti-fouling coatings, sensor devices or tissue engineering. In this chapter, the investigation of parameters influencing adsorption phenomena, and the tuning of those phenomena is reported, as well as its utilization to develop smart materials (**Figure 3**).

Papers #1-#3 are devoted on how to tune protein adsorption of cellulosic materials via preparation of blend films with biopolymers or polysaccharide derivatives. With paper #1 we aimed for protein resistant surfaces by blending cellulose with hydrophobic cellulose derivatives. Paper #2 presents a model for the plant cell wall consisting of cellulose, lignin and fatty acids for the study of biochemical interactions with proteins. Paper #3 was focused on a "green" patterning procedure. Positive and negative type patterning was achieved by phase separation of biopolymers and subsequent developing via enzymatic treatment.

Paper #4 and #5 relate to practical aspects of protein deposition for cell adhesion experiments. In paper #4 polycaprolactone surfaces are tested for tissue engineering purposes, by adsorbing various serum proteins and studying its influence on cell growth. In paper #5, the interaction of specific sugar-binding proteins, lectins, with various surfaces is investigated as pre-test for protein immobilization. The overall goal is to develop cell recognition matrices, which work via detection of oligosaccharides present at the cell surface.

Paper #6 describes how protein adsorption takes place on different cellulosic thin film systems than those derived from TMSC. Therein, cellulose thin films were prepared by spin coating cellulose xanthate.

Figure 3. Overview on the presented topics regarding protein-polysaccharide interaction. Protein-polysaccharide interaction is tested for blends from cellulose and stearic acid (SA), cellulose stearoyl ester (CSE), lignin palmitate (LP) or poly-3-hydroxybutyrate (PHB). The nonspecific protein adsorption of polycaprolactone (PCL) and cellulose thin films prepared from cellulose xanthate (CX) was explored well. Lectin adsorption was studied at various surfaces comprising *N- N-N,*-trimethylchitosan (TMC) and polystyrene (PS).

For all papers, TMSC was used as cellulose precursor, since it is soluble in organic solvents such as chloroform, THF or toluene, facilitating the mixing with other hydrophobic components. Additionally, this allows the preparation of thin model films via a simple spin coating process. The conversion of TMSC to cellulose (**Figure 4**) and the inertness of the other blend components to

the acidic treatment were proven by ATR-IR spectroscopy and contact angle determination for all blends presented in this thesis.
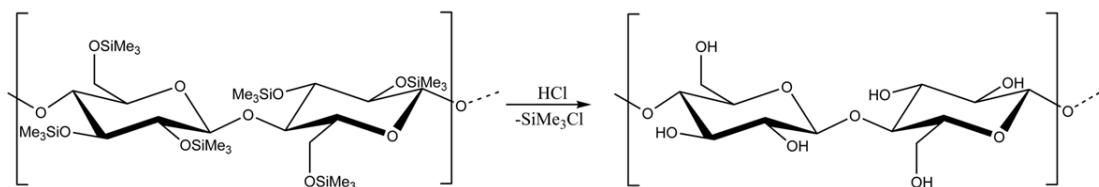

Figure 4. Conversion of TMSC to cellulose by cleaving of the TMS groups with acidic vapor treatment.

In the basic adsorption studies, *bovine serum albumin* (BSA), a widely used marker for nonspecific protein adsorption, was employed in order to guarantee comparability with various studies from literature.

Paper #1 describes the use of cellulose blends with bound or free fatty acids for tuning protein adsorption on cellulosic materials. Model blend thin films were prepared from trimethylsilyl cellulose (TMSC) and either cellulose stearoyl ester (CSE) or stearic acid (SA) at various ratios by spin coating and subsequent regeneration. The morphologies and surface roughness of the blend films were studied by AFM (**Figure 5**). The cellulose:CSE blend showed microphase separation behavior. The phases in the blends were assigned to the compounds by evaluation of the shrinkage of TMSC upon regeneration (63-68%, as reported in literature[74]) and treatment with chloroform (CHCl$_3$) removing CSE. The cellulose:CSE blend at the ratio 3:1 forms a continuous TMSC phase containing round CSE domains, whereas the inverse morphology is observed for the other ratios. The cellulose domain sizes are in the range of 350-400 nm for the cellulose:CSE ratios 3:1 and 1:3 and approximately 780 nm for the 1:1 blend. The phase separation behavior proceeds according to the transient bilayer theory.[75] In the beginning of the spin coating process, the two polymer phases stratify vertically with the polymer displaying lower surface free energy (SFE) migrating to the

polymer-air interface. This is followed by lateral phase separation caused by interfacial instabilities due to evaporation of the solvent leading to dewetting. Interestingly, phase separation of the cellulose:SA blend follows the same theory, although SA is a small molecule.[76] However, different structures compared to binary polymer systems arise. Cellulose builds a continuous phase, which is perforated by small SA domains, at all ratios. Surfaces of all cellulose:SA ratios show the same morphology only differing in the size of the SA domains (30-90 nm). However, for the cellulose:SA blend at the ratio of 1:3 additional SA platelets (2.6 ± 1.1 μm) occur, which could not be explained yet. This trend is represented in the SFE as well. Similar SFEs are found for the cellulose:SA blends at the ratios 1:1 (61.4 ± 0.2 mJ·m^{-2}) and 1:3 (61.8 ± 0.3 mJ·m^{-2}), whereas the blend at a ratio of 3:1 features a lower SFE (42.2 ± 0.1 mJ·m^{-2}).
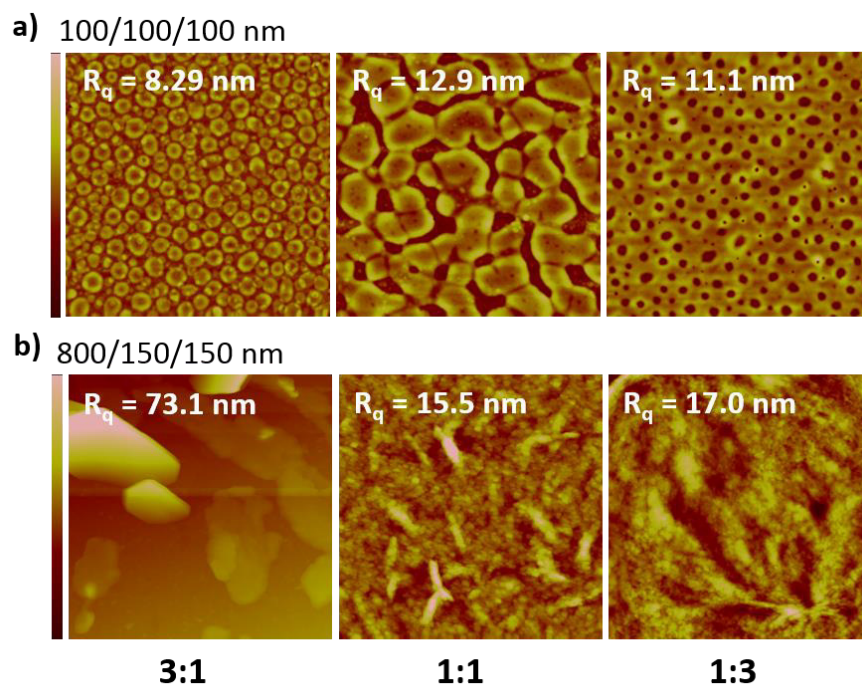
Figure 5. AFM height images and corresponding RMS roughness (R_q) of cellulose:CSE (a) and cellulose:SA (b) blend films at various ratios after exposure to HCl vapors (picture size 10×10 μm^2).

After thorough characterization of the blends, their behavior towards proteins was examined at the example of BSA (**Figure 6**). MP-SPR spectroscopy revealed fast adsorption kinetics for BSA onto the cellulose:CSE surfaces. An overshoot effect showing reorganization of the proteins[2] on the surfaces was detected, which was more pronounced for blends with higher CSE content. The extent of BSA adsorption was higher for the pure CSE surfaces (0.8 ± 0.1 mg·m^{-2}) and the cellulose:CSE blend at the ratio 1:3 (0.7 ± 0.1 mg·m^{-2}), which is referable to the high SFE of those surfaces, thus favoring hydrophobic interactions. Compared to the low protein interaction capacity of cellulose, blends at the ratios 3:1 and 1:1 offer an even lower adsorbed amount. These results can be explained by the adsorption mechanism of BSA.[77] The growth of a BSA monolayer from island-like structures formed in the beginning of the adsorption process is disrupted by the cellulose domains. This effect is less pronounced for the cellulose:CSE ratio 1:3, where the CSE phase is only perforated by small cellulose features.
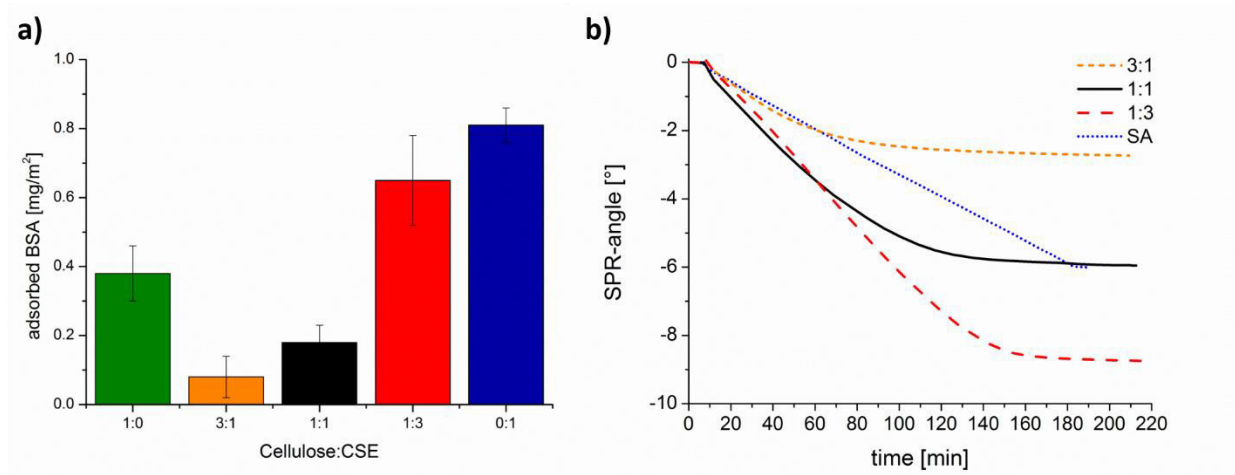

Figure 6. Amounts of adsorbed protein on cellulose:CSE blend films calculated from change in SPR-angle (a) and sensograms of cellulose:SA blends measured at 785 nm during rinsing with 1 mg BSA·ml^{-1} until a steady signal was obtained (b).

Protein adsorption onto the cellulose:SA blends, the fatty acid acts as a sacrificial compound, which is removed upon rinsing with BSA solution. This originates from the ability of BSA to form complexes with fatty acids.[78–80] The increase of SA content in the blend is accompanied by faster removal of more material from the surfaces. It took 80, 130 and 150 min for the cellulose:SA blends of ratios 3:1, 1:1 and 1:3, respectively, to reach a steady signal upon rinsing with BSA solution at a concentration of 1 mg·ml^{-1}. The experiment for pure SA was stopped after 180 min. Surfaces were resistant to protein adsorption at higher BSA concentrations as well, for instance at 50 mg·ml^{-1} which is the concentration of albumin in the blood.[81] In both experiments, the formed BSA-SA complex sticks better to surfaces where the SA residue is embedded in a large SA phase, due to cohesion, rather than in the case where SA is surrounded by cellulose.

In conclusion, the protein adsorption on cellulosic materials is tunable by blending cellulose with bound or free fatty acids. The added amount of hydrophobic compound in cellulose:CSE blends controls the adsorbed amount of protein, whereas cellulose:SA blends display protein resistance. The fundamental insights into nonspecific protein interactions at hydrophobized cellulose surfaces acquired in this study provide the basis for the development of new applications of materials stemming from cellulose in life sciences.

Cellulosic blends can also be utilized to create model systems. In paper #2, a similar system to the cellulose:CSE blends was used to mimic the plant's cell wall. We deployed bicomponent blend thin films consisting of cellulose and esterified lignin to study the interactions at the interface of plant cell walls. Similar as for the fatty acids, we used BSA to explore nonspecific protein adsorption, since various proteins are present in the cell wall. Different cell wall compositions were mimicked by varying the ratio of the polymers. After detailed characterization of the esterified lignin (LP), the blends were prepared by spin coating LP with TMSC at 3 ratios.

Similar thicknesses (40-50 nm) and static water contact angles (approximately 40 °) were determined for the regenerated blends at all ratios. However, the morphology changed with the composition as determined by AFM (**Figure 7**).
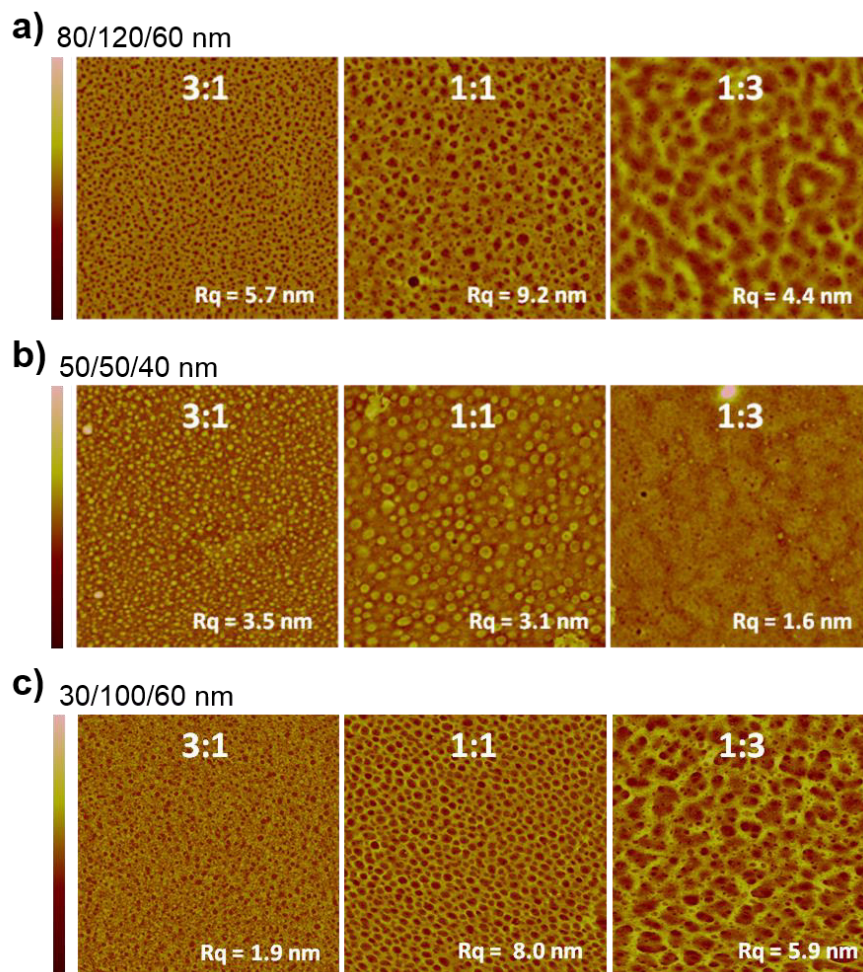
Figure 7. AFM height images and corresponding RMS roughness (R_q) of cellulose:LP blend films (a) after exposure to HCl vapors (b) and treatment with chloroform (picture size 10×10 μm^2).

After the assignment of the phases to the blend components by $CHCl_3$ treatment, which removes LP from the surfaces, continuous cellulose phases exhibiting dot-shaped LP domains were found for all ratios. The cellulose:LP blend at the ratio 1:3 seems to display two continuous phases before removal of the LP part. Increasing LP domain sizes (130-270 nm) are accompanied by increasing

amount of LP in the blend films. The aforementioned transient bilayer theory applies to the cellulose:LP binary polymer system as well. In this case, LP migrates to the substrate-polymer interface due to the higher amount of hydroxyl groups present on the LP backbone (1.7 mmol OH·g^{-1}) compared to the highly substituted TMSC (DS$_{Si}$ = 2.8-3.0). Then dewetting comes into play, one of the layers starts to break up and the resulting holes are filled with the other polymer.

Nonspecific protein adsorption was tested for all surfaces by QCM-D. Surprisingly, LP acts as a sacrificial layer comparable to the free fatty acid in cellulose:fatty acid blends. The higher the amount of LP in the blends, the more material is removed. However, within the timeframe of 120 min a detectable amount of the LP still remains in the blends. The palmitic acid residue of the esterified lignin might form a complex with BSA leading to the removal of LP rather than adsorbing the BSA to the surface as it was observed for cellulose:CSE films. Apparently, LP is less anchored in the cellulose matrix than CSE.

Our model is just the starting step in the investigation of processes occurring at plant cell walls, but nevertheless, we were able to obtain first results leading to a better understanding of interactions between proteins and lignocellulosic cell wall interfaces.

Besides the utilization in model systems, biopolymers can be used in blend thin films to generate patterns by phase separation, as has been shown for several conventional polymer mixtures. In paper #3, we explored how orthogonal enzymes can be exploited to act as selective biodevelopers (in analogy to lithographic developers) to create micro/nanostructured biopolymer thin films. We prepared blend thin films composed of cellulose and poly-3-hydroxybutyrate (PHB) at different ratios to control the domain shapes and sizes.

The blends were prepared by spin coating of TMSC and PHB mixtures at 7 ratios and subsequent conversion of TMSC to cellulose. The transient bilayer theory applies in this case too, whereby PHB is enriched supposedly at the substrate-polymer interface due to its higher SFE and polarity compared to TMSC. The resulting morphologies from phase separation display feature sizes (**Table 1**) in the range of 50 nm to 1.3 µm depending on the composition of the blend. For PHB:cellulose blends at ratios 10:1, 5:1, 3:1 and 1:1, round cellulose domains are distributed within a PHB continuous phase. Whereas, the inverse structures are obtained for the other blend ratios. A bicontinuous film is observed for the PHB:cellulose blend at a ratio of 1:3. RMS roughness increases for all blends upon regeneration due to shrinkage of the TMSC domains. Surfaces of PHB:cellulose blends at ratios 1:1 and 1:10 feature even higher SFEs than pure cellulose after conversion. At this point, it has to be noted that the SFE is not only dependent on the surface functional groups but also on the roughness of the substrate.

Table 1. Average and median feature sizes of PHB:cellulose blends after enzymatic treatment.

PHB:cellulose	3:1	1:1	1:3
average	126 ± 50	534 ± 209	1337 ± 204
median	106 ± 40	498 ± 174	1260 ± 182

The phase separated thin films were subjected to appropriate enzymes (either *PHB depolymerase* or *cellulase*), whereby one of the two biopolymers is selectively degraded, leaving behind the other phase. The surfaces of certain blend ratios are depicted in **Figure 8a** showing complete removal of either cellulose or PHB upon enzymatic treatment. The enzymatic degradation of cellulose thin films was studied extensively already.[82,83] Therefore, only the behavior of *PHB depolymerase* towards the blends was investigated by MP-SPR spectroscopy (**Figure 8b**). The experiments were conducted at 25 °C, which is not the optimum working temperature of the enzyme[84], leading to

slower degradation of PHB. As a reference value, PHB is completely removed from the blends after 20 min upon enzymatic treatment at 37 °C. Initially, the SPR angle increases upon injection of the enzyme into the flow cell followed immediately by a decrease indicating that adsorption of *PHB depolymerase* and degradation of the polymer occur simultaneously. Faster adsorption and earlier start of degradation was monitored for PHB:cellulose blends with large PHB content. The blend with the highest cellulose content is not degraded at all in the MP-SPR experiments. This can be attributed to the polar character of the blend at that ratio, which might impede interactions between the polymer and the enzyme since those are usually of hydrophobic nature.[84,85]
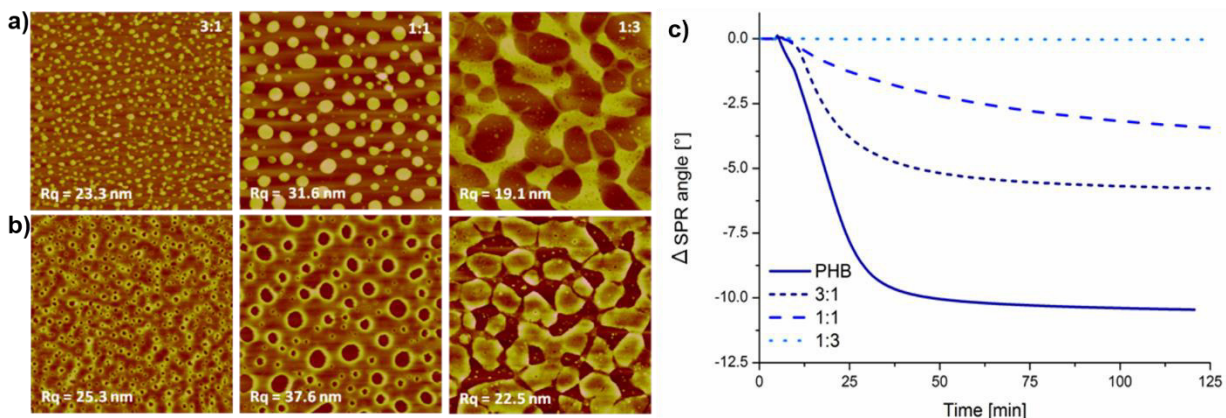

Figure 8. AFM images (size $10 \times 10\ \mu m^2$, z-scale $200\ nm$) after enzymatic degradation of PHB:cellulose thin films with *PHB-depolymerase* (a) or *cellulase* (b). SPR sensograms of enzymatic treatment with *PHB-depolymerase* ($50\ \mu g \cdot ml^{-1}$) acquired at 25 °C (c).

In addition to standard analytical techniques, we provided video AFM studies to visualize the enzymatic developing step of the "biodevelopers" as well. Our patterning approach enables a broad range of possible structures achievable only by blending two substances. Moreover, it provides the basis for further developments in the field of patterning methods facilitating the replacement of fossil based polymers by renewables.

During my doctorate I was not only interested in polysaccharides but also in biopolymers and biodegradable polymers in general, since these materials offer remarkable properties. They are subject to research regarding their utilization in tissue engineering, where protein adsorption is a key factor. However, there is a lack of basic studies concerning the interaction of proteins present in human body with possible tissue engineering materials. Therefore, I conducted MP-SPR experiments in a publication (paper #4) on the interaction of serum proteins with tissue engineering substrates made from polycaprolactone (PCL), wherein the influence of the adsorbed serum proteins on human primary endothelial cells was tested. This study gave insights into interactions between the living biological system, i.e. proteins from blood serum, and the scaffold material, which can be exploited for the applicability of PCL as tissue engineering material for endothelial cells. My contributions to the paper are summarized in the following pages.

PCL thin films were prepared by spin coating at various concentrations (0.1, 0.2, 0.4, 0.6, 0.8, 1.0 wt.%). The films were characterized in terms of thickness, wettability and morphology. Homogenous films were obtained at a concentration of 0.8 wt.% (**Figure 9**) and subjected to further studies. The interaction capacity of serum proteins, such as *fibrinogen* (FIB), BSA and *immunoglobulin G* (IgG), with those films was tested by MP-SPR spectroscopy and QCM-D at various pH values. MP-SPR data provides the dry mass of adsorbed proteins (**Figure 9**). The maximum adsorbed amounts are observed near the isoelectric point (IEP) of the investigated proteins (IPE$_{FIB}$ = 5.5, IEP$_{BSA}$ = 4.8, IEP$_{IgG}$ = 6.4-9), caused by reduced solubility of the proteins at that pH values. At physiological pH value (pH 7.4), the amount of proteins adsorbed follows the trend of IgG>FIB>BSA. The FIB/BSA ratio determined by MP-SPR spectroscopy at pH 7.4 is 3.25 showing hemocompatibility of the material via prevention of blood clot formation by adsorption of BSA instead of FIB.[86] At pH 5, protein adsorption onto PCL follows the trend of

FIB>>IgG>BSA. IgG does not undergo a maximum of adsorption at a particular pH value which is explainable by its high IEP. IgG is positively charged at all examined pH values. FIB and BSA adsorb to a lesser extent when negatively charged compared to when positively charged. This behavior might result from electrostatic repulsion of the substrate, since PCL is negatively charged due to formation of hydroxyl and carboxyl groups upon hydrolyzation in water.[87] In terms of kinetics, IgG adsorbs faster compared to the other proteins reaching an equilibrium after 10 min of adsorption. FIB adsorbs the slowest and does not reach an equilibrium at all, even after 30 min of adsorption.
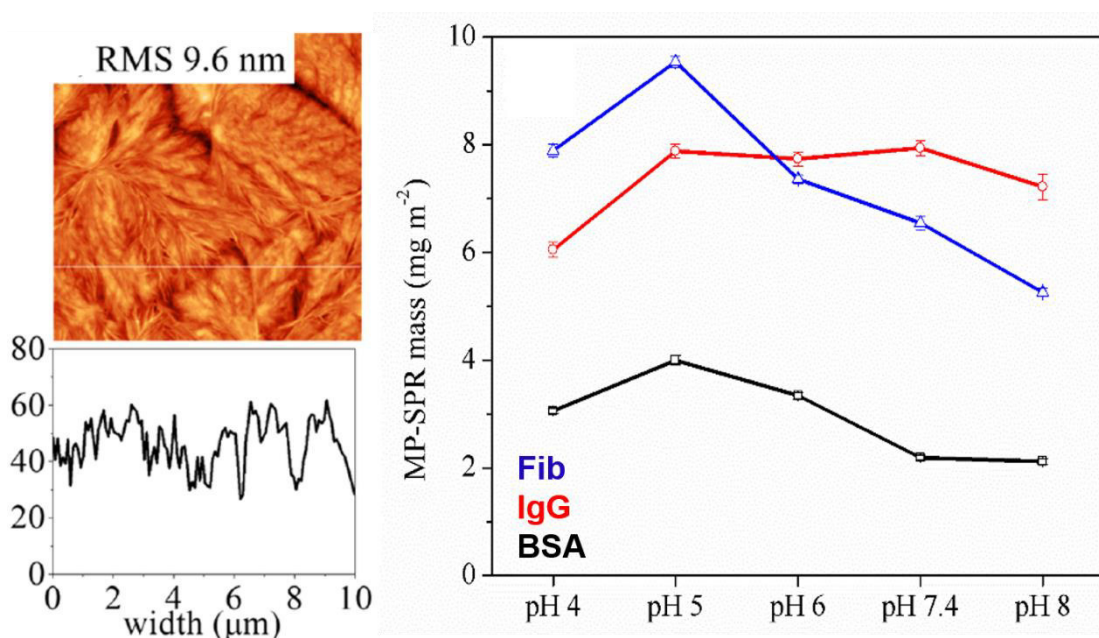

Figure 9. AFM image (z-scale 80 nm) and surface profile of the PCL film spin-coated from a polymer concentration of 0.8 wt.%. Irreversibly adsorbed mass of proteins (1 mg·ml^{-1}) on PCL films at different pH values.

Additionally, water contents of the adsorbed protein layer were calculated by comparing the dry adsorbed mass (MP-SPR spectroscopy) to the wet adsorbed mass (QCM-D). FIB contains the most water while BSA forms the least swollen layer at all pH values except for pH 5, where the FIB

layer comprises less water than the BSA layer. The higher degree of swelling of FIB and the dense packing of BSA is corroborated by the dissipation attained from QCM-D as well. In the paper, the protein treated surfaces were tested for human primary endothelial cell growth, showing PCL's possible application as growth scaffold.

The immobilization of proteins can be exploited in other fields as well, for instance, for the development of sensing devices. In this context, I was working with lectins, which are sugar binding proteins. Lectins display a variety of properties such as, anti-insect, anti-tumor, immunomodulatory, antimicrobial or HIV-I reverse transcriptase inhibitor activities.[88] Immobilized lectins enable the detection of carbohydrates or other compounds containing a sugar moiety. Therefore a basic adsorption study of two specific lectins was performed. A working version of the manuscript (#5) is attached to the thesis in the appendix. Future sensor applications are under investigation.

The adsorption behavior of two lectins (**Figure 10**), namely *ulex europaeus agglutinin I* (UEA - I) and *concanavalin A* (Con A) was examined. UEA-I is a fucose binding lectin extracted from common gorse[89], whereas Con A binds to mannose and glucose units and is extracted from jack bean.[90]

UEA-I
63 kDa
2 sub units

Con A
110 kDa
4 sub units of 4.2 nm x 4.0 nm 3.9 nm
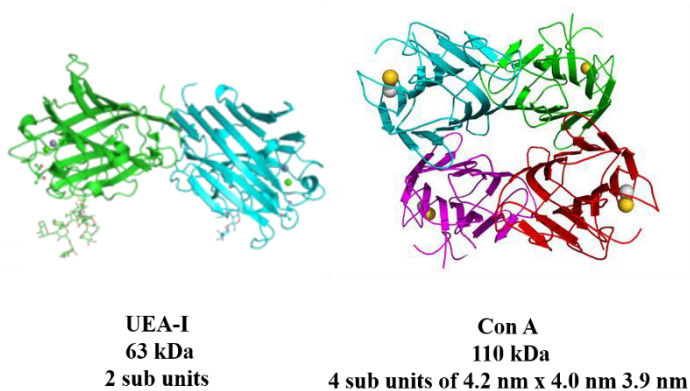
Figure 10. Structures, molecular weights and sizes of UEA-I and Con A.

The adsorption of those specific proteins onto various kinds of substrates was tested in real-time by MP-SPR spectroscopy in order to determine the type of interaction governing the behavior. Hydrophobic polystyrene (PS), gold and two hydrophilic surfaces, cellulose and *N,-N,-N*-trimethyl chitosan chloride (TMC) were employed as substrates. All substrates were characterized in terms of thickness, SFE and morphology. AFM images (**Figure 11**) reveal very homogeneous surfaces with RMS roughness ranging from 0.6-4.3 nm.
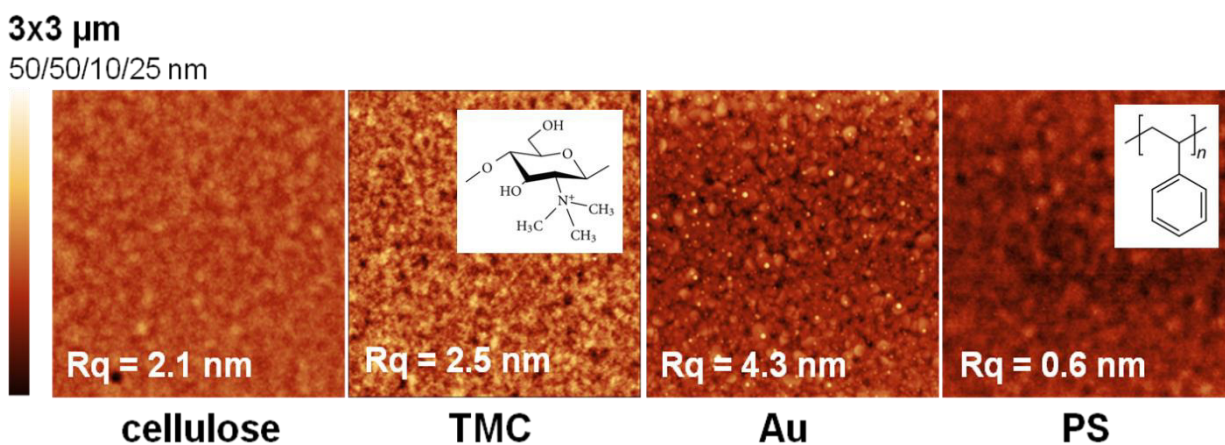

Figure 11. AFM height images of different substrates and corresponding RMS roughness (R_q).

PS displays the lowest SFE solely comprised of disperse contributions, whereas cellulose features the highest SFE. TMC is comparable to cellulose in terms of SFE, but polar contributions are smaller because of the presence of methyl groups.

The extent of protein adsorption (**Figure 12**) was evaluated from the change in SPR angle revealing the least adsorbed amounts for all proteins on the cellulosic substrate. The largest protein amounts were found on the PS surface. Hydrophobic interaction outweighs electrostatic attraction since proteins rather adsorb onto the hydrophobic PS substrate than the cationized TMC surface. Still, deposition of TMC onto cellulose enhances nonspecific interactions towards proteins compared to pure cellulose. At the investigated pH values (pH 5.5, pH 7.4) all of the proteins

display an overall negative charge ($IEP_{BSA} = 4.8$, $IEP_{ConA} = 4.5\text{-}5.5$, $IEP_{UEA\text{-}I} = 4.8$), therefore they are attracted to the cationic TMC surface and rather compelled by the slightly anionic cellulose surface. At the IEP, proteins are less soluble and therefore adsorb better. AFM images of the surfaces after adsorption and drying and the adsorbed amount were correlated. Larger adsorbed amounts are accompanied by a decrease of RMS roughness for cellulose, gold and TMC substrates, unlike the extremely flat PS surface, which exhibits higher roughness in that case.
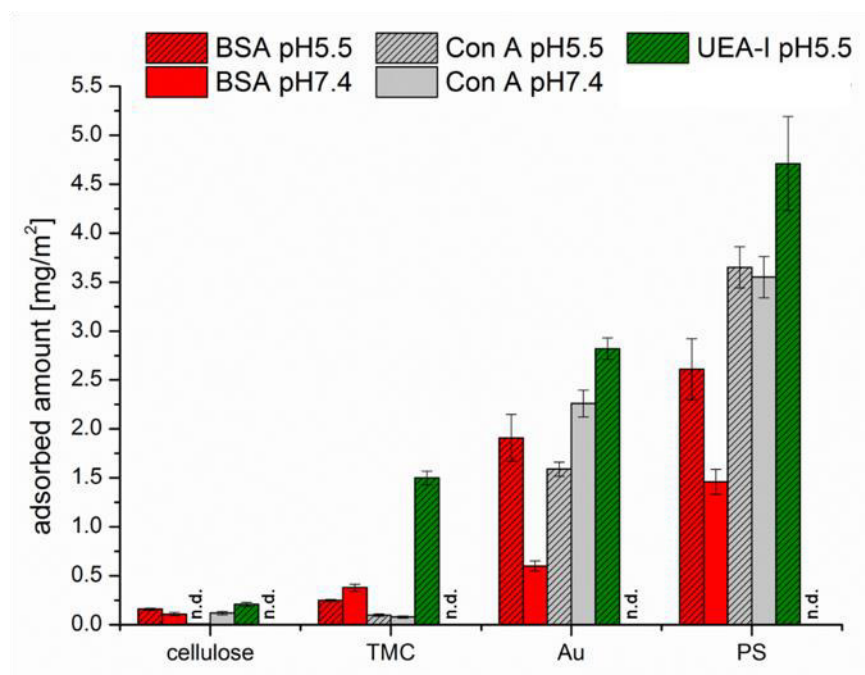
Figure 12. Adsorbed amounts of protein calculated from change in SPR-angle on various substrates at two pH values.

The results can be rationalized in the following way. The adsorption behavior of the lectins is in good agreement with BSA. Larger adsorbed amounts and faster kinetics on the PS surface prove that hydrophobic interactions govern the nonspecific interaction of the studied proteins. The low adsorption capacity of cellulose is of advantage for the utilization in biosensor development since support materials require protein resistance thereby preventing the use of additional blocking agents.

In the abovementioned investigations regarding protein adsorption on cellulose, TMSC was employed as a precursor to prepare homogenous cellulose films with defined properties. However, there are more methods to prepare such films, for example by the use of other cellulose derivatives, dissolution of cellulose or suspensions of cellulose.[74,91,92] In our working group, a recently investigated approach for this purpose is the application of cellulose xanthate (CX), which has mostly been used for the production of regenerated cellulose fibers.
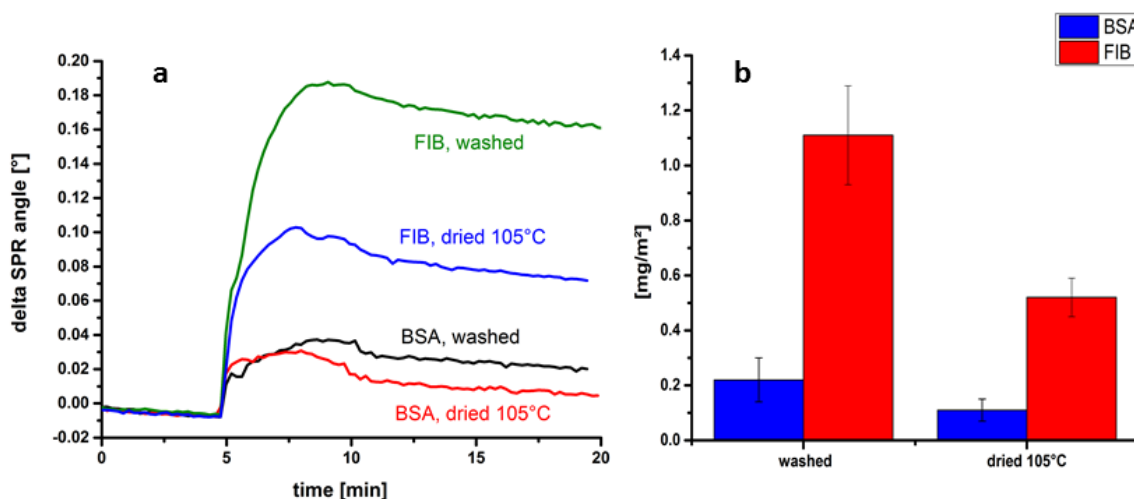

Figure 13. Sensogram recorded at 670 nm during the adsorption of FIB and BSA on washed and heat treated films prepared from 1 wt.% CX solutions (a) and the amount of protein adsorbed on these films (b).

The cellulose films formed from CX as a precursor were – amongst others – tested for protein adsorption by MP-SPR spectroscopy at the example of BSA and FIB. Experiments were conducted with washed cellulose films as well as washed and dried ones (**Figure 13**). The adsorbed amounts on washed surfaces were determined to be 1.11 ± 0.18 mg·m^{-2} and 0.22 ± 0.08 mg·m^{-2} for FIB and BSA, respectively. Preferred adsorption of FIB can be attributed to the high molar mass of FIB (340 kDa) compared to BSA (66 kDa) leading to larger contact area of the protein to the surface. Heat treatment of the films lead to a decrease in adsorbed protein mass (0.55 ± 0.07 mg·m^{-2} for

FIB and 0.11 ± 0.04 mg·m^{-2} for BSA), which is explainable by the reduction of roughness upon drying. As roughness is decreasing, the surface area for protein interaction is minimized too. Adsorption kinetics change insignificantly upon treatment, however, all of the surfaces display an overshoot effect related to reorganization of the proteins upon adsorption.[2]

The last part of this chapter compares results from all of the papers presented concerning protein-polysaccharide interaction (**Figure 14**). Cellulose thin films prepared from CX feature similar behavior towards proteins like those produced from TMSC. The extent of BSA adsorption on films made from CX ranges from 0.1-0.2 mg·m^{-2}, whereas the adsorbed amount onto surfaces spin coated from TMSC is 0.2-0.4 mg·m^{-2}. Depending on the adsorption parameters, e.g. adsorption time, flow rate or ionic strength, values reported in literature range from 0.3-0.6 mg BSA·m^{-2}.[21,24] In general, cellulose offers rather low protein interaction capacity compared substrates of more hydrophobic nature, such as PCL (ca. 2.0-4.0 mg BSA·m^{-2}), PHB (1.25 ± 0.05 mg BSA·m^{-2}) and PS (ca. 1.5-2.5 mg BSA·m^{-2}). The polar cellulose surface seems to hinder interactions with proteins, whereas hydrophobic substrates favor adsorption.

The same trend is observed for PHB:cellulose blends. SFE and polar contributions to the SFE of PHB:cellulose blends at ratios 1:1 and 1:3 are even higher than those of pure cellulose. The extent of BSA adsorption is reduced for these surfaces. However, blends from cellulose and CSE at ratios of 3:1 and 1:1 display lower affinity to BSA but the SFEs are in the same range as the SFE of cellulose. This indicates that reduced protein interaction at binary polymer blends is rather induced by the morphologies obtained from phase separation than solely the orientation of the surface functional groups. Supposedly, the cellulose inside the blends disturbs the growth mechanism of the BSA layer.
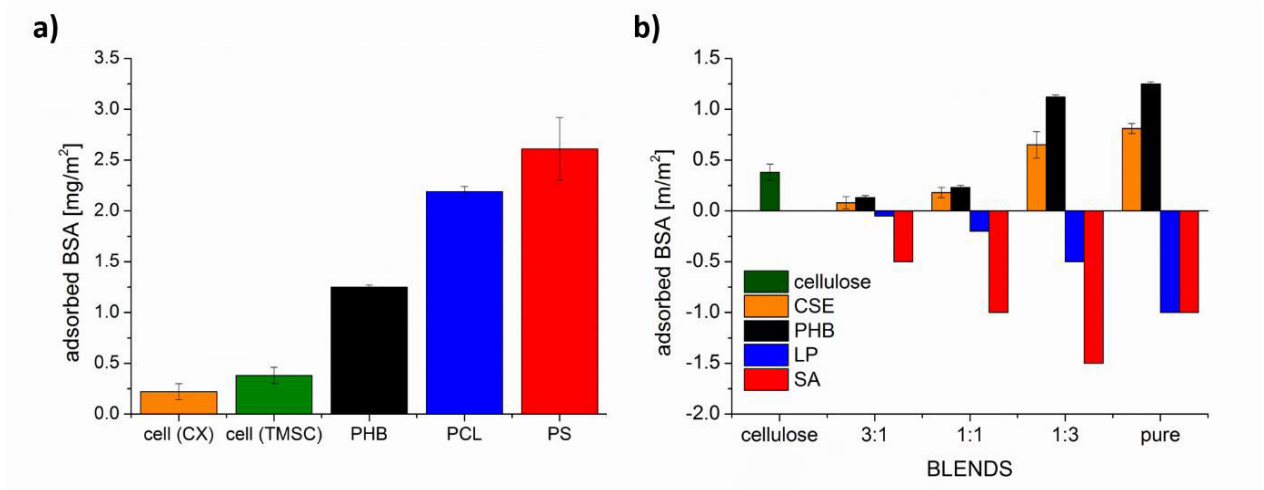
Figure 14. Adsorbed amounts of BSA on different polymers (a) and blend thin films at various ratios (b) measured at pH 7.4 with BSA concentration of 1 mg·ml⁻¹ except for PS (BSA = 0.1 mg·ml⁻¹). Values for LP, SA and corresponding blends are added to show the observed trends and do not display real values.

In contrast to cellulose:CSE and PHB:cellulose blends, which allow the tuning of protein adsorption of cellulosic materials by the amount of CSE or PHB added, surfaces with protein resistance were investigated as well. Those surfaces were prepared by blending cellulose with either LP or SA. In both cases, the fatty acid residue supposedly builds a complex with BSA leading to the removal of LP or SA thereby inhibiting adsorption. Nevertheless, the cellulose:SA blends show faster complete removal of the non-cellulosic compound from the blends upon rinsing with protein solution, which could be disadvantageous with regard to the lifetime of the anti-fouling surface.

PART II – Polysaccharide-Polysaccharide Interactions
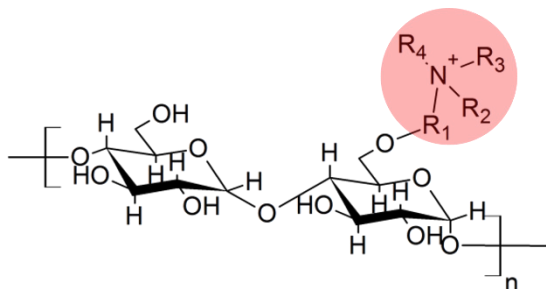
Contents

Polysaccharide-Polysaccharide Interactions

As shown in the first chapter, the interactions occurring at surfaces are governed by the properties of the adsorbing species as well as the surface chemistry and morphology of the substrate. Surface properties and molecular interactions at the surface are tunable by the adsorption of various substances onto a materials surface. For instance, the extent of protein adsorption at cellulosic surfaces is enhanced by adsorbing cationic polysaccharides, as shown by Mohan et al..[21,23] The adsorption behavior of cationic celluloses with different charge density was tested as well. Interestingly, the cationic cellulose displaying more charges on the polymeric backbone adsorbed to a lesser extent than the lowly charged one, presumably due to its better solubility. Comparable amounts of adsorbed protein were found on surfaces treated with either of the compounds indicating that the adsorption behavior of the polysaccharide used to tune protein adsorption plays an important role.

Papers #7 and #8 cover the interaction of cationic starches and xylan with cellulose. Both polymers are highly interesting for paper industry, since they are employed in paper production to control paper properties. Therefore, interaction experiments are performed to enhance product quality.

The adsorption of industrially relevant cationic starches (CS) onto cellulose thin films acting as a model for pulp in this case was examined. The CS (**Figure 15**) stemmed from different sources (potato, pea, corn) and featured rather low degrees of substitution ranging from 0.030 to 0.062 (**Table 2**). Molecular weights were determined by size exclusion chromatography (**Table 2**) and are in good agreement with values from literature. Amylose and amylopectin are reported to feature molar masses of 10^5-10^6 g·mol^{-1} and 10^7-10^8 g·mol^{-1}, respectively.[93] Particle sizes (median hydrodynamic diameters) of the CS in solution range from 57 nm (CS D) to 100 nm (blend, CS C).

Bimodal size distributions were found for all starches except for CS D, which contains only amylopectin, indicating that starch clusters are formed by aggregation of amylose and amylopectin.[94] Both particle size and molecular weight are affected by the amylose/amylopectin ratio.

Figure 15. Structural formula of CS.

Table 2. List of CS including information on source, dry solids content, degree of substitution (DS), molecular weight and polydispersity index (PDI).

Source	Label	Amylose Content [%]	DS[a]	M_n [g·mol^{-1}]	M_w [g·mol^{-1}]	PDI
corn	A	30	0.058	7.7×10^4	1.7×10^5	2.18
potato	B	20	0.030-0.036	4.3×10^5	1.4×10^6	3.20
corn, potato	Blend A:B 80:20	20-30	0.050-0.056	n.d.	n.d.	n.d.
pea	C	40-70	0.047	3.7×10^5	7.4×10^5	1.99
waxy corn	D	0-1	0.062	1.3×10^6	2.4×10^6	1.94

[a] According to the manufacturer. (n.d. non determined)

The interaction of the CS with cellulose was studied by MP-SPR spectroscopy under flow conditions using a concentration of 1.0 mg·ml^{-1} in the absence of any electrolyte. All investigated

starches adsorb irreversibly onto the cellulose thin films. All samples display rather fast kinetics, except for CS B, which can be explained by its high poly dispersity index (PDI). Polymers with high PDI are prone to slow adsorption due to replacement of smaller, faster adsorbing molecules by larger ones.[95] The extent of protein adsorption strongly varies for the employed starches ranging from 0.74 ± 0.15 mg·m^2 (CS D) to 3.94 ± 0.13 mg·m^2 (CS A). CS deposition was further substantiated by XPS experiments, revealing nitrogen, originating from the cationization procedure, on all surfaces treated with CS, whereas no nitrogen was detected on the bare cellulose surface. AFM images after adsorption of CS indicate preferred deposition of the starches in pores and holes of the samples. The SFE and its polar contribution of the thin films increased after adsorption of the charged compounds showing higher hydrophilicity due to the presence of the CS substance. The results (**Figure 16**) were concluded as follows. The adsorption capacity for CS with the same size is governed by the DS. A high DS leads to a higher extent of starch deposition on the cellulosic substrates, since more positive charges of the adsorbing species favor electrostatic attraction to the slightly negatively charged cellulose surface.[96] In these cases, electrostatic interactions outweigh the solubility of the polysaccharide. Whereas, particles size dominates the adsorption behavior for starches with very similar DS. Larger particles are less soluble and therefore adsorb to a higher extent than smaller ones. The conformation of the polymers and concomitant the availability of attachment sites are non-negligible factors as well. Both parameters are mainly affected by the amylose/amylopectin ratio of starch.

Consequently, the interaction of CS and cellulose is primarily influenced by the interplay of electrostatic interaction and solubility, which are in turn affected by e.g. charge density, particle size and conformation. The presented findings are still being evaluated with regard to their transferability to industrially produced cellulose materials.
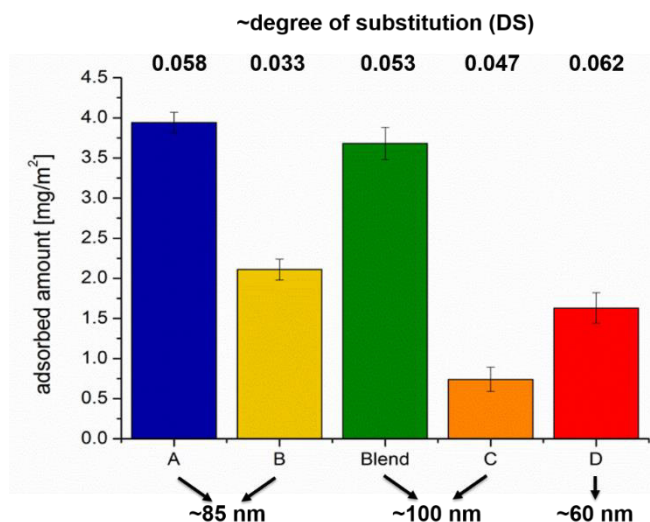
Figure 16. Overview of adsorbed amounts of CS on cellulose, DS and particles sizes of CS in solution.

The DS of the examined CS were low compared to charged polysaccharides applied for changing a material's properties by adsorption.[21,22,24] Therefore, a comparison of the behavior of the CS with the TMC employed in the lectin interaction study (paper #5) is presented. The TMC features a DS of 0.66. The adsorption parameters (30 min, 1 mg·ml^{-1}, 150 mM NaCl, pH 7) for TMC were chosen as reported from Ristić et al.[96], who studied the interaction of various cationized chitosans. The adsorption was monitored in real-time by MP-SPR spectroscopy and zeta potential experiments (**Figure 17**). From the change in SPR angle, the adsorbed amount (0.60 ± 0.05 mg·m^2) was calculated. The zeta potential of the negatively charged cellulose support (-27 mV) changed during adsorption of TMC to a positive value (35 mV). Although TMC features a DS that is approximately 10 times as high as the DS of the investigated CS, the adsorbed amounts are in the same order of magnitude. A high DS, i.e. charge density, leads to a better solubility of the compound, however, electrostatic interactions increase as well. These findings indicate that the adsorption behavior of charged polysaccharides is dominated by the solubility of the compound,

with only minor contributions from the electrostatic attractions between the adsorbing species and the substrate.
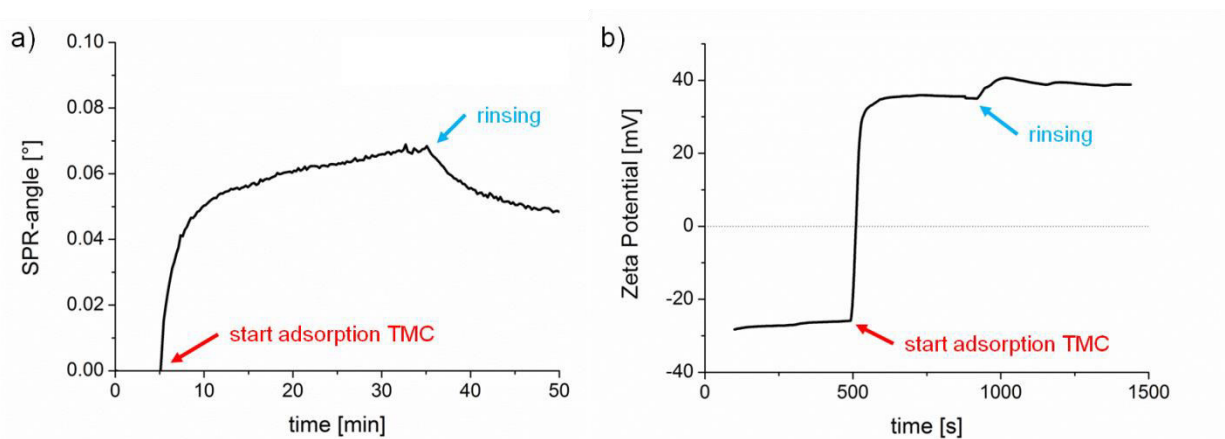
Figure 17. MP-SPR sensogram measured at 785 nm during adsorption of TMC onto a cellulose thin film (a) and the corresponding zeta potential curve (b).

As for slightly negatively charged polysaccharides, xylan (-28 mV at pH 7 in solution) adsorption onto cellulose thin films was studied within the scope of investigations on topography effects on AFM force mapping of xylan decorated cellulose films. The SPR data (**Figure 18**) shows slow adsorption kinetics, which does not reach an equilibrium state, even after one hour of adsorption time. When rinsing with buffer only an insignificant amount of xylan is removed. Since no values of *dn/dc* for xylan were available from literature, the determination of the adsorbed amount by calculation from the change in SPR angle (0.65 ±0.05 ° at 670 nm, 0.41 ± 0.03 ° at 785 nm) was not possible. Therefore, SPR experiments were evaluated by the 2-wavelength and the 2-media approach, resulting in xylan layer thicknesses of 5.1-5.6 nm. With the density of xylan (1.2 g·cm^3), the surface concentrations were calculated to be 6.0-6.7 mg·m^2. At this point, it has to be re-emphasized that SPR provides the dry mass of a sample. When the evaluation is performed with the *dn/dλ* and the refractive index values of non-swollen xylan in air, results refer to pure

xylan in the dry state. The thickness of the xylan in the wet state could be determined by including the *dn/dλ* of the ambient medium in the evaluation procedure, as will be shown in the next chapter.
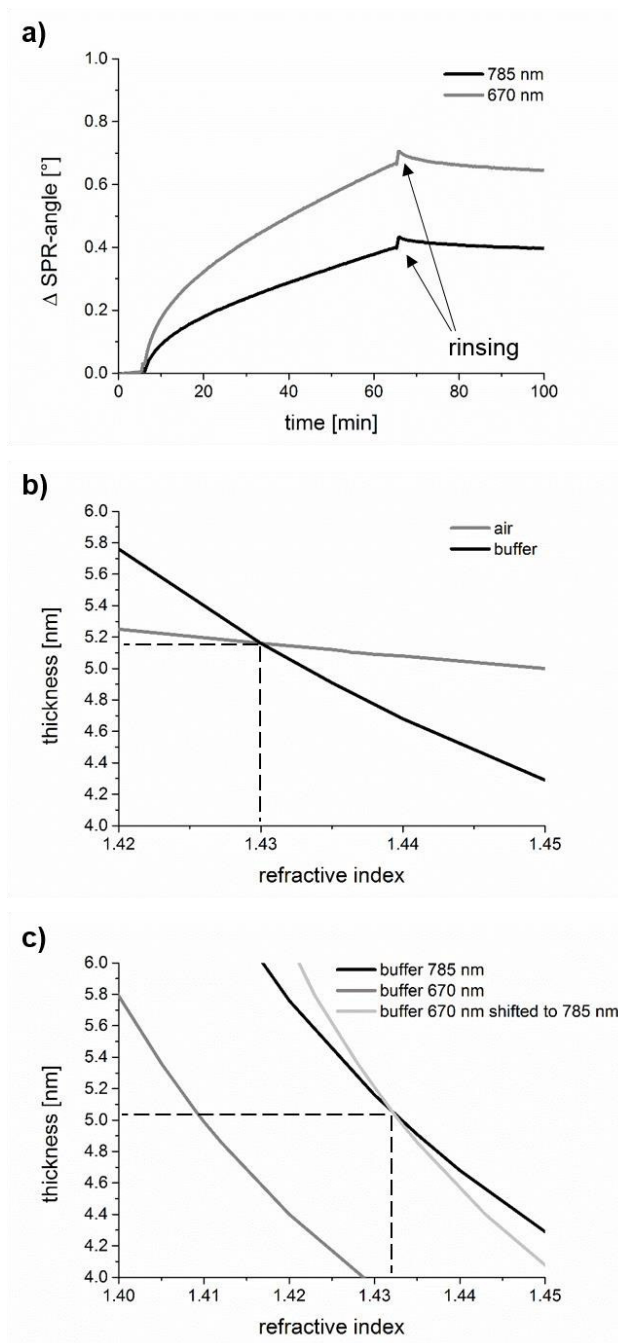
Figure 18. Adsorption of xylan (pH 8, c = 1 g·l⁻¹, flow rate 0.1 ml·min⁻¹) on cellulose thin films in dependence of the SPR angle (a) and data evaluation according to the 2-media (b) and 2-wavelength method (c) (dashed lines in b,c).

PART III – Insights into Adsorption Phenomena via Multilayer Analysis

Contents

Insights into Adsorption Phenomena via Multilayer Analysis

Several techniques are able to monitor adsorption phenomena in real-time, such as SPR spectroscopy and QCM-D. In the case of processes such as adsorption, swelling or chemical surface modification, it is desirable to differentiate between the surface regions and the bulk of a sample.

SPR spectroscopy data is evaluated by a multilayer fitting procedure based on Fresnel equations.[97,98] During evaluation, all of the layers present in the sample (i.e. glass substrate, chromium adhesion layer, gold coating, thin film sample and surrounding medium) are simulated. Up to now, the examined thin films were described by just one layer in this multilayer fitting procedure. In principle, it is possible to split the film into more than one layer, but this approach requires more information to obtain an accurate fit. Therefore, the combination of AFM, giving information about the surface topography, and MP-SPR spectroscopy could lead to a new method enabling the examination of changes in the bulk material and surface regions separately. The refractive index obtained from SPR spectroscopy can be used to calculate the composition i.e. the density of the different layers. Thereby, variations in direction of the z-axis could be detected inside a material.

In paper #9, an approach for such a multilayer analysis was investigated at the example of cellulose thin films. A model describing the examined thin film as a two-layer system was developed (**Figure 19**). The thin film is split into a roughness layer (*RL*), which contains the material (*mf*) and the ambient medium, and a bulk layer (*BL*). The thickness (d_{SPR}) and density (ρ_{SPR}) of the entire films is evaluated from SPR data. The *RLT* is attained from AFM and implemented into the multilayer fitting model used in the MP-SPR spectroscopy method. Then the

film is split into a top and a bottom layer in the simulation. The bottom layer (d_b, ρ_m^b) refers to the *BL*, whereas the top layer (d_t, ρ_m^t) provides information about the material inside the *RL*.
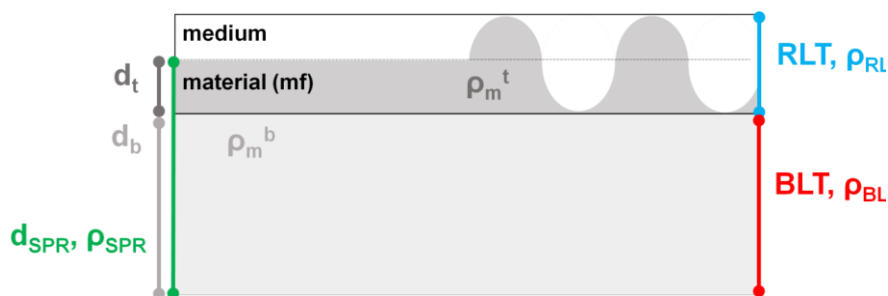
Figure 19. Graphical representation of the multilayer analysis model. The film consists of a roughness layer *RL* and a bulk layer *BL* with certain thickness *T* and density ρ. The thickness d_{SPR} and density ρ_{SPR} of the film are obtained via MP-SPR spectroscopy. The film is then split into a top (d_t, ρ_m^t) and a bottom (d_b, ρ_m^b) layer. The top layer provides information about the material fraction (*mf*) inside the *RL*, whereas the bottom layer refers to the *BL*.

The studied cellulose thin films with low (R_q = 1.6 nm) and high (R_q = 4.5 nm) roughness displayed densities of 1.20 g·cm^{-3} and 1.11 g·cm^{-3}, respectively. By applying the presented multilayer density analysis approach, it was found that the films exhibit higher porosity in the surface regions, shown by a lower density of the outermost layers (smooth film 0.78 g·cm^{-3}, rough film 0.74 g·cm^{-3}), compared to the bulk (smooth film 1.22 g·cm^{-3}, rough film 1.14 g·cm^{-3}).

The validation of the approach was accomplished by comparison of the techniques in terms of material fraction, density and thickness of the surface regions. Therefore, calculations enabling the comparison were conducted. Results are collated in **Table 3** and are in good agreement, indicating good accuracy of the method. The presented multilayer density analysis approach for thin films serves as a tool for a more elaborate investigation of processes occurring at surfaces and interfaces than with standard methods.

Table 3. Comparison of results determined by MP-SPR spectroscopy and AFM of cellulose thin films measured in air. Values highlighted in grey were calculated for comparison.[a]

	low R_q		high R_q	
	AFM	**MP-SPR**	**AFM**	**MP-SPR**
d_t	-	3.5 nm	-	9.9 nm
ρ_m^t	-	0.78 g·cm^{-3} (52%)	-	0.74 g·cm^{-3} (49%)
d_b	-	31.5 nm	-	31.0 nm
ρ_m^b	-	1.22 g·cm^{-3} (81%)	-	1.14 g·cm^{-3} (76%)
RLT	**6.4 nm**	**6.7 nm**	**17.3 nm**	**19.6 nm**
ρ_{RL}	**0.38 g·cm^{-3} (25%)**	**0.42 g·cm^{-3} (28%)**	**0.36 g·cm^{-3} (24%)**	**0.41 g·cm^{-3} (27%)**
mf	**48%**	**55%**	**49%**	**57%**
BLT	-	d_b	-	d_b
ρ_{BL}	-	ρ_m^b	-	ρ_m^b
mf	-	**100%**	-	**100%**

[a]The shown percentages refer to the cellulose content.

Conclusions and Outlook

The thesis summarizes various investigations with the goal to get a better insight into parameters influencing processes occurring at surfaces. The presented studies do not only examine basic principles of adsorption phenomena, but also aim at the exploitation of such for the design of smart materials composed of renewable polymers. The results obtained during my doctoral thesis may lead to applications of, for instance, biopolymer blends for patterning processes or cellulose based blends for anti-fouling coatings. The adsorption study of cationic starches onto cellulose is currently under investigation for transferability to fibers and papers, potentially improving process quality.

Some of the topics covered in the thesis serve as basis for further ongoing research within our group. The multilayer density analysis method can be utilized to examine interaction phenomena in more detail compared to conventional techniques. In the future, we will study the swelling behavior of cellulose thin films. The aim of the research is to gain information on a possible swelling gradient inside the films.

The basic study on lectin adsorption has shown low nonspecific adsorption on cellulose, revealing that it is a good substrate for immobilization of the lectins for sensing applications, since nonspecific interactions decrease the sensitivity of sensor devices. Several approaches to optimize lectin immobilization were already made. This topic is currently under investigation and will address medically relevant issues and aims at the detection of molecules containing sugar moieties.

References

(1)   Nakanishi, K.; Sakiyama, T.; Imamura, K. *J. Biosci. Bioeng.* **2001**, *91* (3), 233–244.

(2)   Rabe, M.; Verdes, D.; Seeger, S. *Adv. Colloid Interface Sci.* **2011**, *162* (1-2), 87–106.

(3)   Jones, K. L.; O'Melia, C. R. *J. Memb. Sci.* **2000**, *165* (1), 31–46.

(4)   Kunz, W.; Henle, J.; Ninham, B. W. *Curr. Opin. Colloid Interface Sci.* **2004**, *9* (1), 19–37.

(5)   Höök, F.; Rodahl, M.; Kasemo, B.; Brzezinski, P. *Proc. Natl. Acad. Sci. U. S. A.* **1998**, *95* (21), 12271–12276.

(6)   Demanéche, S.; Chapel, J.-P.; Monrozier, L. J.; Quiquampoix, H. *Colloids Surf., B* **2009**, *70* (2), 226–231.

(7)   Bremer, M. G. E. G.; Duval, J.; Norde, W.; Lyklema, J. *Colloids Surf., A* **2004**, *250* (1), 29–42.

(8)   Vroman, L.; Adams, A. L. *Surf. Sci.* **1969**, *16*, 438–446.

(9)   Becker, A. L.; Henzler, K.; Welsch, N.; Ballauff, M.; Borisov, O. *Curr. Opin. Colloid Interface Sci.* **2012**, *17* (2), 90–96.

(10)   Mrksich, M.; Whitesides, G. M. *Annu. Rev. Biophys. Biomol. Struct.* **1996**, *25*, 55–78.

(11)   Frank, B. P.; Belfort, G. *Langmuir* **2001**, *17* (6), 1905–1912.

(12)   Whitesides, G. M.; Laibinis, P. E. *Langmuir* **1990**, *6* (1), 87–96.

(13)   Anand, G.; Sharma, S.; Dutta, A. K.; Kumar, S. K.; Belfort, G. *Langmuir* **2010**, *26* (13), 10803–10811.

(14)   Norde, W.; Lyklema, J. *J. Biomater. Sci.* **1991**, *2* (3), 183–202.

(15)   Norde, W.; MacRitchie, F.; Nowicka, G.; Lyklema, J. *J. Colloid Interface Sci.* **1986**, *112* (2), 447–456.

(16)   Facci, P.; Alliata, D.; Andolfi, L.; Schnyder, B.; Kötz, R. *Surf. Sci.* **2002**, *504*, 282–292.

(17)   Rabe, M.; Verdes, D.; Zimmermann, J.; Seeger, S. *J. Phys. Chem. B* **2008**, *112* (44), 13971–13980.

(18)   Wertz, C. F.; Santore, M. M. *Langmuir* **2002**, *18* (4), 1190–1199.

(19)   Minton, A. P. *Biophys. J.* **2000**, *86* (2), 339–247.

(20)   Minton, A. P. *Biophys. J.* **2001**, *80* (4), 1641–1648.

(21)   Mohan, T.; Niegelhell, K.; Zarth, C. S. P.; Kargl, R.; Köstler, S.; Ribitsch, V.; Heinze, T.; Spirk, S.; Stana-Kleinschek, K. *Biomacromolecules* **2014**, *15* (11), 3931–3941.

(22)   Mohan, T.; Ristić, T.; Kargl, R.; Doliska, A.; Köstler, S.; Ribitsch, V.; Marn, J.; Spirk, S.; Stana-Kleinschek, K. *Chem. Commun* **2013**, *49* (98), 11530–11532.

(23)   Mohan, T.; Findenig, G.; Höllbacher, S.; Cerny, C.; Ristić, T.; Kargl, R.; Spirk, S.; Maver, U.; Stana-Kleinschek, K.; Ribitsch, V. *Colloids Surf., B* **2014**, *123*, 533–541.

(24)   Orelma, H.; Filpponen, I.; Johansson, L. S.; Laine, J.; Rojas, O. J. *Biomacromolecules* **2011**, *12* (12), 4311–4318.

(25)   Taajamaa, L.; Rojas, O. J.; Laine, J.; Yliniemi, K.; Kontturi, E. *Chem. Commun.* **2013**, *49* (13), 1318–1320.

(26) Mohan, T.; Niegelhell, K.; Nagaraj, C.; Reishofer, D.; Spirk, S.; Olschewski, A.; Stana Kleinschek, K.; Kargl, R. J. *Biomacromolecules* **2017**, *18* (2), 413–421.

(27) Tang, L.; Eaton, J. W. *J. Exp. Med.* **1993**, *178* (6), 2147–2156.

(28) Liu, Z.; Jiao, Y.; Wang, Y.; Zhou, C.; Zhang, Z. *Adv. Drug Deliv. Rev.* **2008**, *60* (15), 1650–1662.

(29) Yamashita, K.; Aoyogi, Y.; Abe, H.; Doi, Y. *Biomacromolecules* **2001**, *2* (1), 25–28.

(30) Martín-Sampedro, R.; Rahikainen, J. L.; Johansson, L. S.; Marjamaa, K.; Laine, J.; Kruus, K.; Rojas, O. J. *Biomacromolecules* **2013**, *14* (4), 1231–1239.

(31) Banerjee, I.; Pangule, R. C.; Kane, R. S. *Adv. Mater.* **2011**, *23* (6), 690–718.

(32) Magin, C. M.; Cooper, S. P.; Brennan, A. B. *Mater. Today* **2010**, *13* (4), 36–44.

(33) Song, J.; Rojas, O. J. *Pap. Chem.* **2013**, *28* (2), 216–238.

(34) Österberg, E.; Bergström, K.; Holmberg, K.; Riggs, J. A.; Van Alstine, J. M.; Schuman, T. P.; Burns, N. L.; Harris, J. M. *Colloids Surf., A* **1993**, *77* (2), 159–169.

(35) Yang, L.; Li, L.; Tu, Q.; Ren, L.; Zhang, Y.; Wang, X.; Zhang, Z. *Anal. Chem.* **2010**, *82* (15), 6430–6439.

(36) Decher, G.; Schlenoff, J. B. *Multilayer Thin Films*; Wiley-VCH, 2003.

(37) Dobrynin, A. V.; Rubinstein, M. *Prog. Polym. Sci.* **2005**, *30* (11), 1049–1118.

(38) De Feijter, J.; Benjamins, J.; Veer, F. *Biopolymers* **1978**, *17* (7), 1759–1772.

(39) Green, R. J.; Davies, J.; Davies, M. C.; Roberts, C. J.; Tendler, S. J. B. *Biomaterials* **1997**,

18 (5), 405–413.

(40)　Green, R. J.; Frazier, R. A.; Shakesheff, K. M.; Davies, M. C.; Roberts, C. J.; Tendler, S. J. B. *Biomaterials* **2000**, *21* (18), 1823–1835.

(41)　Höök, F.; Vörös, J.; Rodahl, M.; Kurrat, R.; Böni, P.; Ramsden, J. .; Textor, M.; Spencer, N. .; Tengvall, P.; Gold, J.; Kasemo, B. *Colloids Surf., B* **2002**, *24* (2), 155–170.

(42)　Chittur, K. K. *Biomaterials* **1998**, *19* (4-5), 357–369.

(43)　Mudunkotuwa, I. A.; Minshid, A. Al; Grassian, V. H. *Analyst* **2014**, *139* (5), 870–881.

(44)　Mcmillin, C. R.; Walton, A. G. *J. Colloid Interface Sci.* **1974**, *48* (2), 345–349.

(45)　Marx, K. A. *Biomacromolecules* **2003**, *4* (5), 1099–1120.

(46)　Binnig, G.; Quate, C. F. *Phys. Rev. Lett.* **1986**, *56* (9), 930–933.

(47)　Binnig, G.; Rohrer, H. *Surf. Sci.* **1983**, *126* (1-3), 236–244.

(48)　Raether, H. *Phys. Thin Film.* **1977**, *9*, 145–261.

(49)　Geddes, N. J.; Martin, A. S.; Caruso, F.; Urquhart, R. S.; Furlong, D. N.; Sambles, J. R.; Than, K. A.; Edgar, J. A. *J. Immunol. Methods* **1994**, *175*, 149–160.

(50)　Peterlinz, K. a; Georgiadis, R. *Opt. Commun.* **1996**, *130* (4-6), 260–266.

(51)　Peterlinz, K. a; Georgiadis, R. *Langmuir* **1996**, *12* (20), 4731–4740.

(52)　Rodahl, M.; Höök, F.; Krozer, A.; Brzezinski, P.; Kasemo, B. *Rev. Sci. Instrum.* **1995**, *66* (7), 3924–3930.

(53)   Sauerbrey, G. *Zeitschrift für Phys.* **1959**, *155*, 206–222.

(54)   Reviakine, I.; Johannsmann, D.; Richter, R. P. *Anal. Chem.* **2011**, *83* (23), 8838–8848.

(55)   Höök, F.; Kasemo, B.; Nylander, T.; Fant, C.; Sott, K.; Elwing, H. *Anal. Chem.* **2001**, *73* (24), 5796–5804.

(56)   Giessibl, F. J. *Rev. Mod. Phys.* **2003**, *75* (3), 949–983.

(57)   Jalili, N.; Laxminarayana, K. *Mechatronics* **2004**, *14* (8), 907–945.

(58)   Eibinger, M.; Ganner, T.; Bubner, P.; Rošker, S.; Kracher, D.; Haltrich, D.; Ludwig, R.; Plank, H.; Nidetzky, B. *J. Biol. Chem.* **2014**, *289* (52), 35929–35938.

(59)   Kirby, B. J.; Hasselbrink, E. F. *Electrophoresis* **2004**, *25* (2), 187–202.

(60)   Kirby, B. J.; Hasselbrink, E. F. *Electrophoresis* **2004**, *25* (2), 203–213.

(61)   Delgado, A. V.; González-Caballero, F.; Hunter, R. J.; Koopal, L. K.; Lyklema, J. *Pure Appl. Chem.* **2005**, *77* (10), 1753–1805.

(62)   Hollander, J. M.; Jolly, W. L. *Acc. Chem. Res.* **1970**, *3* (6), 193–200.

(63)   Watts, J. F. *Vacuum* **1994**, *45* (6-7), 653–671.

(64)   Zaera, F. *Surf. Sci.* **2011**, *605* (13-14), 1141–1145.

(65)   Schneckenburger, H. *Curr. Opin. Biotechnol.* **2005**, *16* (1), 13–18.

(66)   Enderlein, J.; Ruckstuhl, T.; Seeger, S. *Appl. Opt.* **1999**, *38* (4), 724–732.

(67)   Tian, Y.; Martinez, M. M.; Pappas, D. *Appl. Spectrosc.* **2011**, *65* (4), 115–124.

(68)   Hillger, F.; Nettels, D.; Dorsch, S.; Schuler, B. *J. Fluoresc.* **2007**, *17* (6), 759–765.

(69)   Betzig, E.; Trautman, J. K.; Harris, T. D.; Weiner, J. S.; Kostelak, R. L. *Science* **1991**, *251* (5000), 1468–1470.

(70)   Hell, S. W.; Wichmann, J. *Opt. Lett.* **1994**, *19* (11), 780–782.

(71)   Gustafsson, M. *Proc. Natl. Acad. Sci. USA* **2005**, *102* (37), 13081–13086.

(72)   Betzig, E.; Patterson, G. H.; Sougrat, R.; Lindwasser, O. W.; Olenych, S.; Bonifacino, J. S.; Davidson, M. W.; Lippincott-Schwartz, J.; Hess, H. F. *Science* **2006**, *313* (5793), 1642–1645.

(73)   Rust, M.; Bates, M.; Zhuang, X. *Nat. Methods* **2006**, *3*, 793–796.

(74)   Kontturi, E.; Thüne, P. C.; Niemantsverdriet, J. W. *Langmuir* **2003**, *19* (14), 5735–5741.

(75)   Heriot, S. Y.; Jones, R. A. L. *Nat. Mater.* **2005**, *4* (10), 782–786.

(76)   Piculell, L.; Lindman, B. *Adv. Colloid Interface Sci.* **1992**, *41*, 149–178.

(77)   Wangkam, T.; Yodmongkol, S.; Disrattakit, J.; Sutapun, B.; Amarit, R.; Somboonkaew, A.; Srikhirin, T. *Curr. Appl. Phys.* **2012**, *12* (1), 44–52.

(78)   Cistola, D. P.; Small, D. M.; Hamilton, J. A. *J. Biol. Chem.* **1987**, *262*, 10971–10979.

(79)   Choi, J.-K.; Ho, J.; Curry, S.; Qin, D.; Bittman, R.; Hamilton, J. A. *J. Lipid Res.* **2002**, *43* (7), 1000–1010.

(80)   Curry, S.; Brick, P.; Franks, N. P. *Biochim. Biophys. Acta - Mol. Cell Biol. Lipids* **1999**, *1441* (2-3), 131–140.

(81)   Friedrichs, B. *All about Albumin. Biochemistry, Genetics and Medical Applications*; Wiley-VCH, 1997.

(82)   Josefsson, P.; Henriksson, G.; Wågberg, L. *Biomacromolecules* **2008**, *9* (1), 249–254.

(83)   Mohan, T.; Kargl, R.; Doliška, A.; Ehmann, H. M. A.; Ribitsch, V.; Stana-Kleinschek, K. *Carbohydrate Polymers* **2013**; 93, 191–198.

(84)   Numata, K.; Yamashita, K.; Fujita, M.; Tsuge, T.; Kasuya, K. I.; Iwata, T.; Doi, Y.; Abe, H. *Biomacromolecules* **2007**, *8* (7), 2276–2281.

(85)   Seemann, R.; Herminghaus, S.; Neto, C.; Schlagowski, S.; Podzimek, D.; Konrad, R.; Mantz, H.; Jacobs, K. *J. Phys. Condens. Matter* **2005**, *17* (9), 267–290.

(86)   Sapmaz, I.; Saba, T.; Haberal, C.; Toktamis, A.; Cakmak, M.; Cidek, D. *Int. Cardiovasc. Res. J.* **2011**, *5* (4), 153–154.

(87)   Sousa, A.; Sengonul, M.; Latour, R.; Kohn, J.; Libera, M. *Langmuir* **2006**, *22* (14), 6286–6292.

(88)   Lam, S. K.; Ng, T. B. *Appl. Microbiol. Biotechnol.* **2011**, *89* (1), 45–55.

(89)   Satoh, a; Matsumoto, I. *Anal. Biochem.* **1999**, *275*, 268–270.

(90)   Goldstein, I. J.; Hollerman, C. E.; Smith, E. E. *Biochemistry* **1965**, *4* (5), 876–883.

(91)   Kasai, W.; Kondo, T. *Macromol. Biosci.* **2004**, *4* (1), 17–21.

(92)   Kargl, R.; Mohan, T.; Ribitsch, V.; Saake, B.; Puls, J.; Kleinschek, K. S. *Nord. Pulp Pap. Res. J.* **2015**, *30* (1), 6–13.

(93)   Banks, W.; Greenwood, C. T. *Starch and its Components*; Wiley: New York, 1975.

(94)   Shirazi, M.; Van De Ven, T. G. M.; Garnier, G. *Langmuir* **2003**, *19* (26), 10835–10842.

(95)   Kronberg, B.; Holmberg, K.; Lindman, B. *Surf. Chem. Surfactants Polym.* **2014**, 211–229.

(96)   Ristić, T.; Mohan, T.; Kargl, R.; Hribernik, S.; Doliška, A.; Stana-Kleinschek, K.; Fras, L. *Cellulose* **2014**, *21* (4), 2315–2325.

(97)   Sadowski, J. W.; Korhonen, I. K.; Peltonen, J. P. *Opt. Eng.* **1995**, *34* (9), 2581–2586.

(98)   Kurihara, K.; Nakamura, K.; Suzuki, K. *Sens Actuators, B Chem.* **2002**, *86* (1), 49–57.

List of Abbreviations

AFM	Atomic Force Microscopy
ATR-IR	Attenuated Total Reflexion – Infrared
BL	Bulk Layer
BSA	Bovine Serum Albumin
Con A	Concanavalin A
CS	Cationic Starch
CSE	Cellulose Stearoyl Ester
CX	Cellulose Xanthate
d	Thickness
dn/dc	Refractive Index Increment
$dn/d\lambda$	Chromatic Dispersion
DS	Degree of Substitution
FIB	Fibrinogen
IEP	Isoelectric Point
IgG	Immunoglobulin G
LP	Lignin Palmitate
mf	Material Fraction
MP-SPR	Multi-Parameter Surface Plasmon Resonance
n	Refractive Index
PCL	Polycaprolactone
PDI	Polydispersity Index
PHB	Poly-3-hydroxybutyrate

PS   Polystyrene

QCM-D   Quartz Crystal Microbalance and Dissipation

RL   Roughness Layer

RMS   Root Mean Square

SA   Stearic Acid

SFE   Surface Free Energy

TMC   *N,-N,-N*-Trimethyl Chitosan Chloride

TMSC   Trimethylsilyl Cellulose

UEA-I   Ulex Europaeus Agglutinin I

XPS   X-Ray Photoelectron Spectroscopy

ρ Density

List of Figures

List of Tables

Curriculum Vitae

Personal Data

Name, Title: Dipl.-Ing. Katrin Niegelhell, BSc

Date of Birth: 19.02.1991

Place of Birth: Graz

Nationality: Austria

Education

10.2009-09.2012:	Graz University of Technology, Graz, Austria, Bachelor studies in Chemistry
	Bachelor thesis: "Antimicrobial and biodegradable Composites"
09.2012-09.2014:	Graz University of Technology, Graz, Austria, Master studies in Chemistry of Technology
	Master thesis: "Pre-Studies for Bio-Sensor Development based on Surface-Sensitive Methods"
10.2014-10.2017	Graz University of Technology, Graz, Austria, Doctoral Program in Engineering Sciences, Specialization in Material Sciences
	Doctoral thesis: "Interactions at Polysaccharide Surfaces"

Internships

07.2010   IVOCLAR VIVADENT AG, Bendererstrasse 2, FL-9494 Schaan

Research Stays Abroad

06.2014   Petru Poni Institute, Romanian Academy of Sciences, Iasi, Romania

14.-19.09.2015   ELETTRA Sincrotrone, Trieste, Italy

04.-29.01.2016   Short Term Scientific Mission, Host: Wim Thielemans, KU Leuven, Campus Kortrijk,Belgium

25.04.-02.05.2016   BESSY II Synchrotron, Berlin, Germany

Training Schools and Workshops

25.09. – 30.09.2014   SIPs Summer School – Small Angle Scattering Methods at Synchrotron Facility ELETTRA, Trieste, Italy and Graz University of Technology, Austria

30.10. – 31.10.2014   Multi-Parameter Surface Plasmon Resonance User Meeting by Bionavis, Amsterdam, Netherlands.

18.02. – 20.02.2015   Atomic Force Microscopy Workshop on Advanced Bio- and Materials Characterization and Industrial Applications by Bruker, Graz, Austria.

*Research Interests***:**   Multi-Parameter Surface Plasmon Resonance, Quartz Crystal Microbalance and Polysaccharide based materials

Publications

- **Triggering Protein Adsorption on Tailored Cationic Cellulose Surfaces**
  Tamilselvan Mohan, <u>Katrin Niegelhell</u>, Cíntia Salomão Pinto Zarth, Rupert Kargl, Stefan Köstler, Volker Ribitsch, Thomas Heinze, Stefan Spirk, Karin Stana-Kleinschek, *Biomacromolecules*, **2014**, 15 (11), 3931-3941.
- **Adsorption Studies of Organophosphonic Acids on Differently Activated Gold Surfaces**
  <u>Katrin Niegelhell</u>, Simon Leimgruber, Thomas Griesser, Christian Brandl, Boril Chernev, Robert Schennach, Gregor Trimmel, Stefan Spirk, *Langmuir*, **2016**, 32 (6), 1550-1559.
- **Exploring Nonspecific Protein Adsorption on Lignocellulosic Amphiphilic Bicomponent Films**
  Simone Strasser, <u>Katrin Niegelhell</u>, Manuel Kaschowitz, Sabina Markus, Rupert Kargl, Karin Stana-Kleinschek, Christian Slugovc, Tamilselvan Mohan, Stefan Spirk, *Biomacromolecules*, **2016**, 17 (3), 1083-1092.
- **Enzymes as Biodevelopers for Nano- And Micropatterned Bicomponent Biopolymer Thin Films**
  <u>Katrin Niegelhell</u>, Michael Süßenbacher, Katrin Jammernegg, Thomas Ganner, Daniel Schwendenwein, Helmut Schwab, Franz Stelzer, Harald Plank, Szefan Spirk, *Biomacromolecules*, **2016**, 17 (11), 3743-3749.
- **Topography effects in AFM force mapping experiments on xylan-decorated cellulose thin films**
  Christian Ganser, <u>Katrin Niegelhell</u>, Caterina Czibula, Angela Chemelli, Christian Teichert, Robert Schennach, Stefan Spirk, *Holzforschung*, **2016**, 70 (12), 1115-1123.
- **Interaction of Tissue Engineering Substrates with Serum Proteins and Its Influence on Human Primary Endothelial Cells**
  Tamilselvan Mohan, <u>Katrin Niegelhell</u>, Chandran Nagaraj, David Reishofer, Stefan Spirk, Andrea Olschewski, Karin-Stana Kleinschek, Rupert Kargl, *Biomacromolecules*, **2016**, 18 (2), 413-421.

Publications in Preparation

- **Interaction of Industrially Relevant Cationic Starches with Cellulose**
  <u>Niegelhell Katrin</u>, Chemelli Angela, Hobisch Josefine, Griesser Thomas, Reiter Heidemarie, Hirn Ulrich, Spirk Stefan, *submitted to Carbohydrate Poylmers in July 2017*.
- **Homogeneous Cellulose Thin Films by Regeneration of Cellulose Xanthate – Properties and Characterization**
  Weissl Michael, <u>Niegelhell Katrin</u>, Reishofer David, Zankl Armin, Innerlohinger Josef, Spirk Stefan, *submitted to Cellulose in July 2017*.
- **How Bound and Free Fatty Acids in Cellulose Influence Nonspecific Protein Adsorption**
  <u>Niegelhell Katrin</u>, Süßenbacher Michael, Sattelkow Jürgen, Plank Harald, Wang Yonggui, Zhang Kai, Spirk Stefan, *submitted to Biomacromolecules in August 2017*.
- **Multilayer Density Analysis of Thin Films**
  <u>Niegelhell Katrin</u>, Kontturi Katri, Hirn Ulrich, Spirk Stefan, *submitted to Langmuir in September 2017*.

Scholarships

- KUWI: Stipendium für Kurzfristige Wissenschaftliche Arbeiten - Travel Expense Allowance for visit abroad
- Förderstipendium für Wissenschaftliche Arbeiten 2015 – Travel Expense Allowance for visit abroad
- Travel Grant Doctoral School Chemistry for Oral Presentation, 2015 – Travel Expense Allowance for Conference Participation
- Reisestipendium Gesellschaft Österreichischer Chemiker (GÖCH) – Travel Expense Allowance for conference participation from the Austrian Chemical Society
- Short Term Scientific Mission (STSM) Grant under the COST Action FP1205, 2016
- Förderstipendium für Wissenschaftliche Arbeiten 2016 – Travel Expense Allowance for visit abroad
- Travel Grant Doctoral School Chemistry for Poster Presentation, 2016 – Travel Expense Allowance for conference participation
- Förderstipendium für Wissenschaftliche Arbeiten 2017 – Travel Expense Allowance for visit abroad

Awards

- Poster Award at the 2nd International EPNOE Junior Scientists Meeting, 13th-14th October 2016, Sophia-Antipolis, France
- Student's Presentation Award at the 253rd ACS National Meeting and Exhibition, 2nd-6th April 2017, San Francisco, USA

Participation in Conferences

- EN(ergy)LITE(racy)WEEK, 11th-14th February 2014, Maribor, Slovenia
- 1st European Conference on Smart Inorganic Polymers (EUSIP), 21st-23rd September 2014, Maribor, Slovenia

- 22nd International Conference on Materials and Technology (ICM&T), 20th-22nd October 2014, Portoroz, Slovenia
- 249th ACS National Meeting and Exhibition, 22nd-26th March 2015, Denver, USA
- 6th International Congress Nanotechnology in Medicine and Biology (BioNanoMed), 8th-10th April 2015, Graz, Austria
- 16th Austrian Chemistry Days, 21st-24th September 2015, Innsbruck, Austria
- 4th EPNOE International Polysaccharide Conference, 19th-22nd October 2015, Warsaw, Poland
- 251st ACS National Meeting and Exhibition, 13th-17th March 2016, San Diego, USA
- 2nd International EPNOE Junior Scientists Meeting, 13th-14th October 2016, Sophia-Antipolis, France
- 21st Austrian Carbohydrate Workshop, 16th-17th February 2017, Graz, Austria
- 253rd ACS National Meeting and Exhibition, 2nd-6th April 2017, San Francisco, USA
- 5th EPNOE International Polysaccharide Conference, 20th-24th August 2017, Jena, Germany
- Danube Vltava Sava Polymer Meeting, 5th-8th September, Vienna, Austria

Conference Contributions

Oral Presentations

- Niegelhell, K.; Leimgruber, S.; Grießer, T.; Trimmel, G.; Spirk, S.: Phosphonate Monolayers on Gold Surfaces, EUSIP 2014, Maribor, Slovenia
- Niegelhell, K.; Mohan, T.; Kargl, R.; Köstler, S.; Reishofer, D.; Stana-Kleinschek, K.; Spirk, S.: Triggering Protein Adsorption by Cationization of Cellulose Ultrathin Films - Challenges and Applications, 22nd International Conference on Materials and Technology (ICM&T), Portoroz, Slovenia
- Niegelhell, K.; Mohan, T.; Zarth, C.; Kargl, R.; Ribitsch, V.; Heinze T.; Stana-Kleinschek, K.; Spirk, S.; Köstler, S.: Triggering protein adsorption on tailored cationic cellulose surfaces, 249th ACS National Meeting and Exhibition, Denver, USA
- Niegelhell, K.; Mohan, T.; Reishofer, D.; Stana-Kleinschek, K.; Spirk, S.: Protein Adsorption - A Key Parameter in Tissue Engineering, 16th Austrian Chemistry Days, 21st-24th September 2015, Innsbruck, Austria
- Niegelhell, K.; Jantscher-Krenn, E.; Schmiedt, R.; Mohan, T.; Spirk, S.: Protein-Surface Interaction at Polysaccharide Interfaces – A Key Parameter in Life Science Applications, 4th EPNOE International Polysaccharide Conference, 19th-22nd October 2015, Warsaw, Poland
- Niegelhell, K.; Jantscher-Krenn, E.; Ganner, T.; Payerl, C.; Wrodnigg, T.; Spirk, S.: Lectin-polysaccharide interaction: An MP-SPR study, 251st ACS National Meeting and Exhibition, 13th-17th March 2016, San Diego, USA
- Niegelhell, K.; Süßenbacher, M.; Jammernegg, K.; Ganner, T.; Schwendenwein, D.; Schwab, H.; Plank, H.; Spirk, S.: Phase Separated Bicomponent Biopolymer Thin Films - Enzymatic Patterning and Protein Interaction, 21st Austrian Carbohydrate Workshop, 16th-17th February 2017, Graz, Austria
- Niegelhell, K.; Süßenbacher, M.; Jammernegg, K.; Ganner, T.; Schwendenwein, D.; Schwab, H.; Stelzer, F.; Plank, H.; Spirk, S.: Phase Separated Bicomponent Biopolymer Thin Films – Enzymatic Patterning and Protein Interaction, 253rd ACS National Meeting and Exhibition, 2nd-6th April 2017, San Francisco, USA
- Niegelhell, K.; Süßenbacher, M.; Sattelkow, J.; Zhang, K.; Plank, H.; Mohan, T.; Spirk, S.: Biopolymer Blend Thin Films – Phase Separation and Protein Interaction, 5th EPNOE International Polysaccharide Conference, 20th-24th August 2017, Jena, Germany

- Niegelhell, K.; Süßenbacher, M.; Jammernegg, K.; Ganner, T.; Schwendenwein, D.; Schwab, H.; Stelzer, F.; Plank, H.; Spirk, S.: Enzymatic Patterning of Phase Separated Bicomponent Biopolymer Thin Films, Danube Vltava Sava Polymer Meeting, 5th-8th September, Vienna, Austria

Poster Presentations

- Niegelhell, K.; Leimgruber, S.; Trimmel, G.; Grießer, T.; Spirk, S.: The Effect of SPR Sensor Slide Pre-Treatment on the Adsorption Behavior of Alkyl Phosphonates, MP-SPR User Meeting 2014, Amsterdam, Netherlands
- Niegelhell, K.; Mohan, T.; Kargl, R.; Stana-Kleinschek, K., Köstler S.; Heinze, T.; Spirk, S.: MP-SPRS and QCM-D – Surface Sensitive Techniques for Studying Protein-Surface Interactions, BioNanoMed 2015, Graz, Austria
- Niegelhell, K.; Gspan, C.; Koraimann, G.; Heise, K.; Reishofer, D.; Ehmann H.; Ribitsch V.; Stana-Kleinschek K.; Maver U.; Spirk S.: Nanotechnology in the Engineering of Antibacterial and Anticoagulant Surfaces based on Sulfated Polysaccharides, BioNanoMed 2015, Graz, Austria
- Niegelhell, K.; Süßenbacher, M.; Jammernegg, K.; Ganner, T.; Schwendenwein, D.; Schwab, H.; Plank, H.; Spirk, S.: Enzymatic Treatment for Patterning of Bicomponent Biopolymer Thin Films, 2nd International EPNOE Junior Scientists Meeting, 13th-14th October 2016, Sophia-Antipolis, France

Poster Presentations as Co-Author

- Ehmann, H.; Niegelhell, K.; Gašparič, P.; Werzer, O.; Ribitsch, V.; Stana-Kleinschek, K.; Spirk, S.: Small Angle X-ray Scattering Study of Silane Functionalized Cellulose Materials, EUSIP 2014, Maribor, Slovenia
- Mohan, T.; Niegelhell, K.; Bracic, M.; Cerny, C.; Kargl, R.; Spirk, S.; Stana-Kleinschek, K.; Ribitsch, V.: Applications of QCM-D and MP-SPR for Studying Protein-Surface Interactions, EUSIP 2014, Maribor, Slovenia
- Reishofer, D.; Mohan, T.; Kargl, R.; Niegelhell, K.; Hribernik, S.; Ehmann, H.; Spirk, S.; Stana-Kleinschek, K.: Silylcellulose Derivatives as Precursors for Cellulose Model Systems describing Paper Making Processes, EUSIP 2014, Maribor, Slovenia
- Heise, K.; Ehmann, H.; Niegelhell, K.; Maver, U.; Kaschowitz, M.; Stana-Kleinschek, K.; Spirk, S.; Fischer, S.: Chitosan Ethylsulfates - Synthesis, Characterization and Application in Nanotechnology, 22nd International Conference on Materials and Technology (ICM&T) 2014, Portoroz, Slovenia
- Süßenbacher, M.; Niegelhell, K.; Plank, H.; Zhang, K.; Spirk, S.: Phase Separation of Cellulose with Covalently or Non-Covalently Bound Fatty Acids in Thin Films, 2nd International EPNOE Junior Scientists Meeting, 13th-14th October 2016, Sophia-Antipolis, France

Public-To-Science Activities

- Out of the Box Lab, Maribor 2014, https://www.flickr.com/photos/razumaribor/12495916723/in/set-72157640915858804/,https://www.flickr.com/photos/razumaribor/12495918143/in/set-72157640915858804/

Appendix

PAPER #1

How Bound and Free Fatty Acids in Cellulose Influence Nonspecific

Protein Adsorption

submitted to Biomacromolecules

For this paper, I conducted the AFM and MP-SPR spectroscopy experiments, interpreted the data and wrote a significant part of the manuscript.

How Bound and Free Fatty Acids in Cellulose Influence Nonspecific Protein Adsorption

Katrin Niegelhell[a], Michael Süßenbacher[b], Jürgen Sattelkow[c], Harald Plank[c], Yonggui Wang[d], Kai Zhang[d] and Stefan Spirk[a]*

[a]Graz University of Technology, Institute for Paper, Pulp and Fiber Technology, Inffeldgasse 23, 8010 Graz, Austria.

[b]Graz University of Technology, Institute for Chemistry and Technology of Materials, Stremayrgasse 9, 8010 Graz, Austria.

[c]Graz University of Technology, Institute for Electron Microscopy and Nanoanalysis, Steyrergasse 17, 8010 Graz, Austria.

[d]Georg-August-University of Goettingen, Wood Technology and Wood Chemistry, Büsgenweg 4, 37077 Göttingen, Germany.

Corresponding Author

*E-mail: stefan.spirk@tugraz.at, Phone: +43-316-873-32284

ABSTRACT

The effect of fatty acids and fatty acid esters to impair nonspecific protein adsorption on cellulose thin films is investigated. Thin films are prepared by blending trimethylsilyl cellulose solutions with and either cellulose stearoyl ester or stearic acid at various ratios. After film formation by spin coating, the trimethylsilyl cellulose fraction of the films is converted to cellulose by exposure to HCl vapors. The morphologies and surface roughness of the blends were examined by atomic force microscopy revealing different feature shapes and sizes depending on the blend ratios. Nonspecific protein adsorption at the example of bovine serum albumin towards the blend thin films was tested by means of surface plasmon resonance spectroscopy in real-time. Incorporation of stearic acid into the cellulose leads to highly protein repellent surfaces regardless of the amount added. The stearic acid acts as a sacrificial compound that builds a complex with bovine serum albumin thereby inhibiting protein adsorption. For the blends where stearoyl ester is added to the cellulose films, the cellulose:cellulose stearoyl ester ratios of 3:1 and 1:1 lead to much lower nonspecific protein adsorption compared to pure cellulose, whereas for the other ratios, adsorption increases. Supplementary results were obtained from atomic force microscopy experiments performed in liquid during exposure to protein solution and surface free energy determinations.

KEYWORDS

INTRODUCTION

Fatty acids and their esters represent important biomolecules since they are involved in many biochemical processes. One of their main functions is their involvement in energy storage by formation of mono-, di- and triglycerides in animals and plants. However, there are innumerous biochemical pathways where fatty acid (esters) are involved or even act as co-enzymes such as lipoic acid for instance.[1] Their high abundance in nature makes fatty acids and their esters inexpensive raw materials, which are currently used in a variety of areas. For instance, they are used in food industry as emulsifying, release or glazing agents due to their amphiphilic character. Actually, sodium or potassium salts of fatty acids are able to act as efficient soaps or surfactants.[2,3] Fatty acid esters of biopolymers have attracted significant interest in the past years, since they are easy to manufacture (e.g. by reaction with fatty acid chlorides in the presence of a base), cheap and widely accessible.[4] A particularly interesting field of research was opened by the investigation of cellulose fatty acid esters either as bulk or nanomaterials such as cellulose nanocrystals and nanofibrils.[5–12] The usual fields of application for cellulose fatty acid ester products are food, paper or textile industry and packaging.[13] Therefore, cellulose fatty acid ester materials are tested predominantly for properties concerning such applications, e.g. water and oxygen barrier properties, processability and mechanical properties.[9,14–18] However, in life science applications they have gained less attraction. In these applications, very often a detailed investigation of surface properties is a major issue, e.g. the interaction capacity with proteins. Adsorbed protein layers can lead to the adhesion of particles, bacteria and cells, which is inadvertent when it comes to the promotion of inflammation[19] or fouling processes[20]. Nevertheless, proteins present on a surface can act advantageously as well, for instance, they mediate vascularization in artificial tissue scaffolds[21] or enable the deposition of certain cells[22] or other compounds, such as gold

3

nanoparticles[23]. However, for polymer blend films just little data is available on the interaction with proteins.[24,25]

Our starting point in this research was how the presence of fatty acids affects nonspecific protein adsorption. As model systems, blend films were chosen which contain cellulose and stearic acid (SA) and, for the sake of comparison, cellulose that contains stearoylated cellulose. Various ratios of the blend films have been prepared and after thorough characterization of the surface properties, their interaction behavior with proteins was tested by surface resonance plasmon spectroscopy at low protein concentration (1 mg·ml^{-1} BSA) as well as high concentrations (50 mg·ml^{-1} BSA) which are usually present in blood plasma.

MATERIALS AND METHODS

Materials. Trimethylsilyl cellulose (Avicel, M_w = 185,000 g·mol^{-1}, M_n = 30,400 g·mol^{-1}, PDI = 6.1 determined by GPC in chloroform) with a DS$_{Si}$ value of 2.8 was purchased from TITK (Rudolstadt, Germany). Chloroform (99.3%), disodium phosphate heptahydrate (Na$_2$HPO$_4$· 7H$_2$O), sodium dihydrogen phosphate monohydrate (NaH$_2$PO$_4$·H$_2$O), hydrochloric acid (37%), sodium chloride (Ph.Eur.), sodium hydroxide (99%), *bovine serum albumin* (lyophilized powder, ≥96%, 66.5 kDa) and stearic acid (≥95%) were bought from Sigma Aldrich and used without further purification. Cellulose stearoyl ester (CSE) with the degree of substitution of 3 was prepared according to a literature procedure.[26] SPR gold sensor slides (CEN102AU) were purchased from Cenibra, Germany. Milli-Q water (resistivity = 18.2 MΩ·cm) from a Millipore water purification system (Millipore, USA) was used for contact angle measurements and buffer preparation.

Substrate Cleaning and Film Preparation. SPR gold sensor slides/silicon wafers were immersed in caro's acid (H_2O_2 (30 wt.%)/H_2SO_4 (1:3 v/v)) for 10 min and subsequently rinsed extensively with Milli-Q water followed by drying in a stream of nitrogen gas. Trimethylsilyl cellulose, cellulose stearoyl ester and stearic acid were dissolved in chloroform (0.75 wt.%) by stirring over night at room temperature and filtered through 0.45 μm PVDF filters. The solutions were spin coated either pure or in ratios of 3:1, 1:1 and 1:3 for TMSC:SA and TMSC:CSE by depositing 120 μl solution onto the cleaned substrate and rotating at a spinning speed of 4000 rpm and an acceleration of 2500 rpm·s^{-1} for a period of 60 s. The regeneration of trimethylsilyl cellulose to cellulose was done by treatment with acidic vapors. The substrates were placed in a petri-dish (Ø 5 cm) next to 3 ml of 10 wt.% hydrochloric acid. Then the dish was closed with its cap and the films were exposed to the acidic atmosphere for 15 min. The conversion was confirmed by ATR-IR spectroscopy and water contact angle measurements as reported elsewhere.[27,28]

Buffer and Protein Solution Preparation. In all experiments, a 10 mM phosphate buffer with ionic strength of 100 mM sodium chloride was used. Buffer salts ($Na_2HPO_4 \cdot 7H_2O$ and $NaH_2PO_4 \cdot H_2O$) were dissolved in Milli-Q water and the pH value of the solution was adjusted to a value of 7.4 by adding 0.1 M sodium hydroxide. *Bovine serum albumin* was dissolved in the buffer at a concentration of 1 mg·ml^{-1} and 50 mg·ml^{-1}.

Infrared Spectroscopy. ATR-IR spectra were recorded on an Alpha FT-IR spectrometer (Bruker, Billerica, MA, USA) using an attenuated total reflection (ATR) attachment. Spectra were attained in a scan range between 4000 to 400 cm^{-1} with 48 scans and a resolution of 4 cm^{-1}. The data was analyzed with OPUS 4.0 software.

Stylus Profilometry. Film thicknesses were measured with a DETAK 150 Stylus Profiler from Veeco. Measurements were performed with a scan length of 1000 μm and a force of 3 mg over a

duration of 3 seconds. The resolution and measurement range were 0.333 µm per sample and 6.5 µm, respectively. A diamond stylus with a radius of 12.5 µm was applied. Samples were measured after scratching the film (deposited on a silicon wafer). The resulting profile was used to calculate the thickness of different films. All measurements were performed at least three times.

Contact Angle (CA) and Surface Free Energy (SFE) Determination. Static contact angle measurements were performed with a Drop Shape Analysis System DSA100 (Krüss GmbH, Hamburg, Germany) with a T1E CCD video camera (25 fps) and the DSA1 v 1.90 software. Measurements were conducted with Milli-Q water and di-iodomethane using a droplet size of 3 µl and a dispense rate of 400 µl·min⁻¹. All measurements were performed at least three times. CA were calculated with the Young-Laplace equation and SFE was determined with the Owen-Wendt-Rabel-Kaelble (OWRK) method.[29–31]

Atomic Force Microscopy – AFM. AFM images were attained in tapping mode in ambient atmosphere at room temperature by a Veeco Multimode Quadrax MM scanning probe microscope (Bruker, Billerica, MA, USA) using Si-cantilevers (NCH-VS1-W from NanoWorld AG, Neuchatel, Switzerland) with a resonance frequency of 320 kHz and a force constant of 42 N·m⁻¹. Root mean square (RMS) roughness calculation and image processing was performed with the Nanoscope software (V7.30r1sr3, Veeco). AFM investigations of the films in liquid were performed with a Fast Scan Bio atomic force microscope (Bruker AXS, Santa Barbara, CA, USA) operated by a Nanoscope V controller. All experiments were conducted in a droplet of buffer solution liquid by using Fast Scan D cantilevers with a resonance frequency of 110 kHz and a force constant of 0.25 N·m⁻¹. The samples were measured at air as a reference. Image recording in liquid was done after equilibration of the samples for 30 min in buffer and after treatment with protein solution and subsequent rinsing with buffer. Set points, scan rates and controlling parameters were

chosen carefully to ensure lowest possible energy dissipation to the sample and to exclude tip driven artifacts. Data analysis of the images was performed using Nanoscope Analysis 1.50 (Build R2.103555, Bruker AXS, Santa Barbara, CA, U.S.A.) and Gwyddion 2.38.

Multi Parameter Surface Plasmon Resonance Spectroscopy – MP-SPR. MP-SPR studies were performed with a MP-SPR Navi™ 210A VASA (Bionavis Ltd., Tampere, Finland) equipped with two lasers (λ = 670 nm, 785 nm) in both measurement chambers, using gold coated SPR sensor slides (gold layer 50 nm, chromium adhesion layer 10 nm). All measurements were carried out using a full angular scan (39–78°, scan speed: $8°·s^{-1}$). The MP-SPR experiments were conducted in the following way. The equilibration of the samples coated onto the sensor slides was done by rinsing with Milli-Q water followed by buffer. After a steady signal was observed, protein solution was injected into the flow cell and pumped through at a flow of 50 µl·min^{-1} for a duration of 5 min. The samples were rinsed with buffer again followed by Milli-Q water and dried in a stream of N_2 gas. All experiments were performed in three parallels.

Protein adsorption was quantified according to equation 1, which considers the dependence of the angular response $\Delta\Theta$ of the surface plasmon resonance in dependence of the refractive index increment (*dn/dc*) of the adsorbing layer.[32]

$$\Gamma = \frac{\Delta\Theta \times k \times d_p}{dn/dc} \qquad (1)$$

For thin layers (<100 nm), $k \times d_p$ can be considered constant and can be obtained by calibration of the instrument by determination of the decay wavelength l_d. For the MP-SPR Navi™ 210 A VASA used in this study, $k \times d_p$ values are approximately 1.09×10^{-7} cm/° (at 670 nm) and 1.9×10^{-7} cm/° (at 785 nm) in aqueous systems. The *dn/dc* of proteins in water-based buffer systems was reported to be 0.187 cm^3·g^{-1}, which was used to calculate the amount of adsorbed masses.[33]

RESULTS AND DISCUSSION

Preparation of blend thin films. Blend thin films were prepared by spin coating TMSC and CSE or TMSC and SA mixtures of different ratios. The films were exposed to hydrochloric acid vapors in order to convert TMSC into cellulose to create cellulose/CSE and cellulose/SA blend films. It is important to track changes which occur during the exposure to the HCl vapors. The ATR-IR spectra clearly show that the esters (neither in bulk nor in the film) as well as the fatty acids are not altered by the regeneration procedure (ESI†, Figure S1, S2). Furthermore, the morphology of pure CSE and SA films is not significantly affected as proven by AFM (Fig.1). A further proof for the inertness of CSE and SA films towards HCl vapors is the wettability with water and diiodomethane, which does not change after the HCl treatment (†ESI, Figure S3, S4).

50 nm/20 nm/ 150 nm

a) $R_q = 0.72$ nm $R_q = 0.54$ nm $R_q = 27.6$ nm

b) $R_q = 1.65$ nm $R_q = 0.49$ nm $R_q = 17.0$ nm

TMSC   CSE   SA
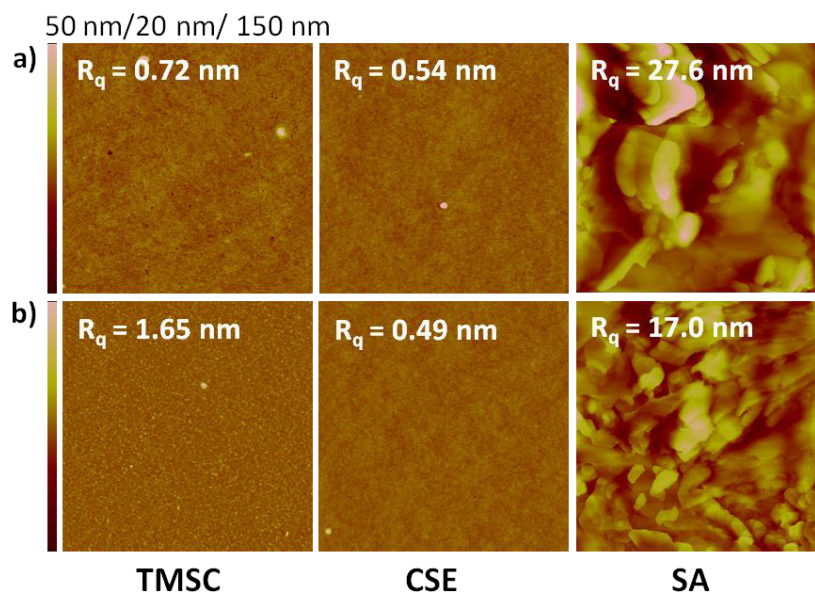
Figure 1. Atomic force microscopy height images and corresponding RMS roughness (R_q) of pure spin coated films before (a) and after (b) treatment with HCl vapors (picture size 10×10 μm^2).

Regeneration of TMSC was verified by ATR-IR spectroscopy (bands attributed to CH_3 of TMSC at 2960 cm^{-1} (ν_{asym}) and 2872 cm^{-1} (ν_{sym}) and Si-C at 1251 cm^{-1} and 842 cm^{-1} disappear, the OH

band between 3600 and 3000 cm^{-1} arises), wettability behavior (static water CA change from 94° to 46°) and thickness determination (shrinkage ca. 60%). For the blend films, conversion was confirmed by ATR-IR spectroscopy; the spectra of the 1:1 ratio for both types of blends is depicted in Figure S5 and S6 (†ESI). Surface free energies (SFE) depicted in Figure 2 further corroborate these findings. The SFE of TMSC changes upon conversion from low to high SFEs and polar contributions to the SFE increase showing the hydrophilic character of cellulose. SFEs of CSE and SA remain constant, which further substantiates the resistance of the substances to acidic vapor treatment. The blends feature similar SFEs at all ratios, which are closer to the value of CSE and SA before regeneration. After conversion, the SFE increases for all ratios, however, some differences arise.
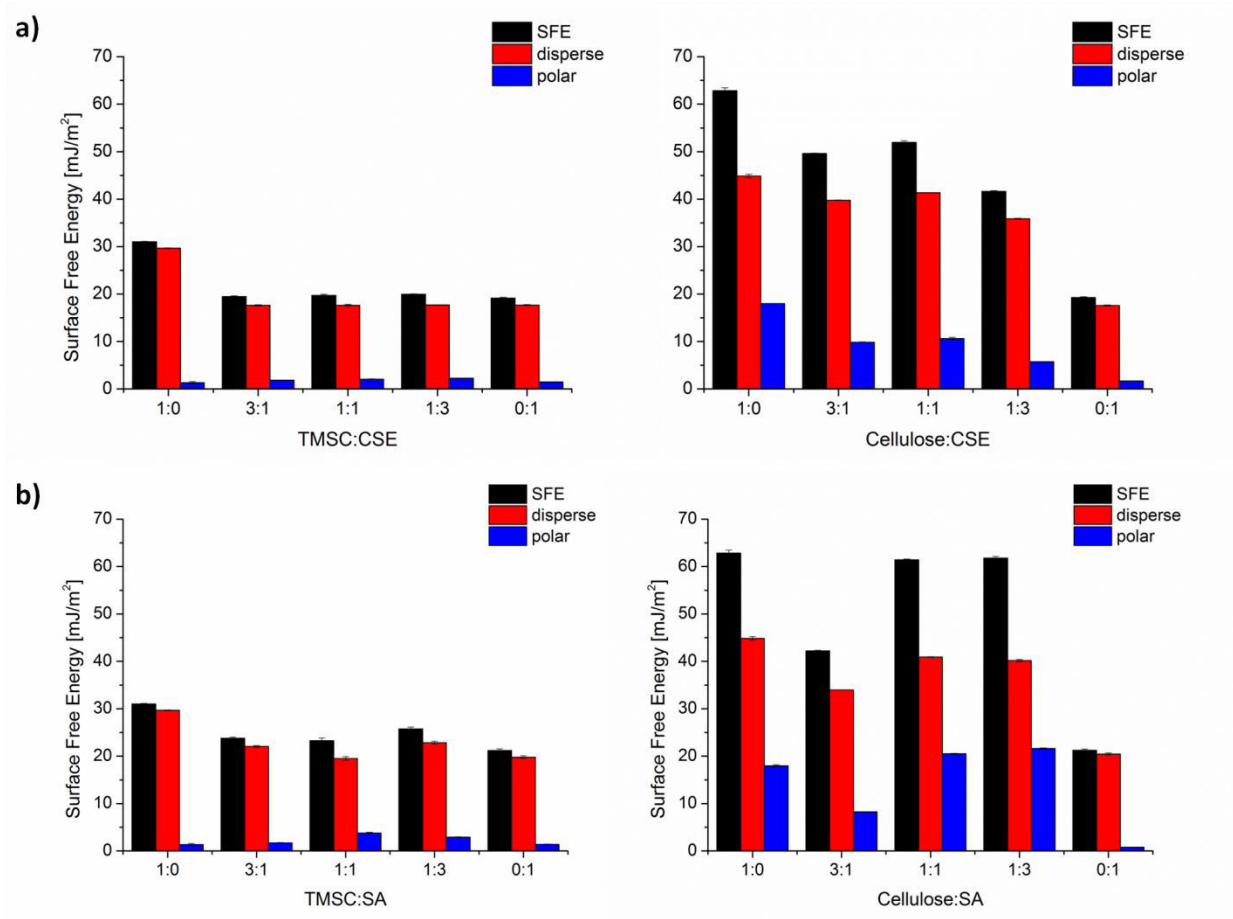
Figure 2. Surface free energies of blend films from cellulose:CSE (a) and cellulose:SA (b) at different ratios before (left) and after (right) regeneration.

Phase separation behavior. The resulting morphologies of the blend thin films were investigated by atomic force microscopy. For the cellulose:CSE blend, microphase separation occurs (Figure 3). The assignment of the resulting phases to the compounds of the blend was accomplished by evaluation of the shrinkage of the TMSC domains upon conversion, which was 63-68 % for all TMSC domains at all ratios as reported in literature for pure TMSC films.[27,28] Additionally, treatment with $CHCl_3$ of the regenerated films was performed leaving only the cellulose part of the films behind. The cellulose:CSE blend at a ratio of 3:1 forms a continuous TMSC phase containing CSE domains, whereas at the other ratios the inverse morphology is found. Domain sizes of the different blend ratios are summarized in Table 1.

The phase separation behavior of the polymer-polymer blend can be explained by the transient bilayer theory, stating vertical stratification of the two polymer phases, followed by lateral phase separation due to interfacial instabilities caused by the evaporation of solvent and a concomitant solvent-concentration gradient in the film.[34] Due to preferential migration to the air-polymer interface of the compound with lower surface free energy, in this case CSE, TMSC forms the layer at the bottom that is in contact with the substrate during the early stages of spin coating. Then, as the solvent proceeds to evaporate, dewetting processes come into play. As for the cellulose:CSE blend at a ratio of 3:1, a thin CSE top layer is present that starts to dewet and contracts into droplets. The emergent voids are then filled with TMSC resulting in a continuous TMSC phase, which contains round CSE domains. Since CSE is the better soluble compound in $CHCl_3$, the solvent remains longer in the CSE than in the TMSC phase, leading to a collapse of the CSE phase at the end of the spin coating process.[35] The arising CSE droplets therefore sink into the surrounding

TMSC phase. This effect was previously observed for other binary polymer blends as well.[36] In the case of the cellulose:CSE blend at a ratio of 1:3, a rather thick CSE layer is present on top of a thin TMSC layer. Dewetting causes this thick layer to break up and generate holes, which are subsequently filled by the polymer from the lower layer favoring the distribution of TMSC inside a continuous CSE phase. The collapse of the better soluble CSE phase is detected for this blend ratio as well. Table 1 summarizes the domain heights for the cellulose:CSE blend. AFM images of the cellulose:CSE blend at a ratio of 1:1 appear to show the formation of two continuous phases, as expected from literature reports.[36] Upon regeneration, the TMSC part shrinks, causing a higher surface area of the CSE domains. Treatment of those surfaces with $CHCl_3$ reveals a morphology which diverges from the expected behavior. Cellulose is distributed in a CSE phase, which is presumably induced by differences in the molar mass of the polymers affecting their mobility.
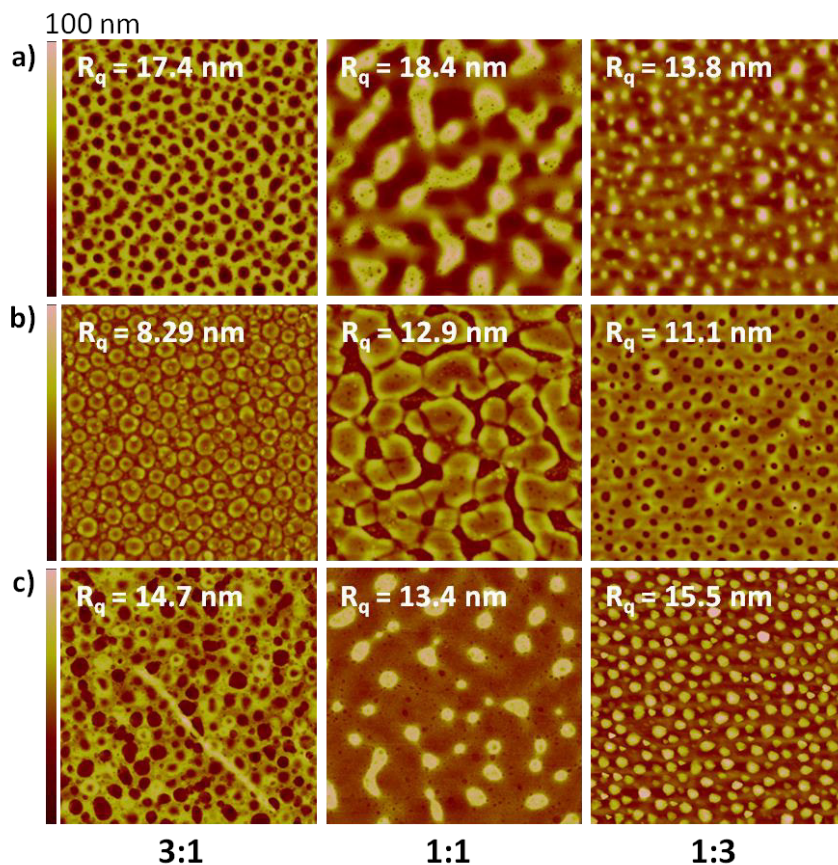
Figure 3. Atomic force microscopy height images and corresponding RMS roughness (R_q) of cellulose:CSE blend films spin coated at different ratios before (a) and after (b) exposure to HCl vapors, as well as after (c) treatment with $CHCl_3$ (picture size 10×10 µm^2).

Table 1. Average TMSC and cellulose domain height in respect to CSE for the different blend ratios and average feature sizes of the cellulose:CSE blend.

TMSC/cellulose:CSE	3:1 [nm]	1:1 [nm]	1:3 [nm]
TMSC domain height	+ 49 ± 9	+ 47 ± 16	+ 58 ± 22
cellulose domain height	- 24 ± 8	- 42 ± 10	- 35 ± 4
feature size	397 ± 73	773 ± 162	365 ± 110

Although SA is a small molecule, phase separation of the cellulose:SA blend proceeds in a similar manner as proposed for polymer-polymer mixtures. SA features a hydrophilic head and a hydrophobic tail and can therefore act as a surfactant. For non-ionic polymer-surfactant mixtures there is usually no strong effective attraction between the compounds, therefore, phase separation is segregative, meaning that two phases are build where one substance is enriched in each phase.[37] According to literature, polymer-surfactant systems show similarities to polymer-polymer systems regarding segregative phase separation.[38] Furthermore, the transient bilayer theory is applicable to certain mixtures of small molecules and polymers. Vertical stratification during spin casting is a known effect in organic thin-film transistor (OFT) production, which is utilized to manufacture two layered systems.[39] Still, SA is much smaller than a polymer and therefore the resulting structures differ from those observed in binary polymer systems. The cellulose:SA blends at ratios of 1:1 and 1:3 display similar morphologies and RMS roughness (Figure 4), whereas the surface of the blend at the ratio of 3:1 looks completely different. This trend is observed in the SFE as well, since the SFE of the cellulose:SA blend ratios of 1:1 (61.4 ± 0.2 mJ·m^{-2}) and 1:3 (61.8 ± 0.3

mJ·m^{-2}) are higher compared to the ratio of 3:1 (42.2 ± 0.1 mJ·m^{-2}). The SFE of the cellulose:SA blend at the ratio of 3:1 is approximately in between values of pure cellulose (62.8 ± 0.6 mJ·m^{-2}) and pure SA (21.2 ± 0.3 mJ·m^{-2}) films. Since the films of cellulose:SA at ratios of 1:1 and 1:3 exhibit low RMS roughness, the SFE can be attributed solely to the influence of the functional groups present at the surface. High roughness and inhomogeneity is observed in the case of the ratio of 3:1, which affects the contact angle and concomitantly the SFE. The orientation of SA might play an important role too, since either the hydrophilic carboxyl head groups or the hydrophobic tails are able to point to the air-polymer interface.

Treatment with CHCl$_3$ was performed to selectively remove the SA phase and thus assign the domains. As expected, the micron sized platelets (2.6 ± 1.1 μm) present on the surface of the cellulose:SA blend at the ratio 3:1, similar to the features existing at the pure SA films, are stemming from the SA phase. The spots where SA platelets were present prior to solvent treatment were still traceable afterwards. Additionally, small holes were found inside the CHCl$_3$ treated film similar to the ones observed at the other ratios. The size of those holes (ranging from 30 to 90 nm) increases with increasing SA content in the blend. These findings basically indicate the same type of morphology for all films. Nevertheless, it is still unclear why huge aggregates arise during spin casting of the films with the lowest SA content.

Figure 4. Atomic force microscopy height images and corresponding RMS roughness (R_q) of cellulose:SA blend films spin coated at different ratios before (a) and after (b) exposure to HCl vapors, as well as after treatment with (c) $CHCl_3$ and (d) BSA (picture size 10×10 μm^2).
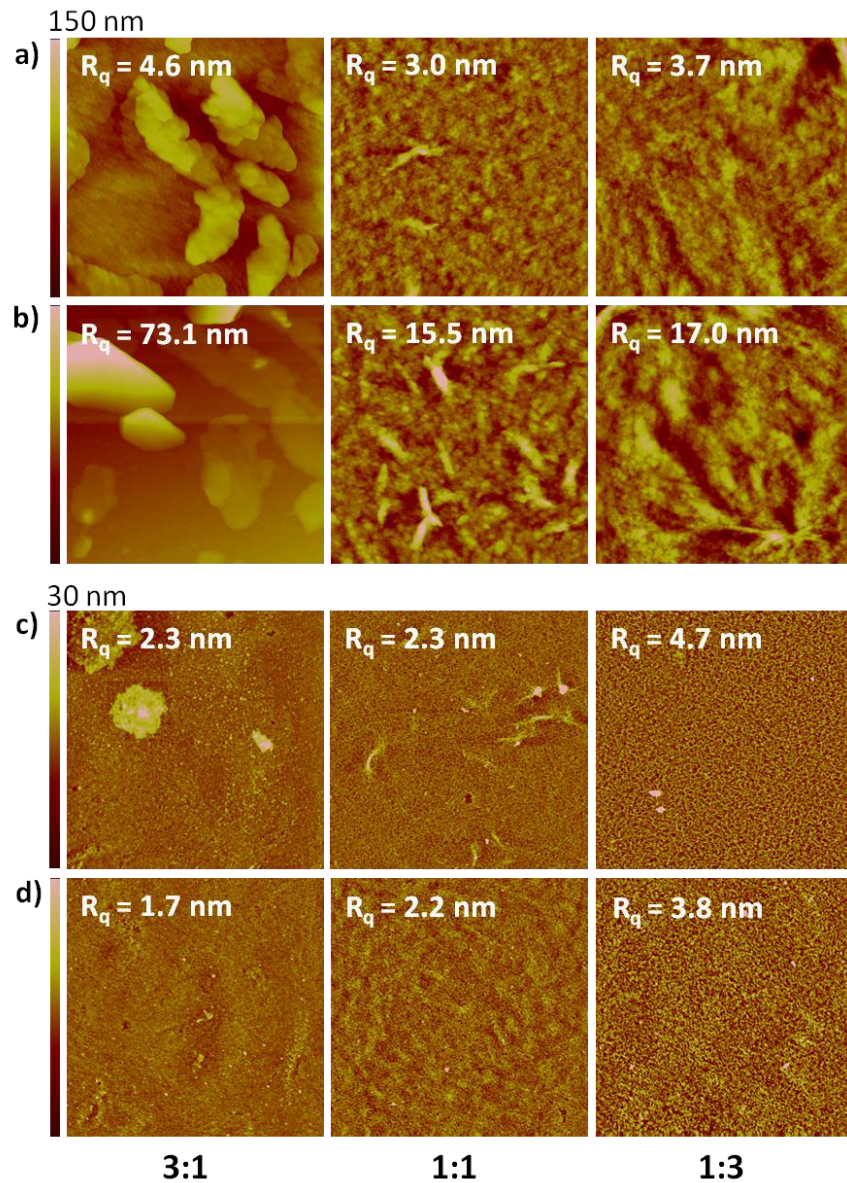
Table 2. Area of cellulose, CSE and SA phases occurring in the blend films at different ratios calculated from atomic force microscopy data.

cellulose:CSE	cellulose [%]	CSE [%]	cellulose:SA	cellulose [%]	SA [%]
3:1	28	72	3:1	57	43
1:1	20	80	1:1	54	46
1:3	11	89	1:3	57	43

Protein interaction at blend surfaces. The interaction of the investigated surfaces and proteins was monitored by multi-parameter surface plasmon resonance spectroscopy (MP-SPR) at the example of *bovine serum albumin* (BSA), which is a commonly used marker for nonspecific protein adsorption. The real-time adsorption behavior of BSA toward the cellulose:CSE blends is depicted in Figure 5. An overshoot effect, presumably caused by reorganization of the protein molecules on the surface[40], and fast adsorption kinetics, represented by the steep slope of the sensogram, is observed for all surfaces. The extent of the overshoot effect is more pronounced for pure CSE and the cellulose:CSE blend at the ratio of 1:3 featuring lower SFE compared to the other films. Hydrophobic interactions are favored on those surfaces yielding higher adsorbed amounts of BSA. Cellulose exhibits low protein adsorption (0.4 ± 0.1 mg·m^{-2}), while hydrophobized cellulose displays a value as twice as high (0.8 ± 0.1 mg·m^{-2}). Protein adsorption of the cellulose:CSE blend at the ratio of 1:3 (0.7 ± 0.1 mg·m^{-2}) is comparable to pure CSE. In contrast, cellulose:CSE blends at ratios of 3:1 and 1:1 exhibit even lower protein adsorption than cellulose. This phenomenon can be probably traced back to the morphology of the blend films since the SFE do not exhibit significant differences. The area of CSE (see Table 2) is approximately the same for all blend ratios and therefore preferential adsorption onto either one or the other blend compound is not the reason for minimized BSA deposition. According to literature,

BSA forms island-like structures during adsorption which fuse into patches until a complete monolayer coverage is realized on the surface.[41] In the case of cellulose:CSE blends at the ratios of 3:1 and 1:1, the growth mechanism of the BSA layer is interrupted by the cellulose domains, whereas at the ratio of 1:3, the CSE phase is only perforated by very small cellulose parts, therefore protein adsorption is not influenced to a high extent. Interestingly, in blends composed of cellulose and lignin fatty acid ester, the latter acts as a sacrificial compound, which is removed upon rinsing with protein solution.[24] In comparison to that, CSE is supposedly better anchored in the cellulose matrix and does not show this particular behavior.
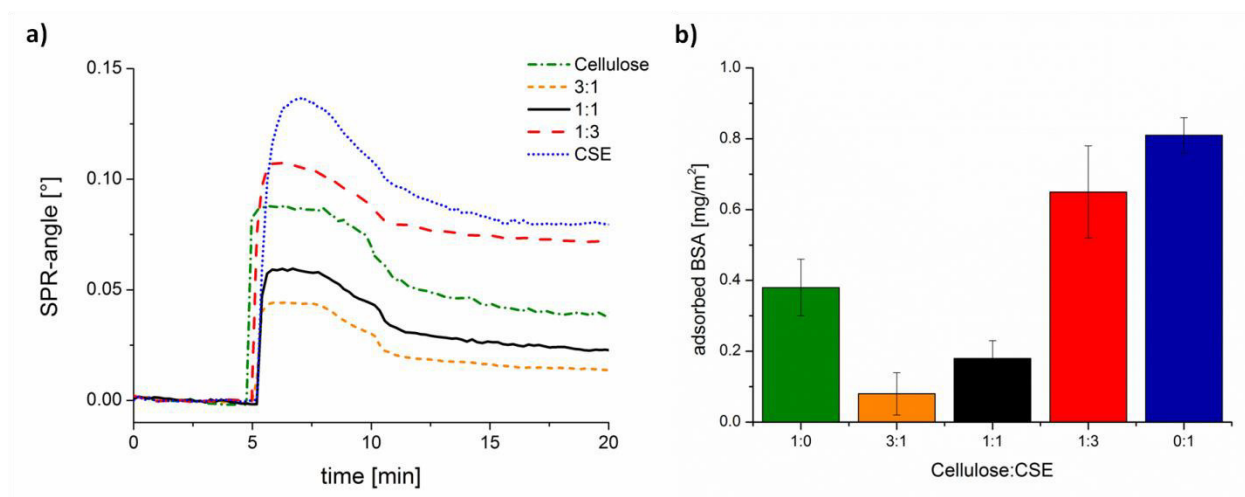
Figure 5. Sensograms (a) measured at 785 nm during adsorption of BSA onto blend films of cellulose and CSE at different ratios and corresponding amounts of adsorbed protein (b) calculated from change in SPR-angle.

Initially, the MP-SPR experiments for the cellulose:SA blends were performed in the same fashion as for the ones containing CSE. We were surprised to observe a strong decrease in SPR angle upon injection of protein solution into the flow cell indicating desorption of material for all

blends containing SA. Therefore, the rinsing step with protein solution was prolonged until a stable signal was detected (Figure 6a), meaning that nothing was removed from the surface anymore.
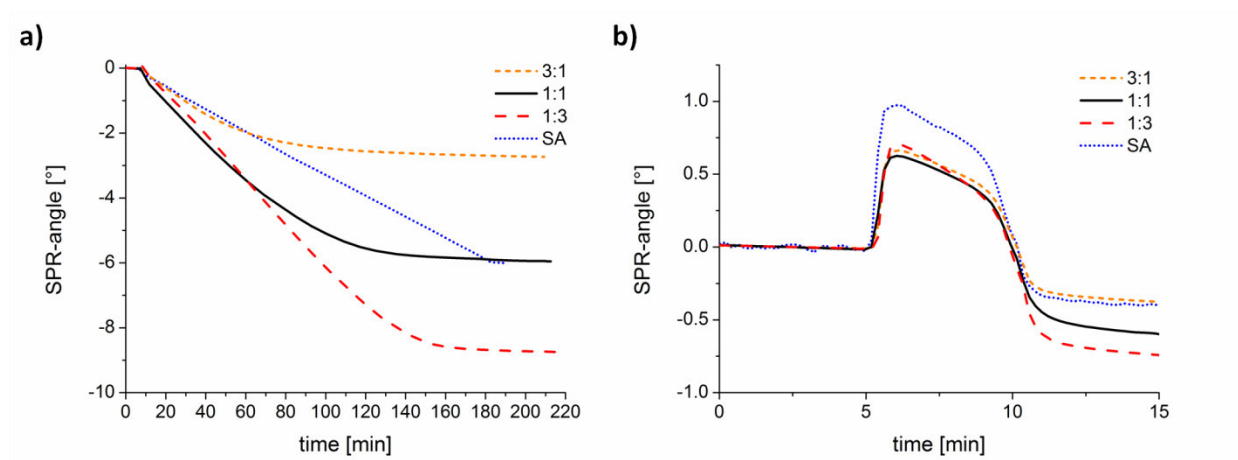
Figure 6. Sensograms measured at 785 nm during rinsing with (a) 1 mg·ml^{-1} BSA until reaching a steady signal and (b) 50 mg·ml^{-1} BSA for a period of 5 min of cellulose:SA blend films at different ratios.

Afterwards, AFM images were recorded and compared to images of surfaces, which were immersed in CHCl$_3$ in order to remove SA. AFM investigations after both treatments displayed very similar results (Figure 4) indicating that the rinsing procedure with BSA leads to the removal of SA from the cellulose matrix. This originates from the ability of BSA to build complexes with fatty acids[42–44], which are then rinsed away by the flow. The higher the SA content of the blend, the more material is removed resulting in smaller SPR angles. The period until all of the SA is depleted from the surfaces takes longer for blends containing a higher amount of SA (80 min, 130 min, 150 min, for cellulose:SA 3:1, 1:1 and 1:3, respectively). The experiment for pure SA was stopped after 180 min, since it clearly showed the slowest SA removal. In terms of kinetics, the slope of the curve during rinsing with protein is steeper, indicating faster desorption, for blends with higher SA content.

Furthermore, the material was tested at higher BSA concentrations to evaluate the borders of this approach. The experiments were conducted at a BSA concentration of 50 mg·ml⁻¹ corresponding to the concentration of human serum proteins.[45] Sensograms (Figure 6b) indicate an initial increase in SPR angle indicating protein adsorption, however, after a maximum of two minutes the signal decreases again. This initial adsorption can be attributed to the BSA deposition onto the cellulose parts of the blends, which is already accompanied by desorption of SA. After a period of 5 min, the surfaces were rinsed with buffer leading to a constant signal, which is below the SPR angle value detected before adsorption for all surfaces. One might argue that the removal of material is simply caused by the forces induced by rinsing, however, when rinsing with buffer without protein the signal is constant. BSA features the same adsorption behavior towards all blends in the beginning of the experiment, except for the pure SA surface, where BSA shows higher affinity. As for the removal of SA, the same trends as noticed for the experiments performed at lower BSA concentration was observed. In both experiments, the pure SA film is less prone to the BSA treatment. Although all cellulose:SA blends depict similar area ratios for the two phases (Table 2), the blends with ratios of 1:3 and 3:1 are rather flat, whereas the films at the ratio of 3:1 and the pure SA films show increased RMS roughness. The presence of platelets on these surfaces results in higher SA surface area than for the other films. Regardless, flat surfaces are apparently better accessible to BSA and the resulting BSA-SA complex diffuses faster from those surfaces. The BSA-SA complex sticks better to the surfaces where the SA residue is embedded in a large SA phase, due to cohesion, rather than in the case where SA is surrounded by cellulose. Therefore, the BSA-SA complex is released easier from the blends with small SA domains, i.e. cellulose:SA at ratios of 1:3 and 1:1.

Moreover, protein interaction at the investigated blend surfaces was monitored with high speed AFM to show the process in real-time and to gain better insight into the mechanisms (Figure S7-S9, †ESI). However, when conducting the experiments, the SA domains were scratched by the cantilever movement revealing the soft nature of the SA residue. In terms of cellulose:CSE blends, protein adsoprtion capacatiy was too low to dedect adsorbed proteins. Hardly any change was observed in the overall morphology.

CONCLUSION

In summary, the influence of fatty acids and fatty esters on nonspecific protein adsorption on cellulosic surfaces was investigated at 1 and 50 mg ml^{-1}. When free fatty acids were present in the films, nonspecific protein adsorption was prevented by complexation of BSA with the fatty acid, finally leading to the removal of the fatty acid from the films. This sacrificial behavior is slightly dependent on the accessibility of the surfaces to BSA, i.e. better accessibility leads to more pronounced complexation. In contrast, the covalently bound fatty acid in CSE affects the films in a different way. Here, complexation of the BSA concomitant with a sacrificial mechanism was not observed. Instead, the morphology of the blends and the surface free energies strongly impact the nonspecific adsorption of proteins since they avoid to form monolayer like coverage of BSA molecules. For pure CSE for instance, higher BSA adsorption was observed compared to cellulose, whereas for the 3:1 blend (cellulose:CSE), adsorption was reduced by a factor of two compared to pure cellulose.

In conclusion, mixing cellulose with cellulose fatty acid ester can be utilized to tune protein adsorption by choosing the added amount of hydrophobic compound. Surfaces resistant to protein adsorption can be manufactured by simply blending cellulose with free fatty acids. In both cases, we were able to attain fundamental insights into the interactions occuring at hydrophobized

cellulosic surfaces, which will serve as basis for new developments concerning materials in life science applications.

ASSOCIATED CONTENT

Supporting Information. Supplementary ATR-IR spectra and AFM images, contact angle data and thickness values.

AUTHOR INFORMATION

Notes

The authors declare no competing financial interests.

ACKNOWLEDGMENT

REFERENCES

(1)   Berg, J. M.; Tymoczko, J. L.; Stryer, L. In *Biochemistry*; W. H. Freeman: New York, 2002.

(2)   Johansson, I.; Svensson, M. *Curr. Opin. Colloid Interface Sci.* **2001**, *6* (2), 178–188.

(3)   Gunstone, F. D. *Fatty Acid and Lipid Chemistry*, 1st ed.; Springer US, 1996.

(4)   Thielemans, W.; Wool, R. P. *Biomacromolecules* **2005**, *6* (4), 1895–1905.

(5)   Edgar, K. J.; Pecorini, T. J.; Glasser, W. G. In *Cellulose Derivatives*; Washington, 1998; pp 38–60.

(6)   Fox, S. C.; Li, B.; Xu, D.; Edgar, K. J. *Biomacromolecules* **2011**, *12* (6), 1956–1972.

(7)   Wang, P.; Tao, B. Y. *J. Appl. Polym. Sci.* **1994**, *52* (6), 755–761.

(8)   Peydecastaing, J.; Vaca-Garcia, C.; Borredon, E. *Cellulose* **2009**, *16* (2), 289–297.

(9)   Huang, F.; Wu, X.; Yu, Y.; Lu, Y.; Chen, Q. *Carbohydr. Polym.* **2017**, *155*, 525–534.

(10) Granström, M.; Kettunen née Pääkkö, M.; Jin, H.; Kolehmainen, E.; Kilpeläinen, I.; Ikkala, O. *Polym. Chem.* **2011**, *2* (8), 1789.

(11) Vuoti, S.; Talja, R.; Johansson, L. S.; Heikkinen, H.; Tammelin, T. *Cellulose* **2013**, *20* (5), 2359–2370.

(12) Freire, C. S. R.; Silvestre, A. J. D.; Pascoal Neto, C.; Belgacem, M. N.; Gandini, A. *J. Appl. Polym. Sci.* **2006**, *100* (2), 1093–1102.

(13) Edgar, K. J.; Buchanan, C. M.; Debenham, J. S.; Rundquist, P. A.; Seiler, B. D.; Shelton, M. C.; Tindall, D. *Prog. Polym. Sci.* **2001**, *26*, 1605–1688.

(14) Bras, J.; Vaca-Garcia, C.; Borredon, M. E.; Glasser, W. *Cellulose* **2007**, *14* (4), 367–374.

(15) Kulomaa, T.; Matikainen, J.; Karhunen, P.; Heikkilä, M.; Fiskari, J.; Kilpeläinen, I. *RSC Adv.* **2015**, *5* (98), 80702–80708.

(16) Willberg-Keyriläinen, P.; Talja, R.; Asikainen, S.; Harlin, A.; Ropponen, J. *Carbohydr. Polym.* **2016**, *151*, 988–995.

(17) Krasnou, I.; Tarasova, E.; Märtson, T.; Krumme, A. *Int. Polym. Process.* **2015**, *30* (2), 210–216.

(18) Krasnou, I.; Gårdebjer, S.; Tarasova, E.; Larsson, A.; Westman, G.; Krumme, A. *Carbohydr. Polym.* **2016**, *152*, 450–458.

(19) Tang, L.; Eaton, J. W. *J. Exp. Med.* **1993**, *178* (6), 2147–2156.

(20) Kalasin, S.; Santore, M. M. *Colloids Surfaces B Biointerfaces* **2009**, *73* (2), 229–236.

(21) Vogel, V.; Baneyx, G. *Annu. Rev. Biomed. Eng.* **2003**, *5*, 441–463.

(22) Mohan, T.; Niegelhell, K.; Nagaraj, C.; Reishofer, D.; Spirk, S.; Olschewski, A.; Stana Kleinschek, K.; Kargl, R. J. *Biomacromolecules* **2017**, *18* (2), 413–421.

(23) Taajamaa, L.; Rojas, O. J.; Laine, J.; Yliniemi, K.; Kontturi, E. *Chem. Commun. (Camb).* **2013**, *49* (13), 1318–1320.

(24) Strasser, S.; Niegelhell, K.; Kaschowitz, M.; Markus, S.; Kargl, R.; Stana-Kleinschek, K.; Slugovc, C.; Mohan, T.; Spirk, S. *Biomacromolecules* **2016**, *17* (3), 1083–1092.

(25) Niegelhell, K.; Süßenbacher, M.; Jammernegg, K.; Ganner, T.; Schwendenwein, D.; Schwab, H.; Stelzer, F.; Plank, H.; Spirk, S. *Biomacromolecules* **2016**, *17* (11), 3743–3749.

(26) Zhang, K.; Geissler, A.; Standhardt, M.; Mehlhase, S.; Gallei, M.; Chen, L.; Marie Thiele, C. *Sci. Rep.* **2015**, *5*, 11011.

(27) Kontturi, E.; Thüne, P. C.; Niemantsverdriet, J. W. *Langmuir* **2003**, *19* (14), 5735–5741.

(28) Mohan, T.; Kargl, R.; Doliška, A.; Vesel, A.; Köstler, S.; Ribitsch, V.; Stana-Kleinschek, K. *J. Colloid Interface Sci.* **2011**, *358* (2), 604–610.

(29) Owens, D. K.; Wendt, R. C. *J. Appl. Polym. Sci.* **1969**, *13* (8), 1741–1747.

(30) Rabel, W. *Farbe und Lack* **1971**, *77* (10), 997–1005.

(31) Kaelble, D. H. *J. Adhes.* **1970**, *2* (2), 66–81.

(32) De Feijter, J.; Benjamins, J.; Veer, F. *Biopolymers* **1978**, *17* (7), 1759–1772.

(33) Robeson, J. L.; Tilton, R. D. *Langmuir* **1996**, *12* (25), 6104–6113.

(34) Heriot, S. Y.; Jones, R. A. L. *Nat. Mater.* **2005**, *4* (10), 782–786.

(35) Walheim, S.; Böltau, M.; Mlynek, J.; Krausch, G.; Steiner, U. *Macromolecules* **1997**, *30* (17), 4995–5003.

(36) Kontturi, E.; Johansson, L.-S.; Laine, J. *Soft Matter* **2009**, *5* (9), 1786–1788.

(37) Piculell, L.; Lindman, B. *Adv. Colloid Interface Sci.* **1992**, *41*, 149–178.

(38) Lindman, B.; Khan, A.; Marques, E.; Miguel, G.; Piculell, L. *Pure Appl. Chem.* **1993**, *65* (5), 953–958.

(39) Zhao, K.; Wodo, O.; Ren, D.; Khan, H. U.; Niazi, M. R.; Hu, H.; Abdelsamie, M.; Li, R.; Li, E. Q.; Yu, L.; Yan, B.; Payne, M. M.; Smith, J.; Anthony, J. E.; Anthopoulos, T. D.; Thoroddsen, S. T.; Ganapathysubramanian, B.; Amassian, A. *Adv. Funct. Mater.* **2016**, *26*, 1737–1746.

(40) Rabe, M.; Verdes, D.; Seeger, S. *Adv. Colloid Interface Sci.* **2011**, *162* (1-2), 87–106.

(41) Wangkam, T.; Yodmongkol, S.; Disrattakit, J.; Sutapun, B.; Amarit, R.; Somboonkaew, A.; Srikhirin, T. *Curr. Appl. Phys.* **2012**, *12* (1), 44–52.

(42) Cistola, D. P.; Small, D. M.; Hamilton, J. a. *J. Biol. Chem.* **1987**, *262*, 10980–10985.

(43) Choi, J.-K.; Ho, J.; Curry, S.; Qin, D.; Bittman, R.; Hamilton, J. A. *J. Lipid Res.* **2002**, *43* (7), 1000–1010.

(44) Curry, S.; Brick, P.; Franks, N. P. *Biochim. Biophys. Acta - Mol. Cell Biol. Lipids* **1999**, *1441* (2-3), 131–140.

(45) Friedrichs, B. *All about Albumin. Biochemistry, Genetics and Medical Applications*; Wiley-VCH, 1997.

Supporting Information #1

How Bound and Free Fatty Acids in Cellulose Influence Nonspecific

Protein Adsorption

submitted to Biomacromolecules
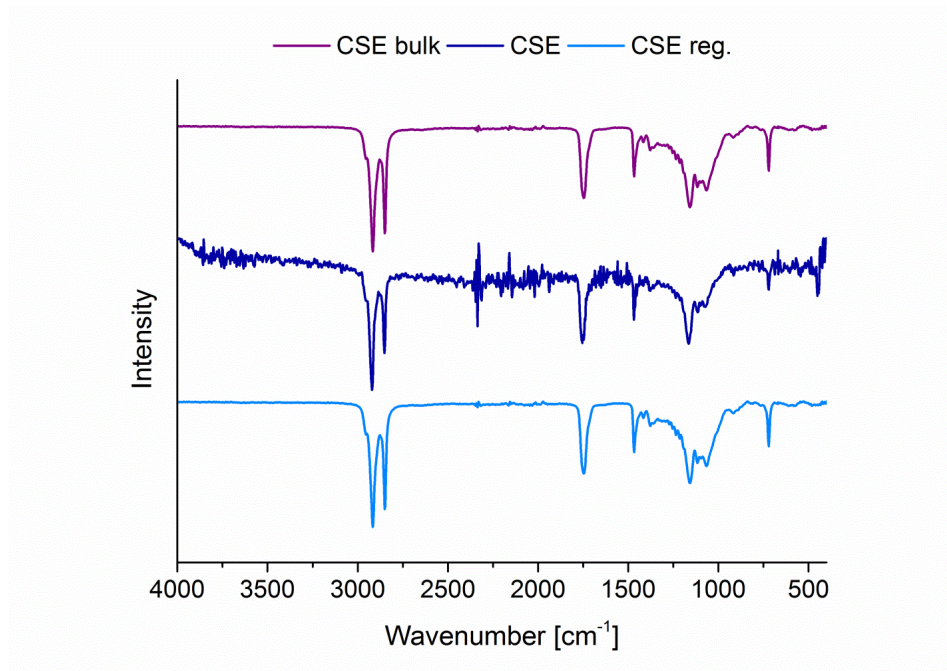
Figure S1. ATR-IR spectra of the bulk CSE material, a non-treated CSE film and a CSE film treated with acidic vapors.
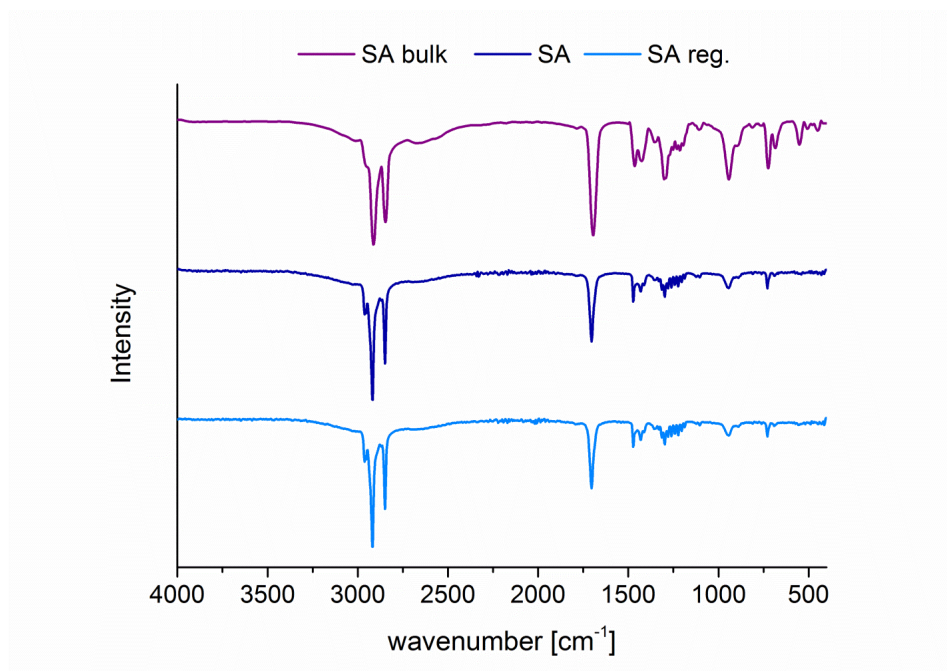
Figure S2. ATR-IR spectra of the bulk SA material, a non-treated SA film and a SA film treated with acidic vapors.
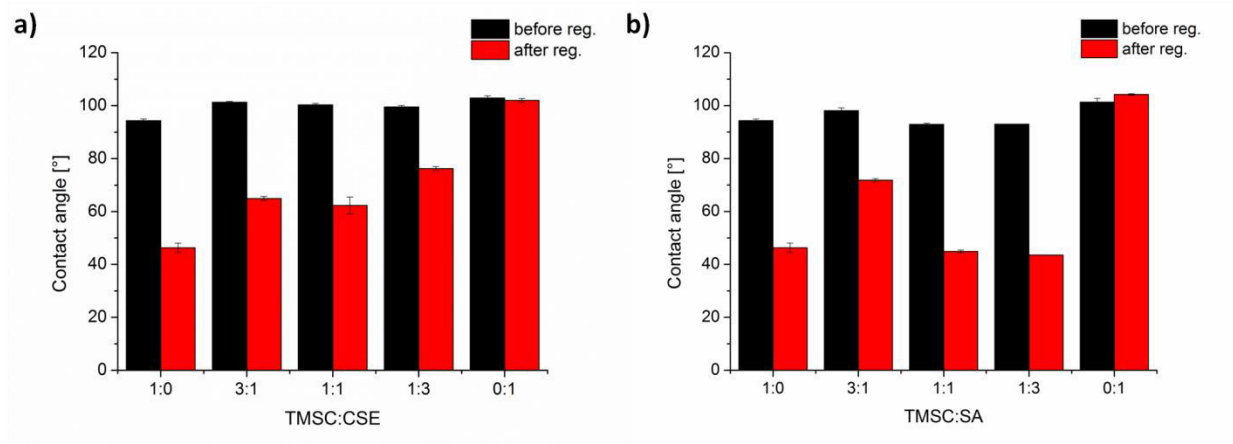
Figure S3. Static water contact angles of TMSC:CSE (a) and TMSC: SA (b) blend films before and after treatment with HCl vapors.
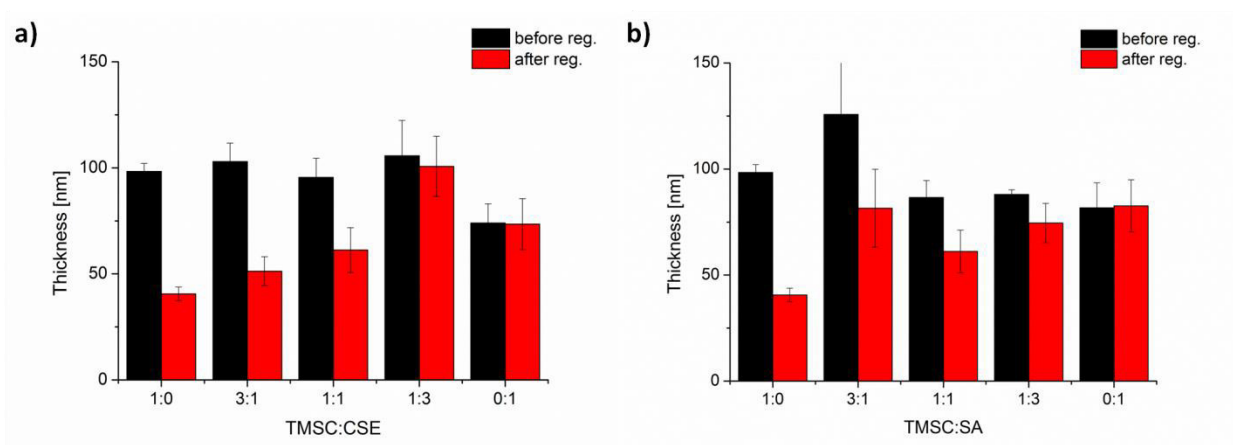
Figure S4. Thickness of TMSC:CSE (a) and TMSC:SA (b) blend films before and after treatment with HCl vapors.
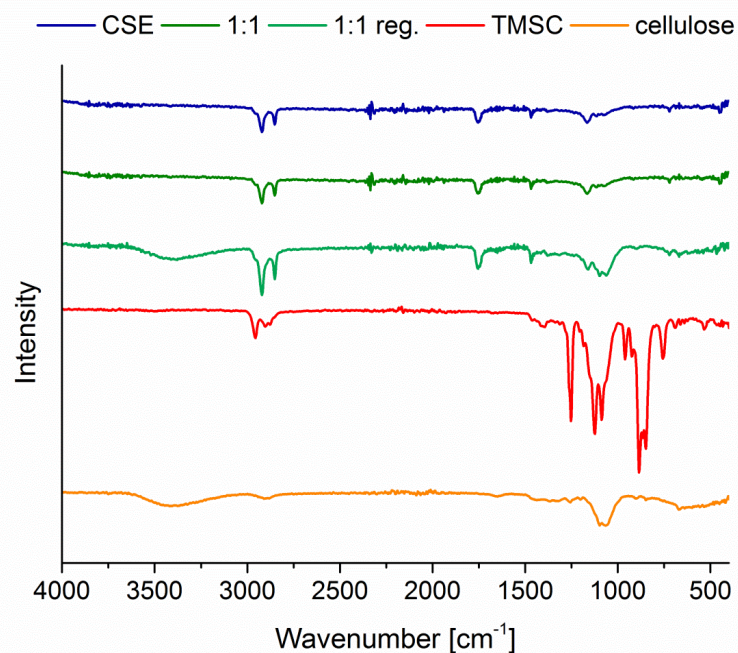
Figure S5. Comparison of ATR-IR spectra of a regenerated and a non-regenerated cellulose:CSE film (at the ratio of 1:1) with pure CSE, TMSC and cellulose thin films.
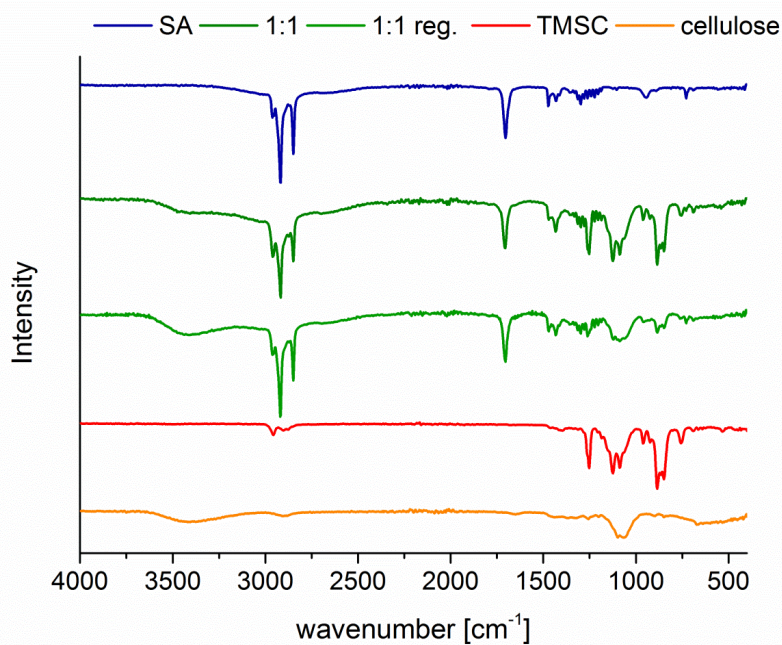
Figure S6. Comparison of ATR-IR spectra of a regenerated and a non-regenerated cellulose:SA film (at the ratio of 1:1) with pure SA, TMSC and cellulose thin films.

65 nm

after buffer treatment   after BSA treatment
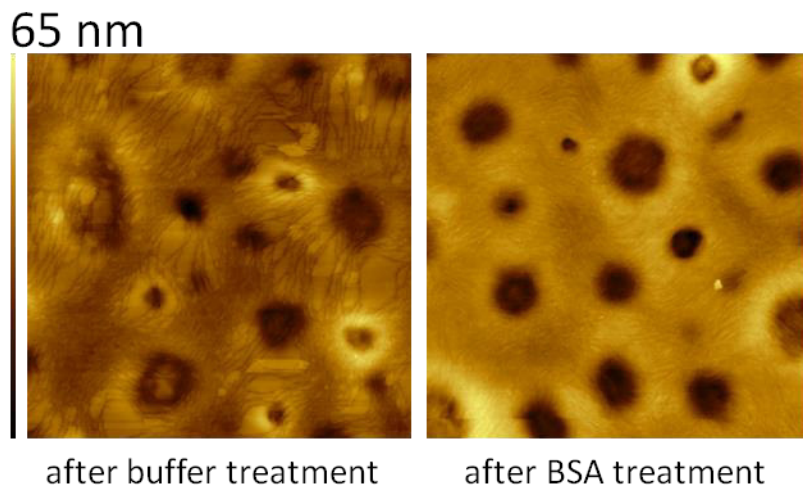
Figure S7. Atomic force microscopy height images (picture size $10 \times 10 \ \mu m^2$) of cellulose:CSE blend films at the ratio of 1:3 before (left) and after (right) adsorption of BSA. Both images were measured in buffer.

1200/300 nm
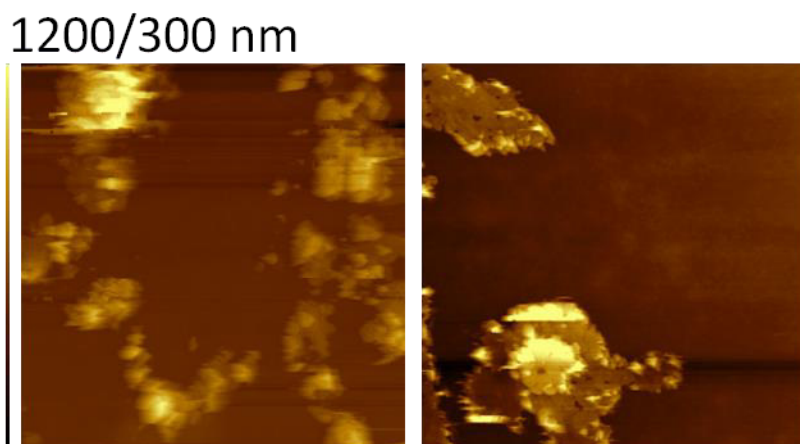
Figure S8. Atomic force microscopy height images (picture size $10 \times 10 \ \mu m^2$) of cellulose:SA blend films at the ratio of 3:1 in buffer. The elevated areas display the SA phase. The measuring error is caused by the soft nature of the SA phase leading to material removal. Therefore, no real-time observation of the treatment with BSA was conducted.
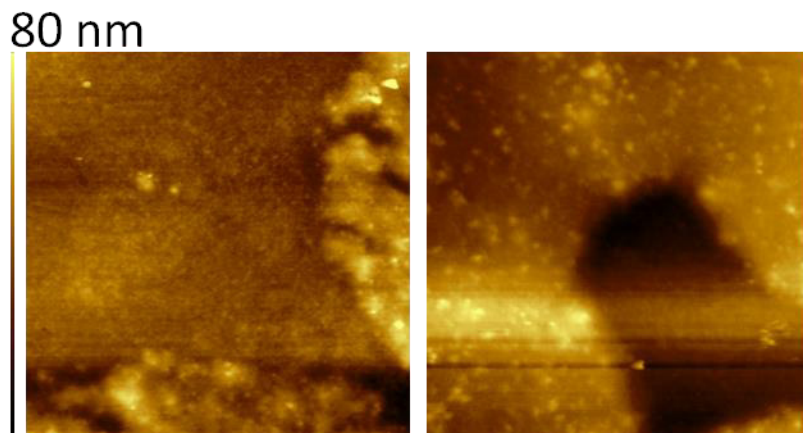
Figure S9. Atomic force microscopy height images (picture size $10 \times 10 \ \mu m^2$) of cellulose:SA blend films at the ratios of 3:1 before (left) and after (right) treatment with BSA. Both images were measured in buffer.
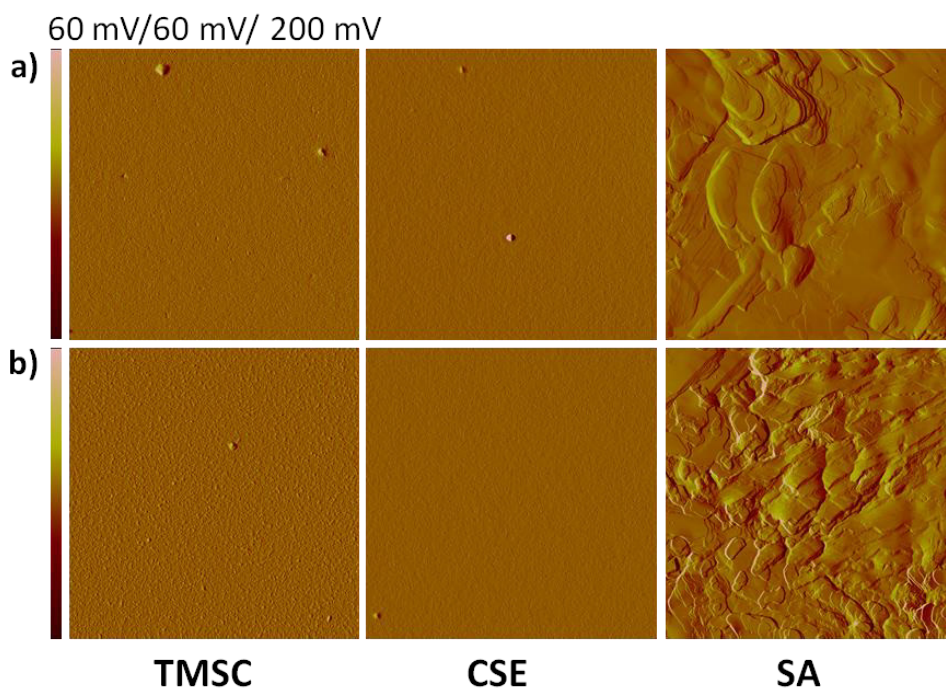
Figure S10. Atomic force microscopy amplitude error images (picture size $10 \times 10 \ \mu m^2$) of spin coated films from pure substances before (a) and after (b) treatment with HCl vapors.
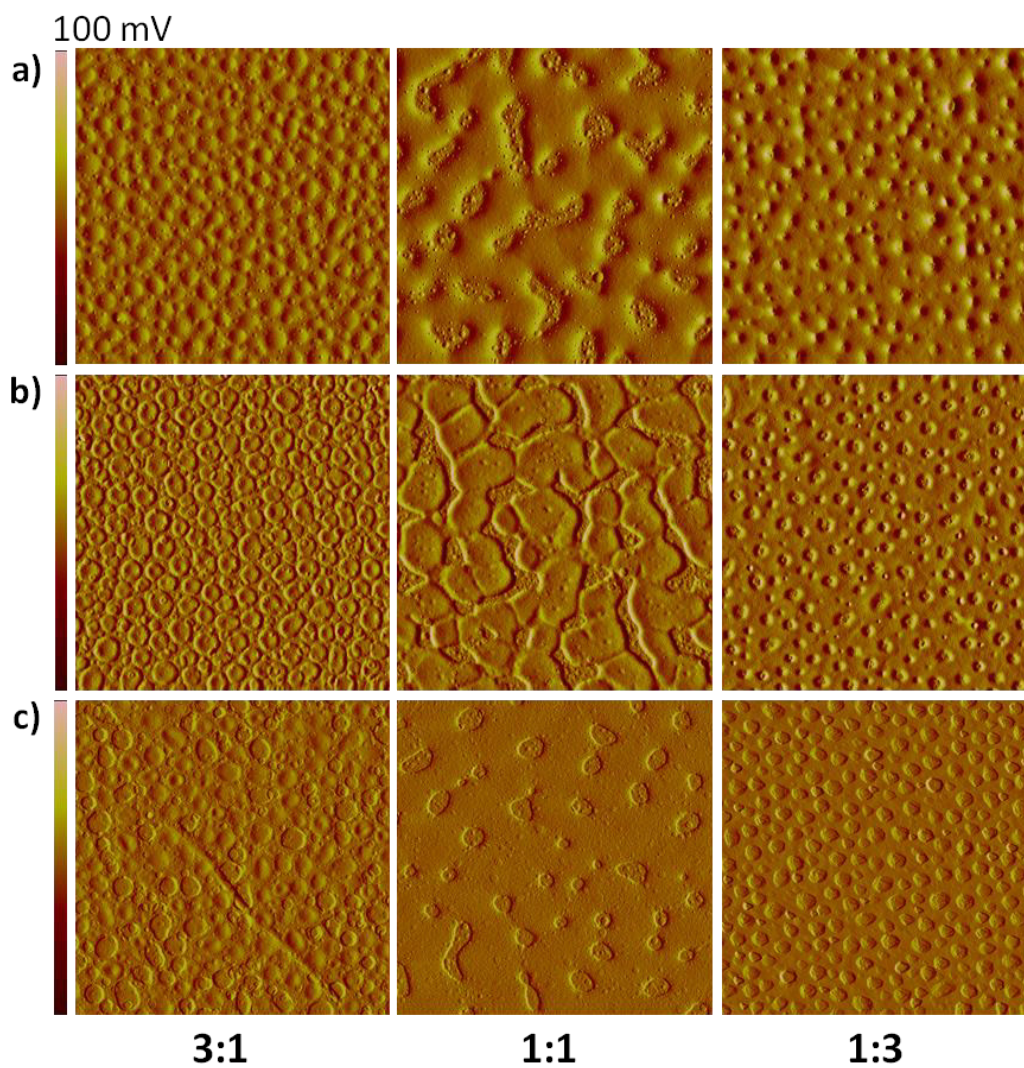
Figure S11. Atomic force microscopy amplitude error images (picture size $10 \times 10 \ \mu m^2$) of cellulose:CSE blend films spin coated at different ratios before (a) and after (b) exposure to HCl vapors, as well as after (c) treatment with CHCl$_3$.
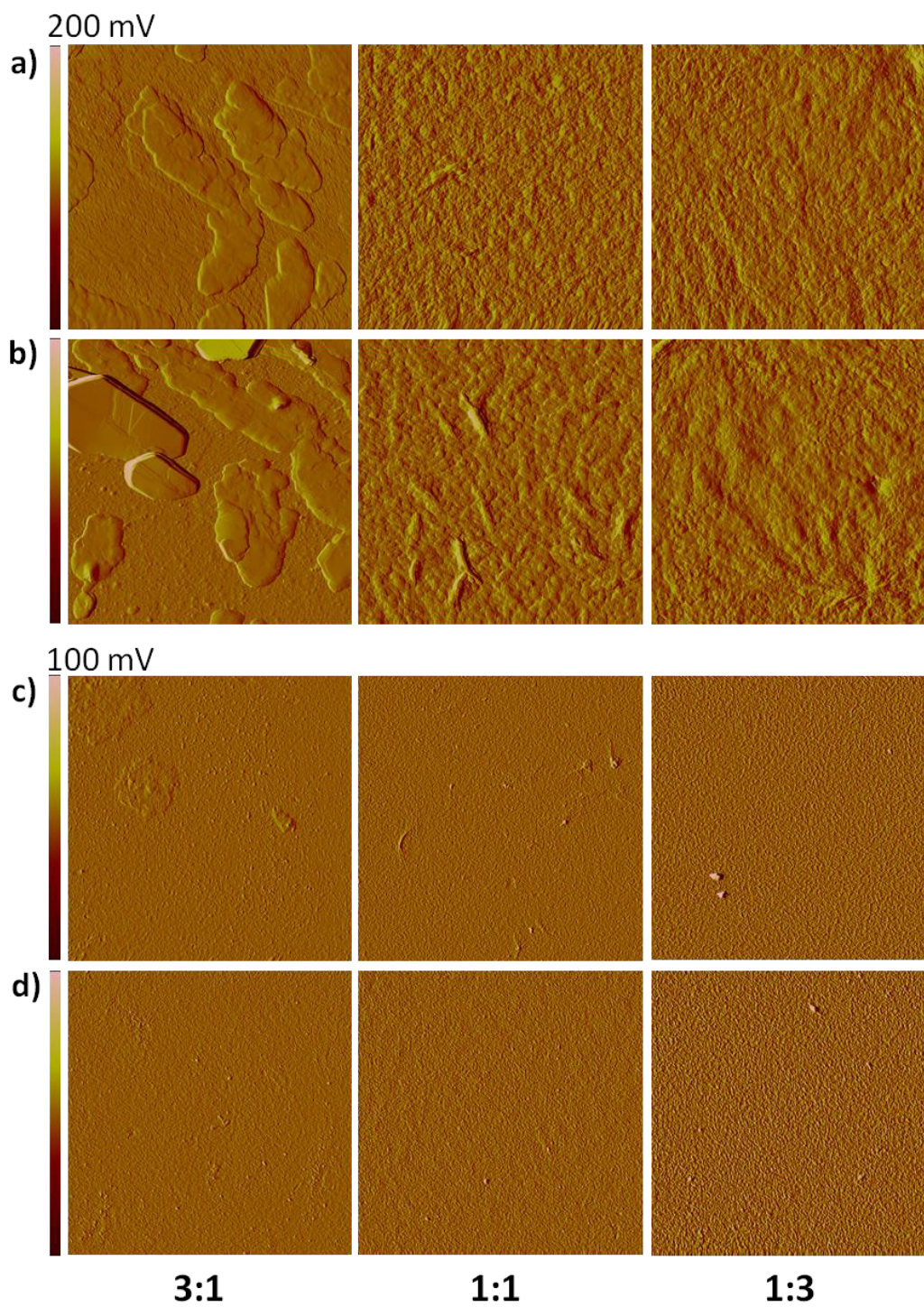
Figure S12. Atomic force microscopy amplitude error images (picture size 10×10 µm^2) of cellulose:SA blend films spin coated at different ratios before (a) and after (b) exposure to HCl vapors, as well as after treatment with (c) CHCl$_3$ and (d) BSA.

PAPER #2

Exploring Nonspecific Protein Adsorption onto Lignocellulosic

Amphiphilic Bicomponent Films

For this paper, I conducted the AFM, ATR-IR spectroscopy, stylus profilometry and contact angle measurements, interpreted the data and wrote a significant part of the manuscript.

Exploring Nonspecific Protein Adsorption on Lignocellulosic Amphiphilic Bicomponent Films

Simone Strasser,[†,‖] Katrin Niegelhell,[†,‖] Manuel Kaschowitz,[†] Sabina Markus,[‡] Rupert Kargl,[†,‡] Karin Stana-Kleinschek,[‡] Christian Slugovc,[†] Tamilselvan Mohan,*[,§] and Stefan Spirk*[,†,‡]

[†]Institute for Chemistry and Technology of Materials, Graz University of Technology, Stremayrgasse 9, 8010 Graz, Austria
[‡]Institute of Engineering and Design of Materials, University of Maribor, Smetanova 17, 2000 Maribor, Slovenia
[§]Institute of Chemistry, University of Graz, Heinrichstrasse 28, 8010 Graz, Austria

Ⓢ Supporting Information

ABSTRACT: In this contribution, we explore the interaction of lignocellulosics and proteins aiming at a better understanding of their synergistic role in natural systems. In particular, the manufacturing and characterization of amphiphilic bicomponent thin films composed of hydrophilic cellulose and a hydrophobic lignin ester in different ratios is presented which may act as a very simplified model for real systems. Besides detailed characterizations of the films and mechanisms to explain their formation, nonspecific protein adsorption using bovine serum albumin (BSA) onto the films was studied using a quartz crystal microbalance with dissipation (QCM-D). As it turns out, the rather low nonspecific protein adsorption of BSA on cellulose is further reduced when these hydrophobic lignins are incorporated into the films. The lignin ester acts in these blend films as sacrificial component, probably via an emulsification mechanism. Additionally, the amphiphilicity of the films may prevent the adsorption of BSA as well. Although there are some indications, it remains unclear whether any kind of protein interactions in such systems are of specific nature.

1. INTRODUCTION

In plant cells, a variety of dynamic processes takes place which are mainly governed by the complex interplay of different types of biomolecules such as lipids, proteins, and polysaccharides, for instance. While parenchyma cells are involved in photosynthesis, others (e.g., sclerenchyma, collenchyma) provide mechanical support due to the formation of a thick secondary cell wall.[1−3] These secondary cell walls are composed of cellulose fibrils that are embedded into a matrix of hemicelluloses, and lignins. There, the lignin i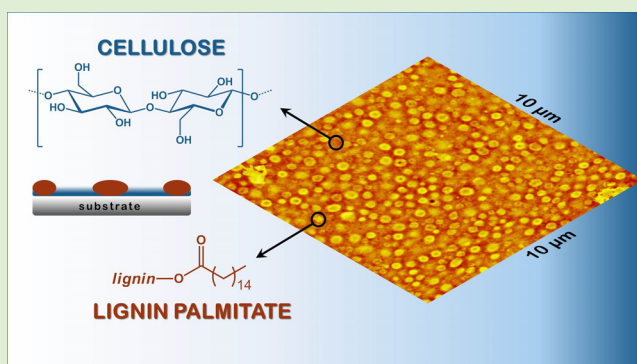s covalently linked to other components forming a complex hybrid material providing mechanical stability, as well as water impermeability.[4] Additionally, structural integrity in plant cells is provided by a variety of proteins as well, for example, hydroxyproline-rich glycoproteins (HRGP), arabinogalactan proteins (AGP), glycine-rich proteins (GRPs), and proline-rich proteins (PRPs), to mention the most important ones.[5] However, the whole range of proteins present in plants and their interaction with plant cell walls are not completely known so far, and therefore, they are still important ongoing research areas for the understanding of cellulose and lignin biosynthesis but also lignocellulosic processing and biorefinery purposes.[6] In this context, Yang and Wyman investigated the adsorption of BSA onto cellulose and lignin-containing materials (corn stover) with the aim to improve enzymatic hydrolysis by cellulases.[7] They showed that on lignin containing materials much more BSA is adsorbed than on Avicel cellulose. A reduction in the nonspecific binding of cellulases and β-glucosidases by adsorbing BSA on the lignocellulose substrates was observed, which resulted in higher glucose yields.

In order to simulate real conditions, recently the Rojas group introduced bicomponent films consisting of acetylated lignin and cellulose.[8] Particularly, the physicochemical properties such as wettability and microphase separation were extensively explored with the focus to gain more knowledge on cellulase activity in respect to improving biorefinery processes. Such acetylated lignins are highly abundant in nature[9] and are rather easy to prepare.[10] However, in the cell wall, other esters are present too which are of high interest for biological reasons, particularly, fatty acid alkyl esters[11] and may therefore significantly contribute to the interaction capacity with biomolecules such as proteins in the case of lignin.[12−14]

In this paper, our approach is to explore such bicomponent films comprising an esterified lignin (namely lignin palmitate,

LP) and cellulose with respect to nonspecific protein adsorption. By variation of the lignin content, different scenarios (in the cell wall) in terms of composition may be simulated in a very simplified manner and the interaction capacity with BSA can be determined.

The paper is constructed as follows: after a short description of the synthesis and characterization of the lignin palmitate, we will focus on the preparation and characterization of bicomponent films consisting of cellulose and the esterified lignin. Finally, the affinity of such surfaces toward BSA, a widely accepted marker for nonspecific protein adsorption is explored using a QCM-D.

2. EXPERIMENTAL SECTION

2.1. Materials. Wheat straw lignin from a sulfur-free pulping process provided by Annikki GmbH (Graz, Austria) was used without any further treatment except drying under vacuum until constant weight was reached. Trimethylsilyl cellulose (TMSC, $DS_{TMS:}$ 2.8, M_w: 149 000 g·mol^{-1} derived from Avicel PH-101) was purchased from Thüringisches Institut für Textil- und Kunststoff-Forschung e.V. (TITK), Germany and used as starting material for lignin-cellulose bicomponent film preparation. Toluene (99.9%), palmitoyl chloride and bovine serum albumin (BSA) were purchased from Sigma-Aldrich, Austria, and used as received. Silica gel (60, 0.03−0.2 mm, product no. P090.5) was purchased from Lactan. QCM-D sensors (QSX301) were purchased from LOT-Oriel (Germany). Milli-Q water from a Millipore water purification system (Millipore) (resistivity = 18.2 MΩ·cm^{-1} at 25 °C) was used for contact angle and QCM-D investigations.

2.2. Size Exclusion Chromatography (SEC). The molecular masses were retrieved from HPLC-SEC measurements in DMF which were performed on an Agilent 1200 Infinity with three TOSOH TSK-GEL Alpha Series columns (TSKgel Alpha-2500, TSKgel Alpha-3000, and TSKgel Alpha-4000) in a row. Approximately 5 mg of sample material was dissolved in 1 mL of DMF + LiBr (1 g·L^{-1}). A volume of 20 μL of this solution was injected for analysis and eluted with a solution of lithium bromide in DMF (1 g·L^{-1} LiBr) at a column temperature of 50 °C (eluation time 90 min). Lignin was detected by UV absorption (280 nm) and measured against polystyrene standards purchased from PSS GmbH, Mainz. Integration was performed until the volume corresponding to the mass of 300 g·mol^{-1}. SEC-HPLC measurements in chloroform were performed on a LC-20 AD system from Shimadzu equipped with separation columns (MZ-Gel Sdplus Linear 5 μm separation columns from MZ Analysentechnik) in line and a refractive index (RD-20A) as well as a UV/vis detector (SPD-20A). Polystyrene standards purchased from Polymer Standard Service were used for calibration. The wheat straw lignin (WSL) used as starting material is characterized by M_n = 1050 g·mol^{-1}, M_w = 4400 g·mol^{-1}, and PDI = 4.2.

2.3. NMR Spectroscopy. The chemical structure of the used lignin was investigated by ^{13}C−^{1}H heteronuclear single quantum coherence nuclear magnetic resonance (^{13}C−^{1}H HSQC) NMR measurements using a Varian Unity INOVA 500 MHz FT NMR instrument. The amount of 50 mg of dry WSL was dissolved in DMSO-d_6 and placed in standard 5 mm glass NMR tubes. Spectra were acquired at 35 °C on a Varian Unity INOVA 500 MHz (^{1}H 499.894 MHz, ^{13}C 125.687 MHz) FT NMR instrument with a ^{1}H [^{15}N−^{31}P] 5 mm PFG Indirect Detection Probe using a standard adiabatic gradient Varian pulse sequence implementation (gHSQCAD). The phase-sensitive HSQC spectra were conducted with an acquisition time of 150 ms with an $F2$ spectral width of 7998 Hz (16 ppm) in 2400 data points using 128 transients for each of 512 $t1$ increments of the $F1$ spectral width of 26393 Hz (210 ppm). Dummy scans (32) were used to establish equilibrium conditions at the start of the experiment. A coupling constant ($^1J_{CH}$) of 146 Hz was used and ^{13}C-decoupling during acquisition was performed by WALTZ40 composite pulse from the high-power output-decoupling channel. For semiquantitative analysis the 2D correlation peaks were

integrated and compared using MestReNova NMR processing software. The DMSO solvent peak was used as an internal reference for all samples (δ_C 39.51 and δ_H 2.50 ppm).

2.4. Determination of Hydroxy Groups in WSL and LP. The amount of hydroxy groups in the lignins was determined by ^{31}P NMR measurements using a Varian Unity INOVA 500 MHz (^{1}H 499.894 MHz, ^{31}P 202.32 MHz) FT NMR instrument with a ^{1}H−^{19}F/^{15}N−^{31}P 5 mm Switchable Probe according to literature protocols.[15−17] At least 256 scans were recorded to accumulate spectra with a delay time of 25 s between two consecutive inverse gated pulses. Lignin samples were phosphitylated with 2-chloro-4,4,5,5-tetramethyl-1,3,2-dioxaphospholane (TMDP) prior to measurements at 25 °C in CDCl$_3$. The obtained ^{31}P chemical shifts are given relative to phosphoric acid and spectra were referenced to phosphitylated cyclohexanol as internal standard (145.2 ppm). The obtained data was analyzed quantitatively using eqs 1 and 2, respectively:

$$[OH] = SF\frac{A}{m \times DD} \tag{1}$$

with

$$SF = \frac{VcP}{M} \tag{2}$$

where [OH] refers to the total hydroxy content [mmol·g^{-1}], A to the integrated peak area [integral value], m to the mass of the sample [g], DD to the degree of dryness (= 1 for a dried sample), SF to the standard factor [mmol], V to the volume [mL], c to the concentration [mmol·g^{-1}], P to the purity (= 0.99 for 99%), and M to the molecular weight of the internal standard (cyclohexanol).

2.5. Elemental Analyses (EA). EA were performed on a Vario EL III Element Analyzer from Elementar GmbH in two parallels.

2.6. Attenuated Total Reflection Infrared (ATR-IR) Spectroscopy. The analyses were performed on a Bruker Alpha FT-IR spectrometer equipped with the ALPHA's Platinum ATR single reflection diamond ATR module in a range from 500 to 4000 cm^{-1} having with a resolution of 4 cm^{-1}.

2.7. Synthesis and Characterization of Lignin Palmitate (LP). WSL was esterified with palmitoyl chloride according to a literature protocol.[10] In a typical procedure, wheat straw lignin (1.003 g, 4.01 mmol OH) was placed in a Schlenk flask and dried for a period of 30 min in vacuo. After venting the flask with N$_2$, lignin was dissolved in dry DMF (6 mL), and triethylamine (556 μL, 4.01 mmol, 1 equiv with regard to lignin hydroxy groups) was added and the mixture was heated to 65 °C. Then palmitoyl chloride (1035 μL, 3.41 mmol, 0.85 equiv with regard to lignin hydroxy groups) was slowly added dropwise. The reaction mixture was allowed to stir for a period of 24 h at 65 °C under N$_2$-atmosphere followed by precipitation in H$_2$O which gave a brown precipitate after filtration. Subsequent drying in vacuo yielded 1.75 g of raw LP. Unreacted, yet hydrolyzed palmitic acid was then removed via column chromatography using silica gel. A proportion of the obtained raw lignin palmitate (1.205 g) was applied onto a plug of silica gel and washed with cyclohexane/ethyl acetate (20:1 (v:v)) until no palmitic acid could be detected via TLC (cyclohexane/ethyl acetate 3:1 (v:v), R_f = 0.28). Thus, 390 mg of palmitic acid was obtained. The remaining lignin ester was then eluted with dichloromethane/methanol (10:1 (v:v)) and finally with pure methanol until the eluent was colorless. The amount of 750 mg of LP was obtained. Elemental analysis: C, 65.5%; 7.9%; N 1.4%. SEC (CHCl$_3$) M_n = 580 g·mol^{-1}, PDI = 1.5. SEC M_n = 2000 g·mol^{-1}, PDI = 7.0. Hydroxy number determination was performed as in case of WSL and results are listed in Table 1. IR (ATR) spectroscopy revealed new ν(C=O) bands for LP at 1761, 1724, and 1710 cm^{-1}.

2.8. Preparation of Bicomponent Thin Films. For the preparation of bicomponent films, TMSC solutions were prepared (54.4 mg in 5 mL CHCl$_3$) and combined with solutions of lignin palmitate (LP, 50.7 mg in 5 mL CHCl$_3$) to end up in different ratios between TMSC and LP, namely 3:1, 1:1, and 1:3 (v/v). For the film preparation, 100 μL of the combined solutions was spin coated (Polos MCD wafer spinner, APT corporation, Germany) on piranha treated silicon wafers (1.5 × 1.5 cm^2) at 4000 rpm for 60 s (acceleration 2500

Table 1. Comparison of the Hydroxy Numbers of WSL and PL,[a] Determined by Quantitative Analysis of the ^{31}P-NMR Spectra after Phosphitylation

entry	type of functional group	WSL [mmol g^{-1}]	PL [mmol·g^{-1}]	reduction [%][b]
1	total OH	4.01	1.70	58
2	aliphatic OH	3.01	1.25	58
3	aromatic OH	1.00	0.45	55
4	uncondensed	0.86	0.39	55
5	syringyl OH	0.07	0.08	−14
6	guaiacyl OH	0.58	0.25	57
7	p-hydroxyphenyl OH	0.22	0.07	73
8	condensed	0.14	0.06	57
9	carboxyl OH	1.07	0.59	45

[a]Determined by ^{31}P NMR spectroscopy of phosphitylated samples; estimated error = ±0.03 mmol·g^{-1}. [b]Reduction of the hydroxy number in percent is calculated as follows: (hydroxy number of WSL − hydroxy number of LP)/hydroxy number of WSL × 100. Please note that the degree of esterification of hydroxy groups cannot be directly obtained from these numbers.

rpm·s^{-1}). In order to obtain LP-cellulose bicomponent films, the coated films were exposed to 3 M HCl vapor (12 wt %) for 12 min to obtain fully regenerated LP/cellulose thin films.

For QCM-D measurements, sensor crystals coated with a gold layer were used as a substrate for spin coating of LP/TMSC thin films. The crystals were soaked into a mixture of H$_2$O/H$_2$O$_2$ (30 wt %)/NH$_4$OH (5:1:1; v/v/v) for 10 min at 70 °C. After that, they were immersed into a piranha solution (H$_2$O$_2$ (30 wt %)/H$_2$SO$_4$ (98 wt %), 1:3; v/v)) for 60 s, rinsed with Milli-Q water again, and finally blow dried with nitrogen gas. For the preparation of LP/cellulose thin films, 70 μL of LP/TMSC solution (dissolved in chloroform) was deposited on the static QCM-D crystal which was then rotated for 60 s with a spinning speed of 4000 rpm and an acceleration of 2500 rpm·s^{-1}. For converting TMSC into cellulose, the coated sensors were placed into a polystyrene Petri dish (5 cm in diameter) containing 3 mL of 3 M HCl. The dish was covered with its cap and the films were exposed to the vapors of HCl for 12 min.

2.9. Profilometry. Layer thickness of the films was determined by profilometry using a DEKTAK 150 Stylus Profiler from Veeco (Plainview, NY). The scan length was set to 1000 μm over the time duration of 3 s. The diamond stylus had a radius of 12.5 μm and the force was 3 mg with a resolution of 0.333 μm/sample and a measurement range of 6.5 μm. The profile was set to hills and valleys. Prior to the surface scanning, the coating was scratched to remove the TMSC/lignin bicomponent films in order to determine the thickness of the coating using a step-height profile. The thickness was determined at 3 independent positions. The samples were measured before and after regeneration.

2.10. Contact Angle (CA) determination. The wettability of the bicomponent thin films was determined by using a Dataphysics contact angle measurement system OCA15+ (Dataphysics, Germany) using the sessile drop method and a drop volume of 3 μL. All measurements were carried out at room temperature. Determination of the static contact angles (SCAs) was based on the analysis of the drop shape and was performed with the software provided by the manufacturer (software version SCA 20). All the measurements were performed with a minimum of four drops per surface and an average value was calculated.

2.11. Atomic Force Microscopy (AFM). AFM images of the films were recorded in tapping mode (noncontact mode) on a Veeco Multimode Quadrax MM AFM (Bruker; Billerica, MA). For the scanning, silicon cantilevers (NCH-VS1-W from NanoWorld AG, Neuchatel, Switzerland) were used with an average spring constant of 42 N/m (Force Constant) and with a resonance frequency of 270–320 kHz (Coating: none). All measurements were performed at room temperature and under ambient atmosphere. The calculation of the

root-mean-square roughness and the image processing was done with the Nanoscope software (V7.30r1sr3; Veeco).

2.12. Quartz Crystal Microbalance with Dissipation (QCM-D). A QCM-D instrument (model E4) from Q-Sense, Gothenburg, Sweden was used. The instrument simultaneously measures changes in the resonance frequency (Δf) and energy dissipation (ΔD) when the mass of an oscillating piezoelectric crystal changes upon increase/decrease in the mass of the crystal surface due to the added/deduced mass. Dissipation refers to the frictional losses that lead to damping of the oscillation depending on the viscoelastic properties of the material. For a rigid adsorbed layer that is fully coupled to the oscillation of the crystal, Δf_n is given by the Sauerbrey equation[18] (eq 3)

$$\Delta m = C \frac{\Delta f_n}{n} \tag{3}$$

where Δf_n is the observed frequency shift, C is the Sauerbrey constant (−0.177 mg·Hz^{-1}·m^{-2} for a 5 MHz crystal), n is the overtone number ($n = 1, 3, 5$, etc.), and Δm is the change in mass of the crystal due to the adsorbed layer. The mass of a soft (i.e., viscoelastic) film is not fully coupled to the oscillation and the Sauerbrey relation is not valid since energy is dissipated in the film during the oscillation. The damping (or dissipation) (D) is defined as

$$D = \frac{E_{\text{diss}}}{2\pi E_{\text{stor}}} \tag{4}$$

where E_{diss} is the energy dissipated and E_{stor} is the total energy stored in the oscillator during one oscillation cycle.

2.13. Adsorption of Bovine Serum Albumin on the Different Bicomponent Thin Films. The coated QCM sensors were mounted in the QCM flow cell and equilibrated first with water for 60 min and then with a phosphate buffered solution (pH 7.4) for 30 min. After equilibration of the films, BSA ($c = 1.0$ mg·mL^{-1}, dissolved in phosphate buffer) was pumped over the sensors at a flow rate of 0.1 mL·min^{-1} for 90 min. After this, the BSA solution was exchanged with PBS in order to remove loosely bound material from the surface. The temperature was kept 21 ± 0.1 °C for all experiments. All adsorption experiments have been performed in triplicates and mean values and standard deviations of third overtone dissipation and frequency were calculated.

3. RESULT AND DISCUSSION

3.1. Synthesis and Characterization of Lignin Palmitate. For this study, wheat straw lignin (WSL) from an Organosolv process was used as the starting material. It was anticipated that the relatively low molecular weight ($M_n = 1050$ g·mol^{-1}, PDI = 4.2 as determined by SEC in DMF/LiBr at 50 °C) of such a type of lignin will yield well organosoluble lignin derivatives after esterification with a fatty acid derivative. The reason, that we aim at organosoluble lignin esters is to ensure solvent compatibility of the lignin ester with the precursor for cellulose, namely trimethylsilyl cellulose, which is readily soluble in less polar solvents such as chloroform and hexanes at DS$_{\text{Si}}$ values larger than 2.3. As fatty acid, palmitic acid (hexadecanoic acid) was selected because it is the most common saturated fatty acid featuring a higher tendency to crystallize (as well as a higher melting point) than their unsaturated congeners.

First, structural information on the starting material WSL was obtained from ^{13}C−^{1}H heteronuclear single quantum coherence nuclear magnetic resonance (HSQC) measurements and from identification and quantification of hydroxy groups. The HSQC spectra were analyzed based on findings disclosed in several studies[19−22] and corresponding spectra are shown in the Supporting Information (Figure S1). The distribution of the three main lignin building blocks, namely, syringyl (S), guaiacyl (G), and p-hydroxyphenol (H), was found to be 1:8.5:3.2. p-
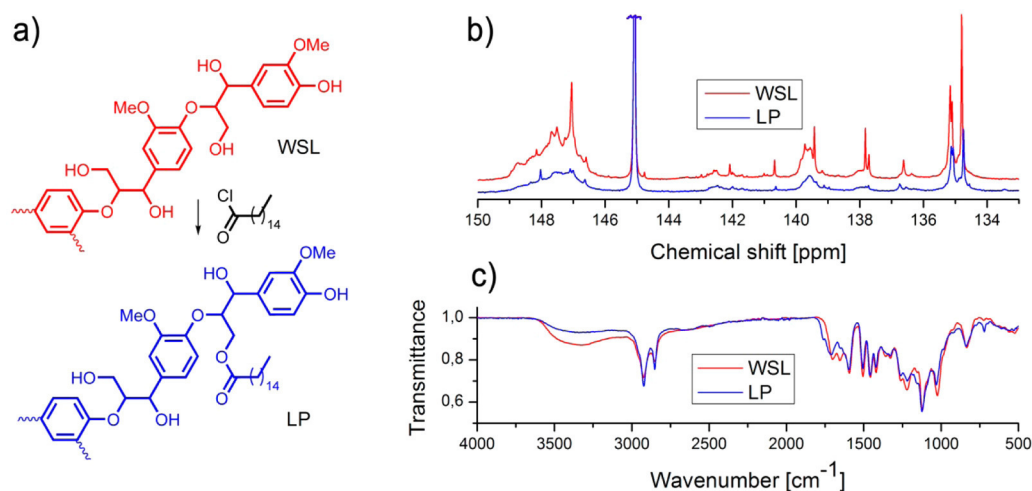
Figure 1. (a) Chemical equation for the preparation of LP showing simplified chemical structures of WSL and LP. Reaction conditions: WSL (4.0 mmol OH), palmitoyl chloride (3.3 mmol), NEt$_3$ (4.0 mmol); solvent = DMF; reaction temperature = 65 °C, reaction time = 24 h. (b) ^{31}P NMR spectra of phosphitylated WSL (red) and phosphitylated LP (blue), signal of the reference truncated. (c) ATR-FT-IR spectra of WSL (red) and LP (blue). For normalization, the band at 1122 cm^{-1} (C−H in plane deformation of G units) was employed.

coumarates (11%) and ferulates (17%) as well as tricin units (4%) were identified. The β-O-4′ aryl ether connectivity is by far the most abundant (85%) lignin interunit linkage. β-5′ Phenylcoumarans (10%) and β-β′ resinol units (5%) were the only other observed connection modes. Other substructures which have already been identified in HSQC spectra of wheat straw lignins, namely, dibenzodioxins, spirodienones, and α,β-diaryl ethers, were not detected in the used WSL. Finally, considerable amounts of saturated and unsaturated fatty acid derivatives were detected in the high field region (δ_C/δ_H 0−50/0−2.4) of the spectrum (as well as by resonances at δ_C/δ_H 127.4 and 129.3/5.33 ppm). The ^{31}P NMR spectroscopy of phosphitylated WSL allowed for the quantification of different hydroxy groups and carboxylic acid groups (Figure 1, Table 1). The measure for total hydroxy groups amounts to 4.0 mmol·g^{-1} WSL and is composed of three-quarters aliphatic and one-quarter aromatic hydroxy groups. In this particular WSL, a relatively high amount of carboxylic acid groups (1.1 mmol·g^{-1}) was observed. This finding is corroborated by ATR-FT-IR spectroscopy. Absorption bands at 1701 cm^{-1} (C=O stretching vibration of carboxylic acids) and 1654 cm^{-1} (asymmetric stretching of the COO-fragment or C=O stretching vibration of α,β-unsaturated carboxylic acids) are indicative for the presence of carboxyl groups.

Esterification of WSL was performed using palmitoyl chloride and triethylamine in dry DMF at 65 °C (see Figure 1a). Palmitoyl chloride was chosen because of its high reactivity and the facile separation of the hydrochloric acid amine adduct formed as byproduct.[10] Workup was done after 24 h reaction time by pouring the reaction mixture into deionized H$_2$O yielding a brown solid powder. Unreacted, yet hydrolyzed palmitoyl acid chloride was removed via column chromatography and isolated as palmitic acid[23] (ca. one-third of the used palmitoyl chloride). Eluting the lignin palmitate (LP) and drying yielded ca. two-thirds of the raw product subjected to column chromatography (see the Supporting Information for details). The obtained LP completely dissolves in solvents like CH$_2$Cl$_2$, CHCl$_3$, tetrahydrofuran or ethyl acetate (solubility at least 5 g·L^{-1}) and was characterized via SEC, quantitative ^{31}P NMR spectroscopy after phosphitylation, HSQC, ATR-IR spectroscopy, and elemental analysis. An interesting feature was

revealed by molar mass determinations using different solvent systems. It turns out that in DMF molecular masses of WSL (M_n = 2000 g·mol^{-1}, PDI = 7.0) higher than in CHCl$_3$ where much lower masses have been found (M_n = 580 g·mol^{-1}, PDI = 1.5). This result points at aggregation in DMF pretending higher molecular masses of WSL in this solvent.

The ATR-FT-IR spectrum of LP showed a distinct decrease of the intensity of the OH-band (see Figure 1c). New absorption maxima at 1762 and 1710 cm^{-1} including a shoulder at 1724 cm^{-1} suggest the formation of aryl and alkyl esters of palmitic acid. Another observation is the reduced absorbance of the band peaking at 1654 cm^{-1} compared to the WSL spectrum, suggesting the removal of carboxylic acid salts originally present in WSL during the isolation of LP. These findings are supported by the ^{31}P NMR measurements of phosphitylated LP (cf. Figure 1b).

The overall amount of hydroxy groups in LP was reduced from 4.0 to 1.7 mmol·g^{-1} (0.5 OH/repeating unit; see the Supporting Information for calculations). From these data, a degree of esterification of LP of 30−35% (of the hydroxy groups present in WSL) can be estimated. As can be seen in Table 1, the amount of both aliphatic and aromatic hydroxy groups was reduced to approximately the same extent (Table 1, entries 2 and 3). However, the different aromatic phenol groups (from S, G and H-units) participated differently in the esterification. Syringyl hydroxy groups hardly reacted while a major proportion share of the p-hydroxyphenyl-type OH-groups have been esterified (Table 1, entries 5−7). Accordingly the ratio of OH bearing S, G and H moieties is changed from 1:8.5:3.2 (S:G:H in SWL) to 1:3.1:0.8 in LP. The amount of carboxylic groups was significantly reduced as well, supporting the statements issued when discussing the ATR-FT-IR spectra of LP.

It should be noted here that the esterification of the WSL did not induce any detectable structural changes in the lignin structure as proven by NMR spectroscopy which is in line with data from literature where structural changes have been reported to take place at higher temperatures (>100 °C) than the ones we used in this study.[22,24]

3.2. Preparation and Characterization of Bicomponent Thin Films. After synthesis of the organosoluble LP, we
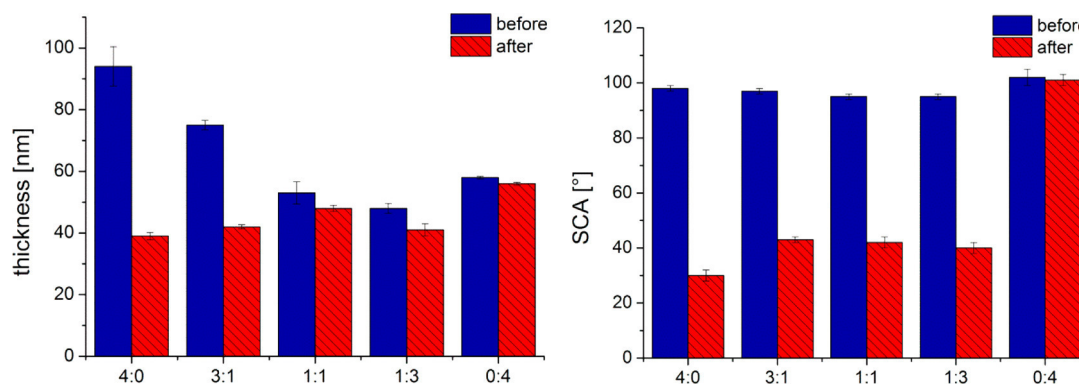
Figure 2. Average layer thickness d [nm] and SCA [deg] of the films exhibiting different TMSC:LP ratios.
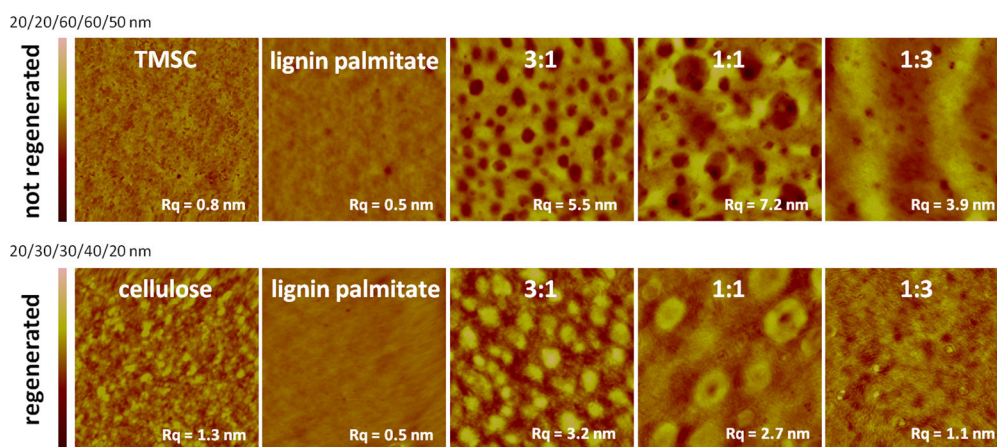
Figure 3. AFM height images (2 μm × 2 μm) of the different films (TMSC:LP) before and after HCl vapor treatment. The z-scales are indicated for each image above the bar left. Note that, for the 1:1 system, some tubelike pillars are present which are filled with cellulose.

aimed at preparing thin films that contain LP as well as cellulose and to explore nonspecific protein adsorption on these films. As already mentioned, there is only little information available on such bicomponent thin films in literature, mainly due to the insolubility of cellulose in most common organic solvents, which are in most cases unsuitable to produce well-defined, homogeneous films. Our approach was to mix organosoluble TMSC (DS$_{Si}$: 2.8) with solutions of the LP in different ratios (1:3, 1:1, 3:1), to subject these mixtures to spin coating, and finally to cleave off the silyl groups using HCl vapors to obtain hydrophilic cellulose areas whereas the hydrophobic lignin domains remain unaffected.

One may argue that the hydrophobic LP may influence the desilylation reaction using HCl vapors but we did not observe any differences compared to the neat films. ATR-IR spectra of a TMSC film, the 1:1 blend film, and the TMSC film exposed to HCl vapors are depicted in the Supporting Information in the region from 700 to 1800 cm^{-1} (Figure S9, Supporting Information). These spectra demonstrate that the silyl groups are cleaved off by HCl exposure (disappearance of ν_{Si-C}, δ_{Si-O-C}, at 1250, 880, and 850 cm^{-1}, respectively) while the C=O band (1701 cm^{-1}) assigned to the LP is unaffected.

It can be clearly seen that all the TMSC/LP bicomponent films feature static water contact angles (SCA) close to 100°, which is more or less identical to the SCA of the neat films of TMSC and LP, respectively (Figure 2). However, after regeneration, there are distinct differences between the various blend ratios and interestingly the trend of SCA does not correlate with the amount of cellulose in the bicomponent films

yielding values of approximately 40° for all of the blend films. One may argue that the HCl treatment affects the LP as well; however, neither the SCA nor the layer thickness is significantly altered after HCl exposure. The rather low contact angles for the 1:1 and 1:3 blend films may originate from the nanostructures present on the surface inducing contact angle hysteresis as known for related cases.[25] However, since the roughness is significantly different for those two systems, this explanation does not fit very well to the experimental evidence. Probably, these low contact angles originate from the presence of a thin cellulose layer on top of the films (see next section), which would result in rather similar static water contact angles despite different film composition.

Besides changes in wettability, additional trends can be observed for the thickness of the regenerated samples. First, the average thickness of the films before regeneration already varies in a wide range for the different blend ratios (40−75 nm) following the trend that by decreasing the TMSC content, films become thinner. This effect is observed after regeneration as well. The layer thickness decrease results from the shrinkage of TMSC during conversion to cellulose (94−39 nm). Therefore, the decrease is greater with increasing cellulose fraction in the film. During the regeneration procedure, the cellulose fraction densifies because of the formation of hydrogen bonds and there are recent indications by GI-SAXS that also other rearrangements take place, probably due to partial depolymerization of the cellulose increasing the mobility of the chains leading to tighter packing.[26,27]
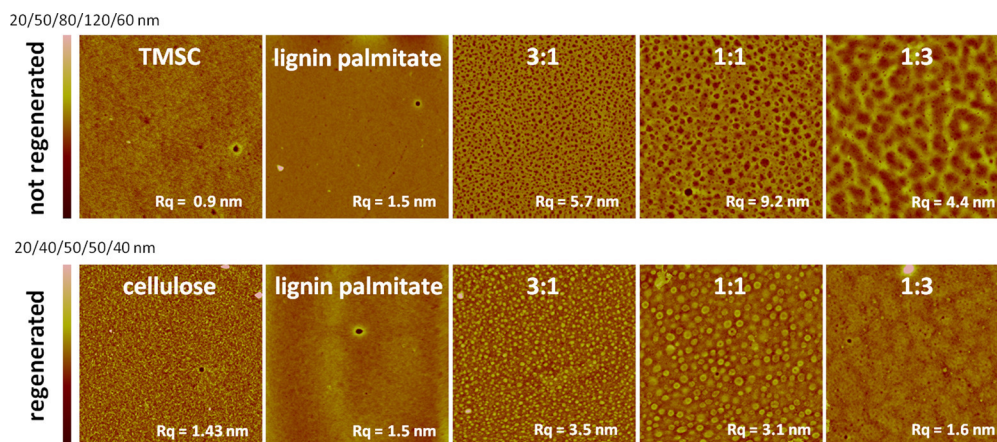
Figure 4. AFM height images (10 μm × 10 μm) of the different films (TMSC:LP) before and after HCl vapor treatment.

Similar to the wettability and thickness, the morphology of the films is significantly changing for the films with different compositions (Figures 3 and 4). The neat TMSC films show a rather low roughness, even after exposure to HCl and subsequent regeneration to cellulose. The situation is different for the blend films, where dependent on the amount of LP in the films different morphologies are obtained. The higher the LP content in the films, the more pronounced is the formation of a bicontinuous phase on the surfaces before regeneration, with regions featuring holes in the nanometer range. These holes can be unambiguously assigned to the LP regions since a subsequent regeneration step leads to an inversion of the structures, meaning that the holes are now pillars. Since it is known and also already stated above that TMSC shrinks significantly upon conversion to cellulose, it is clear that the shrinking regions are composed of the formerly TMSC domains.

A question that could certainly play a role is the stability of the LP upon HCl treatment, since esters may be attacked by strong acids. The result would be rather insoluble lignin and the corresponding fatty acid. Although the SCA of the pure LP surfaces after the HCl treatment remained on the same level, one may argue that fatty acids present on the surfaces may yield also higher contact angles. Additionally, it is difficult to prove in the case of the blend films that this scenario is not taking place. The most elegant way to prove that the LP has not been degraded by the HCl treatment neither in pure nor in the blend films is a simple rinsing step with chloroform after the surfaces have been exposed to HCl vapors. If the LP is untouched, it should be soluble in chloroform whereas the cellulose areas should remain on the substrates as shown for similar systems recently.[28]

After careful rinsing the blend films with chloroform it can be clearly seen by AFM that the structures formerly assigned to LP areas have disappeared and nanostructured cellulose thin films are obtained featuring domain sizes between 130 and 270 nm (Figure 5). Such honeycomb-like structures as presented for the 1:1 ratio have been very rarely reported so far for cellulose based materials.

Formation of the Bicontinuous Films. For the understanding of the film formation behavior and its impact on film morphology, processes taking place during the preparation of the blend films have to be considered. In the case of spin coating of a polymer blend, a macroscopically homogeneous solution of the polymers in a common solvent is placed on the
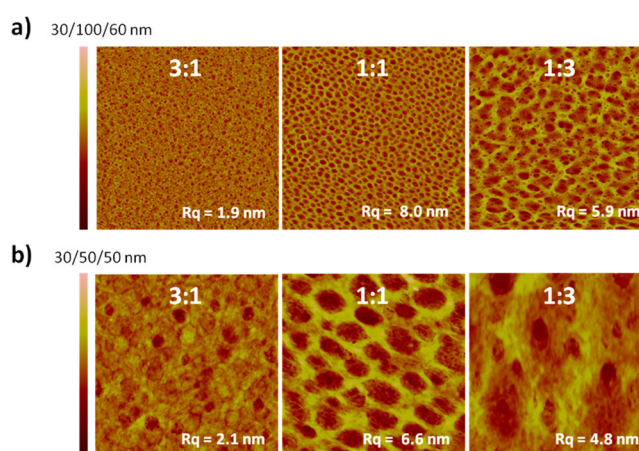
Figure 5. AFM images of the regenerated bicomponent films (cellulose:LP) after washing with chloroform yielding nanostructured cellulose films. (a) 10 μm × 10 μm; (b) 2 μm × 2 μm.

substrate. After spinning has started, a portion of this solvent evaporates and the two polymer phases separate to form a layer directly attached to the substrate and the other one exposed to the air interface due to differences in free surface energies. Upon further evaporation of the solvent, the interfacial layer between the two phases destabilizes, may form different phase morphologies and subsequently lateral phase separation takes place. This behavior, also known as transient bilayer theory,[29,30] is capable to predict the behavior of two (partly) immiscible polymers in a film and has been originally developed for other polymers than cellulose. However, recently a few examples have proven that this concept applies also to cellulose based polymers with some limitations.[8,31,32] These limitations include variations in surface morphology that are caused by differences in humidity and temperature during the preparation of the films.[33] Additional features may occur such as the formation of pores or layer inversion in the case of TMSC/CTA as discussed exhaustively in Taajamaa et al.[34]

When looking at the AFM images depicted in Figures 4 and 5, the transient bilayer theory is potentially applicable to the blend films of TMSC/LP, and in the following the formation of the morphology is explained according to this theory. However, we do not have hard experimental evidence (e.g., by GI-SWAXS during spin coating) how the phase separation works

in very detail but the obtained film morphologies are well reflected by this theory.

If this theory applies, two phases are formed during spin coating which exhibit different rates of solvent evaporation caused by different molecular weights and solubility coefficients of TMSC and LP, respectively (Figure 6). As evaporation
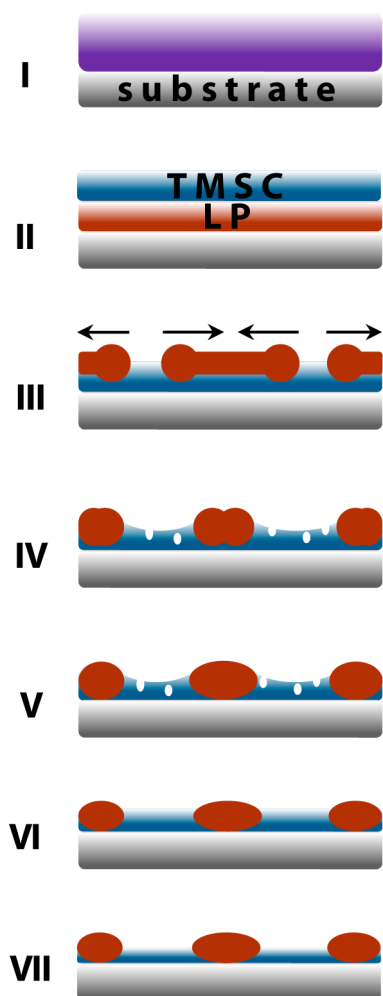
Figure 6. Schematic representation of the different processes which could take place during the preparation of blend films consisting of TMSC and LP. (I) Homogeneous TMSC/LP solution is placed on substrate, (II) formation of enriched domains, vertical phase separation, (III) lateral phase separation, (IV) dewetting, formation of LP aggregates, (V) further evaporation of solvent, (VI) TMSC/LP thin film, and (VII) after exposure to HCl vapors a cellulose/LP thin film is obtained.

progresses, the LP orients toward the substrate, whereas the TMSC is located at the air interface due to the larger amount of OH groups in LP (1.7 mmol OH g^{-1}) than in the highly substituted TMSC (DS$_{Si:}$ 2.8), which contains 0.5 mmol OH g^{-1}. Consequently, LP will enrich at the substrate interface and vertical phase separation is observed in the initial phase of spin coating.

Further evaporation of the solvent leads to a destabilization of the TMSC−LP interface due to its dependence on the interfacial tension of the two polymers, which in turn is strongly dependent on solvent concentration.[30] Subsequent dewetting of the TMSC layer should lead to the formation of holes (lateral phase separation) which are filled with LP, which is

indeed the case for the 3:1 and 1:1 and, less pronounced, for 1:3 blends. At these blend film ratios, a negative type pattern of the structures can be observed after regeneration; that is, the holes are now surrounded by valleys composed of cellulose due to the shrinking upon conversion of TMSC to cellulose.

As already mentioned above, the contact angle data points at layer inversion leading to a thin toplayer of TMSC (and subsequently cellulose) on the LP domains. The behavior of this system is related to the one described by Taajamaa et al., where cellulose triacetate/TMSC blends have been proposed to undergo layer inversion. By minimizing the surface energy of a vertically phase separated polymer blend film, the polymer located at the lower layer is transported toward the air interface during dewetting eventually forming a thin layer. In our case, the aggregation of LP during dewetting offers a nucleation site for layer inversion and finally diffusion into the TMSC rich domains takes place. As a consequence, a proportion of the TMSC may be transported to the outermost surface forming a thin layer.

Based on all the data presented so far, it can be roughly assessed that the films are probably immiscible. In order to gain more insights, further experimental data was gathered including optical inspection of cast films rather than spin coated ones. These films should follow a different formation mechanism than spin coating and allow for a facile procedure to distinguish between phase separated polymers or (partly) miscible ones. As shown in the Supporting Information (Figure S10), these films are clearly phase separated indicating that the phase separation is caused by thermodynamic incompatibility of LP and TMSC respectively.

Further, ATR-IR spectra of the spin coated films do not give any hint for interactions between cellulose and LP since the C=O stretching vibration at 1701 cm^{-1} does not shift to lower wavenumbers after regeneration as reported for related cases where donor−acceptor interactions in blend films have been characterized by IR spectroscopy.[35]

3.3. Adsorption of BSA on the Bicomponent Thin Films. Finally, the behavior of the films toward nonspecific protein adsorption was investigated. For this purpose, BSA, a commonly accepted marker to assess nonspecific protein adsorption was employed. A lot of data on the surface interactions of BSA with different kinds of surfaces is available in literature. Concerning cellulose and lignin thin films, several studies have been performed that intend to investigate the behavior of proteins, particularly BSA, at the interface of pure films.[7,36−40]

In principle, nonspecific protein adsorption involving BSA is mainly governed by hydrophobic interactions between the protein and the surface.[41] As a consequence, the films containing hydrophobic lignins should be more prone to protein adsorption than those without. This behavior, in turn, would then allow for an efficient immobilization of proteins on such surfaces which may then act in a future step as sensor support for the detection of, for example, antibodies or DNA which could be simply exchanged according to the Vroman effect.[42] However, the presence of cellulose domains and the presence of unreacted hydroxy groups may render the film surface amphiphilic preventing protein adsorption, which may act synergistically in combination with the nanostructuring of the different blend films.[43]

The different bicomponent films as well as the neat TMSC and LP films were prepared on hydrophilized gold coated QCM-D sensors, where the same phase separation mechanism
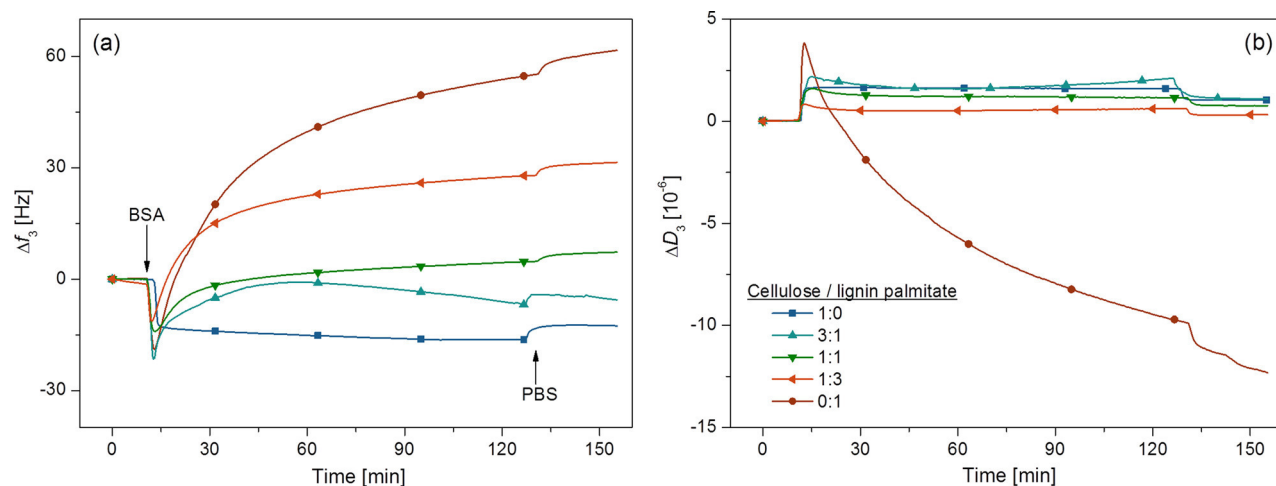
Figure 7. Adsorption of BSA (c = 1.0 mg·mL^{-1} in PBS buffer, pH 7.4, flow rate: 0.1 mL·min^{-1}) on different bicomponent thin films as well as on cellulose and LP films monitored by QCM-D in the (a) frequency (Δf_3) and (b) dissipation channels (ΔD_3). The shown curves are averaged triplicate measurements.

takes place as on silicon wafers (see Figure 11, Supporting Information), and after regeneration using HCl vapors, a steady flow of BSA solution was pumped over the surfaces in a QCM-D chamber and rinsed after 90 min with PBS. As already shown several times in the literature,[38] protein adsorption of BSA on neat cellulose films is rather low and a Δf_3 of ca. −15 Hz is observed after rinsing the surfaces with PBS buffer corresponding to submonolayer coverage of BSA. As expected, the amount of LP in the blend films correlates with the amount of deposited protein, however, in the opposite way as anticipated (Figure 7).

It can be clearly seen that higher LP content in the film leads to lower deposition of BSA on the surface. Additionally, the kinetics of the adsorption experiments reveals an interesting finding. Although the films are very stable in the buffer systems at the chosen pH, when injecting BSA, those films containing LP exhibit a positive change in frequency which is higher with larger lignin fraction in the film. This means that probably the pillarlike structures that are visible in the AFM images after the regeneration are (partly) peeled off by the BSA. Nevertheless, within our QCM-D studies, a complete removal of the LP from the surface was not observed and even for the pure lignin films a Δf_3 value of just +60 Hz was observed, indicating a rather slow complexation process with the BSA considering the film thickness (ca. 60 nm, corresponds to ca. 540 Hz). In order to get information about the morphology of the films after adsorption, AFM images have been acquired of the used QCM-D sensors. After the BSA adsorption, they reveal that parts of the LP are peeled off (Figure S12, Supporting Information) but not to that extent as for the chloroform rinsed surfaces. However, the domain size of the LP in all the films after BSA adsorption is significantly reduced, both laterally and horizontally, which is in agreement with the QCM-D studies. A possible mechanism for this behavior is that just a few BSA molecules are loosely attaching to the surface, but as soon as better interaction partners are passing (such as other BSA molecules), they start desorbing and peeling off the LP by complexation. This means that the LP acts as sacrificial component, preventing protein adsorption by peeling. Another factor that could play a role is amphiphilicity. Lignin esters in general can be regarded as a surfactant,[44] and consequently, the emulsification process with the BSA might be facilitated in the

case of BSA. At this point, it is unclear to which extent the synergies between the different mechanisms contribute to the observed effect, but it is rather clear from the data that BSA is not enriched on the surfaces.

4. CONCLUSIONS

A simple approach to prepare amphiphilic bicomponent films consisting of cellulose and a lignin ester, namely lignin palmitate, was presented. Depending on the amount of the LP in the films, nanometer sized domains were formed consisting of LP pillars surrounded by cellulose domains. The formation of the domains can be related to the transient bilayer theory in combination with further extensions of this theory described by the Rojas group recently. After detailed characterization of the blend films, protein adsorption studies clearly revealed that the surfaces are very resistant toward nonspecific protein adsorption. The mechanism is based on a sacrificial layer of the LP which is peeled off. However, the amount of LP to removed from the films is rather low indicating that there are other mechanisms in place preventing nonspecific deposition of proteins. Since in the used LP the lignin's hydroxy groups are only partly esterified, the balance between flexibility and hydrophilicity/hydrophobicity may strengthen or even cause the observed effects. Although these are the first studies tackling nonspecific protein adsorption in bicomponent lignocellulosic films, there are some limitations of the approach particularly when compared to real systems in plants. It is clear that the investigated systems only address very specific cases where cellulose and fatty acid esters of lignin are physically mixed, while in real systems the lignin is covalently attached to, for example, hemicelluloses. Although a wide range of acetylated lignins has been reported,[9,45] fatty acid esters involving lignins account for a rather low proportion of the total lignin and it is not sure whether they exist in nature at all.[46,47] However, there are other aromatic compounds such as suberins and urushiols where phenolic fatty acid esters are major constituents determining the structure and the function of cell wall components (e.g., cork). Moreover, it is assumed by some authors that suberins may be linked covalently to polyaromatic compounds such as lignins.[48,49]

Therefore, the impact of these results goes beyond the simple question of nonspecific protein adsorption on a certain

blend film system but may be a starting point for developing suitable models for the further understanding of the interaction of proteins with lignocellulosics under environmental conditions, particularly at the interfaces of the cell walls. These interfaces are the key point for all types of transport mechanisms in cells, and determine the interaction capacity with other biomolecules and even microorganisms. Future studies to investigate proteins other than BSA are underway and may yield new insights into the complex behavior of proteins with lignocellulosic materials in plants.

ASSOCIATED CONTENT

Supporting Information

The Supporting Information is available free of charge on the ACS Publications website at DOI: 10.1021/acs.biomac.5b01700.

> HSQC NMR spectra, tables containing the composition of the lignin starting material, ATR-IR spectra and ^{31}P NMR spectra after phosphitylation of the WSL and LP (PDF)

AUTHOR INFORMATION

Corresponding Authors

*E-mail: stefan.spirk@tugraz.at. Tel: +43 316 873 32284 (S.S.).
*E-mail: tamilselvan.mohan@uni-graz.at. Tel: +43 316 380 5413 (T.M.).

Author Contributions

‖S. Strasser and K. Niegelhell contributed equally.

Notes

T. Mohan and S. Spirk members of NAWI Graz and the European Polysaccharide Network of Excellence (EPNOE). The authors declare no competing financial interest.

ACKNOWLEDGMENTS

REFERENCES

(1) Evert, R. F. Parenchyma and Collenchyma. In *Esau's Plant Anatomy*; John Wiley & Sons, Inc.: New York, 2006; pp 175−190.
(2) Leroux, O. Collenchyma: a versatile mechanical tissue with dynamic cell walls. *Ann. Bot.* **2012**, *110*, 1083−1098.
(3) Thomas, L. H.; Forsyth, V. T.; Sturcova, A.; Kennedy, C. J.; May, R. P.; Altaner, C. M.; Apperley, D. C.; Wess, T. J.; Jarvis, M. C. Structure of cellulose microfibrils in primary cell walls from collenchyma. *Plant Physiol.* **2013**, *161*, 465−476.
(4) Martinez, A. T.; Speranza, M.; Ruiz-Duenas, F. J.; Ferreira, P.; Camarero, S.; Guillen, F.; Martinez, M. J.; Gutierrez, A.; del Rio, J. C. Biodegradation of lignocellulosics: Microbial, chemical, and enzymatic aspects of the fungal attack of lignin. *Int. Microbiol.* **2005**, *8*, 195−204.
(5) Showalter, A. M. Structure and function of plant cell wall proteins. *Plant Cell* **1993**, *5*, 9−23.
(6) Cosgrove, D. J. Loosening of plant cell walls by expansins. *Nature* **2000**, *407*, 321−326.
(7) Yang, B.; Wyman, C. E. BSA treatment to enhance enzymatic hydrolysis of cellulose in lignin containing substrates. *Biotechnol. Bioeng.* **2006**, *94*, 611−617.
(8) Hoeger, I. C.; Filpponen, I.; Martin-Sampedro, R.; Johansson, L.-S.; Österberg, M.; Laine, J.; Kelley, S.; Rojas, O. J. Bicomponent Lignocellulose Thin Films to Study the Role of Surface Lignin in Cellulolytic Reactions. *Biomacromolecules* **2012**, *13*, 3228−3240.
(9) Del Río, J. C.; Marques, G.; Rencoret, J.; Martínez, Á. T.; Gutiérrez, A. Occurrence of Naturally Acetylated Lignin Units. *J. Agric. Food Chem.* **2007**, *55*, 5461−5468.
(10) Thielemans, W.; Wool, R. P. Lignin Esters for Use in Unsaturated Thermosets: Lignin Modification and Solubility Modeling. *Biomacromolecules* **2005**, *6*, 1895−1905.
(11) Graça, J.; Santos, S. Suberin: A Biopolyester of Plants' Skin. *Macromol. Biosci.* **2007**, *7*, 128−135.
(12) Osipow, L.; Snell, F. D.; Marra, D.; York, W. C. Surface Activity of Monoesters Fatty Acid Esters of Sucrose. *Ind. Eng. Chem.* **1956**, *48*, 1462−1464.
(13) Ferrer, M.; Comelles, F.; Plou, F. J.; Cruces, M. A.; Fuentes, G.; Parra, J. L.; Ballesteros, A. Comparative Surface Activities of Di- and Trisaccharide Fatty Acid Esters. *Langmuir* **2002**, *18*, 667−673.
(14) Phankosol, S.; Sudaprasert, K.; Lilitchan, S.; Aryusuk, K.; Krisnangkura, K. Estimation of surface tension of fatty acid methyl ester and biodiesel at different temperatures. *Fuel* **2014**, *126*, 162−168.
(15) Argyropoulos, D. S. Quantitative Phosphorus-31 NMR Analysis of Lignins, a New Tool for the Lignin Chemist. *J. Wood Chem. Technol.* **1994**, *14*, 45−63.
(16) Argyropoulos, D. S. Quantitative Phosphorus-31 NMR Analysis of Six Soluble Lignins. *J. Wood Chem. Technol.* **1994**, *14*, 65−82.
(17) Granata, A.; Argyropoulos, D. S. 2-Chloro-4,4,5,5-tetramethyl-1,3,2-dioxaphospholane, a Reagent for the Accurate Determination of the Uncondensed and Condensed Phenolic Moieties in Lignins. *J. Agric. Food Chem.* **1995**, *43*, 1538−1544.
(18) Sauerbrey, G. Verwendung von Schwingquarzen zur Wägung dünner Schichten und zur Mikrowägung. *Eur. Phys. J. A* **1959**, *155*, 206−222.
(19) Yelle, D.; Kaparaju, P.; Hunt, C.; Hirth, K.; Kim, H.; Ralph, J.; Felby, C. Two-Dimensional NMR Evidence for Cleavage of Lignin and Xylan Substituents in Wheat Straw Through Hydrothermal Pretreatment and Enzymatic Hydrolysis. *BioEnergy Res.* **2013**, *6*, 211−221.
(20) Trajano, H. L.; Engle, N. L.; Foston, M.; Ragauskas, A. J.; Tschaplinski, T. J.; Wyman, C. E. The fate of lignin during hydrothermal pretreatment. *Biotechnol. Biofuels* **2013**, *6*, 110.
(21) del Río, J. C.; Rencoret, J.; Prinsen, P.; Martínez, Á. T.; Ralph, J.; Gutiérrez, A. Structural Characterization of Wheat Straw Lignin as Revealed by Analytical Pyrolysis, 2D-NMR, and Reductive Cleavage Methods. *J. Agric. Food Chem.* **2012**, *60*, 5922−5935.
(22) Samuel, R.; Cao, S.; Das, B. K.; Hu, F.; Pu, Y.; Ragauskas, A. J. Investigation of the fate of poplar lignin during autohydrolysis pretreatment to understand the biomass recalcitrance. *RSC Adv.* **2013**, *3*, 5305−5309.
(23) Hult, E.-L.; Koivu, K.; Asikkala, J.; Ropponen, J.; Wrigstedt, P.; Sipilae, J.; Poppius-Levlin, K. Esterified lignin coating as water vapor and oxygen barrier for fiber-based packaging. *Holzforschung* **2013**, *67*, 899−905.
(24) Huijgen, W. J. J.; Telysheva, G.; Arshanitsa, A.; Gosselink, R. J. A.; de Wild, P. J. Characteristics of wheat straw lignins from ethanol-based organosolv treatment. *Ind. Crops Prod.* **2014**, *59*, 85−95.
(25) Marmur, A. Soft contact: measurement and interpretation of contact angles. *Soft Matter* **2006**, *2*, 12−17.
(26) Ehmann, H. M. A.; Werzer, O.; Pachmajer, S.; Mohan, T.; Amenitsch, H.; Resel, R.; Kornherr, A.; Stana-Kleinschek, K.; Kontturi, E.; Spirk, S. Surface-Sensitive Approach to Interpreting Supramolecular Rearrangements in Cellulose by Synchrotron Grazing Incidence Small-Angle X-ray Scattering. *ACS Macro Lett.* **2015**, *4*, 713−716.
(27) Mohan, T.; Spirk, S.; Kargl, R.; Doliska, A.; Vesel, A.; Salzmann, I.; Resel, R.; Ribitsch, V.; Stana-Kleinschek, K. Exploring the

rearrangement of amorphous cellulose model thin films upon heat treatment. *Soft Matter* **2012**, *8*, 9807−9815.

(28) Wolfberger, A.; Petritz, A.; Fian, A.; Herka, J.; Schmidt, V.; Stadlober, B.; Kargl, R.; Spirk, S.; Griesser, T. Photolithographic patterning of cellulose: a versatile dual-tone photoresist for advanced applications. *Cellulose* **2015**, *22*, 717−727.

(29) Heriot, S. Y.; Jones, R. A. L. An interfacial instability in a transient wetting layer leads to lateral phase separation in thin spin-cast polymer-blend films. *Nat. Mater.* **2005**, *4*, 782−786.

(30) Wang, P.; Koberstein, J. T. Morphology of Immiscible Polymer Blend Thin Films Prepared by Spin-Coating. *Macromolecules* **2004**, *37*, 5671−5681.

(31) Nyfors, L.; Suchy, M.; Laine, J.; Kontturi, E. Ultrathin Cellulose Films of Tunable Nanostructured Morphology with a Hydrophobic Component. *Biomacromolecules* **2009**, *10*, 1276−1281.

(32) Kontturi, E.; Johansson, L.-S.; Laine, J. Cellulose decorated cavities on ultrathin films of PMMA. *Soft Matter* **2009**, *5*, 1786−1788.

(33) Hecht, U.; Schilz, C. M.; Stratmann, M. Influence of Relative Humidity during Film Formation Processes on the Structure of Ultrathin Polymeric Films. *Langmuir* **1998**, *14*, 6743−6748.

(34) Taajamaa, L.; Kontturi, E.; Laine, J.; Rojas, O. J. Bicomponent fibre mats with adhesive ultra-hydrophobicity tailored with cellulose derivatives. *J. Mater. Chem.* **2012**, *22*, 12072−12082.

(35) Coleman, M. M.; Xu, Y.; Painter, P. C. Compositional heterogeneities in hydrogen-bonded polymer blends: infrared spectroscopic results. *Macromolecules* **1994**, *27*, 127−134.

(36) Salas, C.; Rojas, O. J.; Lucia, L. A.; Hubbe, M. A.; Genzer, J. On the Surface Interactions of Proteins with Lignin. *ACS Appl. Mater. Interfaces* **2013**, *5*, 199−206.

(37) Martín-Sampedro, R.; Rahikainen, J. L.; Johansson, L.-S.; Marjamaa, K.; Laine, J.; Kruus, K.; Rojas, O. J. Preferential Adsorption and Activity of Monocomponent Cellulases on Lignocellulose Thin Films with Varying Lignin Content. *Biomacromolecules* **2013**, *14*, 1231−1239.

(38) Mohan, T.; Niegelhell, K.; Zarth, C.; Kargl, R.; Köstler, S.; Ribitsch, V.; Heinze, T.; Spirk, S.; Stana-Kleinschek, K. Triggering Protein Adsorption on cationically rendered cellulose surfaces. *Biomacromolecules* **2014**, *15*, 3931−3941.

(39) Mohan, T.; Ristic, T.; Kargl, R.; Doliska, A.; Köstler, S.; Ribitsch, V.; Marn, J.; Spirk, S.; Stana-Kleinschek, K. Cationically rendered biopolymer surfaces for high protein affinity support matrices. *Chem. Commun.* **2013**, *49*, 11530−11532.

(40) Orelma, H.; Filpponen, I.; Johansson, L.-S.; Laine, J.; Rojas, O. J. Modification of Cellulose Films by Adsorption of CMC and Chitosan for Controlled Attachment of Biomolecules. *Biomacromolecules* **2011**, *12*, 4311−4318.

(41) Roach, P.; Farrar, D.; Perry, C. C. Interpretation of Protein Adsorption: Surface-Induced Conformational Changes. *J. Am. Chem. Soc.* **2005**, *127*, 8168−8173.

(42) Vroman, L.; Adams, A. L. Findings with the recording ellipsometer suggesting rapid exchange of specific plasma proteins at liquid/solid interfaces. *Surf. Sci.* **1969**, *16*, 438−446.

(43) Malmsten, M.; Van Alstine, J. M. Adsorption of Poly(Ethylene Glycol) Amphiphiles to Form Coatings Which Inhibit Protein Adsorption. *J. Colloid Interface Sci.* **1996**, *177*, 502−512.

(44) Orlando, J. R.; Johnny, B.; Fredy, Y.; Ana, F.; Jean, L. S.; Dimitris, S. A. Lignins as Emulsion Stabilizers. In *Materials, Chemicals, and Energy from Forest Biomass*; Argyropoulos, D. S., Ed.; American Chemical Society: Washington, DC, 2007; Vol. *954*, pp 182−19910.1021/bk-2007-0954.ch012.

(45) Ralph, J.; Lu, F. The DFRC Method for Lignin Analysis. 6. A Simple Modification for Identifying Natural Acetates on Lignins. *J. Agric. Food Chem.* **1998**, *46*, 4616−4619.

(46) Lundqvist, R. Tall oil components. II. Fatty acid composition of lignin ester. *Ark. Kemi* **1966**, *25*, 429−434.

(47) Tran, A. V.; Chambers, R. P. Behaviors of southern red oak hemicelluloses and lignin in a mild sulfuric acid hydrolysis. *Biotechnol. Bioeng.* **1986**, *28*, 811−817.

(48) Bernards, M. A. Demystifying suberin. *Can. J. Bot.* **2002**, *80*, 227−240.

(49) Mattinen, M.-L.; Filpponen, I.; Järvinen, R.; Li, B.; Kallio, H.; Lehtinen, P.; Argyropoulos, D. Structure of the Polyphenolic Component of Suberin Isolated from Potato (Solanum tuberosum var. Nikola). *J. Agric. Food Chem.* **2009**, *57*, 9747−9753.

Supporting Information #2

Exploring Nonspecific Protein Adsorption on Lignocellulosic

Amphiphilic Bicomponent Films

Exploring Non-specific Protein Adsorption on Lignocellulosic Amphiphilic Bicomponent Films

Simone Strasser,[†,⊥] Katrin Niegelhell[†,⊥] Manuel Kaschowitz,[†] Sabina Markus,[§] Rupert Kargl[†,§], Karin Stana-Kleinschek[§], Christian Slugovc[†], Tamilselvan Mohan[‡,1]*, Stefan Spirk[†,§,1]*

[†]Institute for Chemistry and Technology of Materials, Graz University of Technology, Stremayrgasse 9, 8010 Graz, Austria.

[§]Institute of Engineering and Design of Materials, University of Maribor, Smetanova 17, 2000 Maribor, Slovenia.

[‡]Institute of Chemistry, University of Graz, Heinrichstrasse 28, 8010 Graz, Austria.

[1]Members of NAWI Graz

Members of the European Polysaccharide Network of Excellence (EPNOE).

To whom correspondence should be addressed:

* E-Mail: stefan.spirk@tugraz.at, Tel.:+43 316 873 32284.
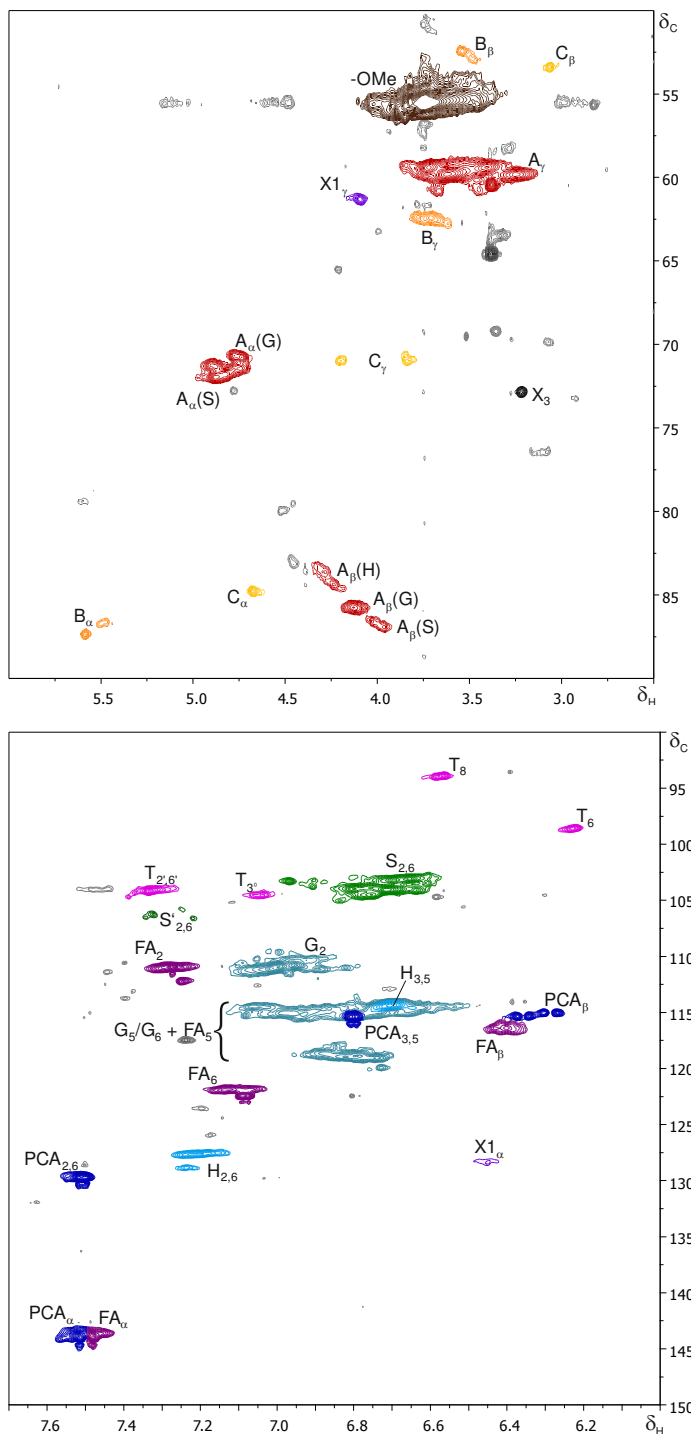
Figure S1. Expanded aliphatic sidechain (δ_C/δ_H 50–90/2.5–6.0 ppm) and aromatic (δ_C/δ_H 90–150/6.0–8.0 ppm) regions of the ^{13}C-^{1}H HSQC NMR spectrum of wheat straw lignin (WSL). (50 mg, 25 °C, 500 MHz, DMSO-d_6).

Table S1. Labeled ^{13}C-^{1}H cross signals in the HSQC NMR spectrum of wheat straw lignin (WSL).

Label	wheat strat lignin (WSL)	
Aliphatics	δ_C/δ_H / ppm	**Assignment**
C_β	53.4 / 3.06	C_β-H_β in β-β resinol substructures (C)*
C_γ	71.0 / 3.83 and 4.19 (low intensity)	C_γ-H_γ in β-β resinol substructures (C)
C_α	84.8 / 4.67 (low intensity)	C_α-H_α in β-β resinol substructures (C)
OMe	55.6 / 3.75	C-H in methoxyls
A_γ	60.4 / 3.38	C_γ-H_γ in β-O-4' substructures (A)
	59.4 / 3.41 and 3.72	C_γ-H_γ in γ-hydroxylated β-O-4' substructures (A)
	59.8 / 3.24 and 3.62	C_γ-H_γ in β-O-4' substructures (A)
A_α(G)	70.7 / 4.76 and 71.4 / 4.76	C_α-H_α in β-O-4' substructures (A) linked to a G-unit
A_α(S)	71.3 / 4.89 and 71.9 / 4.85	C_α-H_α in β-O-4' substructures (A) linked to a S-unit
A_β(H)	83.6 / 4.28 and 84.4 / 4.23	C_β-H_β in β-O-4' substructures (A) linked to a H-unit
A_β(G)	85.8 / 4.12	C_β-H_β in β-O-4' substructures (A) linked to a G-unit
A_β(S)	86.8 / 3.99	C_β-H_β in β-O-4' substructures (A) linked to a S-unit
B_α	86.7 / 5.48 and 87.4 / 5.58	B_α-B_α in β-5' substructures (B)
B_β	52.4 / 3.54 and 52.9 / 3.48	B_β-B_β in β-5' substructures (B)
B_γ	62.5 / 3.70	B_γ-B_γ in β-5' substructures (B)
$X1_\gamma$	61.3 / 4.09	C_γ-H_γ in cinnamyl alcohol end groups (X1)
Aromatics	δ_C/δ_H / ppm	**Assignment**
$X1_\alpha$	128.2 / 6.46 (low intensity)	C_α-H_α in cinnamyl alcohol end groups (X1)
$X1_\beta$	128.2 / 6.23 (very low intensity)	C_β-H_β in cinnamyl alcohol end groups (X1)
T_8	93.9 / 6.56	C_8-H_8 in tricin (T)
T_6	98.7 / 6.22	C_6-H_6 in tricin (T)
$T_{2',6'}$	104.1 / 7.33	$C_{2'}$-$H_{2'}$ and $C_{6'}$-$H_{6'}$ in tricin (T) linked to syringyl units at C_2
T_3	104.5 / 7.05	C_3-H_3 in tricin (T)
$S_{2,6}$	103.7 / 6.67	C_2-H_2 and C_6-H_6 in syringyl units (S)
$S'_{2,6}$	106.3 / 7.33 and 106.2 / 7.23	C_2-H_2 and C_6-H_6 in α-ketone syringyl units (S')
G_2	110.7 / 6.95	C_2-H_2 in guaiacyl units (G)
G_5/G_6	115.1 / 6.87 and 118.7 / 6.80	C_5-H_5 and C_6-H_6 in guaiacyl units (G)
FA_2	110.9 / 7.27	C_2-H_2 in ferulate (FA)
FA_6	121.9 / 7.11	C_6-H_6 in ferulate (FA)

(Table S1continued).

FA$_5$	*within G$_5$/G$_6$ correlation peak*	C$_5$-H$_5$ in ferulate (FA)
FA$_\beta$	116.4 / 6.40	C$_\beta$-H$_\beta$ in ferulate (FA)
PCA$_\beta$	115.2 / 6.32	C$_\beta$-H$_\beta$ in *p*-coumarate (PCA)
FA$_\alpha$	143.9 / 7.48	C$_\alpha$-H$_\alpha$ in ferulate (FA)
PCA$_\alpha$	144.0 / 7.52	C$_\alpha$-H$_\alpha$ in *p*-coumarate (PCA)
PCA$_{3,5}$	115.4 / 6.80	C$_3$-H$_3$ and C$_5$-H$_5$ in *p*-coumarate (PCA)
PCA$_{2,6}$	129.7 / 7.51	C$_2$-H$_2$ and C$_6$-H$_6$ in *p*-coumarate (PCA)
H$_{3,5}$	114.4 / 6.72	C$_3$-H$_3$ and C$_5$-H$_5$ in *p*-hydroxyphenyl units (H)
H$_{2,6}$	127.6 / 7.21 and 128.9 / 7.24	C$_2$-H$_2$ and C$_6$-H$_6$ in *p*-hydroxyphenyl units (H)

* assigned as B$_\beta$ in other works[1]

Based on the integral values of the correlation peaks of S, G and H moieties, the relative monomeric ratio of the wheat straw lignin was calculated. According to the common practice in literature, the X1, PCA and FA content as well as the T content are given as a percentage of the sum of regular aromatic lignin monomers (S+G+H).[2] The determined ratios are listed in Table S2 and the integral values used for the calculation are listed in Table S4.

Table S2. Monomeric ratio of main monomeric units as well as *p*-hydroxycinnamic acids (*p*HCA) and tricin (T) present in WSL. Additionally, the relative abundance of the different interunit linkages is indicated.

Lignin aromatic units	
S / %	38
G / %	56
H / %	6
S / G / H ratio	6 / 9 / 1
Lignin interunit linkages	
β-O-4' aryl ethers (A$_\gamma$) / %	85
β-5' phenylcoumarans (B$_\gamma$) / %	10
β-β' resinols (C$_\gamma$) / %	5
A / B / C ratio	17 / 2 / 1
dibenzodioxins (D) / %	n.d.
α,β-diaryl ethers (E) / %	n.d.
spirodienones (F) / %	n.d.
p-Hydroxycinnamates (pHCAs)	
p-coumarates (PCA) / %	11
ferulates (FA) / %	17
PCA / FA ratio	0.6
Lignin end groups	
cinnamyl alcohol end groups (X1) / %	3

[1] J.-L. Wen, S.-L. Sun, B.-L. Xue, R.-C. Sun, *Holzforschung* **2013**, *67(6)*, 613-627.
[2] F. Zikeli, T. Ters, K. Fackler, E. Srebotnik, J. Li, *Industrial Crops and Products* **2014**, *61*, 249-257.

SUPPORTING INFORMATION

Tricin	4

n.d. = not detected

Additionally, the ratio of lignin monomeric units was determined in a slightly altered way, which provides, at least to our understanding, a more comprehensive picture of the wheat straw lignin sample. Thus, α-oxidized and *p*HCA structures are included into the term 'main lignin units' and expressed as share of the according aromatic moiety. Structures X1 and T are set as part of the main units as well, but are expressed as separate units due to their different or not clearly assignable substructure. Therefore, the ratios of the monomeric units are determined from the sum of integrals belonging to all detected moieties: (S+S')+(G+FA)+(H+PCA)+X1+T (**Error! Reference source not found.**). According to this evaluation, a significantly different S / G / H ratio of 2 / 4 / 1 is specified since the integral value of H units (including PCA) is set to 1.

Table S3. Ratio of lignin monomeric units including *p*-hydroxycinnamic acids (*p*HCA), end group X1, tricin (T) and different interunit linkages.

Ratio of lignin aromatic units	
S	2.4
6.2 % in α-oxidized form (S')	
G	4.2
24 % as ferulates (FA)	
H	1
64 % as p-coumarates (PCA)	
cinnamyl alcohol end groups (X1)	0.2
tricin	0.3
Ratio of lignin interunit linkages	
β-O-4' aryl ethers (A$_\gamma$)	17
β-5' phenylcoumarans (B$_\gamma$)	2
β-β resinols (C$_\gamma$)	1

Table S4. Integrals used for the semi-quantitative determination of lignin substructures from the ^{13}C-^{1}H HSQC NMR spectrum of WSL.

Label	δ_C / δ_H Correlation / ppm	Integral	Hs	Integral normalized to 1 H	
OMe	55.6 / 3.75	set to 300	3	100	
A_α(G+S)	70.8 / 4.76 and 71.3 / 4.88 and 72.0 / 4.87	19.21	2	9.61	A / B / C
B_α	86.7 / 5.48 and 87.4 / 5.57	1.98	1	1.98	7 1.5
C_α	84.8 / 4.67	1.36	1	1.36	1.0
A_β (H)	83.7 / 4.29 and 84.4 / 4.24	4.95			A / B / C
A_β (G)	85.8 / 4.12	4.85	1	12.05	
A_β (S)	86.7 / 4.02 and 87.0 / 3.95	2.25			11
B_β	52.5 / 3.54	2.28	1	2.28	2
C_β	53.5 / 3.07	1.09	1	1.09	1.0
A_γ	60.4 / 3.38 59.4 / 3.41 and 3.72 59.8 / 3.24 and 3.62	60.90	2	20.3	A / B / C 18
B_γ	62.5 / 3.70	4.65	2	2.325	2
C_γ	71.0 / 3.83 and 4.19	2.28	2	1.14	1.0
$X1_\gamma$	61.3 / 4.09	2.03	2	1.015	
T_8	93.9 / 6.56	1.43	1	1.43	
T_6	98.7 / 6.22	1.12	1	1.12	average =
$T_{2',6'}$	104.1 / 7.33	3.53	2	1.765	1.38
T_3	104.5 / 7.05	1.20	1	1.20	
$S'_{2,6}$	106.3 / 7.33 and 106.2 / 7.23	1.60	2	0.80	
$S_{2,6}$	103.7 / 6.67	24.40	2	12.20	
FA_2	110.9 / 7.27	6.44	1	6.44	
FA_6	121.9 / 7.11	5.87	1	5.87	average =
FA_β	116.4 / 6.40	4.39	1	4.39	5.57
$H_{2,6}$	127.6 / 7.21 and 128.9 / 7.24	3.97	2	1.985	
G_2	110.7 / 6.95	17.68	1	17.68	
$PCA_{2,6}$	129.7 / 7.51	6.47	2	3.235	average =
PCA_β	115.2 / 6.32	3.84	1	3.84	3.54
fatty acids (all)	33.38 / 2.19	22.50	2	11.25	
unsaturated fatty acids	129.32 / 5.33	1.88	1	1.88	
S+G+H				31.865	
X1+PCA+FA				10.125	
S+S'				13	
G+FA				23.25	
H+PCA				5.525	sum = 44.17
X1				1.015	
T				1.38	
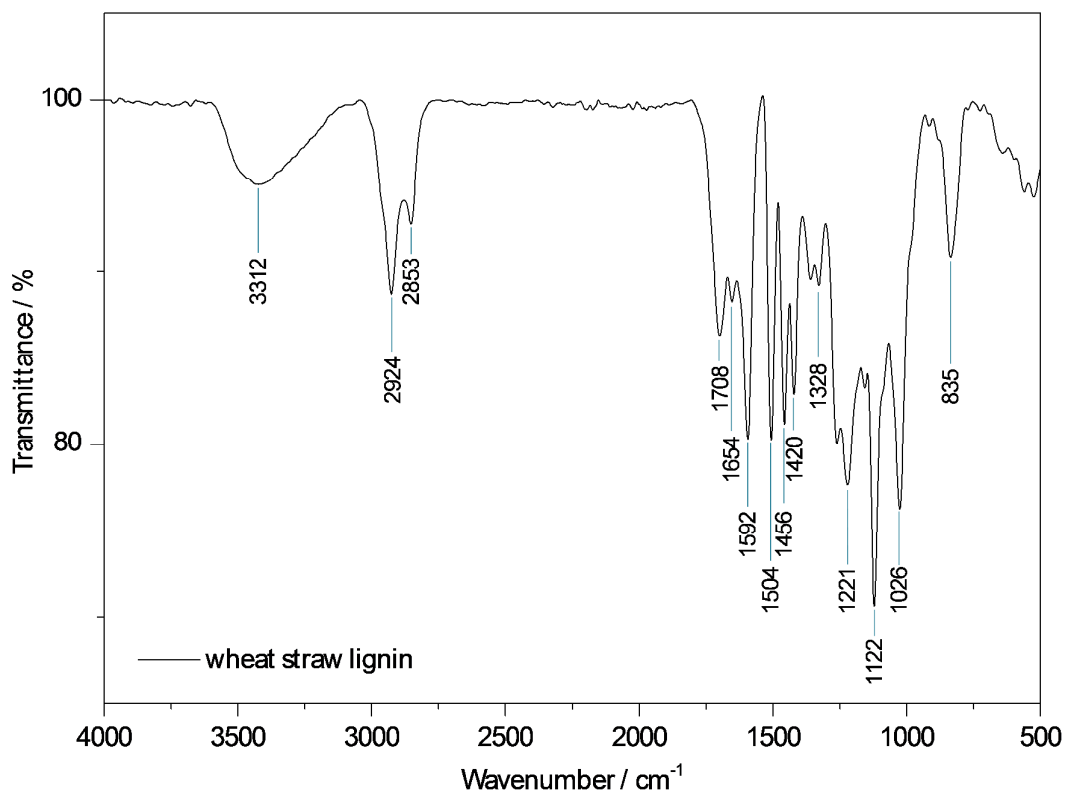
Figure S2. ATR-FT IR spectrum of WSL.

FT-IR-bands / cm^{-1}	Assignment
3617-3076	O-H
2924	aliphatic C-H / C-O
2853	aliphatic C-H / C-O
1740	C=O stretch (ester)
1708	C=O stretch (carboxylic acid)
1654	aliphatic C=C
1592	aromatic C-C (skeleton vibration)
1504	aromatic C-C (skeleton vibration)
1456	C-H deformation (asym -CH$_3$ and -CH$_2$-) combined with aromatic ring vibration
1420	aromatic C-C (skeleton vibration) combined with C-H in plane deformation
1360	phenolic OH and aliphatic C-H in methyl groups
1328	S units breathing with C-O stretching (β-O-4 linkage)
1262	G units breathing with C-O stretching (β-O-4 linkage)
1221	C-O phenolic / C-C and C=O stretching
1157	C-H in plane deformation of G units
1122	C-H in plane deformation of S units
1026	C-O deformation associated with C-C stretching / aromatic C-H deformation
835	aromatic C-H (out of plane vibration of H^{2,6} of S units)
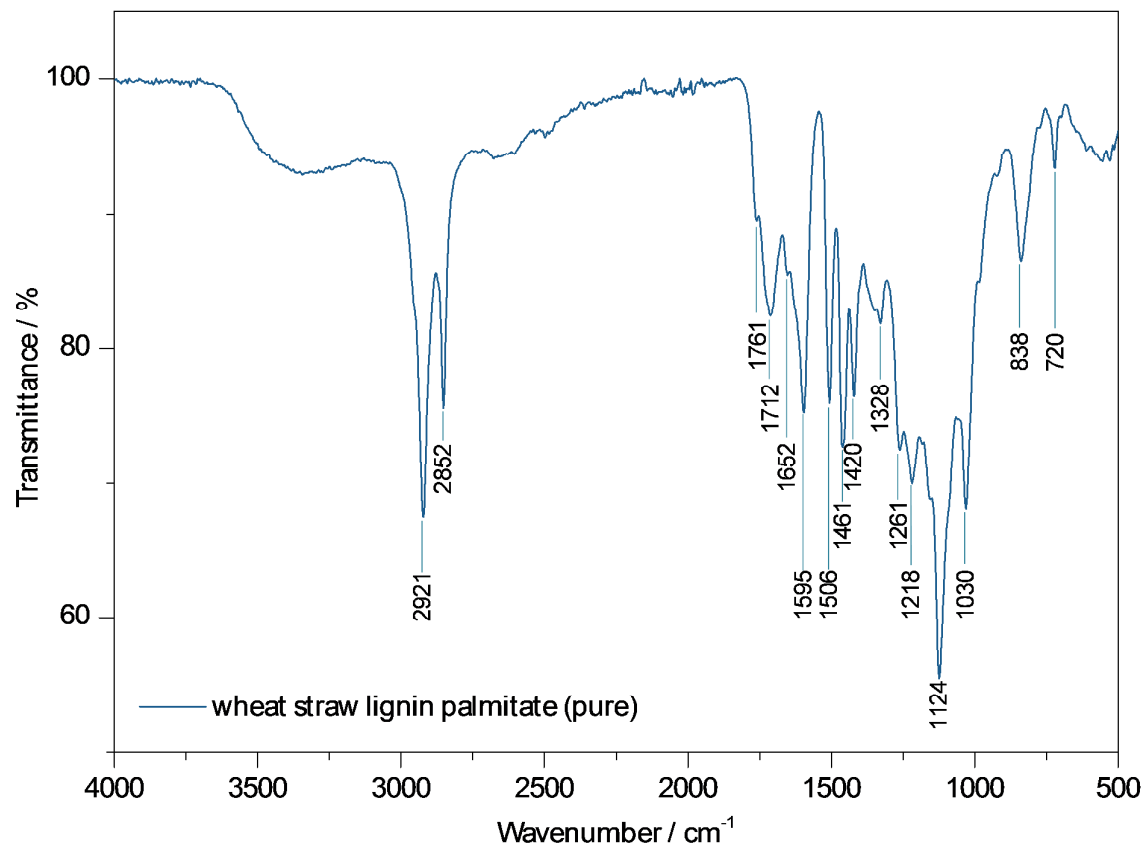
Figure S2. ATR-FT IR spectrum of wheat straw lignin palmitate.

SUPPORTING INFORMATION

Figure S3. ^{31}P NMR spectrum of WSL after phosphitylation with TMDP (25 °C, CDCl$_3$).

Figure S4. ^{31}P NMR of phosphitylated wheat straw lignin palmitate (pure) (25 °C, CDCl$_3$).

Figure S5. ^{1}H NMR spectrum of wheat straw lignin palmitate (pure) (25 °C, CDCl$_3$).

Figure S6. ^{1}H NMR spectrum of wheat straw lignin palmitate (pure) (higher intensity) (25 °C, CDCl$_3$).
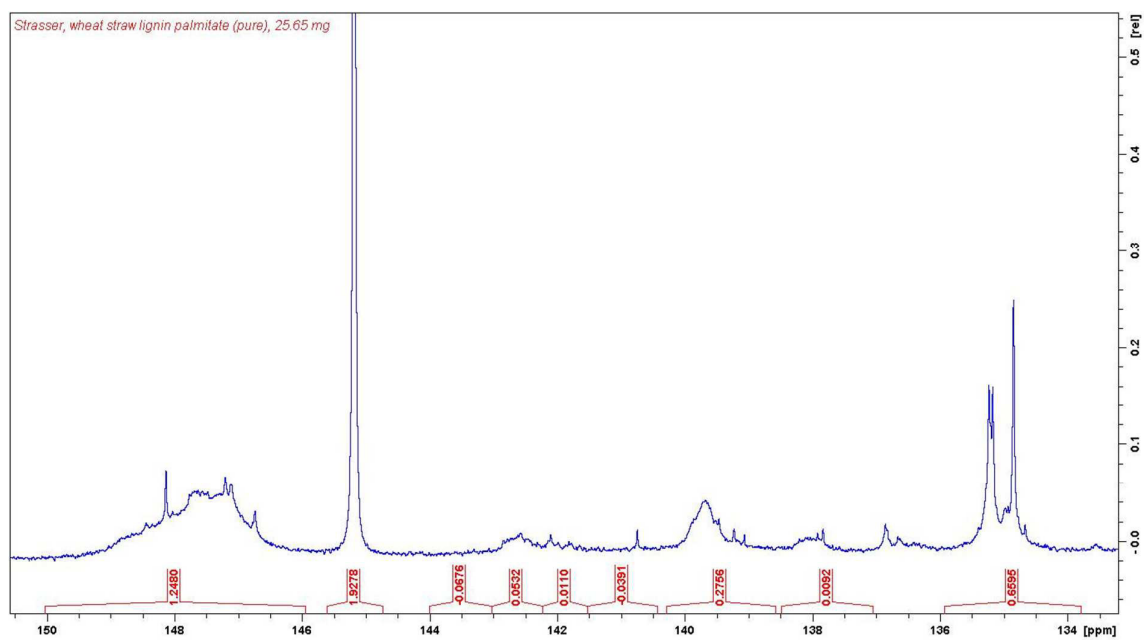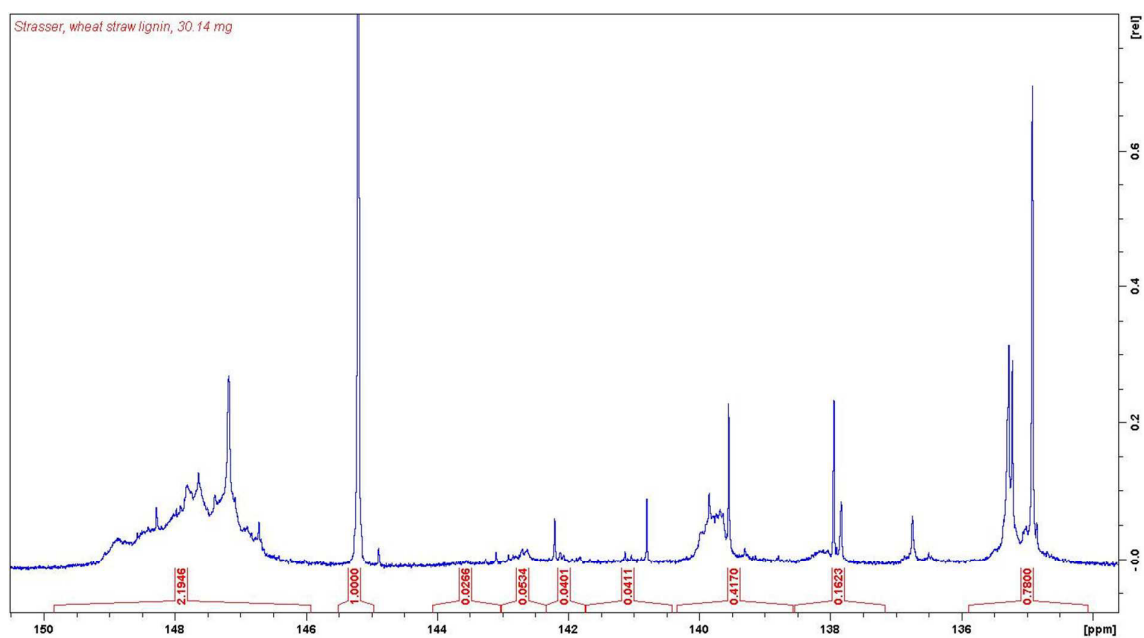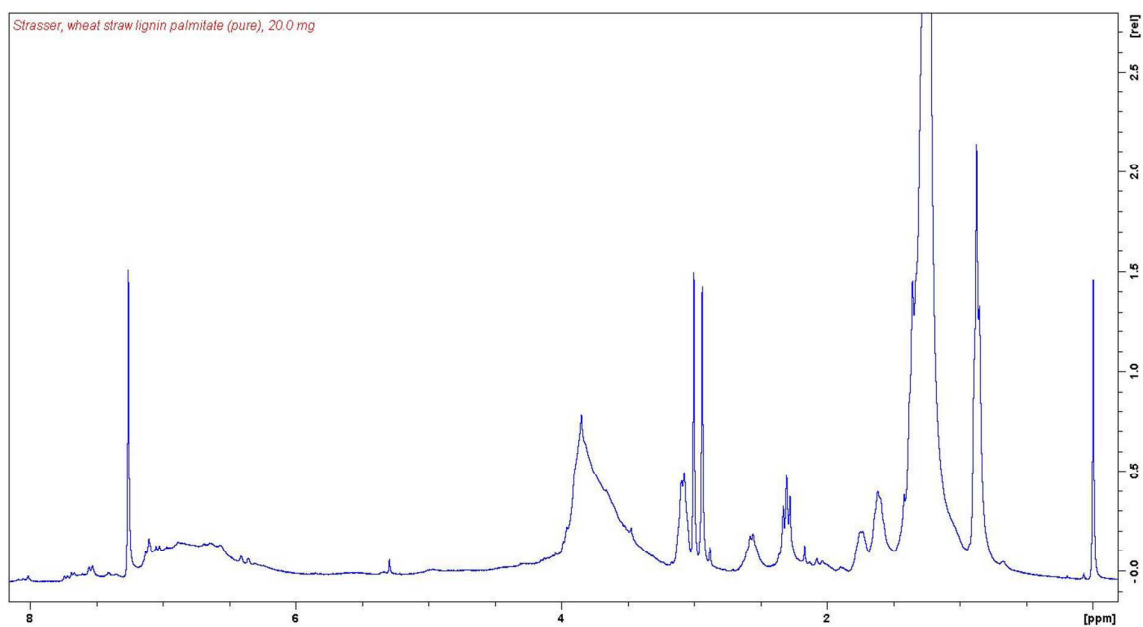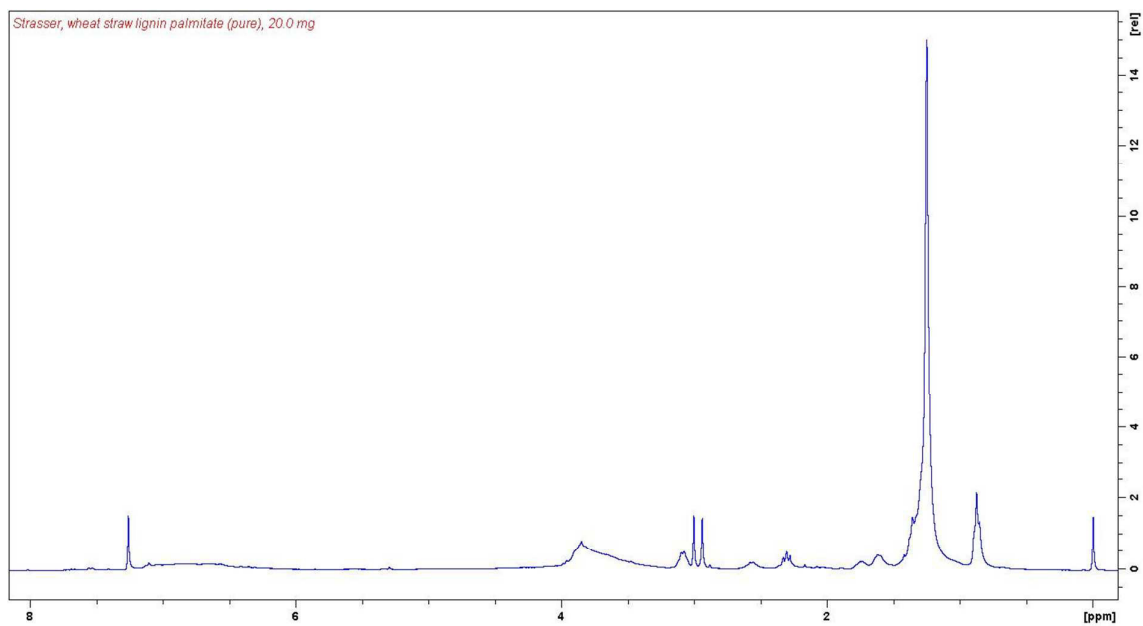
SUPPORTING INFORMATION

Calculations for the determination of the degree of esterification (DE) of LP

Approach 1; mass balance of preparation:

Originally 1.003 g WSL and and 1.03 mL palmitoyl chloride (PC) were used.

1.003 ml PC (98%, d = 0.906 g/mL, MW = 274.87 g/mol) = 3.34 mmol PC

Assuming full conversion to LP: 3.34 mmol $COC_{15}H_{31}$ are attached to WSL (=0.800 g $COC_{15}H_{31}$)

Maximum yield of LP = 1.803 g – recover yield of raw LP = 1.75 g (97%).

i.e. it is assumed that during the purification for raw LP neither WSL, nor fatty acid was removed

For chromatographic purification 1.205 g raw PL was used which is composed of 671 mg Lignin and 634 mg PC.

634 mg PC correspond to 592 mg palmitic acid (PA)

Column chromatography resulted in isolation of 390 mg PA which means 202 mg PA are missing (corresponding to the amount of PC which underwent esterification)

202 mg PA corresponds to 189 mg $COC_{15}H_{31}$

750 mg purified LP was isolated containing 189 mg $COC_{15}H_{31}$ – meaning 561 mg WSL are contained in the purified LP sample (and 110 mg WSL was lost during purification).

189 mg $COC_{15}H_{31}$ = 0.79 mmol $COC_{15}H_{31}$ i.e. 0.79 mmol OH reacted
561 mg WSL correspond to 2.24 mmol OH (hydroxy number of WSL = 4 mmol/g)

Degree of esterification (DE) = 0.79 • 100 / 2.24 = <u>35 %</u>

Control; using the hydroxy number determined for LP (1.7 mmol/g):

0.79 mmol $COC_{15}H_{31}$ are contained in 750 mg LP which corresponds to 1.05 mmol $COC_{15}H_{31}$ in 1 g LP.

Hypothetical hydroxy number of LP (hOH_{LP}): 1.7 + 1.05 = 2.75 mmol/g

Hydroxy number of WSL • $MW_{RP(WSL)}$ = hOH_{LP} • $MW_{RP(LP)}$
    …with MW of the repeating unit of WSL (MW_{RPWSL}) = 193 g/mol (from elemental analysis of WSL; see below)

$MW_{RP(LP)}$ = 4 • 196 / 2.75 = 281 g/mol

meaning that the $MW_{RP(LP)}$ is 88 g/mol higher which corresponds to the attachment of 0.37 mol $COC_{15}H_{31}$ / mol repeating unit (1 x $COC_{15}H_{31}$ per 2.7 repeating units of lignin)

The amount of OH / RP_{WSL} = 4 * 193 /1000 = 0.8 mol/RP_{WSL}

<u>**DE**</u> = 0.37 • 100 / 0.8 = <u>**46 %**</u>

Approach 2; evaluating the elemental analysis of LP:

Experimental elemental analysis: C, 65.5; H, 7.9; N, 1.3
Calculated elemental analysis for 1 x $COC_{15}H_{31}$ and 4 theoretical repeating units of lignin: C, 65.61; H, 7.87.
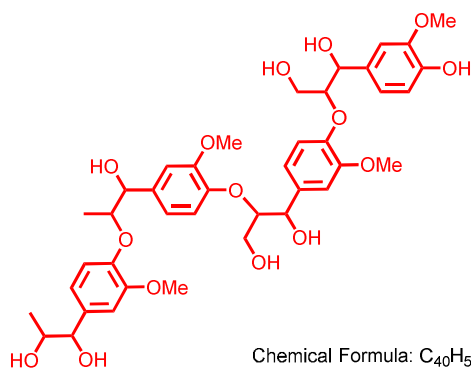
Chemical Formula: $C_{40}H_{50}O_{15}$
Molecular Weight: 770,82 $MW_{RP(WSL)}$ = 193 g/mol
Elemental Analysis: C, 62.33; H, 6.54; O, 31.13
found: C, 62.4%; H, 6.5%; N 1.3%; S 0.4%
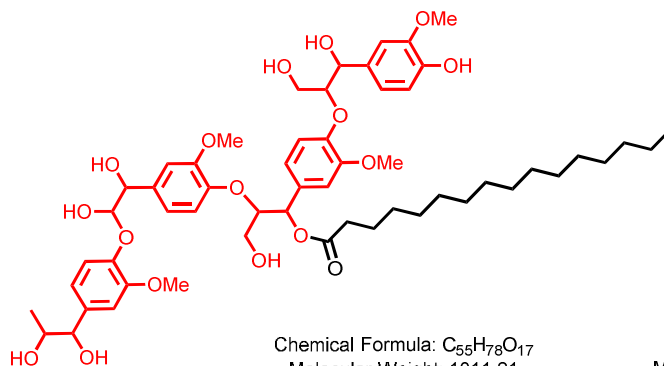
Chemical Formula: $C_{55}H_{78}O_{17}$
Molecular Weight: 1011,21 $MW_{RP(LP)}$ = 253 g/mol
Elemental Analysis: C, 65.33; H, 7.78; O, 26.90
found: C, 65.5%; H, 7.8%; N 1.3%

$MW_{RP(LP)} - MW_{RP(WSL)}$ = 253 g/mol - 193 g/mol = 60 g/mol

Figure S8: Hypothetical chemical structures of WSL and LP approximating the experimental elemental analysis (note that these structures are not in accordance with the determined hydroxy numbers)

meaning that the $MW_{RP(LP)}$ is 60 g/mol higher which corresponds to the attachment of 0.25 mol $COC_{15}H_{31}$ / mol repeating unit (1 x $COC_{15}H_{31}$ per 4 repeating units of lignin)

The amount of OH / RP_{WSL} = 4 * 193 /1000 = 0.8 mol/RP_{WSL}

<u>**DE**</u> = 0.25 • 100 / 0.8 = <u>**31 %**</u>
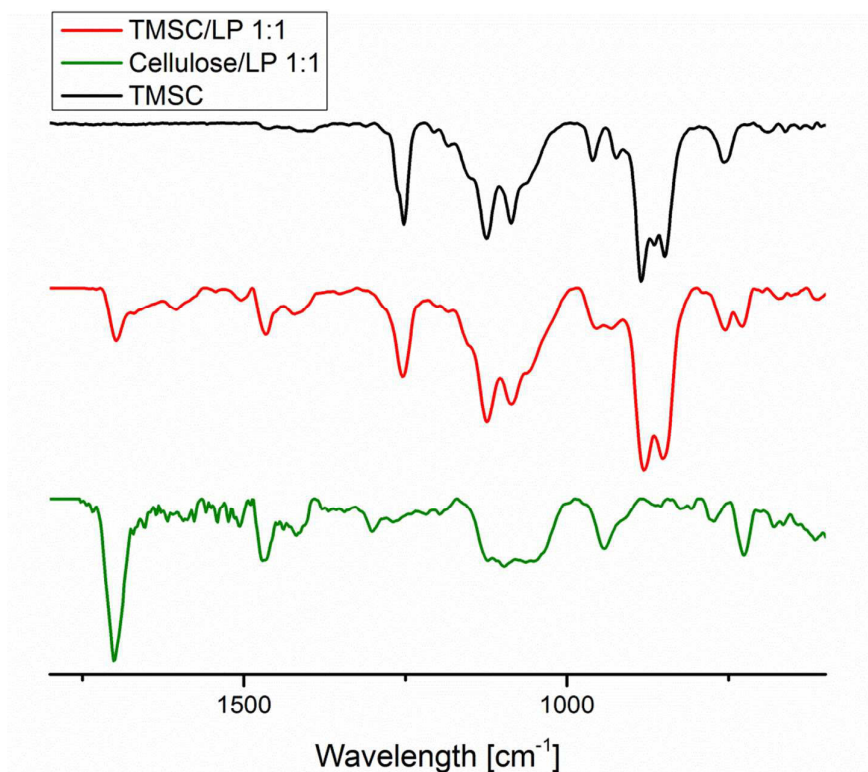
Figure S9. ATR –IR spectra of a TMSC film, a TMSC/LP film (1:1) and a cellulose/LP film (1:1) deposited on gold coated glass slides. The spectrum for the cellulose/LP film is enhanced three times in intensity to clearly show that there are not any silyl groups remaining in the film after regeneration.

Figure S10. Optical microscopy images (50x magnification) of casted films of regenerated TMSC/LP in different ratios (left 3:1, middle: 1:1, right: 1:3)
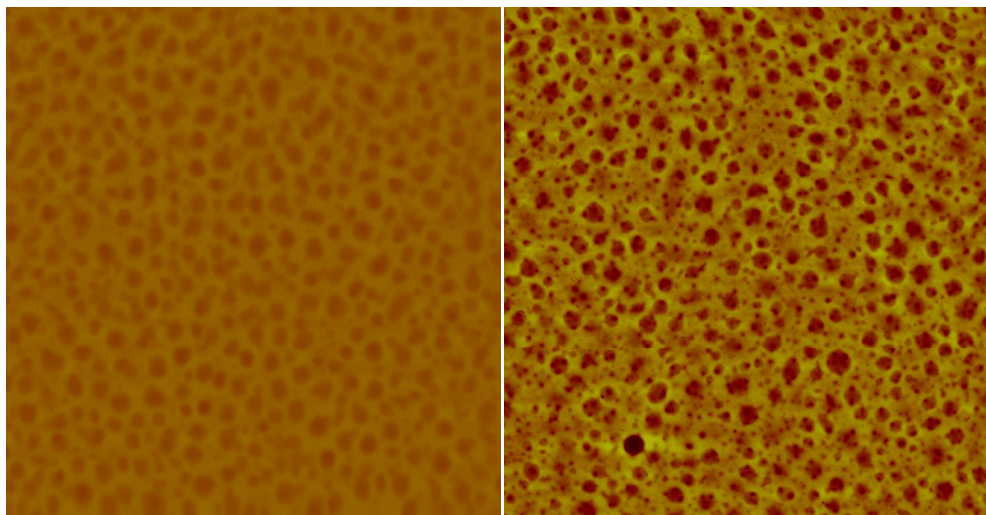
Figure S11. Comparison of AFM images (10 μm x 10 μm) of a TMSC-LP thin film (1:1) on a gold (left) and SiO$_2$ substrate (right).
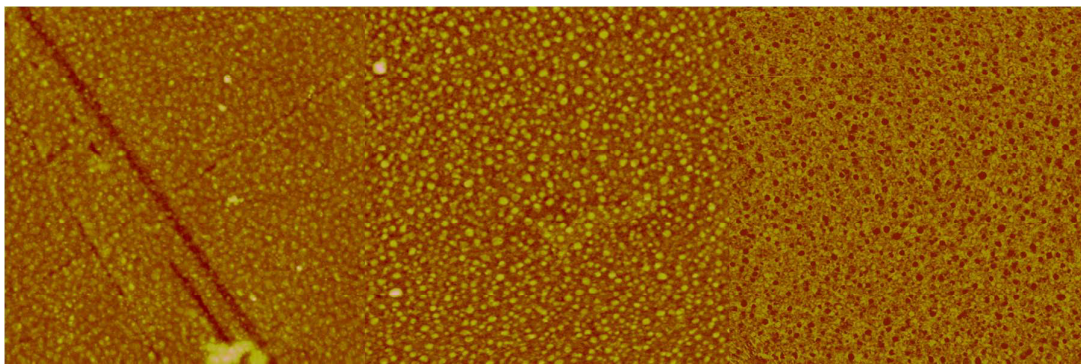
Figure S12a. Comparison of AFM images (10 μm x 10 μm) of a cellulose-LP thin film (3:1) after protein adsorption (left), as prepared (middle) and after rinsing with chloroform (right).
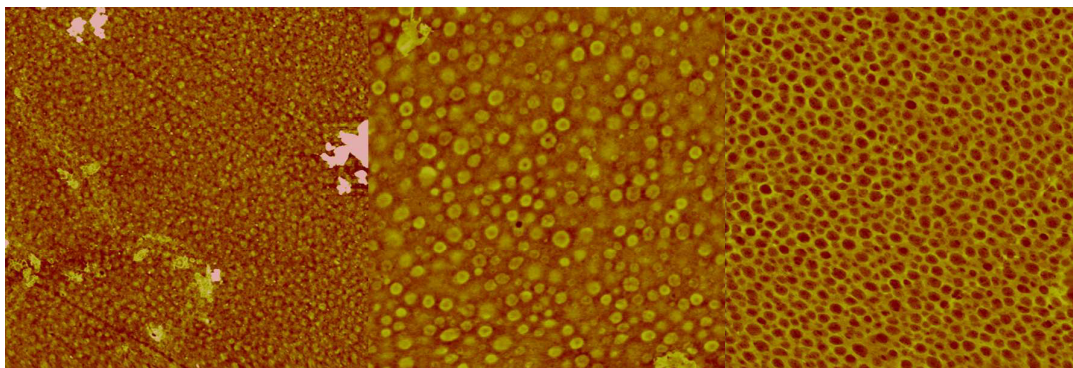
Figure S12b. Comparison of AFM images (10 µm x 10 µm) of a cellulose-LP thin film (1:1) after protein adsorption (left), as prepared (middle) and after rinsing with chloroform (right). Please note that the large aggregates in the left are probably due to buffer residuals.
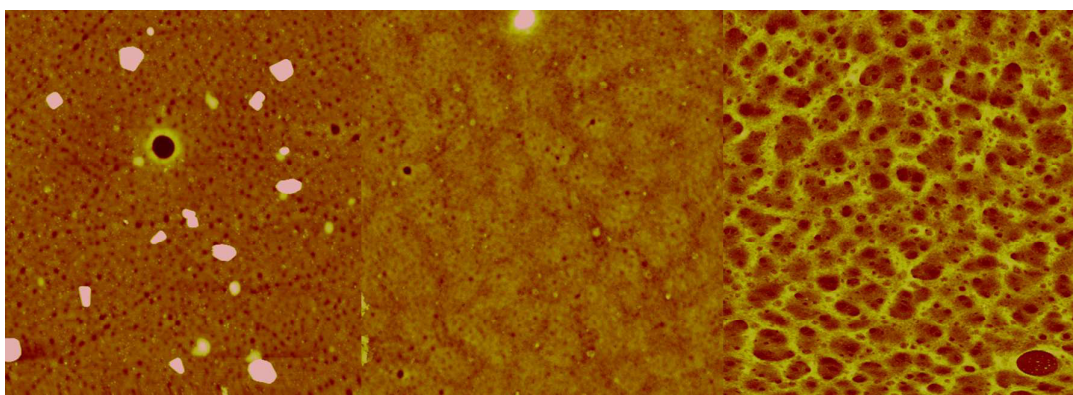
Figure S12c. Comparison of AFM images (10 µm x 10 µm) of a cellulose-LP thin film (1:3) after protein adsorption (left), as prepared (middle) and after rinsing with chloroform (right). Please note that the large aggregates in the left are probably due to buffer residuals.

PAPER #3

Enzymes as Biodevelopers for Nano- and Micropatterned

Bicomponent Biopolymer Thin Films

For this paper, I conducted the AFM and MP-SPR spectroscopy experiments, interpreted the data and wrote a significant part of the manuscript.

Enzymes as Biodevelopers for Nano- And Micropatterned Bicomponent Biopolymer Thin Films

Katrin Niegelhell,[†] Michael Süßenbacher,[†] Katrin Jammernegg,[†] Thomas Ganner,[‡] Daniel Schwendenwein,[§] Helmut Schwab,[§] Franz Stelzer,[†] Harald Plank,[*,‡] and Stefan Spirk[*,†,‖]

[†]Graz University of Technology, Institute for Chemistry and Technology of Materials, Stremayrgasse 9, 8010 Graz, Austria
[‡]Graz University of Technology, Institute for Electron Microscopy and Nanoanalysis, Steyrergasse 17, 8010 Graz, Austria
[§]Graz University of Technology, Institute for Molecular Biotechnology, Petersgasse 14, 8010 Graz, Austria
[‖]University of Maribor, Institute for Engineering and Design of Materials, Smetanova Ulica 17, 2000 Maribor, Slovenia

Ⓢ *Supporting Information*

ABSTRACT: The creation of nano- and micropatterned polymer films is a crucial step for innumerous applications in science and technology. However, there are several problems associated with environmental aspects concerning the polymer synthesis itself, cross-linkers to induce the patterns as well as toxic solvents used for the preparation and even more important development of the films (e.g., chlorobenzene). In this paper, we present a facile method to produce micro- and nanopatterned biopolymer thin films using enzymes as so-called biodevelopers. Instead of synthetic polymers, naturally derived ones are employed, namely, poly-3-hydroxybutyrate and a cellulose derivative, which are dissolved in a common solvent in different ratios and subjected to spin coating. Consequently, the two biopolymers undergo microphase separation and different domain sizes are formed depending on the ratio of the biopolymers. The development step proceeds via addition of the appropriate enzyme (either PHB-depolymerase or cellulase), whereas one of the two biopolymers is selectively degraded, while the other one remains on the surface. In order to highlight the enzymatic development of the films, video AFM studies have been performed in real time to image the development process in situ as well as surface plasmon resonance spectroscopy to determine the kinetics. These studies may pave the way for the use of enzymes in patterning processes, particularly for materials intended to be used in a physiological environment.

INTRODUCTION

The patterning of thin films is a key step to realize advanced technologies in many emerging areas such as optics, electronics and biotechnology.[1,2] The wide spectrum of thin film applications ranges from surface coatings[3] and optoelectronic devices[4] to microarrays[5] and cell scaffolds,[6] to name a few. When it comes to biopolymers, the use of classic patterning strategies (e.g., photolithography, soft lithography) is very often hampered by the degradative nature of the patterni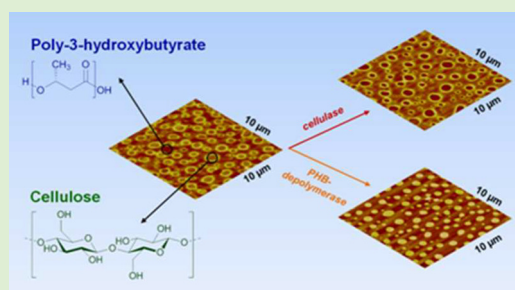ng procedure itself. Only a few examples exist in literature on how patterns of cellulose, the major biopolymer on earth, can be created in a nondestructive way by lithographic techniques.[7,8] However, for very complex patterns, lithography is very often not straightforward, since suitable masks need to be manufactured for each pattern, which becomes costly and laborious at a certain point. An alternative approach to lithographic techniques is to exploit phase separation of polymers for the formation of micro- and nanopatterns. The idea is to mix two (or more) polymers (dissolved in a common solvent), which phase separate upon processing and to control the morphology and geometry of the domains by choosing the appropriate processing conditions.[1,2] While the method of blend preparation is essential for surface morphology, the

polymer molecular structures, molecular weights and the composition of the blends play an important role as well.[9,10] In the case of spin coating, phase separation occurs upon solvent evaporation, leaving the film in a thermodynamical nonequilibrium state, giving rise to different surface morphologies depending on the parameters mentioned above.

Having these facts in mind, we became interested in whether we could exploit the concept of microphase separation of biopolymers to create micropatterns. There are only a few examples known where biopolymer blends have been used to realize such structures.[11−13] In this paper, we extend this approach and combine it with orthogonally active enzymes acting as biodevelopers to obtain micro- and nanopatterned biopolymer structures.
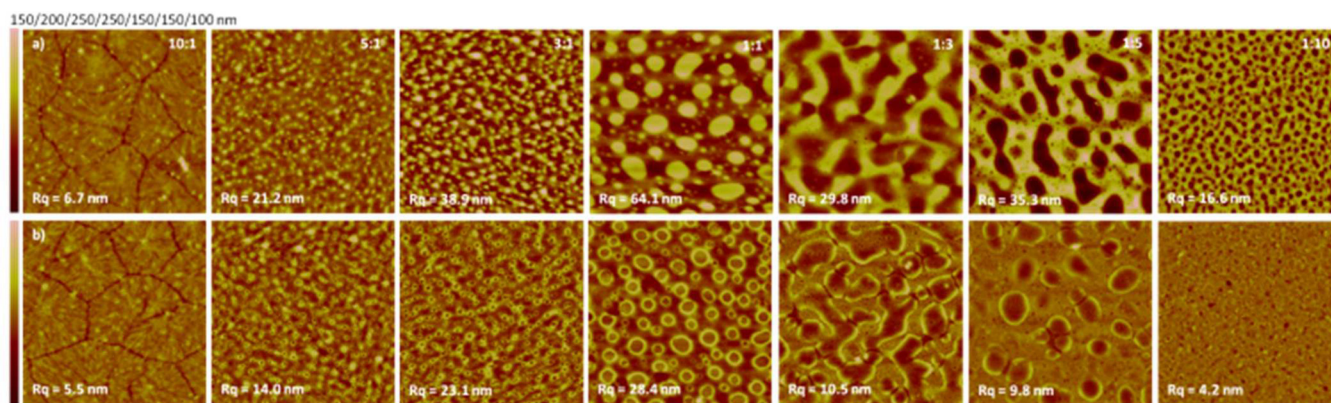
MATERIALS AND METHODS

Materials. Poly-3-hydroxybutyrate (PHB, Biocycle L 91, M_w = 260900 g·mol^{-1}, M_n = 111000 g·mol^{-1}, PDI = 2.3 determined by SEC in chloroform) was purchased from PHB Industrial S.A. (Brazil) and

150/200/250/250/150/150/100 nm

Figure 1. AFM images $10 \times 10 \ \mu m^2$ of PHB/TMSC thin films (different ratios) before (a) and after exposure to HCl vapor (b).

purified by dissolution in chloroform followed by precipitation in cold ethanol. Afterward it was dried under vacuum at 50 °C for 2 days. The process was repeated twice. Trimethylsilyl cellulose (TMSC, Avicel, $M_w = 185000 \ \text{g·mol}^{-1}$, $M_n = 30400 \ \text{g·mol}^{-1}$, PDI = 6.1 determined by SEC in chloroform) with a DS_{Si} value of 2.8 was purchased from TITK (Rudolstadt, Germany). Chloroform (99.3%), potassium phosphate dibasic (KH_2PO_4, 99%), hydrochloric acid (37%), sodium acetate (99%), sodium hydroxide (99%), and cellulase from *Trichoderma viride* were purchased from Sigma-Aldrich and used as received. PHB-depolymerase was isolated from *Acidovorax* sp. and expressed in *E. coli* bI21. Silicon wafers were cut into $1.5 \times 1.5 \ cm^2$ squares. SPR gold sensor slides (CEN102 AU) were purchased from Cenibra, Germany. Milli-Q water (resistivity = 18.2 $\Omega^{-1} \cdot cm^{-1}$) from a Millipore water purification system (Millipore, U.S.A.) was used for contact angle, SPR investigations, and buffer preparation.

Substrate Cleaning and Film Preparation. Prior to spin coating, SPR gold sensor slides/silicon wafers were immersed in a "piranha" solution containing H_2O_2 (30 wt %)/H_2SO_4 (1:3 v/v) for 10 min, then extensively rinsed with Milli-Q water and blow dried with N_2 gas. PHB and TMSC were dissolved in chloroform by stirring overnight at room temperature and filtered through 0.45 μm PVDF filters. PHB and TMSC solutions (0.75 wt %) were mixed in different ratios (10:1, 5:1, 3:1, 1:1, 1:3, 1:5, 1:10). A total of 100 μL of solution were deposited onto the substrate and then rotated for 60 s at a spinning speed of 4000 rpm and an acceleration of 2500 rpm·s^{-1}. To convert TMSC into pure cellulose, the sensors/wafers were placed in a polystyrene Petri-dish (5 cm in diameter) containing 3 mL of 10 wt % hydrochloric acid (HCl). The dish was covered with its cap and the films were exposed to the vapors of HCl for 15 min. The regeneration of cellulose from TMSC was verified by water contact angle, XPS and ATR-IR measurements, as reported elsewhere.[14−16]

Enzymatic Treatment of Thin Films. Buffer salts were dissolved in Milli-Q water. The pH value of the solutions was adjusted with 0.1 M acetic acid/hydrochloric acid or 0.1 M NaOH. PHB-depolymerase was dissolved in a phosphate buffer ($c = 100 \ mM$) at pH 7.4 at a concentration of 50 $\mu g \cdot ml^{-1}$. Cellulase was dissolved in an acetate buffer ($c = 100 \ mM$) at pH 4.8 at a concentration of 5 mg·mL^{-1}. Enzymatic degradation was performed by depositing 100 μL of enzyme solution onto the bicomponent films at a temperature of 37 °C for a time period of 20 min (PHB-depolymerase) and 2 h (cellulase), respectively. After enzyme treatment all samples were rinsed with Milli-Q water and dried in a stream of N_2 gas.

Infrared Spectroscopy. IR spectra were attained by an Alpha FT-IR spectrometer (Bruker; Billerica, MA, U.S.A.) using an attenuated total reflection (ATR) attachment. Spectra were obtained in a scan range between 4000 to 400 cm^{-1} with 48 scans and a resolution of 4 cm^{-1}. The data was analyzed with OPUS 4.0 software.

Profilometry. Film thicknesses were acquired with a DETAK 150 Stylus Profiler from Veeco. The scan length was set to 1000 μm over a duration of 3 s. Measurements were performed with a force of 3 mg, a resolution of 0.333 μm per sample and a measurement range of 6.5 μm. A diamond stylus with a radius of 12.5 μm was used. Samples

were measured after scratching the film (deposited on a silicon wafer). The resulting profile was used to calculate the thickness of different films. All measurements were performed three times.

Contact Angle (CA) and Surface Free Energy (SFE) Determination. Static contact angle measurements were performed with a Drop Shape Analysis System DSA100 (Krüss GmbH, Hamburg, Germany) with a T1E CCD video camera (25 fps) and the DSA1 v 1.90 software. Measurements were done with Milli-Q water and di-iodomethane using a droplet size of 3 μL and a dispense rate of 400 $\mu L \cdot min^{-1}$. All measurements were performed at least three times. SCA were calculated with the Young−Laplace equation and the SFE was determined with the Owen-Wendt-Rabel-Kaelble (OWRK) method.[17−19]

Atomic Force Microscopy (AFM). Surface morphology and roughness of the films were obtained in tapping mode in ambient atmosphere at room temperature by a Veeco Multimode Quadrax MM scanning probe microscope (Bruker; Billerica, MA, U.S.A.) using Si-cantilevers (NCH-VS1-W from NanoWorld AG, Neuchatel, Switzerland) with a resonance frequency of 320 kHz and a force constant of 42 N·m^{-1}. Root mean square (RMS) roughness calculation and image processing was performed with the Nanoscope software (V7.30r1sr3, Veeco).

AFM investigations of the enzymatic degradation were carried out using a FastScan Bio Atomic Force Microscope (Bruker AXS, Santa Barbara, CA, U.S.A.) operated by a Nanoscope V controller. All experiments were conducted in a small-volume (60 μL) flow cell (Bruker AXS, Santa Barbara, CA, U.S.A.) and FastScan D cantilevers with a nominal spring constant of 0.3 N·m^{-1} in tapping mode. A vacuum chuck was used to immobilize the silicon wafer specimen with the corresponding PHB/cellulose thin films. Degassed buffer solution was then injected into the small-volume cell with attached probe and carefully lowered onto the film. Preliminary to image scanning the experimental setup was allowed to equilibrate to the air conditioned room temperature of 22 °C. Prior to injection of enzymes, multiple reference images were recorded. Continuous image scanning was started by injecting 180 μL of a buffer enzyme mixture with enzyme concentrations of 50 $\mu g \cdot mL^{-1}$ for either the PHB-depolymerase or 5 mg·mL^{-1} for the cellulase. Please note, 180 μL correspond to 3× the volume of the cell and ensures a complete exchange of buffer to buffer/enzyme solution. Image recording was performed until either all PHB or cellulose was degraded. Set points, scan rates, and controlling parameters were chosen carefully to ensure lowest possible energy dissipation to the sample and to exclude tip driven artifacts. Data analysis of images was performed using Nanoscope Analysis 1.50 (Build R2.103555, Bruker AXS, Santa Barbara, CA, U.S.A.) and Gwyddion 2.38 (Released 2014−09−18, http://gwyddion.net/). Movie presentations were compiled using Windows Movie Maker (version 2012, Build 16.4.3508.0205, Microsoft Corporation, Redmond, WA, U.S.A.). All images were plane fitted at first order unless otherwise stated.

Multi Parameter Surface Plasmon Resonance Spectroscopy (MP-SPR). MP-SPR spectroscopy was accomplished with a SPR Navi

Table 1. Average TMSC/Cellulose Domain Height (in nm) in Respect to PHB for the Different Blend Ratios before and after the Regeneration Step

PHB/TMSC	10:1	5:1	3:1	1:1	1:3	1:5	1:10
TMSC domain height	36 ± 9	83 ± 24	128 ± 45	100 ± 18	88 ± 8	116 ± 14	57 ± 11
cellulose domain height	−17 ± 4	−15 ± 7	−8 ± 6	−40 ± 14	30 ± 12	24 ± 4	18 ± 10
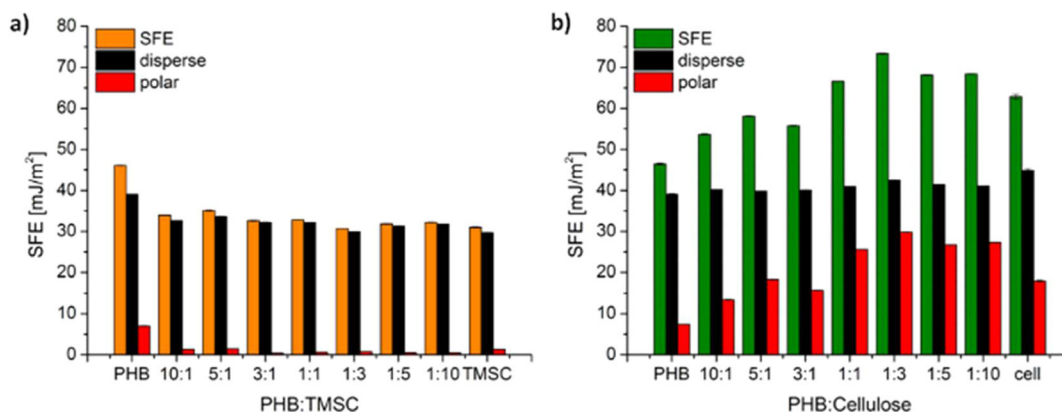
Figure 2. Surface free energy of bicomponent thin films before (a) and after (b) exposure to HCl vapor. Please note that the error bars are very small and hardly visible in the diagrams.

200 from Bionavis Ltd., Tampere, Finland, equipped with two different lasers (670 and 785 nm, respectively) in both measurement channels, using gold-coated glass slides as substrate (gold layer 50 nm, chromium adhesion layer 10 nm). All measurements were performed using a full angular scan (39−78°, scan speed: 8°·s^{-1}).

Enzymatic degradation was performed by exposing the films to enzyme solution at a flow rate of 50 μL·min^{-1} and a temperature of 25 °C for a time period of 5 min, followed by rinsing with buffer.

RESULTS AND DISCUSSION

For the proof of concept, we chose blend thin films composed of poly-3-hydroxybutyrate, a biopolymer produced by bacteria, and cellulose. Both biopolymers are readily degradable by enzymes developing either selectively PHB (by PHB-depolymerase) or cellulose (by cellulases) micro/nanopatterns. In terms of the experimental approach, a soluble precursor for cellulose, which is solvent compatible to PHB, has to be used, since cellulose is insoluble in common organic solvents. A suitable precursor for this purpose is trimethylsilyl cellulose (TMSC), as its solubility can be easily adjusted by the degree of substitution with TMS groups. The concept is to convert organosoluble TMSC (DS$_{Si}$ ca. 2.8) back to cellulose after spin-casting using HCl vapors; a procedure which has been extensively employed during the past years.[20,21]

In order to create different micro/nanopatterns, PHB and TMSC are dissolved in chloroform at different ratios and subjected to spin coating. Afterward, the morphology of the resulting films is investigated before and after exposure to HCl vapors and the enzymatic development of PHB and cellulose is studied. As revealed in the AFM images (Figure 1), the microphase separation seemingly proceeds according to the transient bilayer theory, describing the vertical stratification of the two phases, followed by interfacial instabilities, caused by a solvent-concentration gradient troughout the film, leading to lateral phase separation.[22]

The final structure of the resulting domains is defined by a variety of factors, such as film thickness,[23,24] relative humidity,[11,25] temperature,[26] the type of substrate,[27] solubility of the blend components in the solvent used,[23,27−29] and

surface segregation,[30−32] which is the preferential migration of one component to the interface, depending on surface free energy. This complex interplay of parameters complicates the explanation of the emerging phase structures without evidence from time-resolved, small-angle X-ray scattering or light reflectivity during the spin coating process. In the herein investigated system, PHB probably forms the bottom layer and TMSC the top layer during the initial phase of spin coating, due to the relatively high surface free energy and higher polarity of PHB, compared to the highly substituted TMSC (DS$_{Si}$ ca. 2.8). Therefore, interaction of PHB with the hydrophilized gold/silicon support is more pronounced. Additionally, the lower surface free energy compound TMSC tends to migrate to the air−polymer interface. Apparently, a rather thin TMSC layer is present for blend films with PHB/TMSC ratios of 10:1, 5:1, 3:1, and 1:1 during vertical stratification, which contracts to droplets,[33,34] that will be surrounded by the second phase at the end of the spin-coating process, seen in the droplet-shaped cellulose domains that are distributed in a continuous PHB phase. A thicker layer of TMSC during the early phase of spin coating favors PHB distribution in a continuous cellulose phase, due to a dewetting process, leading to hole formation and subsequent filling with the polymer from the lower layer.[33] This is observed for PHB/TMSC ratios of 1:5 and 1:10. Films with a PHB/TMSC ratio of 1:3 exhibit two continuous laterally separated phases, which usually occur at ratios close to one; however, this deviation can be attributed to the difference in molecular weight of the polymers. The resulting morphologies are different compared to other TMSC-based blend films known in literature. PHB/TMSC films with ratios of 10:1, 5:1, 3:1, and 1:1 show circular TMSC domains embedded in a PHB matrix, similar to those reported by Kontturi et al.[34] for PMMA/TMSC films. For these blend films, the TMSC domains form cavities with a depth of up to 10 nm (before and after regeneration) compared to the PMMA phase. Further, polystyrene/TMSC blend films show low roughness and protruding polystyrene domains are only obtained after HCl treatment.[35] A special case is the lignin palmitate/TMSC system, where the 3:1 ratio yielded rather flat films, while the

150/150/200/200/150/100/100nm
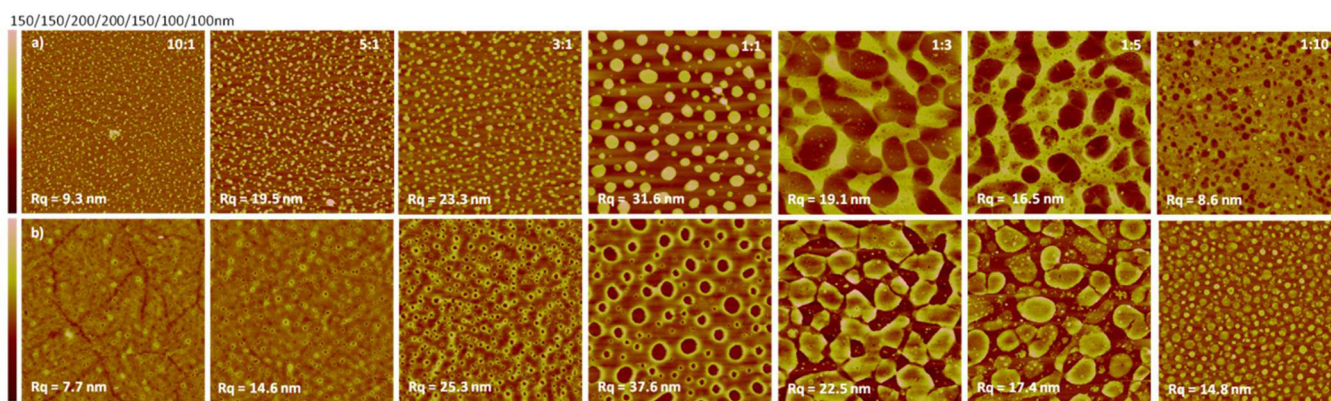
Figure 3. AFM images (size 10 × 10 μm^2) of enzymatic degradation of PHB/cellulose thin films with PHB-depolymerase (a) or cellulase (b).

Table 2. Average and Median Feature Sizes of PHB/Cellulose Blends after Enzymatic Treatment

PHB/cellulose	10:1	5:1	3:1	1:1	1:3	1:5	1:10
average	50 ± 15	71 ± 28	126 ± 50	534 ± 209	1337 ± 204	1405 ± 380	126 ± 65
median	49 ± 12	57 ± 24	106 ± 40	498 ± 174	1260 ± 182	1430 ± 290	100 ± 48
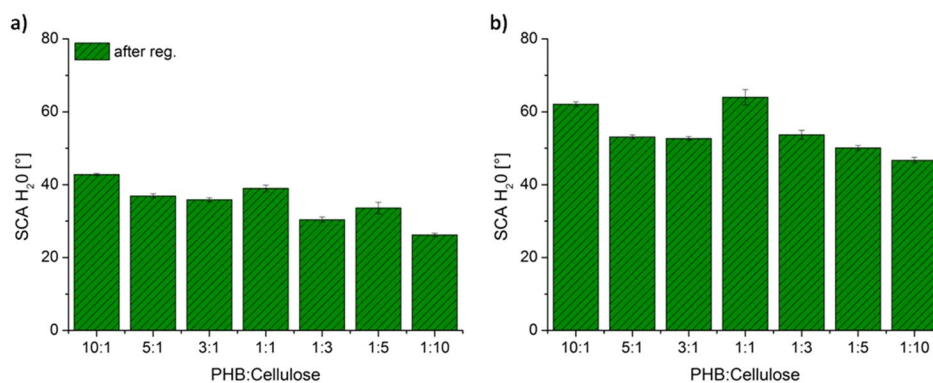
Figure 4. Static water contact angle of bicomponent thin films after treatment with PHB-depolymerase (a) or cellulase (b).

1:3 ratio led to the formation of lignin palmitate cavities.[13] After regeneration, these cavities inverted into protruding pillar like domains due to shrinkage of the TMSC after conversion. In contrast to that, all the herein investigated PHB/TMSC films showed protruding TMSC features (see Table 1), which were converted into cavities just after the regeneration step. For the PHB/TMSC blend films with ratios of 1:3, 1:5, and 1:10, the situation was different since the continuous phase was inverted. The protruding domains shrank but instead of cavities rather flat films (in terms of height difference) were obtained after regeneration. The shrinkage amounts to approximately 60−70%, which agrees well with values reported in literature.[20,35]

Before enzymatic development is performed, it is of crucial importance to confirm the conversion of TMSC to cellulose and to exclude any influence of HCl vapors on the PHB domains of the films. Comparing the ATR-IR spectra (Figure S1) of TMSC and cellulose,[20] it can be clearly seen that the characteristic bands for methyl groups of TMSC at 2960 cm^{-1} (ν_{asym}) and 2872 cm^{-1} (ν_{sym}) and the Si−C contributions at 1251 and 842 cm^{-1} vanish in the regenerated TMSC film and TMSC containing blends. Additionally, the OH stretching band between 3600 and 3000 cm^{-1} appears due to the formation of cellulose. ATR-IR spectra (Figure S2) of PHB bulk and PHB films before and after the regeneration step confirm that there is no influence of HCl vapor on PHB. This is further corroborated by AFM studies (Figure S3), profilometry

(constant thickness), and wettability (constant contact angles) determinations as well. However, a change in thickness of films containing TMSC is observed due to shrinkage of TMSC domains by cleaving off TMS groups during conversion. As expected, the shrinkage is higher for films containing a larger amount of TMSC (Figure S4). During the regeneration step, surfaces change from rather hydrophobic to more hydrophilic. Figure 2 depicts this shift of surface free energy from about 30 mJ·m^{-2} with hardly any polar contribution for nonregenerated blends to higher values with increased polar contributions for regenerated ones. Interestingly, the highest surface free energies are determined for blend films with PHB/cellulose ratios of 1:1 to 1:10, which are even higher than for pure cellulose (63 ± 1 mJ·m^{-2}). Maybe, this behavior originates from the roughness of the films, which is a major factor besides the presence of chemical groups for variations in SCA and SFE.

The phase separated blend thin films were subjected to enzymatic development (37 °C) aiming at bioorthogonal degradation of one component without influencing the other. For this purpose, the films have been exposed to enzyme solutions for different periods of time. It was observed that PHB-depolymerase degrades PHB very fast (20 min) under the chosen conditions. In contrast, the cellulose films were degraded after 2 h, which is in line with specific investigations on the degradation of cellulose films.[36−38] However, since in these studies different cellulase cocktails and operating

conditions had been employed, further quantitative comparisons are not possible.

After drying the films, AFM investigations (Figure 3) confirm the selective removal of PHB by PHB-depolymerase and of cellulose by cellulases from blend films of all tested ratios, while the other phase was left intact. Remaining pillars and pores/cavities after enzymatic treatment are in the nano to micro size range depending on the PHB/cellulose ratio. An overview on the average and median feature sizes of the blend films after enzymatic degradation is presented in Table 2. Further, the wettability of the remaining patterned biopolymer phases was nearly identical for all PHB and cellulose phases and in the same range as pure PHB or cellulose films (Figure 4).

The high efficiency of PHB-depolymerase from *Acidovorax* sp. led us to examine its adsorption behavior onto the herein investigated blends by means of surface plasmon resonance spectroscopy (SPR). The adsorption of PHB-depolymerases is a fundamental step for the degradation function of the enzyme. Usually, these kinds of enzymes dock to the surface with a substrate binding domain and linker regions, followed by a conformational change activating the catalytic domain. However, we were not able to monitor the complete adsorption process of PHB-depolymerase, because almost immediate degradation of PHB set in at the chosen concentration (50 μg·mL^{-1}). This is even more astonishing since all SPR experiments were performed at 25 °C, keeping in mind that the optimum working temperature of the used PHB-depolymerase is 37 °C.[39] The SPR-angle increases slightly upon enzyme injection (5 min, 250 μL, 50 μg mL^{-1}), followed by an immediate decrease for neat PHB and PHB/cellulose blend ratios of 3:1 and 1:1. This indicates that both processes, adsorption, and degradation, proceed at the same time, whereas the blend film with a PHB/cellulose ratio of 1:3 is not degraded at all at 25° (Figures 5 and S5). A closer look reveals that we
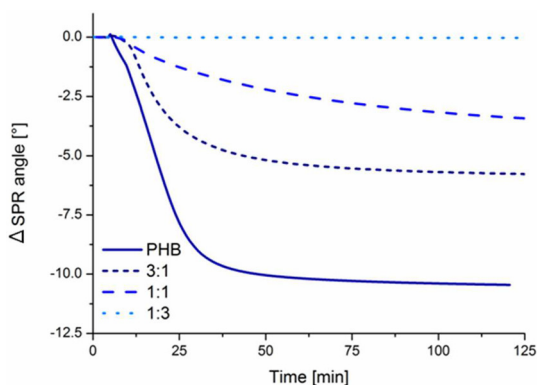
Figure 5. SPR sensograms of enzymatic treatment with PHB-depolymerase (50 μg·mL^{-1}) of PHB/cellulose bicomponent thin films acquired at 25 °C.

monitor faster adsorption of PHB-depolymerase (steeper slope of increasing SPR angle) and earlier start of degradation (decrease in SPR angle) with increasing PHB contents in the films (Figure S6). However, for blend films with a PHB/cellulose ratio of 1:3, we did not observe any activity of the enzyme at this concentration. A potential explanation for this is the lower temperature (25 °C) in the SPR experiments compared to the patterning trials (37 °C) concomitant with lower activity of the enzyme in general. Furthermore, the surface free energy of the 1:3 PHB/cellulose blend film is the

highest among all investigated films, which may impede efficient interactions of the enzyme with the remaining PHB in the blends, since the main binding interactions of PHB-depolymerase are of hydrophobic nature.[40,41]

In order to gain better insights into the degradation process, the enzymatic treatment of PHB/cellulose blend ratio 1:1 was monitored in real time by fast scan AFM (ESI). The resulting videos further substantiate our findings concerning PHB-depolymerase, revealing initial swelling of the PHB domains, followed by fast degradation compared to other enzymes of this kind.[41,42] The swelling step could be an indication for a change in PHB surface morphology upon enzyme adsorption[43−45] or a very thin cellulose layer on top of the PHB phase, which is swollen by the buffer, thereby breaks up and is then penetrated by the enzyme, which is then able to digest the underlying polymer; however there is no evidence for both assumptions. In situ AFM investigations regarding the reverse patterning of the blends by enzymatic degradation of cellulose domains by cellulase reveals a slower process compared to PHB depolymerase. This behavior originates from the different types of enzymes that need to work cooperatively in the case of cellulases (glucosidases, exo- and endoglucanases, etc.), whereas PHB-depolymerase consists just of a single enzyme.

Further, it is known that similarly to PHB-depolymerase the optimum working temperature of cellulase from *Trichoderma viride* to digest cellulose thin films is 37 °C.[36] However, the outcome of the enzymatic digestion experiments at lower temperature is in good agreement with results from degradation at optimum temperature. In contrast to PHB, cellulose pillar-like domains are degraded uniformly from top to bottom, generating holes with a size of approximately 500 nm. PHB-depolymerase initially degrades only some parts of the continuous PHB domains, which in turn are nearly completely digested. As soon as the first domains have been degraded, it seems that the film gets more accessible to the enzymes and further breakdown of PHB is observed.

■ CONCLUSION

In summary, an efficient approach for bioorthogonal templating of biopolymer blend films is presented at the example of PHB and cellulose. Depending on the ratio of the components in the blend films, different surface morphologies and feature sizes were obtained. This prestructuring by phase separation is then further utilized to create micro- and nano-sized domains by selective enzymatic development of just one of the two biopolymers. While patterning at 37 °C is working very well for all blend film systems, a decrease of temperature to 25 °C showed that the activity of the PHB-depolymerase decreased significantly for those films that feature rather high surface free energies. This behavior is particularly pronounced for the film with the highest surface free energy among all films (PHB/cellulose 1:3) where hardly any degradation can be observed at 25 °C. Currently, we are investigating how to exploit this very interesting phenomenon, namely to induce switchable temperature triggered development of biopolymer films, which can be further tuned by variation of enzyme concentration to increase the activity.

The enzymatic developing step of this "bioresist" was further visualized by video AFM studies which revealed different degradation mechanisms for the corresponding biopolymer types relating to the different enzymes (one component vs multicomponent in the case of cellulases). Furthermore, the herein demonstrated approach presents a general method

which is applicable for templating purposes with various other renewable or biobased polymer systems, aiming at the replacement of polymers derived from fossil resources. The resulting patterned surfaces may be subject of further investigations concerning their utilization in various fields such as biosensors or antifouling surfaces.

■ ASSOCIATED CONTENT

Ⓢ Supporting Information

The Supporting Information is available free of charge on the ACS Publications website at DOI: 10.1021/acs.biomac.6b01263.

> Materials, detailed experimental procedures, supplementary IR spectra, and contact angle data (Figures S1–S6; PDF).
>
> AFM video of enzymatic degradation (AVI).
>
> AFM video of enzymatic degradation (AVI).

■ AUTHOR INFORMATION

Corresponding Authors

*E-mail: harald.plank@felmi-zfe.at. Phone: +43-316-873-8821.
*E-mail: stefan.spirk@tugraz.at. Phone: +43-316-873-32284.

Notes

The authors declare no competing financial interest.

■ ACKNOWLEDGMENTS

■ REFERENCES

(1) Rodríguez-Hernández, J. Nano/Micro and Hierarchical Structured Surfaces in Polymer Blends. *Nanostructured Polymer Blends* **2014**, 357−421.

(2) Xue, L.; Zhang, J.; Han, Y. Phase Separation Induced Ordered Patterns in Thin Polymer Blend Films. *Prog. Polym. Sci.* **2012**, *37*, 564−594.

(3) Walheim, S.; Schäffer, E.; Mlynek, J.; Steiner, U. Nanophase-Separated Polymer Films as High-Performance Antireflection Coatings. *Science* **1999**, *283*, 520−522.

(4) Corcoran, N.; Arias, A. C.; Kim, J. S.; MacKenzie, J. D.; Friend, R. H. Increased Efficiency in Vertically Segregated Thin-Film Conjugated Polymer Blends for Light-Emitting Diodes. *Appl. Phys. Lett.* **2003**, *82*, 299−301.

(5) Zemła, J.; Lekka, M.; Raczkowska, J.; Bernasik, A.; Rysz, J.; Budkowski, A. Selective Protein Adsorption on Polymer Patterns Formed by Self-Organization and Soft Lithography. *Biomacromolecules* **2009**, *10*, 2101−2109.

(6) Li, L.; Chen, C.; Li, J.; Zhang, A.; Liu, X.; Xu, B.; Gao, S.; Jin, G.; Ma, Z. Robust and Hydrophilic Polymeric Films with Honeycomb Pattern and Their Cell Scaffold Applications. *J. Mater. Chem.* **2009**, *19*, 2789−2796.

(7) Wolfberger, A.; Petritz, A.; Fian, A.; Herka, J.; Schmidt, V.; Stadlober, B.; Kargl, R.; Spirk, S.; Griesser, T. Photolithographic Patterning of Cellulose: A Versatile Dual-Tone Photoresist for Advanced Applications. *Cellulose* **2015**, *22*, 717−727.

(8) Kargl, R.; Mohan, T.; Köstler, S.; Spirk, S.; Doliška, A.; Stana-Kleinschek, K.; Ribitsch, V. Functional Patterning of Biopolymer Thin Films Using Enzymes and Lithographic Methods. *Adv. Funct. Mater.* **2013**, *23*, 308−315.

(9) Li, X.; Han, Y.; An, L. Surface Morphology Control of Immiscible Polymer-Blend Thin Films. *Polymer* **2003**, *44*, 8155−8165.

(10) Müller-Buschbaum, P.; Gutmann, J. S.; Stamm, M. Influence of Blend Composition on Phase Separation and Dewetting of Thin Polymer Blend Films. *Macromolecules* **2000**, *33*, 4886−4895.

(11) Taajamaa, L.; Rojas, O. J.; Laine, J.; Kontturi, E. Phase-Specific Pore Growth in Ultrathin Bicomponent Films from Cellulose-Based Polysaccharides. *Soft Matter* **2011**, *7*, 10386−10394.

(12) Hoeger, I. C.; Filpponen, I.; Martin-Sampedro, R.; Johansson, L.-S.; Österberg, M.; Laine, J.; Kelley, S.; Rojas, O. J. Bicomponent Lignocellulose Thin Films to Study the Role of Surface Lignin in Cellulolytic Reactions. *Biomacromolecules* **2012**, *13*, 3228−3240.

(13) Strasser, S.; Niegelhell, K.; Kaschowitz, M.; Markus, S.; Kargl, R.; Stana-Kleinschek, K.; Slugovc, C.; Mohan, T.; Spirk, S. Exploring Nonspecific Protein Adsorption on Lignocellulosic Amphiphilic Bicomponent Films. *Biomacromolecules* **2016**, *17*, 1083−1092.

(14) Mohan, T.; Spirk, S.; Kargl, R.; Doliška, A.; Vesel, A.; Salzmann, I.; Resel, R.; Ribitsch, V.; Stana-Kleinschek, K. Exploring the Rearrangement of Amorphous Cellulose Model Thin Films upon Heat Treatment. *Soft Matter* **2012**, *8*, 9807.

(15) Mohan, T.; Kargl, R.; Doliška, A.; Vesel, A.; Köstler, S.; Ribitsch, V.; Stana-Kleinschek, K. Wettability and Surface Composition of Partly and Fully Regenerated Cellulose Thin Films from Trimethylsilyl Cellulose. *J. Colloid Interface Sci.* **2011**, *358*, 604−610.

(16) Mohan, T.; Spirk, S.; Kargl, R.; Doliška, A.; Ehmann, H. M. a; Köstler, S.; Ribitsch, V.; Stana-Kleinschek, K. Watching Cellulose Grow - Kinetic Investigations on Cellulose Thin Film Formation at the Gas-Solid Interface Using a Quartz Crystal Microbalance with Dissipation (QCM-D). *Colloids Surf., A* **2012**, *400*, 67−72.

(17) Owens, D. K.; Wendt, R. C. Estimation of the Surface Free Energy of Polymers. *J. Appl. Polym. Sci.* **1969**, *13*, 1741−1747.

(18) Rabel, W. Einige Aspekte Der Benetzungstheorie Und Ihre Anwendung Auf Die Untersuchung Und Veränderung Der Oberflächeneigenschaften von Polymeren. *Farbe Lack* **1971**, *77*, 997−1005.

(19) Kaelble, D. H. Dispersion-Polar Surface Tension Properties of Organic Solids. *J. Adhes.* **1970**, *2*, 66−81.

(20) Kontturi, E.; Thüne, P. C.; Niemantsverdriet, J. W. Cellulose Model Surfaces-Simplified Preparation by Spin Coating and Characterization by X-Ray Photoelectron Spectroscopy, Infrared Spectroscopy, and Atomic Force Microscopy. *Langmuir* **2003**, *19*, 5735−5741.

(21) Ehmann, H. M. A.; Werzer, O.; Pachmajer, S.; Mohan, T.; Amenitsch, H.; Resel, R.; Kornherr, A.; Stana-Kleinschek, K.; Kontturi, E.; Spirk, S. Surface-Sensitive Approach to Interpreting Supramolecular Rearrangements in Cellulose by Synchrotron Grazing Incidence Small-Angle X-Ray Scattering. *ACS Macro Lett.* **2015**, *4*, 713−716.

(22) Heriot, S. Y.; Jones, R. A. L. An Interfacial Instability in a Transient Wetting Layer Leads to Lateral Phase Separation in Thin Spin-Cast Polymer-Blend Films. *Nat. Mater.* **2005**, *4*, 782−786.

(23) Tanaka, K.; Takahara, A.; Kajiyama, T. Film Thickness Dependence of the Surface Structure of Immiscible Polystyrene/Poly(methyl methacrylate) Blends. *Macromolecules* **1996**, *29*, 3232−3239.

(24) Tanaka, K.; Yoon, J.-S.; Takahara, A.; Kajiyama, T. Ultra-thinning-Induced Surface Phase Separation of Polystyrene/ Poly(vinyl methyl ether) Blend Film. *Macromolecules* **1995**, *28*, 934−938.

(25) Sprenger, M.; Walheim, S.; Budkowski, A.; Steiner, U. Hierarchic Structure Formation in Binary and Ternary Polymer Blends. *Interface Sci.* **2003**, *11*, 225−235.

(26) Hecht, U.; Schilz, C. M.; Stratmann, M. Influence of Relative Humidity during Film Formation Processes on the Structure of Ultrathin Polymeric Films. *Langmuir* **1998**, *14*, 6743−6748.

(27) Walheim, S.; Böltau, M.; Mlynek, J.; Krausch, G.; Steiner, U. Structure Formation via Polymer Demixing in Spin-Cast Films. *Macromolecules* **1997**, *30*, 4995−5003.

(28) Hopkinson, I.; Myatt, M. Phase Separation in Ternary Polymer Solutions Induced by Solvent Loss. *Macromolecules* **2002**, *35*, 5153−5160.

(29) Schmidt, J. J.; Gardella, J. A.; Salvati, L. Surface Studies of Polymer Blends. 2. An ESCA and IR Study of Poly(methyl

methacrylate)/Poly(vinyl chloride) Homopolymer Blends. *Macromolecules* **1989**, *22*, 4489−4495.

(30) Reich, S.; Cohen, Y. Phase Separation of Polymer Blends in Thin Films. *J. Polym. Sci., Polym. Phys. Ed.* **1981**, *19*, 1255−1267.

(31) Nesterov, A.; Horichko, V.; Lipatov, Y. Phase Separation of Poly(vinyl acetate)-Poly(methyl methacrylate) Mixtures in Thin Films. *Makromol. Chem., Rapid Commun.* **1991**, *12*, 571−574.

(32) Wang, P.; Wang, P.; Koberstein, J. T.; Koberstein, J. T. Morphology of Immiscible Polymer Blend Thin Films Prepared by Spin-Coating. *Macromolecules* **2004**, *37*, 5671−5681.

(33) Reiter, G. Dewetting of Thin Polymer Films. *Phys. Rev. Lett.* **1992**, *68*, 75−78.

(34) Kontturi, E.; Johansson, L.-S.; Laine, J. Cellulose Decorated Cavities on Ultrathin Films of PMMA. *Soft Matter* **2009**, *5*, 1786−1788.

(35) Nyfors, L.; Suchy, M.; Laine, J.; Kontturi, E. Ultrathin Cellulose Films of Tunable Nanostructured Morphology with a Hydrophobic Component. *Biomacromolecules* **2009**, *10*, 1276−1281.

(36) Mohan, T.; Kargl, R.; Doliška, A.; Ehmann, H. M. A.; Ribitsch, V.; Stana-Kleinschek, K. Enzymatic Digestion of Partially and Fully Regenerated Cellulose Model Films from Trimethylsilyl Cellulose. *Carbohydr. Polym.* **2013**, *93*, 191−198.

(37) Suchy, M.; Linder, M. B.; Tammelin, T.; Campbell, J. M.; Vuorinen, T.; Kontturi, E. Quantitative Assessment of the Enzymatic Degradation of Amorphous Cellulose by Using a Quartz Crystal Microbalance with Dissipation Monitoring. *Langmuir* **2011**, *27*, 8819−8828.

(38) Josefsson, P.; Henriksson, G.; Wågberg, L. The Physical Action of Cellulases Revealed by a Quartz Crystal Microbalance Study Using Ultrathin Cellulose Films and Pure Cellulases. *Biomacromolecules* **2008**, *9*, 249−254.

(39) Vigneswari, S.; Lee, T. S.; Bhubalan, K.; Amirul, A. A. Extracellular Polyhydroxyalkanoate Depolymerase by Acidovorax Sp. DP5. *Enzyme Res.* **2015**, *2015*, 1−8.

(40) Seemann, R.; Herminghaus, S.; Neto, C.; Schlagowski, S.; Podzimek, D.; Konrad, R.; Mantz, H.; Jacobs, K. Dynamics and Structure Formation in Thin Polymer Melt Films. *J. Phys.: Condens. Matter* **2005**, *17*, 267−290.

(41) Numata, K.; Yamashita, K.; Fujita, M.; Tsuge, T.; Kasuya, K. I.; Iwata, T.; Doi, Y.; Abe, H. Adsorption and Hydrolysis Reactions of Poly(hydroxybutyric acid) Depolymerases Secreted from Ralstonia Pickettii T1 and Penicillium Funiculosum onto poly[(R)-3-hydroxybutyric acid]. *Biomacromolecules* **2007**, *8*, 2276−2281.

(42) Phithakrotchanakoon, C.; Daduang, R.; Thamchaipenet, A.; Wangkam, T.; Srikhirin, T.; Eurwilaichitr, L.; Champreda, V. Heterologous Expression of Polyhydroxyalkanoate Depolymerase from Thermobifida Sp. in Pichia Pastoris and Catalytic Analysis by Surface Plasmon Resonance. *Appl. Microbiol. Biotechnol.* **2009**, *82*, 131−140.

(43) Kikkawa, Y.; Suzuki, T.; Tsuge, T.; Kanesato, M.; Doi, Y.; Abe, H. Phase Structure and Enzymatic Degradation of poly(L-lactide)/atactic poly(3- hydroxybutyrate) Blends: An Atomic Force Microscopy Study. *Biomacromolecules* **2006**, *7*, 1921−1928.

(44) Kikkawa, Y.; Hirota, T.; Numata, K.; Tsuge, T.; Abe, H.; Iwata, T.; Doi, Y. In-Situ Atomic Force Microscopy Observation of Enzymatic Degradation in Poly(hydroxyalkanoic acid) Thin Films: Normal and Constrained Conditions. *Macromol. Biosci.* **2004**, *4*, 276−285.

(45) Kikkawa, Y.; Yamashita, K.; Hiraishi, T.; Kanesato, M.; Doi, Y. Dynamic Adsoption Behavior of poly(3-hydroxybutyrate) Depolymerase onto Polyester Surface Investigated by QCM and AFM. *Biomacromolecules* **2005**, *6*, 2084−2090.

Supporting Information #3

Enzymes as Biodevelopers for Nano- and Micropatterned Bicomponent Biopolymer Thin Films
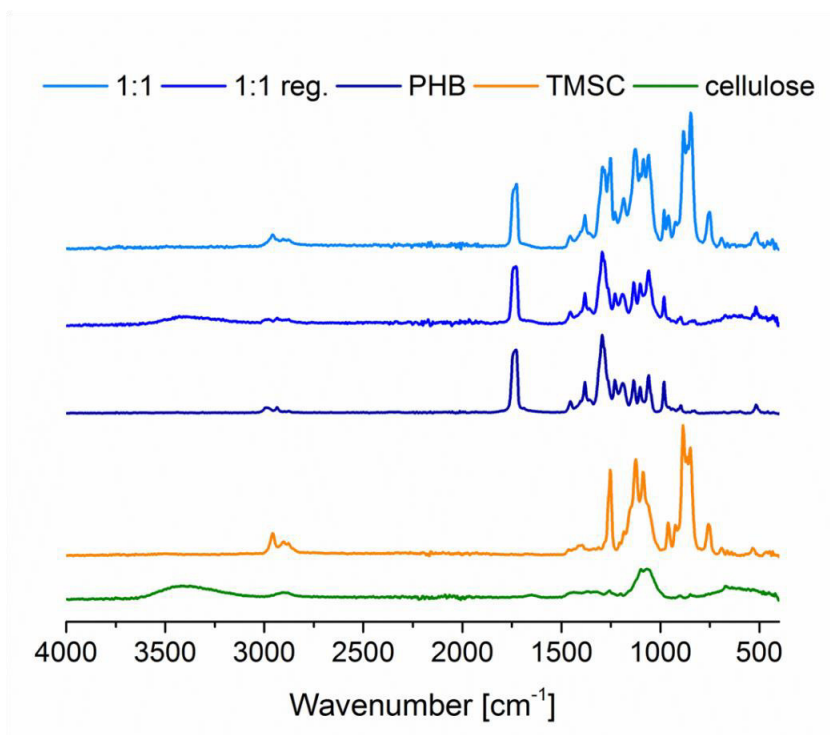
Figure S1. ATR-IR spectra of PHB, TMSC and PHB/TMSC thin films before and after the regeneration step.
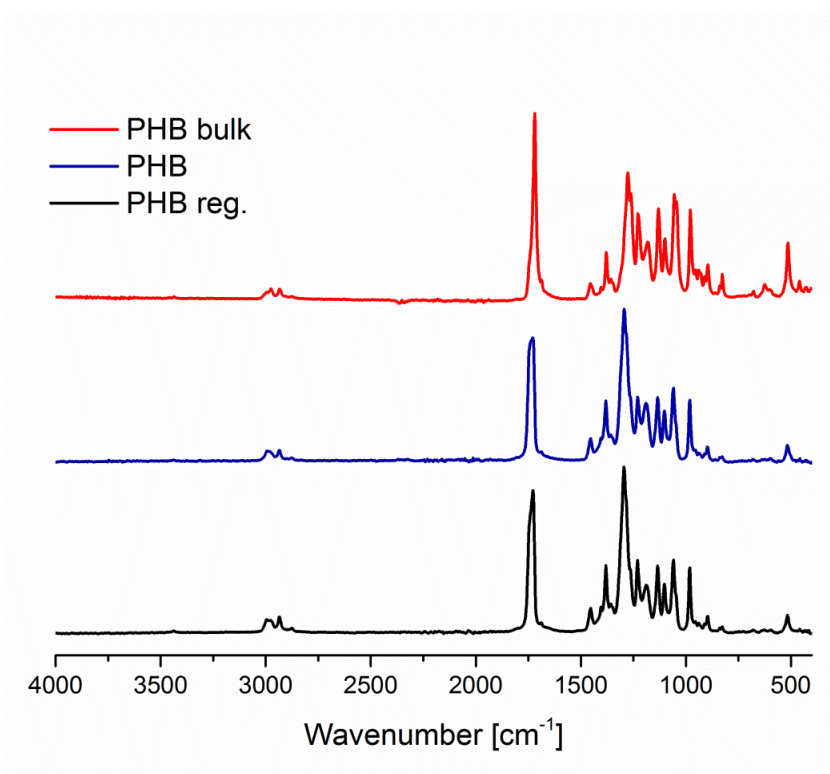
Figure S2. Comparison of ATR-IR spectra of PHB bulk and PHB thin films before and after treatment with hydrochloric acid.
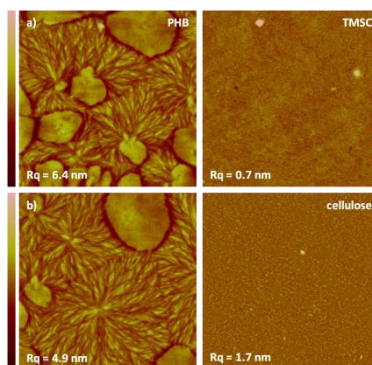
Figure S3. AFM images (size 10 × 10 μm^2) of PHB (z-scale 70 nm) and TMSC (z-scale 20 nm) thin films before **(a)** and after **(b)** exposure to HCl gas.
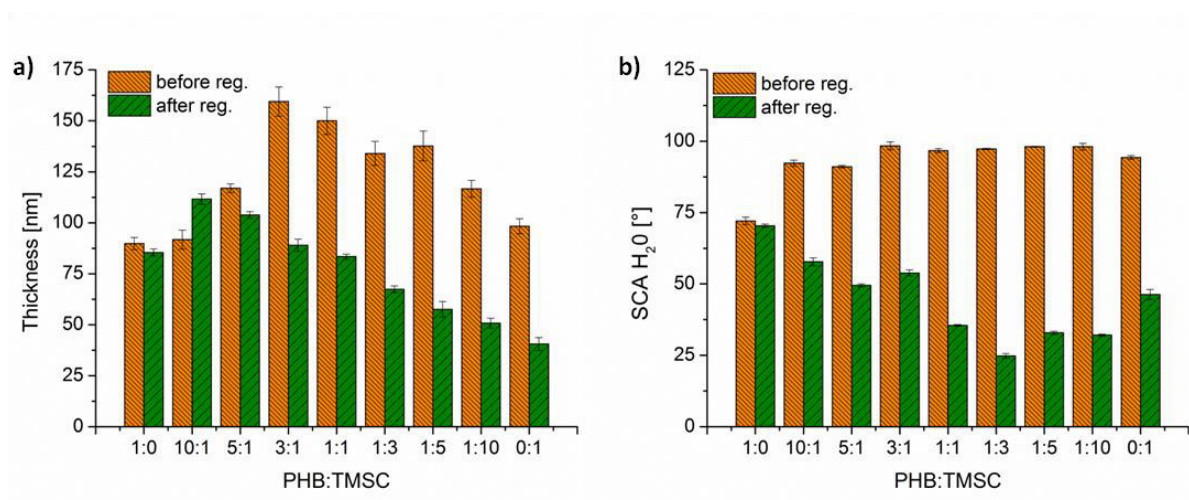
Figure S4. Thicknesses **(a)** and static water contact angle **(b)** of PHB, TMSC and PHB/TMSC thin films before and after the regeneration step.
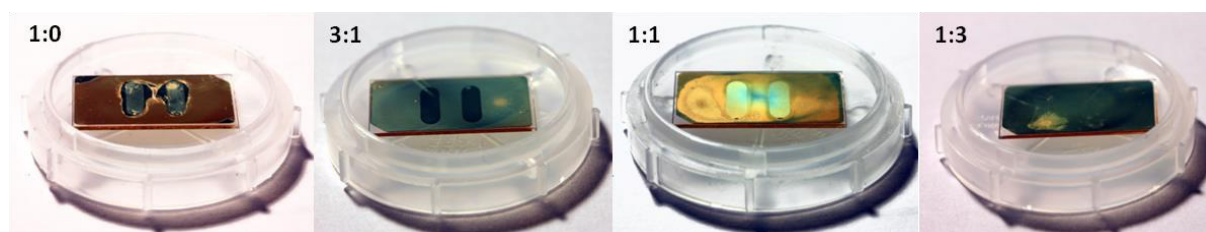
Figure S5. Pictures of SPR sensors slides with PHB/Cellulose films after treatment with *PHB-depolymerase.*
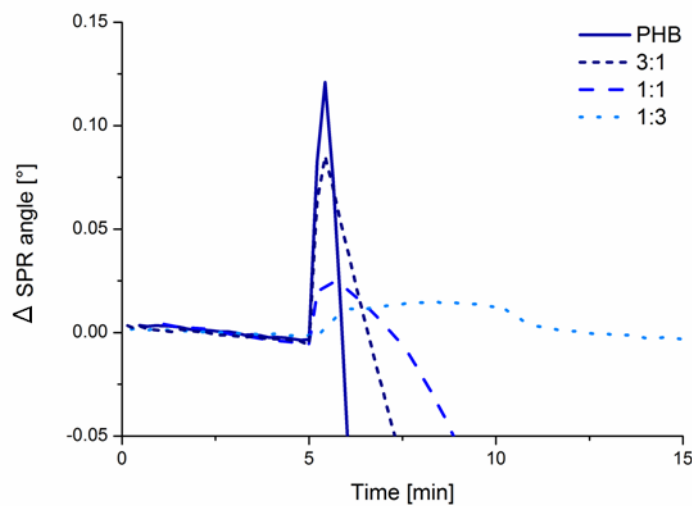
Figure S6. SPR sensograms of enzymatic treatment (injection of PHB-depolymerase) of PHB/cellulose bicomponent thin films.

References

(1)   Mohan, T.; Spirk, S.; Kargl, R.; Doliška, A.; Vesel, A.; Salzmann, I.; Resel, R.; Ribitsch, V.; Stana-Kleinschek, K. *Soft Matter* **2012**, *8*, 9807.

(2)   Mohan, T.; Kargl, R.; Doliška, A.; Vesel, A.; Köstler, S.; Ribitsch, V.; Stana-Kleinschek, K. *J. Colloid Interface Sci.* **2011**, *358*, 604–610.

(3)   Mohan, T.; Spirk, S.; Kargl, R.; Doliška, A.; Ehmann, H. M. a; Köstler, S.; Ribitsch, V.; Stana-Kleinschek, K. *Colloids Surfaces A Physicochem. Eng. Asp.* **2012**, *400*, 67–72.

(4)   Owens, D. K.; Wendt, R. C. *J. Appl. Polym. Sci.* **1969**, *13*, 1741–1747.

(5)   Rabel, W. *Farbe und Lack* **1971**, *77*, 997–1005.

(6)   Kaelble, D. H. *J. Adhes.* **1970**, *2*, 66–81.

PAPER #4

Interaction of Tissue Engineering Substrates with Serum Proteins and

Its Influence on Human Primary Endothelial Cells

For this paper, I conducted the MP-SPR spectroscopy experiments, a part of the AFM measurements and interpreted the corresponding data.

Interaction of Tissue Engineering Substrates with Serum Proteins and Its Influence on Human Primary Endothelial Cells

Tamilselvan Mohan,*,[†] Katrin Niegelhell,[‡] Chandran Nagaraj,[§,‖] David Reishofer,[‡,⊥] Stefan Spirk,[‡,⊥] Andrea Olschewski,[§,‖] Karin Stana Kleinschek,[⊥] and Rupert Kargl*,[⊥,‡] [ID]

[†]Institute of Chemistry, University of Graz, Heinrichstraße 28, 8010 Graz, Austria

[‡]Institute for Chemistry and Technology of Materials, Graz University of Technology, Stremayrgasse 9, 8010 Graz, Austria

[§]Ludwig Boltzmann Institute for Lung Vascular Research, Stiftingtalstrasse 24, 8010 Graz, Austria

[‖]Institute of Physiology, Medical University of Graz, Harrachgasse 21/V, 8010 Graz, Austria

[⊥]Laboratory for Characterization and Processing of Polymers (LCPP), University of Maribor, Smetanova 17, 2000 Maribor, Slovenia

S *Supporting Information*
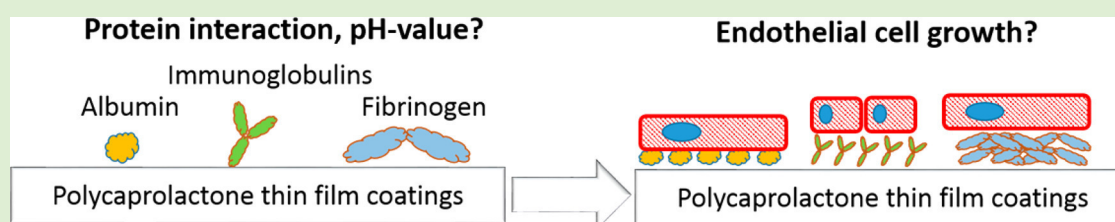
ABSTRACT: Polymer-based biomaterials particularly polycaprolactone (PCL) are one of the most promising substrates for tissue engineering. The surface chemistry of these materials plays a major role since it governs protein adsorption, cell adhesion, viability, degradation, and biocompatibility in the first place. This study correlates the interaction of the most abundant serum proteins (albumin, immunoglobulins, fibrinogen) with the surface properties of PCL and its influence on the morphology and metabolic activity of primary human arterial endothelial cells that are seeded on the materials. Prior to that, thin films of PCL are manufactured by spin-coating and characterized in detail. A quartz crystal microbalance with dissipation (QCM-D), a multiparameter surface plasmon resonance spectroscopy instrument (MP-SPR), wettability data, and atomic force microscopy are combined to elucidate the pH-dependent protein adsorption on the PCL substrates. Primary endothelial cells are cultured on the protein modified polymer, and conclusions are drawn on the significant impact of type and form of proteins coatings on cell morphology and metabolic activity.

## 1. INTRODUCTION

The past decades have witnessed significant advances in regenerative medicine, tissue engineering, wound healing angiogenesis and vascular or orthopedic surgery.[1−7] Besides enormous contributions from cell biology and medicine, many of these advances were based on understanding and designing the physicochemical properties and biological efficacy or inertness of biomaterials. Investigating the chemical, physical and biological influence of cellular activity, scaffolds, implants, vascular grafts, sutures, or wound dressings was always crucial for successful applications or further improvements of their properties.[8,9] Most of the material parameters are governed by molecular interactions at the interface between the living biological system and the biomaterial.[10−13] An in-depth understanding of their surface chemistry is therefore a key for the discovery of new phenomena and the exploitation in the form of new products.[14] Due to their versatility and the ease of processing synthetic polymer-based biomaterials are one of the most important classes for the aforementioned applications.[15,16] There are many biodegradable polymers of which polycaprolactone (PCL) might be one of the most studied and used.[17,18]

In tissue engineering, PCL is commonly utilized in the form of porous foams or nanofibers/nanowires capable of providing a large surface area for various types of cells.[19,20] However, this porosity and irregular morphology often prohibits the use of modern surface analytical tools that would otherwise give detailed insights into surface phenomena such as protein adsorption or wetting. Nanometer thin, well-defined films of PCL that can be prepared by spin-coating are therefore an alternative object of interest for investigating and elucidating the basics of mentioned surface phenomena and their influence on the viability of cells.[21−23]

Even though attempts have aimed at the surface modification of PCL,[24−26] to our knowledge, no studies exist that correlate the adsorption of the serum proteins albumin, fibrinogen, and immunoglobulins with the viability and morphology of primary vascular cells (e.g., endothelial cells). However, slow or insufficient vascularization of tissue-engineered grafts is one

of the major limiting factors toward their clinical implementation. The endothelium is crucial for normal physiological conductance of blood in the vessels. The endothelial cell forms/covers the inner lumen of these vessels. With tight junction in-between, the endothelial cells form the adjustment cells to form a monolayer, which gives them an ability to function as a barrier against macromolecules. Apart from regulating the vascular tone of the pulmonary arteries, the endothelial cells from pulmonary arteries (PAECs) are unique as they in addition, also maintain the gas exchange in the lung. These cells are important for studying diseases, the response toward CO_2 and O_2 partial pressure, mechanical properties of cell layers, and the endothelization of biomaterial implants and, thus, for therapeutic angiogenesis. Many biodegradable polymer based substrates for the growth of these cells do not exist up to now and no details are known about the response of the cells toward surface modifications of PCL thin films with proteins. This study therefore aims at systematically investigating the preparation and modification of spin-coated PCL thin films using common serum proteins (immunoglobulins (IgG) as model antibodies, bovine serum albumin (BSA) as the most common protein in blood, and fibrinogen (FIB) as the core protein in the blood coagulation cascade) with state-of-the-art surface analytical tools (a quartz crystal microbalance with dissipation QCM-D, multiparameter surface plasmon resonance MP-SPR, and atomic force microscopy AFM). Subsequently the influence of the bound protein layers on the morphology and metabolic activity of human primary pulmonary arterial endothelial cells (PAECs) was assessed with fluorescence microscopy and spectrophotometry. Results from this study should extend the understanding and applicability of PCL for the biomaterial tissue engineering of endothelial cells or its use as implant material.

2. EXPERIMENTAL SECTION

2.1. Materials. Polycaprolactone (average molecular weight: M_n 80 kDa) and chloroform (≥99%) were purchased from Sigma-Aldrich, Austria. Three bovine proteins, namely, serum albumin (BSA, lyophilized powder, ≥96%), fibrinogen (FIB, Type I−S, 65−85% protein) and immunoglobulin G (IgG) were purchased from Sigma-Aldrich, Austria (Table 1). Sodium acetate (anhydrous), disodium

Table 1. Physicochemical Properties of the Bovine Serum Proteins Employed in This Study

protein	mol wt (kDa)	dimensions (nm)	IEP	reference
BSA	66.5	14 × 4 × 4 (heart-shaped)	4.8	27
IgG	150	14 × 10 × 4.5 (Y-shaped)	6.4−9	28
FIB	340	47 × 4.5 (trinodular)	5.5	29

phosphate heptahydrate ($Na_2HPO_4 \cdot 7H_2O$) and sodium dihydrogen phosphate monohydrate ($NaH_2PO_4 \cdot H_2O$) were acquired from Sigma-Aldrich Austria and used as received. Gold-coated QCM-D sensors (QSX301) were obtained from LOT-Oriel (Darmstadt, Germany). Milli-Q (18.2 MΩ cm) water from a Millipore water purification system (Billerica, U.S.A.) was used for contact angle measurements, MP-SPR and QCM-D investigations.

2.1.1. Polycaprolactone Thin Film Preparation. Film Preparation for QCM-D. Prior to spin coating of PCL films, the QCM-D sensors were soaked into a mixture of H_2O/H_2O_2 (30 wt %)/NH_4OH (25 wt %) (5:1:1; v/v/v) for 10 min at 70 °C, then immersed in a "piranha" solution containing H_2O_2 (30 wt %)/H_2SO_4 (98 wt %) (1:3; v/v) for 60 s (caution during mixing and use, piranha solution is highly corrosive) and then rinsed with Milli-Q-water and finally blow dried with N_2 gas. For spin coating of PCL, 80 μL of PCL solution (0.1, 0.2,

0.4, 0.6, 0.8, 1% (w/v), dissolved in chloroform) was deposited onto the static substrate, rotated for 60 s at a spinning speed of 4000 rpm and an acceleration of 2500 rpm s^{-1}.

Film Preparation for SPR. Prior to the experiments, the sensor slides are cleaned by immersion into piranha solution (T < 90°) over a period of 30 min followed by extensive rinsing in Milli-Q water followed by drying in a stream of nitrogen. The polycaprolactone films have been prepared by placing 180 μL of PCL (0.8% (w/v) in chloroform) on the slides followed by spin coating, as described in section 2.1.1

Film Preparation for Cell Growth. The PCL films for cell growth experiments were prepared on glass slides in the same way as in the QCM-D experiments. Glass slides with four chambers were used for PCL coating followed by protein adsorption. For PCL coating, the same spin coating procedure as mentioned above and 150 μL of PCL solution (0.8%, w/v) were used.

2.1.2. Preparation of Protein Samples. Protein (BSA or IgG or FIB) was dissolved (1 mg mL^{-1}) in a 10 mM buffer at pH 4 and 5 (sodium acetate/acetic acid buffer), pH 6, 7.4, and 8.2 (phosphate buffer). The pH of the buffer solution was adjusted using either glacial acetic acid (pH 4 and 5) or 0.1 M NaOH (pH 6, 7.4, and 8.2). The ionic strength of all three buffer solution was adjusted to 100 mM with NaCl electrolyte.

2.2. Profilometry. Layer thickness of the PCL coated films was determined by profilometry using a DEKTAK 150 Stylus Profiler from Veeco (Plainview, NY, U.S.A.). The scan length was set to 1000 μm over the time duration of 3 s. The diamond stylus had a radius of 12.5 μm and the force was 3 mg with a resolution of 0.333 μm/sample and a measurement range of 6.5 μm. The profile was set to hills and valleys. Prior to the surface scanning, the coating was scratched to remove the PCL films in order to determine the thickness of the coating using a step-height profile. The thickness was determined at 3 independent positions.

2.3. Quartz Crystal Microbalance with Dissipation (QCM-D). A QCM-D instrument (model E4) from Q-Sense, Gothenburg, Sweden was used. The instrument simultaneously measures changes in the resonance frequency (Δf) and energy dissipation (ΔD) when the mass of an oscillating piezoelectric crystal changes upon increase/decrease in the mass of the crystal surface due to the added/deduced mass. Dissipation refers to the frictional losses that lead to damping of the oscillation depending on the viscoelastic properties of the material. For a rigid adsorbed layer that is fully coupled to the oscillation of the crystal, Δf_n is given by the Sauerbrey equation[30] (1)

$$\Delta m = C \frac{\Delta f_n}{n} \tag{1}$$

where Δf_n is the observed frequency shift, C is the Sauerbrey constant (-0.177 mg Hz^{-1} m^{-2} for a 5 MHz crystal), n is the overtone number (n = 1, 3, 5, etc.), and Δm is the change in mass of the crystal due to the adsorbed layer. The mass of a soft (i.e., viscoelastic) film is not fully coupled to the oscillation and the Sauerbrey relation is not valid since energy is dissipated in the film during the oscillation. The damping (or dissipation; D) is defined as

$$D = \frac{E_{diss}}{2\pi E_{stor}} \tag{2}$$

where E_{diss} is the energy dissipated and E_{stor} is the total energy stored in the oscillator during one oscillation cycle. The condition for using the Sauerbrey equation is that the adsorbed film is rigid, homogeneous and evenly distributed on the sensors. Equation 3 was used to calculate the dry mass of the coated PCL film. For that purpose, the third overtone resonance frequency of the sensor before and after film deposition was measured for at least 10 min. Furthermore, it is possible to calculate the effective layer thickness (d_{eff}) using the Sauerbrey mass if the density of the coated layer is known (eq 3). A density value of 1145 kg m^{-3} was taken for the thickness calculation.[31] All calculations were carried out using the software package QTools 3.1.25.604 (Q-Sense).
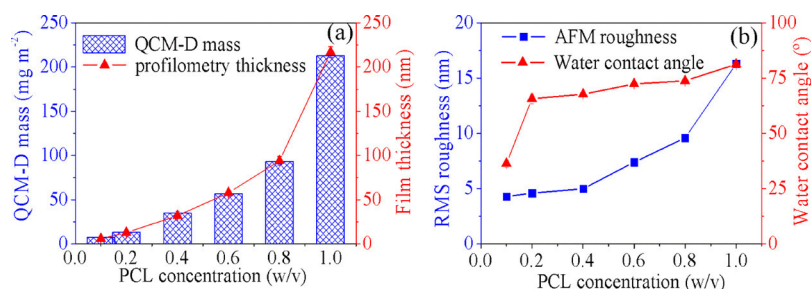
Figure 1. QCM-D mass, profilometry thickness, AFM RMS roughness (10 μm $\times$ 10 μm), and static water contact angle of PCL films prepared from different solution concentrations.

$$d_{\text{eff}} = \frac{\Delta m}{\rho_{\text{eff}}} \quad (3)$$

Adsorption of Protein on Polycaprolactone-Coated Surface. QCM-D crystals coated with polycaprolactone films (0.8%, w/v) were mounted in the QCM flow cell, and equilibrated with Milli-Q water and a buffer solution (either acetate buffer or phosphate buffer) until a stable change in frequency was established. After establishing a constant baseline with buffer, protein solutions were introduced into the QCM flow cell. The different protein (BSA or IgG or FIB) solutions were pumped through the QCM-D cell for 30 min followed by corresponding buffer solution for 30 min. The flow rate was kept at 0.1 mL min^{-1} throughout all experiments. The temperature was kept at 21 $\pm$ 0.1 °C for all experiments. All adsorption experiments have been performed in three parallel and a mean value and standard deviation of third overtone dissipation and frequency was calculated.

Viscoelastic Modeling. The viscoelastic Voigt model was applied for calculating the adsorbed mass (Γ_{QCM}), film thickness (h_f), viscosity (η_f), and elastic shear modulus (μ_f) of the protein layer. In this model, the adsorbed layer was treated as a viscoelastic layer between the quartz crystal and a semi-infinite Newtonian liquid layer. More details on the Voigt modeling can be found elsewhere.[32,33] For data evaluation or fitting the different overtones (n = 3, 5, 7, 9, and 11) of frequency and dissipation were used. All calculations were carried out using the software package QTools 3.1.25.604 (Q-Sense). The fitting parameters used the modeling are viscosity, from 1 $\times$ 10^{-4} to 0.01 N·s·m^{-2}; elastic shear modulus, from 1 $\times$ 10^4 to 1 $\times$ 10^8 N·m^{-2}; and thickness, from 1 $\times$ 10^{-10} to 1 $\times$ 10^{-6} m. It is important to note that the values of h_f and ρ_f were not independent variables. In order to calculate the effective thickness and adsorbed mass (eq 4), the density ρ_f values was varied between 1000 and 1190 kg m^{-3}. It turned out that no mass change for protein coated layer occurred by changing the density value and therefore the density (ρ_f) of 1130 kg m^{-3} was used for all calculation (eq 4).

$$\Gamma_{\text{QCM}} = h_f \rho_f \quad (4)$$

2.4. Multi-Parameter Surface Plasmon Resonance (MP-SPR). MP-SPR spectrsocopy was done on a SPR Navi 200 from Bionavis Ltd., Tampere; Finland using Au-coated glass slides as substrate (SPR102-AU) equipped with two different lasers (670 and 785 nm, respectively) in both measurement channels. All measurements are performed using a full angular scan (39–78°, scan speed: 8° s^{-1}). Before the protein adsorption, the films were equilibrated with Milli-Q water and with corresponding buffers (acetate or phosphate) in the same way as described in the QCM-D experiments. The adsorption of proteins (BSA, IgG, or FIB) was performed in acetate buffer (at pH 4 and 5) and in phosphate buffer (at pH 6, 7.4, and 8.2) at a protein concentration of 1 mg mL^{-1} under flow conditions (flow rate 0.1 mL min^{-1}). After 30 min of adsorption, the films were rinsed with corresponding buffers in order to remove loosely bound material. The adsorption of protein onto the PCL-coated surfaces was quantified according to eq 5, which considers the dependence of the angular response of the surface plasmon resonance in dependence of the refractive index increment (dn/dc) of the adsorbing layer.

$$\Gamma = \frac{\Delta\Theta \times k \times d_p}{\text{d}n/\text{d}c} \quad (5)$$

For thin layers (<100 nm), $k \times d_p$ can be considered constant and can be obtained by calibration of the instrument by determination of the decay wavelength l_d. For the SPR Navi 200 used in this study, $k \times d_p$ values are approximately 1.09 $\times$ 10^{-7} cm/° (at 670 nm) and 1.9 $\times$ 10^{-7} cm/° (at 785 nm) in aqueous systems. For BSA, IgG, and FIB, dn/dc in water-based buffer systems were reported as 0.187 cm^3 g^{-1} and were used to calculate the amount of adsorbed masses.[34] SPR signal, in contrast to QCM, is not affected by the amount of coupled water in the adsorbed layer. Therefore, the water content of the adsorbed layer can be calculated through a combination of both methods according to eq 6.

$$\%\text{water content} = 100\frac{(\text{mass}_{\text{QCM}} - \text{mass}_{\text{SPR}})}{\text{mass}_{\text{QCM}}} \quad (6)$$

2.5. Atomic Force Microscopy (AFM). AFM images of the films were recorded in tapping mode (noncontact mode) on a Veeco Multimode Quadrax MM AFM (Bruker; Billerica, MA, U.S.A.). For the scanning silicon cantilevers (NCH-VS1-W from NanoWorld AG, Neuchatel, Switzerland) were used with an average spring constant of 42 N/m (force constant) and with a resonance frequency of 270–320 kHz (coating: none). All measurements were performed at room temperature and under ambient atmosphere. The calculation of the root-mean-square roughness and the image processing was done using Gwyddion software package 2.40.

2.6. Cell Culture. After PCL coating, 1.5 mL of protein solution at corresponding pH value (pH 4–8.2) was dropped on each chamber and shaken for 30 min at 130 rpm at room temperature. After that, the protein solution was replaced with 1.5 mL of corresponding buffer solution (pH 4–8.2) and shaken for 60 min at 130 rpm at room temperature. For protein samples coated at pH 5, the protein-coated surfaces were additionally rinsed with pH 7.4 buffer solution for 60 s after rinsing with pH buffer solution. The glass chamber was then blow-dried with N$_2$ gas and used directly for cellular experiments.

Human pulmonary artery endothelial cells (hPAECs) were obtained from Lonza (Allendale, New Jersey) and were cultured according to the manufacturer's instructions. The endothelial specific media with growth factor supplements (EBM-2, Lonza) was changed every third day. A total of 80000 cells in passages 5–8 were used for the experiments. To measure the influence of strain on the metabolic activity of the primary hPAECs in the different surface coating, the nontoxic alamarBlue (Invitrogen) assay was used according to the manufacturer's instructions. The cell permeable compound resazurin is the active ingredient of the alamarBlue reagent, that is blue in color and virtually nonfluorescent and also nontoxic. Once entering cells, resazurin is reduced to resorufin, a compound that is red in color and highly fluorescent. Viable or metabolically active cells continuously convert resazurin to resorufin, increasing the fluorescence.[35] Briefly, the alamar blue was added to the cell culture medium in ratio of 1:10 (alamarBlue/cell culture medium). The mixture was allowed to incubate at 37 °C for 3–4 h on the cells. After the incubation, the cell along with the supernatant was measured by carefully removing from
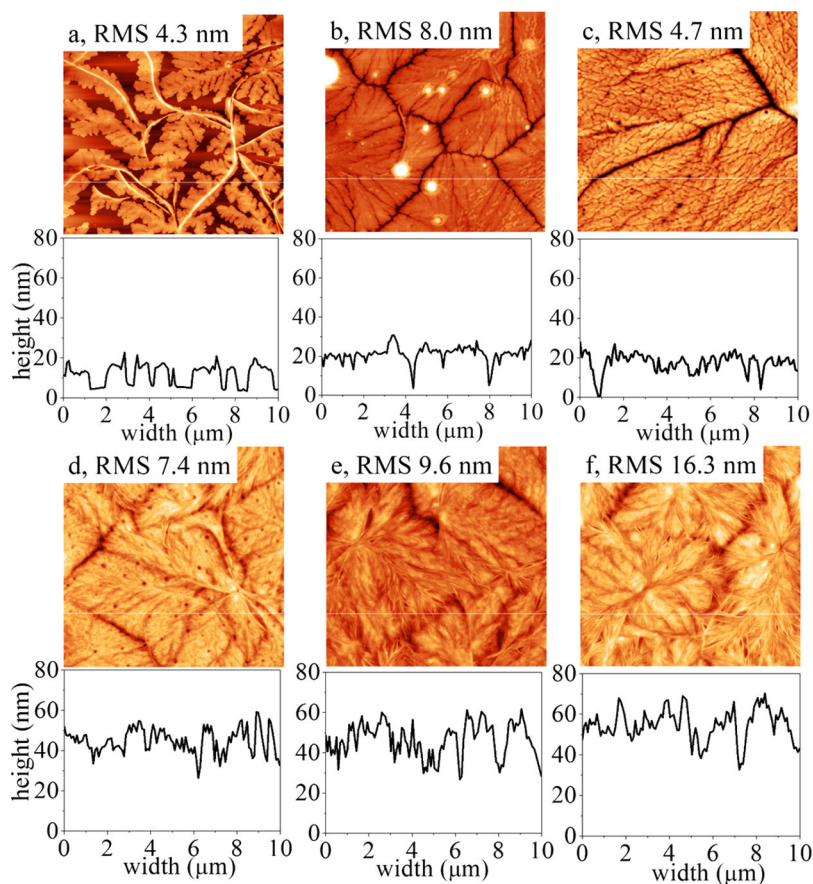
Figure 2. AFM images and surface profiles of PCL films spin-coated from different polymer concentrations (w/v): (a) 0.1, (b) 0.2, (c) 0.4, (d) 0.6, (e) 0.8, and (f) 1%. The RMS AFM roughness is given in each image. The z-scale is 80 nm.
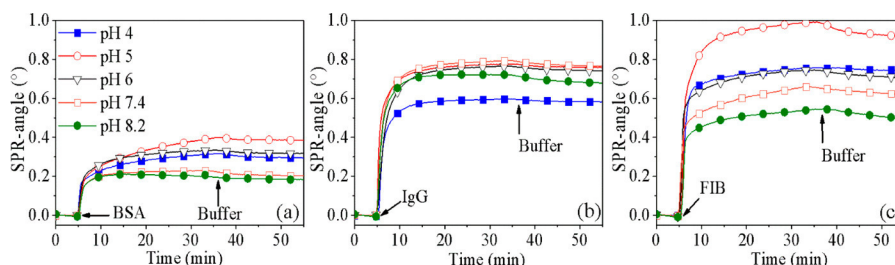
Figure 3. SPR measurements showing the response in resonance angle for the adsorption of proteins at different pH values: BSA (a), IgG (b), and FIB (c).

the chamber slide into black 96 (Nunc) well plates. The fluorescence intensity was measured in a plate reader at 570 nm excitation and 585 nm emissions. The fluorescent intensity directly corresponds to the metabolic activity of the cells. The assay was performed after cells were grown for 48 h on the respective surface treatment. All the experiments were performed in triplicates. Numerical values are given as means ± standard deviation for Figure 8. Statistical analysis was performed using GraphPad Prism 5 (Graph Pad Software Inc., U.S.A.). Group differences were assessed by a t test as appropriate. P-values < 0.05 were considered significant.

Endothelial Cell Morphology. For F-actin staining, the cells grown on the cover slide treated with respective surface treatment, were incubated with Alexa555 conjugated-phalloidin (Molecular Probes) for 20 min, and later washed with PBS and fixed with 4% formaldehyde for 30 min at 4 °C, and mounting was performed with antifading embedding medium (Vector Laboratories) with DAPI counterstaining to visualize the nucleus. Images were obtained in an Olympus inverted fluorescent microscope with olyVIA software (Olympus Gmbh Austria).

3. RESULTS AND DISCUSSION

3.1. Film Thickness, Mass, Wetting, and Morphology. Under the conditions given the preparation of PCL thin films by spin-coating is a very reproducible process as shown by the observed film properties Figure 1 and Supporting Information. Thickness, AFM RMS roughness, and water contact angle increase with increasing polymer concentration. An apparently higher static contact angle is found on rougher and thicker films. For the thinnest film, the higher wettability with water can be explained by a contribution of the substrate (SiO_2) to the contact angle, confirming a noncontinuous coating. This is also evidenced by the morphological appearance and roughness profiles of the films (Figure 2), with continuous coatings starting at a solution concentration of 0.4%. At 0.2%, PCL tends to crystallize in clearly separated branched structures, a behavior which is often found for polymer thin films.[36] For all
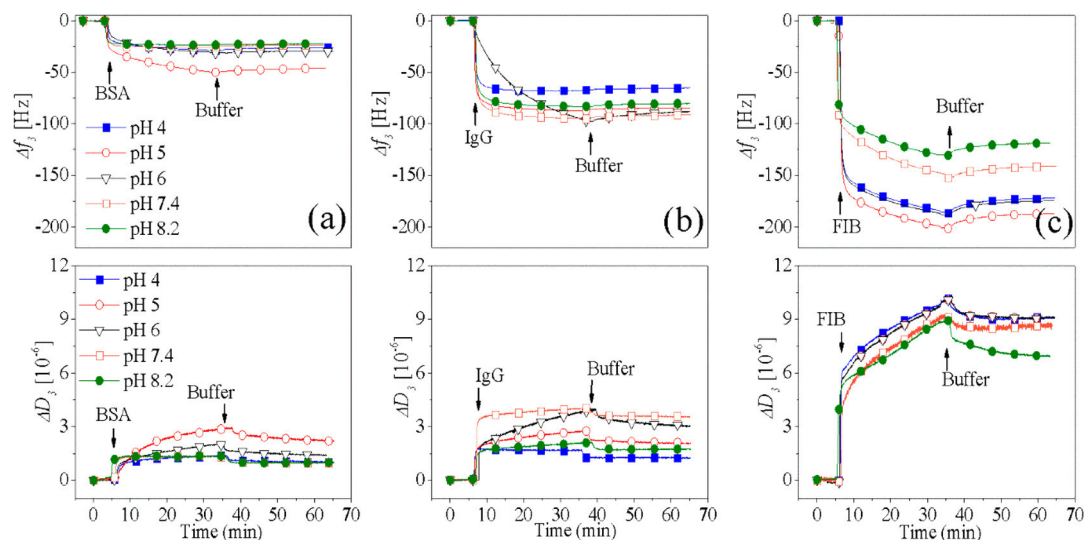
Figure 4. QCM-D frequency (top) and dissipation (bottom) change for the adsorption of proteins at different pH values on PCL: BSA (a), IgG (b), and FIB (c).
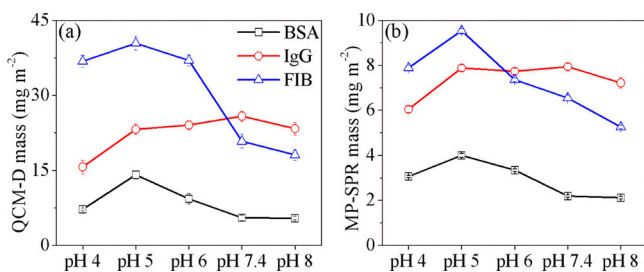
Figure 5. Irreversibly adsorbed mass of proteins (1 mg mL^{-1}) on PCL films at different pH values: (a) QCM-D; (b) MP-SPR.

films, this branched structure is still visible and becomes even more pronounced at higher concentrations, resulting in an increased surface roughness. Thickness values obtained mechanically from profilometry and gravimetrically from QCM-D (assuming constant film densities) correlate well, which demonstrates the reliability of both methods for the characterization of PCL thin films and the reproducibility with which the film preparation is performed. Roughness values are lower for the profilometry measurements, which can be attributed to the lower sensitivity of the profilometer and differences in the measured sizes (10 μm × 10 μm for AFM; 1 mm line profile for profilometry).

3.2. Protein Adsorption. *3.2.1. Amount of Adsorbed Proteins.* Films prepared from 0.8% PCL in chloroform where chosen for subsequent adsorption studies of three bovine serum proteins (1 mg mL^{-1}) at different pH values in buffer (MP-SPR Figure 3, QCM-D Figure 4, irreversibly bound amounts after rinsing Figure 5). This polymer concentration allows for the preparation of films that definitely cover the whole substrate, but are thin enough to warrant proper sensitivity of the QCM-D and MP-SPR during protein adsorption. For all three proteins adsorption kinetics is fast, and more than 90% saturation is observed under all conditions after 30 min, except for BSA at pH 5. Both QCM-D and MP-SPR data show very similar pH-dependent trends with QCM-D, giving generally higher values due to the amount of bound water in the adsorbed protein layer to which MP-SPR is less sensitive.[12] The adsorption maximum for all proteins is observed close to their isoelectric point (IEP$_{BSA}$: 4.8; IEP$_{IgG}$: 6.4−9; IEP$_{FIB}$: 5.5) where
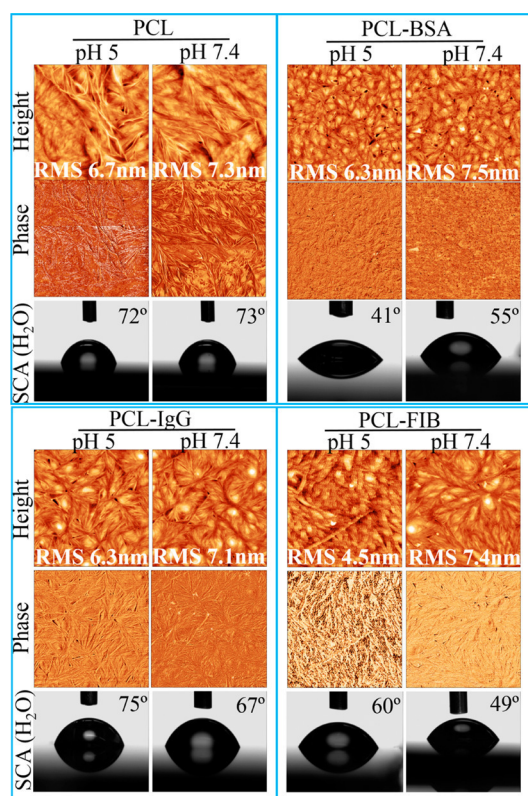
Figure 6. AFM height (top) and phase (bottom) images of proteins adsorbed at pH 5 and 7.4 on PCL. Image size is 5 × 5 μm^2; Z-scale for height image 100 nm and phase image 80°.

electrostatic repulsion and solubility are minimized and attractive forces between surface and protein are dominating. At pH 7.4 the adsorbed mass on PCL thin films follows the trends IgG > FIB > BSA with a FIB/BSA ratio of QCM: 2.57; SPR: 3.25. This ratio is considered by other authors as an indication of the hemocompatibility of a material due to the prevention of blood clot formation by reducing the amount of deposited fibrinogen and increasing the amount of bound albumin.[37] At a pH value of 5, the trend FIB ≫ IgG > BSA can be observed. IgG does not show a clear maximum of adsorption
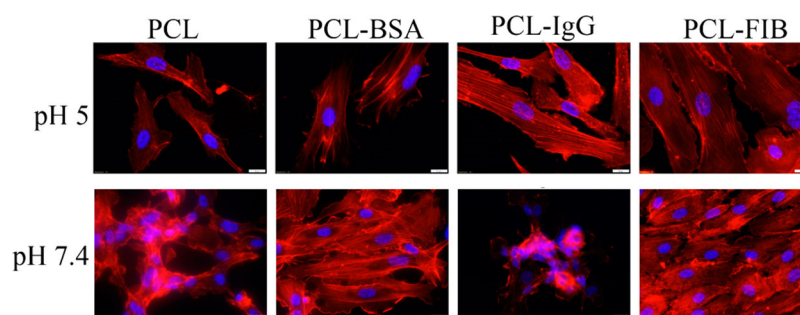
Figure 7. Fluorescence microscopy of human primary endothelial cells seeded on uncoated and coated PCL with BSA, FIB, and IgG at pH 5 and 7.4. The scale bar is 20 μm.
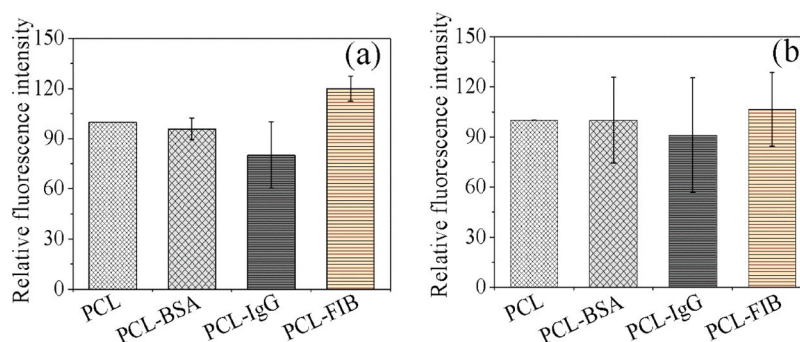
Figure 8. Metabolic activity of human primary arterial endothelial cells seeded on uncoated and protein-coated PCL at pH 5 (a) and 7.4 (b).

Table 2. Viscoelastic Properties of Proteins on PCL Films at Different pH Values[a]

protein	pH	thickness h_f (nm)	viscosity $n_f \times 10^{-3}$ (N s m^{-2})	elastic shear modulus $\mu_f \times 10^5$ (N m^{-2})	ΔD	coupled water (%)
BSA	4	7.2 ± 0.8	2.9 ± 0.02	6.3 ± 0.4	1.0	58
	5	**14.1 ± 0.4**	**2.4 ± 0.01**	**5.7 ± 0.9**	**2.3**	**72**
	6	9.3 ± 0.2	2.7 ± 0.01	6.0 ± 1.1	1.4	64
	7.4	5.5 ± 0.2	4.4 ± 0.01	8.6 ± 0.2	1.0	60
	8.4	5.4 ± 0.1	5.5 ± 0.03	19.6 ± 0.7	1.0	61
IgG	4	15.7 ± 0.3	13.1 ± 0.02	95.5 ± 0.1	1.2	61
	5	23.2 ± 0.3	13.0 ± 0.05	17.3 ± 0.3	2.1	66
	6	24.1 ± 1.2	6.1 ± 0.07	16.6 ± 1.4	3.0	68
	7.4	**25.8 ± 1.3**	**3.6 ± 0.08**	**12.1 ± 0.1**	**3.5**	**69**
	8.4	25.3 ± 1.1	4.9 ± 0.06	11.3 ± 0.2	1.8	69
Fib	4	36.8 ± 0.9	5.8 ± 0.05	19.1 ± 0.1	8	79
	5	**40.4 ± 0.7**	**1.5 ± 0.1**	**13.3 ± 0.8**	**8**	**76**
	6	37.2 ± 1.3	5.3 ± 0.3	17.2 ± 1.2	8	80
	7.4	20.8 ± 1.1	5.8 ± 0.03	220.2 ± 1.5	8	69
	8.4	18.1 ± 1.3	33.3 ± 0.04	258.8 ± 1.2	7	71

[a]Values in bold are at maximum adsorption.

in dependence of the pH which can be attributed to the high IEP value and, therefore, a permanent positive charge over the entire pH range investigated. In contrast, more FIB is bound at lower pH, where it reaches charge neutrality and subsequently lower solubility. Compared to the two other proteins, FIB is a relatively large molecule with a high aspect ratio, allowing for the adsorption in a flat extended conformation close to the IEP, presumably in the form of multilayers with many interaction sites. In addition, also protein denaturation may play a role for the increased adsorbed amounts.

3.2.2. Water Content of Adsorbed Layers. By comparing adsorbed masses from QCM-D and MP-SPR one can obtain the amount of water in the bound protein layers assuming that MP-SPR delivers solely the mass of protein optically whereas QCM-D gravimetrically measures bound water and adsorbed

protein (Table 2).[12] The amount of water in the irreversibly adsorbed layers follows the trend FIB > IgG > BSA at each pH value (except pH 5, where BSA contains more water than IgG), indicating a more swollen FIB and a more densely packed and thinner BSA coating, which also correlates with the size, molecular mass, and shape of the proteins. This is also reflected in the dissipation values found on the QCM-D showing higher ΔD values following the trend FIB > IgG > BSA in all cases except at pH 5. Owing to the measurement principle of QCM-D high ΔD values usually cause an underestimation of the amount of bound mass and thickness of the protein layer since more swollen layers couple less with the oscillator. Viscoelastic modeling was introduced which considers the ratio of ΔD versus Δf and allows for a calculation of the thickness (h_f (nm), Table 2) of the adsorbed protein layer. However, even with this

modeling, the same trend as for the mass is found for the thickness with FIB ≫ IgG > BSA at pH 5 and IgG > FIB > BSA at pH 7.4. Modeling gives also access to the viscosity n_f and the elastic shear modulus μ_f of the adsorbed layers. Both viscosity and shear modulus of the layers are the lowest at the maximum of adsorption where the water content is the highest. In this state, all proteins are bound to the surface but in a swollen, nonrigid conformation leading to low viscosity and low rigidity of the adsorbate water system. Interestingly, FIB forms a very rigid layer at physiological pH with a drastically higher elastic shear modulus than all other protein coatings. This can be attributed to the nature of FIB, which serves as the source of fibrin in the blood coagulation cascade.[38] Obviously already in this stage of adsorption the shape, size, and interaction within FIB and with PCL has a high impact on the mechanical and viscoelastic properties of these nanolayers. It can be summarized that fibrinogen and IgG cause a significantly thicker protein layer on PCL than BSA at both pH values. Fibrinogen shows in addition a more pH-dependent adsorption with the highest amounts deposited at pH 5. In most cases, FIB and IgG contain more water in the adsorbed state than BSA. More rigid FIB layers show large differences in the mechanical properties compared to IgG and BSA, especially at physiological pH value.

3.3. Morphology and Wetting after Protein Adsorption. *3.3.1. Morphology.* Since pH values of 7.4 and 5 showed the most significant differences in terms of adsorbed protein amounts, water content and nanomechanical properties, surfaces coated under these conditions were analyzed with respect to their wettability by contact angle studies and morphological appearance by atomic force microscopy. Figure 6 shows the AFM height and phase images of PCL films after protein coatings at both pH values in air. Especially phase images show differences in the form of the deposit depending on the protein with BSA, giving a more evenly distributed and denser coating. A slight reduction of the RMS roughness can be observed stemming from the smoothing effect of the adsorbed proteins. Significant differences in the morphology are especially visible for FIB adsorbed at pH 5, where the highest amounts of protein were deposited according to QCM-D and SPR. A coverage of the PCL base morphology is visible in this case.

3.3.2. Wetting with Water. All coated proteins, except IgG, significantly reduce the contact angle of PCL with BSA being, despite its lower adsorbed mass, the most effective. Static water contact angles follow the trend IgG > BSA > FIB for pH 7.4 and IgG > FIB ≫ BSA for pH 5.

Contact angle measurements with water conducted at pH 7 will cause either a negative (BSA, FIB) or a neutral/slightly positive (IgG) surface charge and, therefore, a more hydrophobic coating of IgG than of the other proteins. The amount and exposure of hydrophobic amino acid residues and the denaturation of IgG fragments during adsorption will also strongly contribute to this hydrophobicity.[39]

It is worth noting that contact angles were obtained on dried surfaces after coating. Hydrophilicity therefore not necessarily correlates with the water content of the adsorbed proteins determined by QCM-D and MP-SPR. Drying and subsequent reswelling will result in conformational changes and hysteresis effects. Denaturation in solution can be expected for all proteins at pH 5, which is far beyond the natural conditions in which they are found in the serum. Larger proteins adsorbed in higher amounts and a flat conformation (FIB pH 5, IgG pH 7.4) might

provide a more hydrophobic surface once they are dried, especially when adsorbed close to their IEP, where charge complexation between amines and carboxylic groups can occur efficiently due to a balanced charge ratio, leading to water insoluble hydrophobic coatings. Small spherical BSA might not expose solely hydrophobic domains to the air/water interface, leading to the more hydrophilic character. Overall protein-coated PCL surfaces provide a variety of physicochemical properties in terms of charge, wettability, and amino acid composition, whose influence on the attachment, morphology, and growth of human primary endothelial cells is discussed in the next section.

3.4. Cellular Activity. *3.4.1. Cellular Metabolic Activity and Morphology.* Human primary endothelial cells grow on protein coated and pristine PCL in a different morphology depending on the type of protein and coating conditions used. On PCL treated at a pH value of 7.4 (Figure 7, left) cells do not completely cover the surface, and close distances between nuclei confirm an agglomeration and lower amounts of F-actin (red) present. In contrast, BSA-coated surfaces (pH 7.4) show a larger average nuclei distance, the formation of more F-actin and the distribution of cells almost over the entire material. It might suggest that hydrophilicity (CA 55°) favors cell spreading compared to pure PCL (CA 74°). This homogeneous distribution is even more pronounced for FIB coated surfaces (CA 49°), where almost a complete coverage of a cell-monolayer is achieved and cells form an interconnected closed web with pronounced f-actin filaments. Owing to the low differences in contact angle between BSA and FIB coated PCL however this observation can not only be attributed to hydrophilicity alone. FIB evidently favors cell spreading and monolayer formation by providing a thicker and denser protein coating with a higher elastic shear modulus than BSA.

Most significantly, IgG surfaces coated at pH 7.4 cause a strong agglomeration of the cells, which might be attributed to the hydrophobicity of the surface (CA: 67°). IgG seems to prevent cells from actively distributing over the entire substrate by its neutral/positive charge and unfavorable interaction with the cell layer.

The above-discussed positive effects of hydrophilicity and FIB coatings are less pronounced for PCL coated at pH 5 (Figure 7). Even though trends are comparable, cells agglomerate less on PCL and IgG surfaces. PCL is also influenced by the treatment with sodium acetate/acetic acid buffer and adsorbed ions or partial surface hydrolysis of ester bonds might cause a negative charge, hydrophilicity, and better distribution of cells. BSA and FIB still show improved cell layer formation but less agglomeration was observed on IgG coating despite its higher hydrophobicity (CA 75°). It is assumed that denaturation in solution and during adsorption significantly changes the specific structure of the proteins and cell response is therefore less distinct on the different coatings when compared to pH 7.4. This is an indirect evidence of the importance of the shape, the conformation, and the charge of the proteins and the buffer conditions during adsorption and its influence on cell morphology.

Statistically significant differences with increased metabolic activity (*t*-test, uncoated PCL as reference, alamarBlue assay) were observed only for FIB coatings at pH 5. Under these conditions the thickest (40.4 ± 0.7 nm) but not most hydrophilic (water contact angle: 60°) coating of all proteins is formed, providing a biocompatible layer for the endothelial cells. Adsorbed fibrinogen could be denaturated to fibrin by

thrombin released by the cells leading to a more compatible layer. However, with the methods employed here denaturation was not determined and would require deeper insights by, for example, QCM-D studies during cell cultivation on the surface. Compared to FIB-coated surfaces IgG, BSA, and uncoated PCL appear to inhibit cells in their activity, presumably through a higher hydrophobicity, but most likely also specific interactions with the adsorbed protein structure. Even though cell morphology differs significantly between the protein coatings, metabolic activity is less influenced. It is worth mentioning that the alamarBlue assay used under the conditions given measures a sum parameter of the whole cell layer rather than the activity per single cell. It is therefore a reliable measure of the formation of a metabolically active cell layer on the surface. However, for a detailed elucidation of the reasons and mechanisms of cell/protein interactions and the increase in activity on pH 5 FIB coatings further detailed studies also including cultivation under flow conditions typical for vascular grafts are necessary and envisaged.

4. CONCLUSION

Thin films of polycaprolactone were prepared by spin-coating and characterized with respect to thickness, roughness, morphology, and water wettability. Stable nanolayers (95 nm) of the polymer with a low roughness profile (<8 nm) were obtained. A quartz crystal microbalance and surface plasmon resonance were used to determine in detail the adsorption of bovine serum albumin, immunoglobulin and fibrinogen on the polymer. For all proteins, adsorption is most pronounced close to the iso-electric point where solubility is lowest. Fibrinogen causes the thickest protein layers at low pH and shows differences in the nanomechanical properties with more rigid layers at pH 7.4. Immunoglobulin adsorption results in thicker and hydrophobic layers compared to thin hydrophilic albumin. Human primary arterial endothelial cells spread better and show higher metabolic activities on fibrinogen-coated surfaces than on all other proteins and pristine polycaprolactone. Immunoglobulin coatings significantly prevent even cell distribution and reduce metabolic activity due to the specific protein structure of the antibodies.

■ ASSOCIATED CONTENT

Ⓢ Supporting Information

The Supporting Information is available free of charge on the ACS Publications website at DOI: 10.1021/acs.biomac.6b01504.

> The properties of PCL thin films obtained from profilometry film thickness, QCM-D thickness, profilometry roughness, AFM roughness, water contact angle, and QCM-D mass is given in Table S1 (PDF).

■ AUTHOR INFORMATION

Corresponding Authors
*E-mail: tamilselvan.mohan@uni-graz.at. Tel.: +43 316 380 5413.
*E-mail: rupert.kargl@um.si. Tel.: +386 2220 7947.

ORCID Ⓘ
Rupert Kargl: 0000-0003-4327-7053

Notes
The authors declare no competing financial interest.

■ REFERENCES

(1) Wobma, H.; Vunjak-Novakovic, G. *Tissue Eng., Part B* **2016**, *22*, 101−113.
(2) Ficai, D.; Albu, M. G.; Sonmez, M.; Ficai, A.; Andronescu, E. In *Nanobiomaterials in Soft Tissue Engineering*; William Andrew Publishing, 2016; p 355.
(3) Langer, R.; Vacanti, J. *J. Pediatr. Surg.* **2016**, *51*, 8−12.
(4) Mercado-Pagán, Á. E.; Stahl, A. M.; Ramseier, M. L.; Behn, A. W.; Yang, Y. *Mater. Sci. Eng., C* **2016**, *64*, 61−73.
(5) Dewez, J. L.; Lhoest, J. B.; Detrait, E.; Berger, V.; Dupont-Gillain, C. C.; Vincent, L. M.; Schneider, Y. J.; Bertrand, P.; Rouxhet, P. G. *Biomaterials* **1998**, *19*, 1441−1445.
(6) Sun, M.; Deng, J.; Gao, C. *J. Colloid Interface Sci.* **2015**, *448*, 231−237.
(7) Hicks, B. G.; Lopez, E. A.; Eastman, R., Jr.; Simonovsky, F. I.; Ratner, B. D.; Wessells, H.; Voelzke, B. B.; Bassuk, J. A. *Biomaterials* **2011**, *32*, 797−807.
(8) O'Brien, F. J. *Mater. Today* **2011**, *14*, 88−95.
(9) Keane, T. J.; Badylak, S. F. *Semin. Pediatr. Surg.* **2014**, *23*, 112−118.
(10) Ismail, F. S. M.; Rohanizadeh, R.; Atwa, S.; Mason, R. S.; Ruys, A. J.; Martin, P. J.; Bendavid, A. *J. Mater. Sci.: Mater. Med.* **2007**, *18*, 705−714.
(11) Bhattacharyya, D.; Xu, H.; Deshmukh, R. R.; Timmons, R. B.; Nguyen, K. T. *J. Biomed. Mater. Res., Part A* **2010**, *94*, 640−648.
(12) Mohan, T.; Niegelhell, K.; Zarth, C. S. P.; Kargl, R.; Köstler, S.; Ribitsch, V.; Heinze, T.; Spirk, S.; Stana-Kleinschek, K. *Biomacromolecules* **2014**, *15*, 3931−3941.
(13) Kargl, R.; Vorraber, V.; Ribitsch, V.; Köstler, S.; Stana-Kleinschek, K.; Mohan, T. *Biosens. Bioelectron.* **2015**, *68*, 437−441.
(14) Li, D.; Zheng, Q.; Wang, Y.; Chen, H. *Polym. Chem.* **2014**, *5*, 14−24.
(15) Kohane, D. S.; Langer, R. *Pediatr. Res.* **2008**, *63*, 487−491.
(16) Khan, F.; Tanaka, M.; Ahmad, S. R. *J. Mater. Chem. B* **2015**, *3*, 8224−8249.
(17) Nyitray, C. E.; Chang, R.; Faleo, G.; Lance, K. D.; Bernards, D. A.; Tang, Q.; Desai, T. A. *ACS Nano* **2015**, *9*, 5675−5682.
(18) Woodruff, M. A.; Hutmacher, D. W. *Prog. Polym. Sci.* **2010**, *35*, 1217−1256.
(19) Leszczak, V.; Baskett, D. A.; Popat, K. C. *J. Biomed. Nanotechnol.* **2015**, *11*, 1080−1092.
(20) Ku, S. H.; Park, C. B. *Biomaterials* **2010**, *31*, 9431−9437.
(21) Pai, B. G.; Kulkarni, A. V.; Jain, S. *J. Biomed. Mater. Res., Part B* **2016**, n/a.
(22) Xu, L.; Yamamoto, A. *Colloids Surf., B* **2012**, *93*, 67−74.
(23) Rohman, G.; Pettit, J. J.; Isaure, F.; Cameron, N. R.; Southgate, J. *Biomaterials* **2007**, *28*, 2264−2274.
(24) Zhu, Y.; Gao, C.; Liu, X.; Shen, J. *Biomacromolecules* **2002**, *3*, 1312−1319.
(25) Yuan, S.; Xiong, G.; Wang, X.; Zhang, S.; Choong, C. *J. Mater. Chem.* **2012**, *22*, 13039−13049.
(26) de Luca, A. C.; Terenghi, G.; Downes, S. *J. Tissue Eng. Regener. Med.* **2014**, *8*, 153−163.
(27) Larsericsdotter, H.; Oscarsson, S.; Buijs, J. *J. Colloid Interface Sci.* **2005**, *289*, 26−35.
(28) Grabbe, E. S. *Langmuir* **1993**, *9*, 1574−1581.
(29) Hall, C. E.; Slayter, H. S. *J. Biophys. Biochem. Cytol.* **1959**, *5*, 11−27.
(30) Sauerbrey, G. *Eur. Phys. J. A* **1959**, *155*, 206−222.
(31) Gross, R. A.; Kalra, B. *Science* **2002**, *297*, 803−807.
(32) Höök, F.; Kasemo, B.; Nylander, T.; Fant, C.; Sott, K.; Elwing, H. *Anal. Chem.* **2001**, *73*, 5796−5804.
(33) Voinova, M. V.; Rodahl, M.; Jonson, M.; Kasemo, B. *Phys. Scr.* **1999**, *59*, 391.
(34) Zhao, H.; Brown; Patrick, H.; Schuck, P. *Biophys. J.* **2011**, *100*, 2309−2317.
(35) Schreer, A.; Tinson, C.; Sherry, J. P.; Schirmer, K. *Anal. Biochem.* **2005**, *344*, 76−85.

(36) Reiter, G.; Castelein, G.; Sommer, J.-U. In *Polymer Crystallization: Observations, Concepts and Interpretations*; Reiter, G.; Sommer, J.-U., Eds.; Springer: Berlin, Heidelberg, 2003; p 131.

(37) Sapmaz, I.; Saba, T.; Haberal, C.; Toktamis, A.; Cakmak, M.; Cicek, D. *Int. Cardiovasc Res. J.* **2011**, *5*, 153−154.

(38) Doliška, A.; Strnad, S.; Stana, J.; Martinelli, E.; Ribitsch, V.; Stana-Kleinschek, K. *J. Biomater. Sci., Polym. Ed.* **2012**, *23*, 697−714.

(39) Vermeer, A. W. P.; Giacomelli, C. E.; Norde, W. *Biochim. Biophys. Acta, Gen. Subj.* **2001**, *1526*, 61−69.

Supporting Information #4

Interaction of Tissue Engineering Substrates with Serum Proteins and

Its Influence on Human Primary Endothelial Cells

Table S1 shows the detailed surface property data of spin coated polycaprolactone thin films from different polymer concentrations

Table S1: Thickness, surface roughness, wettability and QCM-D mass of PCL thin films

PCL (%, w/v)	Profilometry Film thickness (nm)	QCM-D thickness (nm)	Profilometry surface roughness (nm)	AFM surface roughness (nm)	Water contact angle (deg)	QCM-D mass (mg m^{-2})
0.1	6 ± 1	7.9 ± 1	1 ± 0.1	4.3	36.4 ± 1.7	7.8 ± 0.6
0.2	13 ± 1	13 ± 2	2 ± 0.3	4.6	65.7 ± 2.3	13.1 ± 1.2
0.4	32 ± 2	35 ± 1	3.9 ± 0.7	5.2	67.7 ± 0.3	35.2 ± 2
0.6	58 ± 3	56 ± 2	5.5 ± 0.1	7.4	72.4 ± 0.1	56.7 ± 2
0.8	94 ± 5	93 ± 2	7.6 ± 0.2	9.6	73.8 ± 0.1	93.2 ± 3
1	217 ± 6	215 ± 0.6	16 ± 2	16.3	81.3 ± 0.3	213 ± 2

PAPER #5

Adsorption Behavior of Lectins – A MP-SPR Study

Working Version

For this paper, I conducted the contact angle, ATR-IR spectroscopy and MP-SPR spectroscopy measurements, interpreted the data and wrote a significant part of the manuscript.

Adsorption Behavior of Lectins – A MP-SPR Study

Katrin Niegelhell[†], Thomas Ganner[‡], Claudia Payerl[*], Harald Plank[‡], Evelyn Jantscher-Krenn[§] and Stefan Spirk[†]

[†]Graz University of Technology, Institute for Paper-, Pulp- and Fiber Technology, Inffeldgasse 23, 8010 Graz, Austria.

[‡]Graz University of Technology, Institute for Electron Microscopy and Nanoanalysis, Steyrergasse 17, 8010 Graz, Austria.

[*]Graz University of Technology, Institute for Chemistry and Technology of Materials, Stremayrgasse 9, 8010 Graz, Austria.

[§]Medical University of Graz, Department for Obstetrics and Gynecology, Auenbruggerplatz 14, 8036 Graz, Austria.

Corresponding Author

*E-mail: stefan.spirk@tugraz.at, Phone: +43-316-873-32284

1

ABSTRACT

Lectins are sugar binding proteins that play an important role in, for instance, the control over pathogens or the development of anti-cancer drugs. The interaction of two specific lectins, namely *Concanavalin A* and *Ulex Europaeus Agglutinin-I*, with substrates of various kinds was investigated by means of multi-parameter surface plasmon resonance spectroscopy. All of the experiments were performed with *Bovine Serum Albumin*, a widely use marker for non-specific protein adsorption, too. In order to test the preferred type of interaction during adsorption, hydrophobic and hydrophilic as well as positively and negatively charged materials such as polystyrene, cellulose, *N,-N,-N*-trimethyl chitosan chloride and gold were chosen and characterized in terms of wettability, surface free energy, zeta potential and morphology. Atomic force microscopy images of surfaces after protein adsorption correlated very well with the observed mass of adsorbed protein. Surface plasmon resonance studies reveal low adsorbed amounts and slow kinetics for all of the investigated proteins for hydrophilic surfaces, making those resistant to non-specific interactions substrates favorable supports for biosensors, since the use of blocking agents is not necessary.

INTRODUCTION

Lectins are carbohydrate binding proteins featuring at least one non-catalytic domain that binds reversibly to specific mono- or oligosaccharides.[1] These sugar binding proteins are classified in terms of structure, source; (1) plants, (2) mushrooms, (3) animals, or carbohydrate specificity; (1) glucose/mannose binding lectins, (2) galactose binding lectins, (3) lectins with affinity to sialic acid and (4) lectins, which recognise fucose.[2,3] Lectins display a great variety of properties, such as anti-insect, anti-tumor, immunomodulatory, antimicrobial or HIV-I reverse transcriptase inhibitor activities.[4] This astonishing class of proteins is subject in biomedical sciences and therapeutic industry e.g. for development of anti-tumor and anti-viral drugs. Many human pathogens use glycans present on the cell surface of the host to initiate adhesion and infection. *Escherichia coli*, for instance, binds to mannosides and the *Influenza* virus attaches via sialic acid residues on the host's cell surface. Lectins are able to interfere the interaction between bacteria, fungi or viruses and the host's cell surface and therefore enable the control over pathogens.[2,5]

The carbohydrate binding affinity of lectins is exploited for the detection of glycans or glycan containing molecules as well. Lectin microarrays are applied to separate, isolate and identify mono-, oligo- or polysaccharides, glycoproteins and glycolipids. Additionally, lectins are employed in biosensors to analyze lectin-carbohydrate interactions, such as specificity, affinity and kinetics.[3] When it comes to biosensors, protein adsorption is a very critical factor, since non-specific interactions of the protein with the substrate influence sensitivity and selectivity. Therefore blocking agents are employed to minimize those factors.[6]

Many parameters are affecting the adsorption behavior of proteins, among others the nature of the substrates, such as hydrophilicity or hydrophobicity and surface morphology. Therefore fundamental adsorption studies assist to predict the behavior of proteins in the environment of a

certain substrate e.g. used in a biosensor. Despite the countless number of lectin applications, there are only a few studies concerning non-specific adsorption of lectins found in literature. For instance, Amim et al. investigated the effect of the use of amino-terminated substrates for cellulose ester films and the concomitant change of surface free energy on the lectin-carbohydrate interaction.[7] Whereas, Zemla et al. determined the preferred adsorption of lectins on parts of phase separated polymer thin films.[8]

In this study, we chose to examine the adsorption behavior of two lectins, namely *Ulex Europaeus Agglutinin-I* (UEA-I), a fucose binding lectin which is extracted from common gorse[9], and *Concanavalin A* (Con A), a lectin with mannose and glucose specificity extracted from jack bean[10]. Their adsorption behavior was compared with *Bovine Serum Albumin* (BSA), which is a widely used marker for non-specific protein interaction. The interaction capacity of the proteins with substrates of various kinds, such as hydrophilic, hydrophobic and charged (positively and negatively), was tested in real time by means of multi-parameter surface plasmon resonance spectroscopy (MP-SPR) in order to determine not only the adsorbed amount but also the adsorption kinetics. The herein presented results give insight into the type of interaction that governs the adsorption behavior of these specific proteins.

MATERIALS AND METHODS

Materials. Trimethylsilyl cellulose (TMSC, Avicel, M_w = 185,000 g·mol^{-1}, M_n = 30,400 g·mol^{-1}, PDI = 6.1 determined by GPC in chloroform) with a DS$_{Si}$ value of 2.8 was purchased from TITK (Rudolstadt, Germany). Chloroform (99.3%), Toluene (99.9%), disodium phosphate heptahydrate (Na$_2$HPO$_4$· 7H$_2$O), sodium dihydrogen phosphate monohydrate (NaH$_2$PO$_4$·H$_2$O), hydrochloric acid (37%), sodium chloride (Ph.Eur.), sodium hydroxide (99%), polystyrene (PS, M_w = 35,000

g·mol^{-1}), *Bovine Serum Albumin* (lyophilized powder, ≥96%, 66.5 kDa), *Ulex Europaeus Agglutinin* (lyophilized powder ≥80%, 63 kDa) and *Concanavalin A* (Type IV, lyophilized powder, 110 kDa) were purchased from Sigma Aldrich and used as received. *N,N,N*-trimethyl chitosan chloride (TMC, M_w = 90 kDa, medical grade, $D_{Acetylation}$: 32%, $DS_{Me3+Cl-}$: 66%) was purchased from Kitozyme, Belgium. Silicon wafers were cut into 1.5 × 1.5 cm^2. SPR gold sensor slides (CEN102AU) were purchased from Cenibra, Germany. Milli-Q water (resistivity = 18.2 Ω^{-1}·cm^{-1}) from a Millipore water purification system (Millipore, USA) was used for contact angle and zeta-potential measurements and SPR investigations.

Substrate Cleaning and Film Preparation. Prior to spin coating, SPR gold sensor slides/silicon wafers were immersed in a "piranha" solution containing H_2O_2 (30 wt.%)/H_2SO_4 (1:3 v/v) for 10 min. Then substrates were extensively rinsed with Milli-Q water and blow dried with N_2 gas. TMSC was dissolved in chloroform by stirring over night at room temperature and filtered through 0.45 μm PVDF filters. 120 μl of TMSC (1 wt.%) solution were deposited onto the substrate and then rotated for 60 s at a spinning speed of 4000 rpm and an acceleration of 2500 rpm·s^{-1}. For converting TMSC into pure cellulose, the sensors/wafers were placed in a polystyrene petri-dish (5 cm in diameter) containing 3 ml of 10 wt.% hydrochloric acid (HCl). The dish was covered with its cap and the films were exposed to the vapors of HCl for 15 min. The regeneration of TMSC to cellulose was verified by ATR-IR (Figure S1) and water contact angle (Figure S2) measurements as reported elsewhere.[11–13] PS was dissolved in toluene by stirring over night at room temperature and filtered through 0.45 μm PVDF filters afterwards. 120 μl of PS (1 wt.%) solution were deposited onto the substrate and then rotated for 30 s at a spinning speed of 3000 rpm and an acceleration of 4500 rpm·s^{-1}. TMC films were prepared by adsorption of TMC (1 mg·ml^{-1} dissolved in water, ionic strength was adjusted to 150 mM NaCl and pH value was

adjusted to pH 7) onto cellulose substrates at a flow rate of 50 µl·min^{-1} for 5 min. TMC adsorption was monitored by MP-SPR.

Infrared Spectroscopy. IR spectra were attained by an Alpha FT-IR spectrometer (Bruker, Billerica, MA, USA) using an attenuated total reflection (ATR) attachment. Spectra were obtained in a scan range between 4000 to 400 cm^{-1} with 48 scans and a resolution of 4 cm^{-1}. The data was analyzed with OPUS 4.0 software.

Profilometry. Film thicknesses were acquired with a DETAK 150 Stylus Profiler from Veeco. The scan length was set to 1000 µm over a duration of 3 seconds. Measurements were performed with a force of 3 mg, a resolution of 0.333 µm per sample and a measurement range of 6.5 µm. A diamond stylus with a radius of 12.5 µm was used. Samples were measured after scratching the film (deposited on a silicon wafer). The resulting profile was used to calculate the thickness of different films. All measurements were performed three times.

Contact Angle (CA) and Surface Free Energy (SFE) Determination. Static contact angle measurements were performed with a Drop Shape Analysis System DSA100 (Krüss GmbH, Hamburg, Germany) with a T1E CCD video camera (25 fps) and the DSA1 v 1.90 software. Measurements were done with Milli-Q water and di-iodomethane using a droplet size of 3 µl and a dispense rate of 400 µl·min^{-1}. All measurements were performed at least 3 times. CA were calculated with the Young-Laplace equation and SFE was determined with the Owen-Wendt-Rabel-Kaelble (OWRK) method.[14–16]

Atomic Force Microscopy – AFM. Surface morphology and roughness of the films were obtained in tapping mode in ambient atmosphere at room temperature by a Veeco Multimode Quadrax MM scanning probe microscope (Bruker; Billerica, MA, USA) using Si-cantilevers (NCH-VS1-W from NanoWorld AG, Neuchatel, Switzerland) with a resonance frequency of 320

kHz and a force constant of 42 N·m⁻¹. Root mean square (RMS) roughness calculation and image

processing was performed with the Nanoscope software (V7.30r1sr3, Veeco).

Zeta Potential Measurements. The zeta potential measurements were performed by using a

commercial electrokinetic analyzer (SurPASS^{TM}3, Anton Paar GmbH, Graz, Austria). For each

sample, two zeta potential/pH value functions have been measured in 0.001 M KCl solution. For

statistical reasons, four streaming potentials were measured at each pH value. The mean value of

these data was used to calculate the potential/pH function.

Multi Parameter Surface Plasmon Resonance Spectroscopy – MP-SPR. MP-SPR

spectroscopy was accomplished with a SPR Navi 200 from Bionavis Ltd., Tampere, Finland,

equipped with two different lasers (670 and 785 nm, respectively) in both measurement channels,

using gold coated glass slides as substrate (gold layer 50 nm, chromium adhesion layer 10 nm).

All measurements were performed using a full angular scan (39–78°, scan speed: $8°·s^{-1}$).

Gold sensor slides coated with the investigated thin films were mounted in the SPR, equilibrated

with water and then with 10 mM PBS with an ionic strength of 100 mM NaCl at pH 5.5/7.4 (The

pH value of the buffers was adjusted with 0.1 M hydrochloric acid or 0.1 M NaOH.). After

equilibration, protein at a concentration of 0.1 mg·ml⁻¹ (dissolved in the same buffer used for

equilibration) is introduced into the flow cell. The protein is pumped through the cell with a flow

rate of 50 µl·min⁻¹ over a period of 5 min. After rinsing with buffer, the shift of SPR angle was

determined and used to evaluate the amount of adsorbed protein. After protein adsorption all

samples were rinsed with Milli-Q water and dried in a stream of N_2 gas. All experiments have been

performed in three parallels.

Protein adsorption was quantified according to equation 1, which considers the dependence of the angular response of the surface plasmon resonance in dependence of the refractive index increment (*dn/dc*) of the adsorbing layer.[17]

$$\Gamma = \frac{\Delta\Theta \times k \times d_p}{dn/dc} \qquad (1)$$

For thin layers (<100 nm), $k \times d_p$ can be considered constant and can be obtained by calibration of the instrument by determination of the decay wavelength l_d. For the SPR Navi 200 used in this study, $k \times d_p$ values are approximately 1.09×10^{-7} cm/° (at 670 nm) and 1.9×10^{-7} cm/° (at 785 nm) in aqueous systems. For proteins, *dn/dc* in water-based buffer systems was reported 0.187 cm³·g⁻¹, which was used to calculate the amount of adsorbed masses.[18] For TMC the *dn/dc* value of chitosan (0.192 cm³·g⁻¹)[19] was used for the calculation of adsorbed mass.

RESULTS AND DISCUSSION

In order to provide a variety of interaction possibilities for the proteins, hydrophobic polystyrene (PS), gold and hydrophilic substrates such as negatively charged cellulose and positively charged *N,-N,-N*-trimethyl chitosan (TMC) were chosen as substrates for this adsorption study. Prior to adsorption experiments, all substrates were characterized in terms of film thickness, surface free energy and morphology. As gold substrates, cleaned SPR sensor slides consisting of 50 nm gold deposited on a glass substrate with an adhesion layer of chromium in between (as reported from manufacturer), were used. Cellulosic substrates were prepared from spin coating trimethylsilyl cellulose (TMSC) and subsequent regeneration to cellulose by treatment with HCl vapors, which yielded in films with a thickness of 30 ± 2 nm as determined by stylus profilometry measurements. Polystyrene films were spin coated as well, leading to film thicknesses of 58 ± 1 nm. The thickness of the positively charged TMC substrate could not be determined since the substrate was prepared

by adsorption of TMC onto cellulose resulting in thicknesses that were too low for detection with stylus profilometry. The different substrates were then subjected to atomic force microscopy (Figure 1). The high RMS roughness (R_q = 4.3 nm) of the gold substrate is certainly caused by the cleaning procedure with piranha, a very harsh treatment that removes all of the adventitious carbon which was adsorbed from the atmosphere. The cellulosic and TMC substrate display similar RMS roughness (R_q = ca. 2 nm) originating from the fact that TMC was adsorbed onto the cellulose thin films, while PS shows the lowest RMS roughness (R_q = 0.6 nm). All of the substrates are very homogenous and free of any visible contamination.

3x3 μm
50/50/10/25 nm

| Rq = 2.1 nm | Rq = 2.5 nm | Rq = 4.3 nm | Rq = 0.6 nm |
| cellulose | TMC | Au | PS |
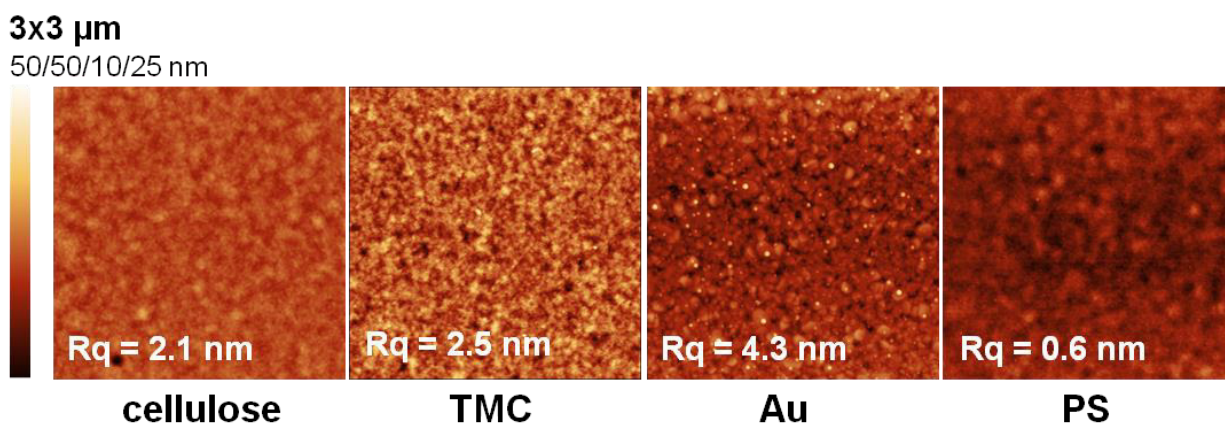
Figure 1. Atomic force microscopy height images of the different substrates and corresponding RMS roughness (R_q).

As mentioned above, the positively charged substrate was prepared by adsorption of TMC onto cellulose thin films. Modification of cellulose substrates with TMC as an approach to control protein adsorption behavior was already reported by coworkers.[20,21] The appropriate adsorption conditions for preparation of the cationic TMC substrates were adopted from these studies. In this work, TMC adsorption was monitored by multi-parameter surface plasmon resonance spectroscopy (MP-SPR) and zeta potential measurements (Figure 2.). First, we observed a steady

equilibration (rinsing with buffer) signal with MP-SPR, associated with a negative zeta potential (ca. -27 mV) for the pure cellulose film. Upon injection of TMC solution, the SPR-angle increased and the zeta potential changed to positive values. Loosely bound material was clearly removed upon rinsing. However, the zeta potential of the adsorbed TMC layer shifted when rinsed with buffer to higher values (from 35 mV to 38 mV) which might be due to a change in conformation of the adsorbed layer. After adsorption, the MP-SPR sensogram showed a change of SPR-angle of 0.05° which corresponds to an adsorbed amount of 0.6 ± 0.05 mg·m^{-2}. This result could not be compared to the findings from Mohan et al.[20] since only the frequency shift upon adsorption was determined by quartz crystal microbalance and no calculation of adsorbed amounts were done. However, in comparison to the adsorbed mass of cationic starch (1.2 mg·m^{-2}), with similar charge density as the herein used TMC, on cellulosic substrates[22], which were prepared in the same fashion as we did, TMC adsorbs to a lesser extent.
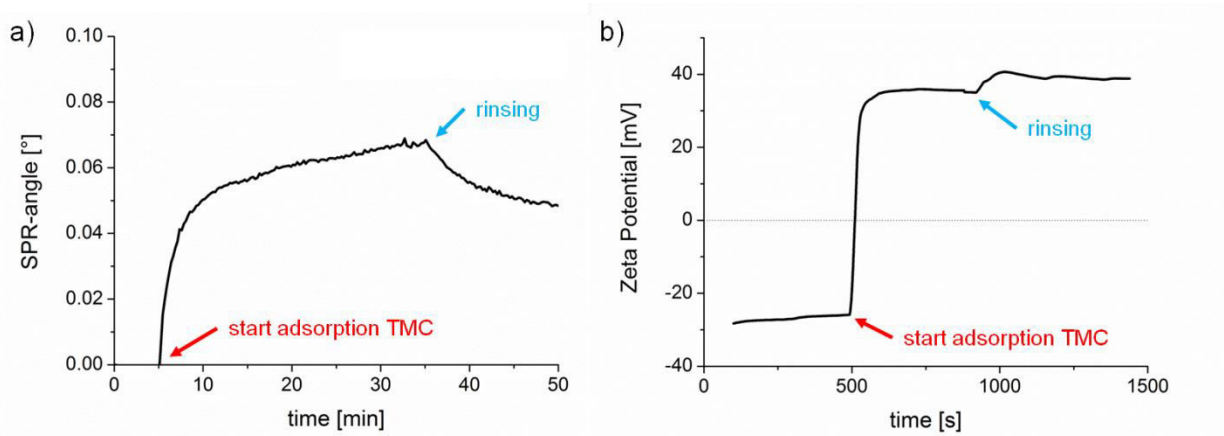
Figure 2. MP-SPR sensogram measured at 785 nm during adsorption of TMC onto a cellulose thin film (a) and the corresponding zeta potential curve (b).

Compared to the other substrates used in this study, TMC is the only one featuring a positive zeta potential. According to literature, gold displays a negative zeta potential above pH 5[23], as well as PS showing negative surface charge of -20 to -30 mV around pH 7.[24] The negative zeta potential

for the cellulose thin films used in this study is supported by values reported in literature (-13 mV to -17 mV at pH 4.7-7.2).[20]
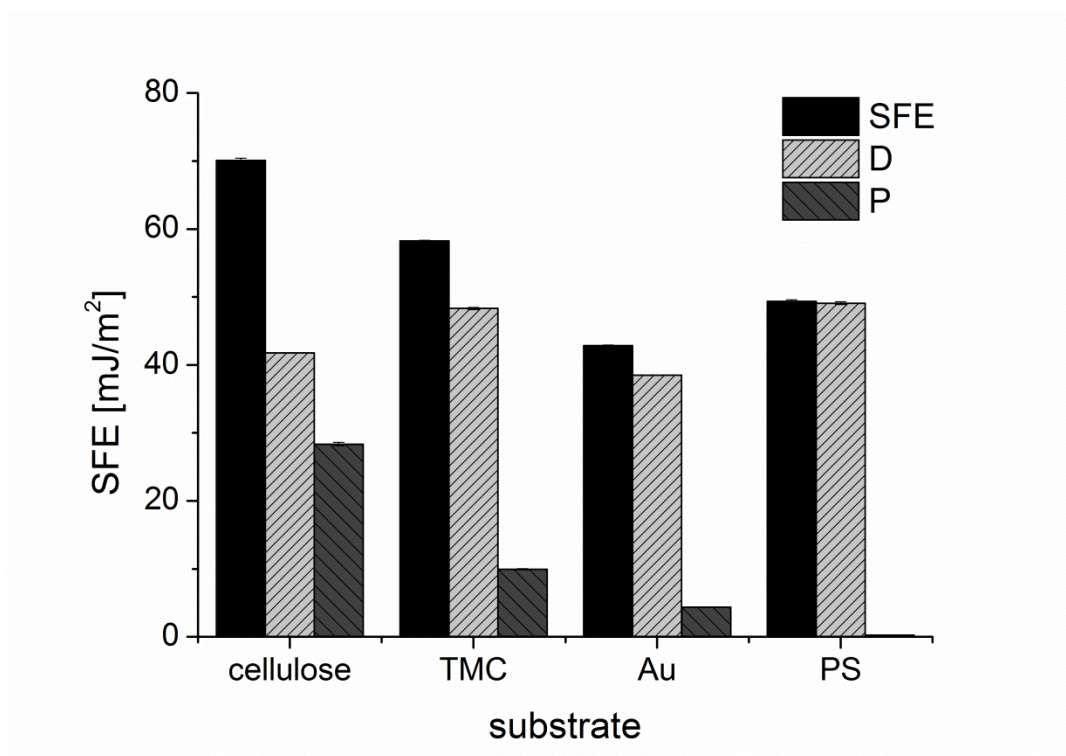
Figure 3. Surface free energies (SFE) and disperse (D) and polar (P) contributions to the SFE of different substrates used in the adsorption study.

The surface free energies (SFE) of the substrates were calculated from static contact angle measurements (Figure S3) and are presented in Figure 3. Cellulose and TMC surfaces both display a hydrophilic character. Although TMC displays a higher zeta potential than cellulose, cellulose shows higher SFE and larger polar contributions than TMC, which could be attributed to different conformation of the adsorbed polymer in the dry state during contact angle measurements compared to the wet state in the zeta potential determination. PS exhibits, as expected, a hydrophobic surface without any significant polar contribution to the SFE. The lowest SFE of the investigated substrates is presented by the gold substrate. It is important to note, that the gold

substrates were immediately used after the cleaning procedure for the adsorption experiments and for the other characterization tests too. Thereby it is guaranteed that the determined SFE is representative for all the samples in this work.
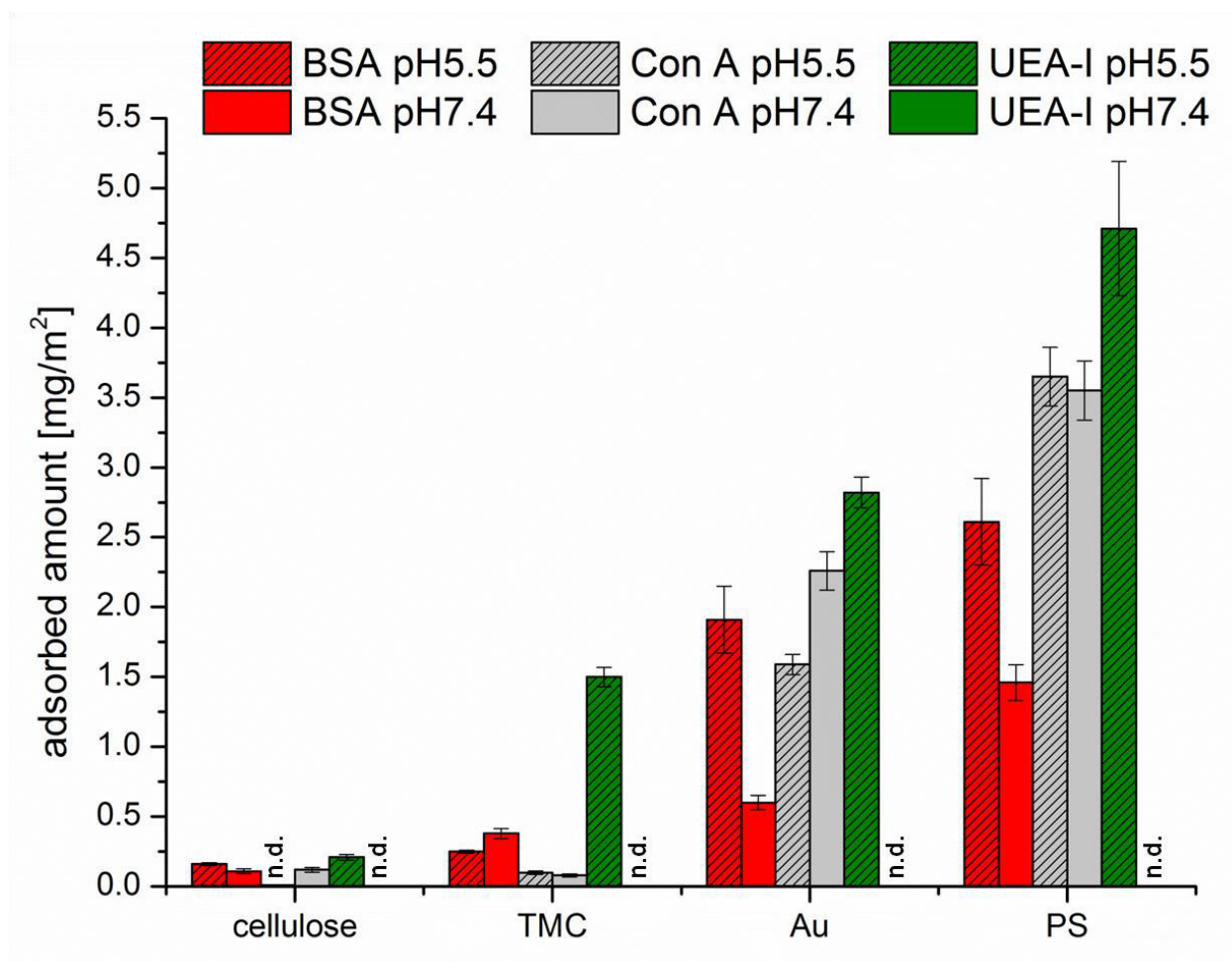
Figure 4. Adsorbed amount of protein calculated from change in SPR-angle for different substrates at two pH values.

After proper characterization of the substrates, the adsorption behavior of the different proteins was monitored by MP-SPR and the adsorbed amounts were calculated by the change in SPR-angle (Figure 4). All of the examined proteins did adsorb to the least extent on the cellulose surface and to the highest on PS. This can be attributed to the apolar nature of the PS substrate leading to hydrophobic interactions between protein and substrate. There is less electrostatic repulsion

between surface and protein in the case of PS than for cellulose, still the hydrophobic attraction overrules the electrostatic attractions as seen by comparison of PS and TMC. At the investigated pH values, all of the proteins are negatively charged, because the pH values are above the isoelectric points (IEP_{BSA} = pH 4.7[25], $IEP_{Con\,A}$ = pH 4.5-5.5[26], IEP_{UEA-I} = pH 4.8). Enhanced protein adsorption was found when adsorbing onto TMC modified cellulose compared to pure cellulose, since TMC is positively charged and more electrostatic attraction occurs, whereas in the case of negatively cellulose proteins are rather compelled at the investigated pH values.[27]

In general, the highest extent of protein adsorption is reached at the pH value near the isoelectric point, where the proteins are not charged. The balance of positive and negative charges leads to reduced solubility at pH 5.5 for all three proteins investigated, whereas at pH 7.4 the proteins are negatively charged which increases solubility and causes smaller adsorbed amounts. This effect is highly pronounced for BSA on all the examined surfaces, except for the TMC substrate. Since TMC is positively charged, it prefers the interaction with the negatively charged BSA at pH 7.4 rather than the more or less neutral BSA at pH 5.5. As for Con A, adsorption onto hydrophilic substrates was extremely low; for cellulose at pH 5.5 it was not even detectable. Deposited amounts of UEA-I on TMC and PS were the same at both pH values, while for the gold surface an influence of the pH value was observed. UEA-I was only investigated at one pH value and showed the highest interaction capacity of all proteins and all pH values with all types of surfaces.
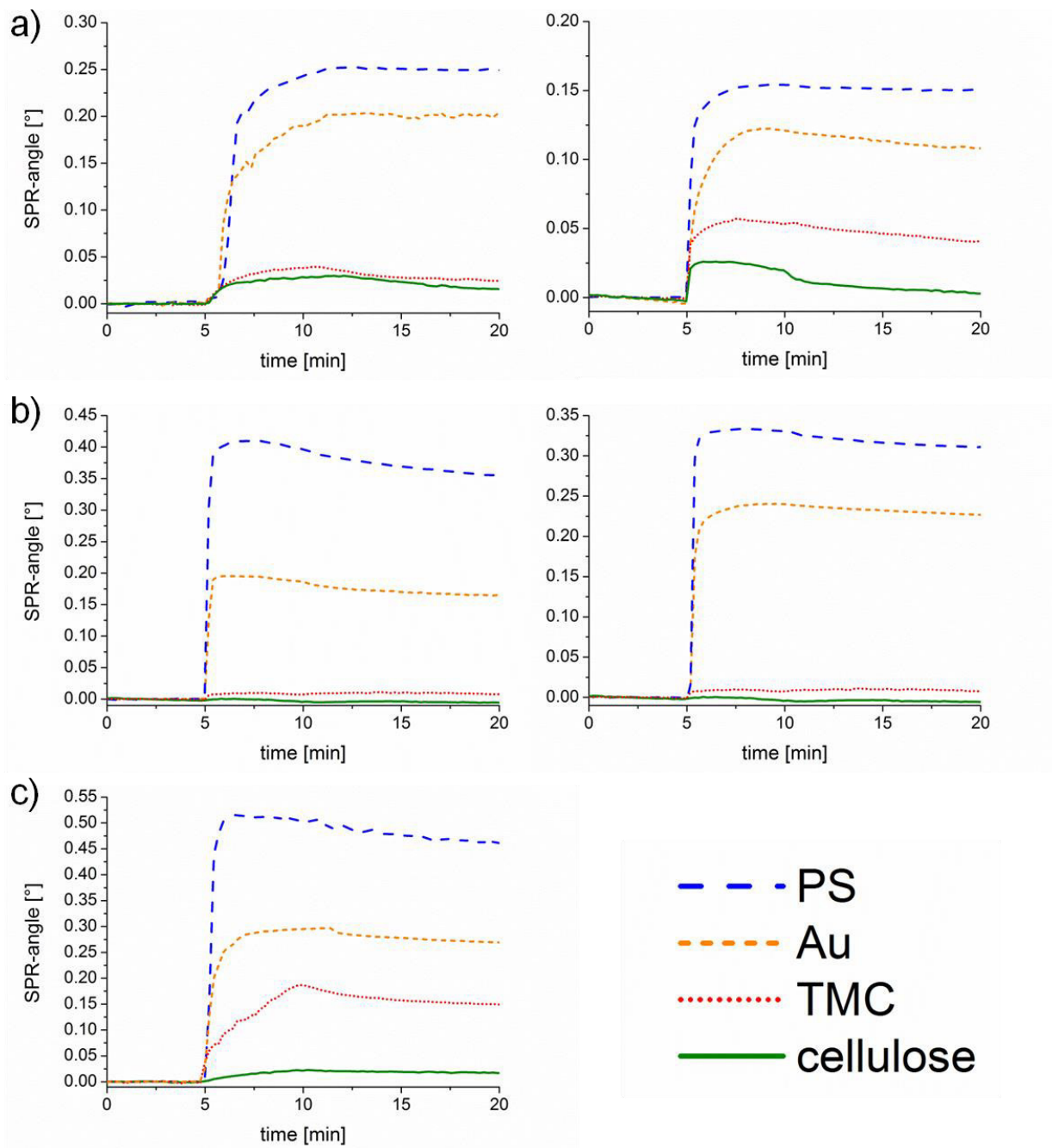
Figure 5. Sensograms measured by MP-SPR at 785 nm for different proteins; (a) BSA, (b) Con A and (c) UEA-I at pH value 5.5 (left) and pH value 7.4 (right).

The sensograms shown in Figure 5 give insight into the adsorption behavior observed in real-time and thereby allow statements on the kinetics. BSA adsorbs extremely fast (steep slope and

quickly reaching an equilibrium) at pH 7.4 onto PS and cellulose, whereas adsorption is rather slow at pH 5.5. The interactions with PS and gold are strong since no material is removed upon rinsing. Only minor adsorption of Con A is detectable on the cellulose and TMC surface. However, extremely fast adsorption onto PS and gold is monitored indicating a high affinity to the substrates. At pH 7.4 only small amounts detached during rinsing, whereas at pH 5.5 an overshoot effect occurs, which is in the case of proteins usually explained by the so-called rollover model describing a reorientation of end-on into side-on adsorbed proteins.[28] The same effect is observed for UEA-I adsorption onto PS. Adsorption of UEA-I onto TMC and cellulose is very slow, not even reaching an equilibrium in the observed timeframe.
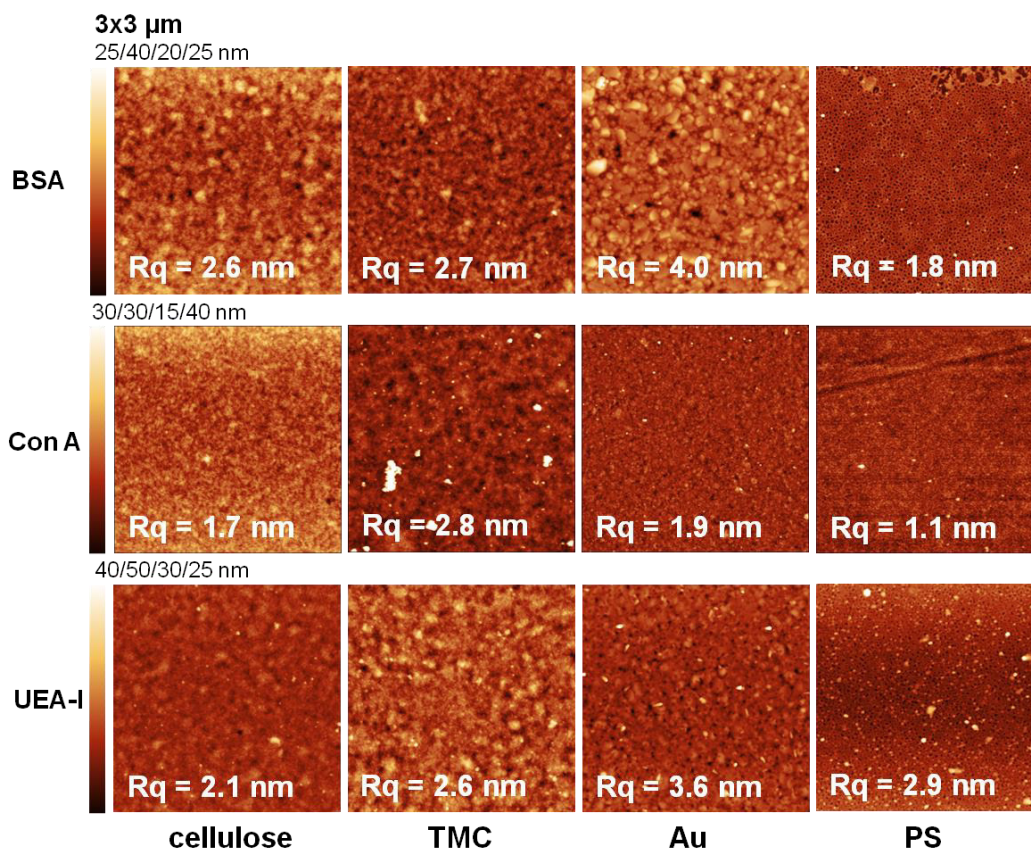
Figure 6. Atomic force microscopy height images of different substrates after protein adsorption at pH 5.5.

All of the surfaces were rinsed with water, dried and measured with atomic force microscopy (AFM) directly after protein adsorption. The images (Figure 6, Figure 7) depict the adsorbed amount obtained by MP-SPR. For some surfaces there is hardly any change in surface topography, because the adsorbed amount was too low to be detected by AFM. In general, the more protein adsorbed the lower the roughness for cellulose, gold and TMC was detected, which is a strong indication for proteins adsorbing preferably into holes and pores of the substrates. However, for the extremely flat surface of PS ($R_q = 0.6$ nm), it is vice versa meaning that the roughness increases upon protein deposition. There, the proteins form island like features which fuse into a patch like morphology with increasing adsorbed amount before full coverage is achieved.[29] This is represented best by comparing the AFM images of BSA adsorbed onto PS. At pH 5.5 we observe nearly full coverage with a roughness of 1.8 nm, whereas at pH 7.4 islands of BSA lead to a higher roughness (2.8 nm).
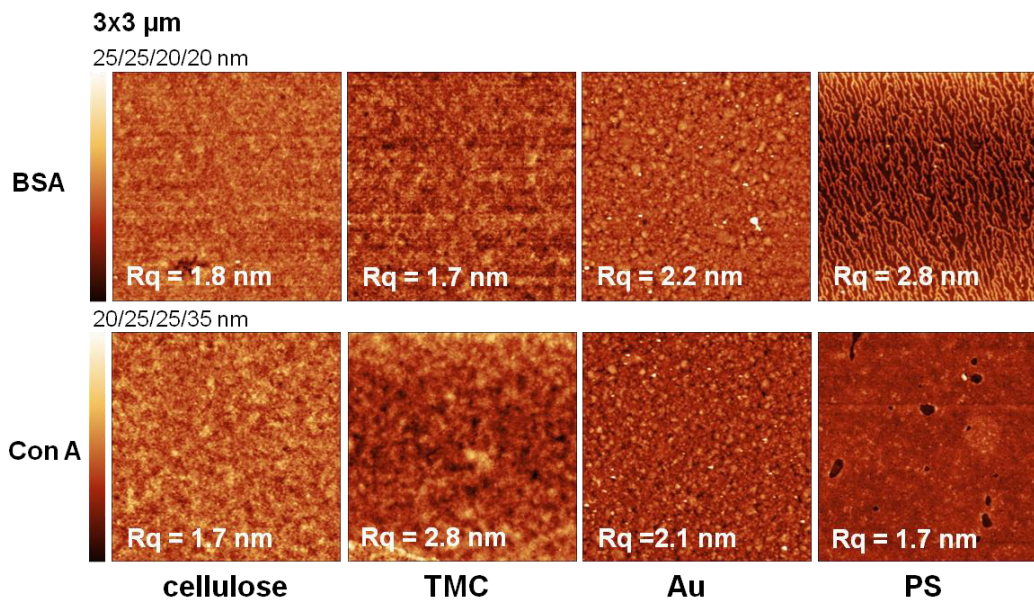
Figure 7. Atomic force microscopy height images of different substrates after protein adsorption at pH 7.4.

CONCLUSION

The results of this adsorption study can be rationalized in the following way. The adsorption behavior of the examined lectins is comparable to BSA in terms of affinity to substrates of differents types. The largest adsorbed amounts and fastest kineticts were observed on the hydrophilic PS surface indicating that hydrophobic interactions govern the attraction of the investigated proteins to the substrate. The preferred adsorption onto gold is most likely caused by interactions of the thiol groups of the proteins, because of the good interaction capacity of sulfur and gold. The affinity to the hydrophilic substrates was exceptionally low, even when positive charges were introduced by adsorbing TMC. An insignificant change upon altering the surface charge was monitored in the case of BSA, as well as pH dependence of the adsorbed amount, whereas no pronounced effect of pH was seen for the lectins. Although Con A is a mannose/glucose binding lectin, which could interact with the glucose residues from cellulose, no adsorption was detected at all, due to the small amount of available end groups of the cellulose.

In conclusion, the binding interactions of BSA, UEA-I and Con A are primarily of hydrophobic nature, therefore hydrophilic substrates such as cellulose and TMC, compared to for instance PS, offer huge advantages for the utilization in biosensor development. They are not only stemming from renewable resources but when used as a support material they are resistant to non-specific protein adsorption meaning the introduction of blocking agents is redundant.

ASSOCIATED CONTENT

Supporting Information.

ATR-IR spectra, static contact angle data.

AUTHOR INFORMATION

Notes

ACKNOWLEDGMENT

REFERENCES

(1)   Rini, J. M. *Annu. Rev. Biophys. Biomol. Struct.* **1995**, *24* (1), 551–577.

(2)   Kumar, Kk.; Reddy, Gs.; Reddy, B.; Shekar, Pc.; Sumanthi, J.; Chandra, Kl. P. *J. Orofac. Sci.* **2012**, *4* (1), 20.

(3)   Safina, G. *Anal. Chim. Acta* **2012**, *712*, 9–29.

(4)   Lam, S. K.; Ng, T. B. *Appl. Microbiol. Biotechnol.* **2011**, *89* (1), 45–55.

(5)   Hamid, R.; Masood, A.; Wani, I. H.; Rafiq, S. *J. Appl. Pharm. Sci.* **2013**, *3* (4SUPPL.1).

(6)   Jeyachandran, Y. L.; Mielczarski, J. a.; Mielczarski, E.; Rai, B. *J. Colloid Interface Sci.* **2010**, *341* (1), 136–142.

(7)   Amim, J.; Petri, D. F. S. *Mater. Sci. Eng. C* **2012**, *32* (2), 348–355.

(8)   Zemła, J.; Lekka, M.; Raczkowska, J.; Bernasik, A.; Rysz, J.; Budkowski, A. *Biomacromolecules* **2009**, *10* (8), 2101–2109.

(9)   Matsumoto, I.; Osawa, T. *Arch. Biochem. Biophys.* **1970**, *140* (2), 484–491.

(10) Goldstein, I. J.; Hollerman, C. E.; Smith, E. E. *Biochemistry* **1965**, *4* (5), 876–883.

(11) Kontturi, E.; Thüne, P. C.; Niemantsverdriet, J. W. *Langmuir* **2003**, *19* (14), 5735–5741.

(12) Mohan, T.; Kargl, R.; Doliška, A.; Vesel, A.; Köstler, S.; Ribitsch, V.; Stana-Kleinschek, K. *J. Colloid Interface Sci.* **2011**, *358* (2), 604–610.

(13) Mohan, T.; Kargl, R.; Doliška, A.; Ehmann, H. M. A.; Ribitsch, V.; Stana-Kleinschek, K. In *Carbohydrate Polymers*; 2013; Vol. 93, pp 191–198.

(14) Owens, D. K.; Wendt, R. C. *J. Appl. Polym. Sci.* **1969**, *13* (8), 1741–1747.

(15) Rabel, W. *Farbe und Lack* **1971**, *77* (10), 997–1005.

(16) Kaelble, D. H. *J. Adhes.* **1970**, *2* (2), 66–81.

(17) De Feijter, J.; Benjamins, J.; Veer, F. *Biopolymers* **1978**, *17* (7), 1759–1772.

(18) Robeson, J. L.; Tilton, R. D. *Langmuir* **1996**, *12* (25), 6104–6113.

(19) Nguyen, S.; Hisiger, S.; Jolicoeur, M.; Winnik, F. M.; Buschmann, M. D. *Carbohydr. Polym.* **2009**, *75* (4), 636–645.

(20) Ristić, T.; Mohan, T.; Kargl, R.; Hribernik, S.; Doliška, A.; Stana-Kleinschek, K.; Fras, L. *Cellulose* **2014**, *21* (4), 2315–2325.

(21) Mohan, T.; Findenig, G.; Höllbacher, S.; Cerny, C.; Ristić, T.; Kargl, R.; Spirk, S.; Maver, U.; Stana-Kleinschek, K.; Ribitsch, V. *Colloids Surfaces B Biointerfaces* **2014**, *123*, 533–541.

(22) Mohan, T.; Niegelhell, K.; Zarth, C. S. P.; Kargl, R.; Köstler, S.; Ribitsch, V.; Heinze, T.; Spirk, S.; Stana-Kleinschek, K. *Biomacromolecules* **2014**, *15* (11), 3931–3941.

(23) Giesbers, M.; Kleijn, J. M.; Stuart, M. a C. *J. Colloid Interface Sci.* **2002**, *248* (1), 88–95.

(24) Kirby, B. J.; Hasselbrink, E. F. *Electrophoresis* **2004**, *25* (2), 203–213.

(25) Böhme, U.; Scheler, U. *Chem. Phys. Lett.* **2007**, *435* (4-6), 342–345.

(26) Entlicher, G.; Koštíř, J. V.; Kocourek, J. *BBA - Protein Struct.* **1971**, *236* (3), 795–797.

(27) Privalov, P. L.; Gill, S. J. *Pure Appl. Chem.* **1989**, *61* (6), 1097–1104.

(28) Rabe, M.; Verdes, D.; Seeger, S. *Adv. Colloid Interface Sci.* **2011**, *162* (1-2), 87–106.

(29) Wangkam, T.; Yodmongkol, S.; Disrattakit, J.; Sutapun, B.; Amarit, R.; Somboonkaew, A.; Srikhirin, T. *Curr. Appl. Phys.* **2012**, *12* (1), 44–52.

Supporting Information #5

Adsorption Behavior of Lectins – A MP-SPR Study

Working Version
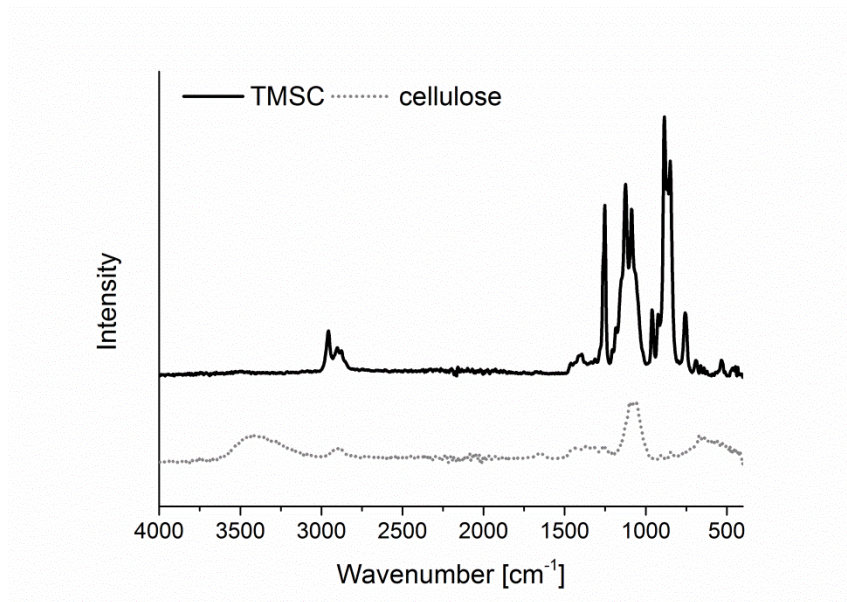
Figure S1. ATR-IR spectra of a TMSC thin film before and after regeneration. Conversion to cellulose upon HCl treatment is proven.
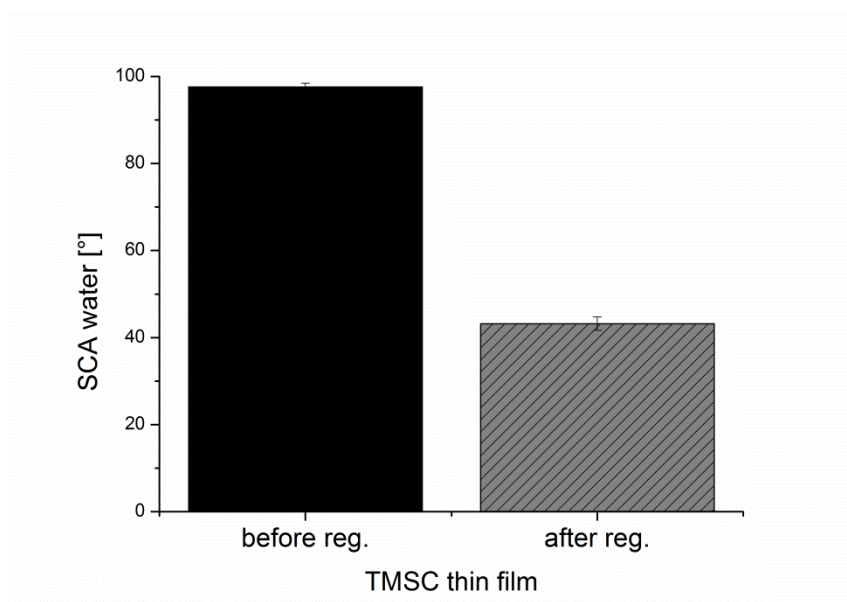
Figure S2. Static water contact angles of a TMSC thin film before and after regeneration to cellulose.
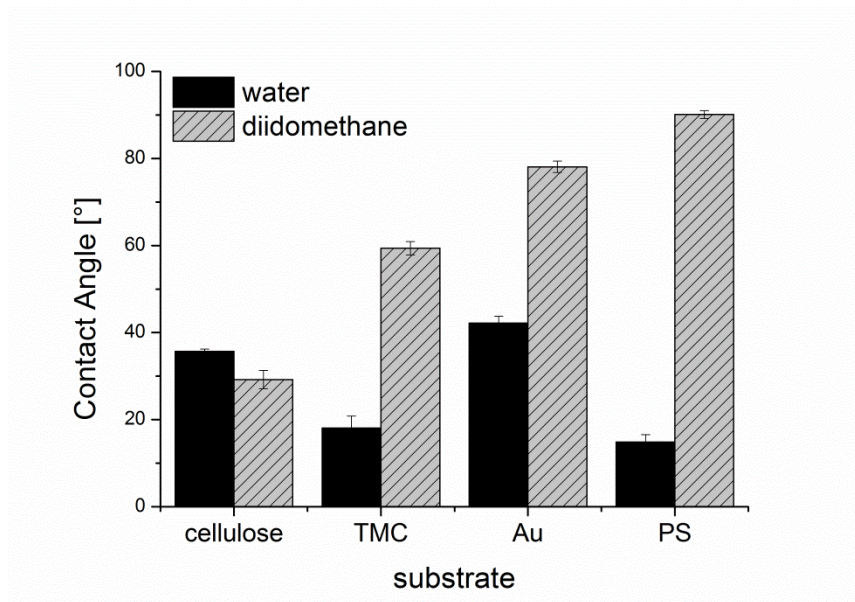
Figure S3. Contact angles measured with water and diiodomethane of different substrates used in the adsorption study. This data was used to calculate the surface free energies of the substrates by the OWRK method.

PAPER #6

Homogeneous Cellulose Thin Films by Regeneration of Cellulose

Xanthate – Properties and Characterization

submitted to Cellulose

For this paper, I conducted the AFM and MP-SPR spectroscopy experiments, interpreted the data and wrote the corresponding part of the manuscript.

Homogeneous Cellulose Thin Films by Regeneration of Cellulose Xanthate – Properties and Characterization

Michael Weißl[1,2], Katrin Niegelhell[2], David Reishofer[2], Armin Zankel[3], Josef Innerlohinger[4], and Stefan Spirk[2]

1) Graz University of Technology, Institute for Chemistry and Technology of Materials, Stremayrgasse 9 8020 Graz

2) Graz University of Technology, Institute for Paper, Pulp and Fibre Technology, Inffeldgasse 23A 8010 Graz

3) Institute for Electron Microscopy and Nanoanalysis, NAWI Graz, Graz University of Technology and Centre for Electron Microscopy, Steyrergasse 17, 8010 Graz, Austria

4) Lenzing AG, Werkstrasse 2, 4860 Lenzing, Austria.

Correspondence:

Stefan Spirk

stefan.spirk@tugraz.at

+43 (316) 873 – 30763

ABSTRACT

The preparation and characterization of cellulose thin films derived from cellulose xanthate is reported. The films are prepared by depositing alkaline aqueous solutions of cellulose xanthate onto silicon wafers, followed by a spin coating step. Depending on the xanthate concentration used for spin coating, films with 50 and 700 nm thickness are obtained. The cellulose xanthate is converted to cellulose by exposing the films to HCl vapors over a period of 20 minutes. The conversion is monitored by ATR-IR spectroscopy, which allows for tracking the rupture of C-S and C=S bonds during the regeneration process. The conversion is accompanied by a reduction of the film thickness of ca 40 % due to the removal of the bulky xanthate group. The films feature a homogenous, but porous morphology as shown by atomic force microscopy. Further, the films were investigated towards their interaction with Bovine Serum Albumin (BSA) and fibrinogen by means of multi-parameter surface plasmon resonance spectroscopy. Similar as other cellulose thin films BSA adsorption is low while fibrinogen adsorbs to some extent at physiological pH (7.4).

KEYWORDS

Cellulose thin films, xanthate, vapor phase hydrolysis, protein adsorption

INTRODUCTION

In recent years, cellulose thin films have attracted significant interest in both basic and applied research since they provide a confined two dimensional environment with defined morphology and chemistry.(E. Kontturi, Tammelin, & Österberg, 2006; Eero Kontturi, Thüne, & Niemantsverdriet, 2003; K. S. Kontturi, Kontturi, & Laine, 2013) Therefore, they have been proposed as supports for biosensors, as matrix for catalysis as well as material for optoelectronic devices such as transistors and solar cells.(Blomstedt, Kontturi, & Vuorinen, 2007; Filpponen et al., 2012; Niegelhell et al., 2016; Hannes Orelma, Filpponen, Johansson, Laine, & Rojas, 2011; Hannes; Orelma, Johansson, Filpponen, Rojas, & Laine, 2012; Reishofer et al., 2017; Taajamaa, Rojas, Laine, Yliniemi, & Kontturi, 2013; Archim Wolfberger et al., 2015) Further, these films have been employed as models to investigate and to better understand interactions of water with cellulose, particularly in the context of cell wall structure and their relation to industrially applied drying processes. (Ehmann et al., 2015; Niinivaara, Faustini, Tammelin, & Kontturi, 2016; Niinivaara, Faustini, Tanunelin, & Kontturi, 2015)

The strategies to prepare such films are based on three main approaches which comprise either i) the use of cellulose suspensions, ii) the dissolution of cellulose or (iii) the employment of cellulose derivatives which are converted back to cellulose after the film forming process.(E. Kontturi et al., 2006) The advantage of using suspensions is to avoid the use of organic solvents but the obtained films are not completely flat due to the (nano)fibrous or particulate nature of the cellulosic starting materials. In contrast, the preparation of cellulose thin films derived from dissolved cellulose requires tedious dissolution procedures (e.g. DMA/LiCl or ionic liquids).(Kargl et al., 2015) Additionally, the solvent (and/or salt) needs to be removed from the films, which requires extensive washing procedures of the films. An elegant method to prepare

cellulose thin films overcoming these problems has been introduced by Klemm in 1993 and further developed by Kontturi in the beginning of the century.(Eero Kontturi et al., 2003; Schaub, Wenz, Wegner, Stein, & Klemm, 1993) The method employs an acid labile organosoluble cellulose derivative, trimethylsilyl cellulose (TMSC), which is converted to cellulose after processing by simple exposure to HCl vapors. Since the whole process runs via gas phase reaction and since only volatile side products are formed, washing steps are not necessary. In addition, the solubility of this cellulose derivative can be tuned by variation of the DS_{TMS} and therefore allows easy manufacturing, e.g. by spin coating, the most common thin film formation technique. The films obtained by this process are smooth and featureless with RMS roughnesses of down to 1.5 nm as determined by atomic force microscopy. However, although TMSC is a commercial cellulose derivative, and although the production is in principle scalable, it is a rather expensive material. Although eco-solvents such as ethyl acetate have been proposed as solvents for TMSC, the use of an aqueous cellulose solution for film formation would be desirable.(A. Wolfberger, Kargl, Griesser, & Spirk, 2014; Archim Wolfberger et al., 2015)

In this context, a widely used, water soluble cellulose derivative, which can be easily converted back to cellulose, is cellulose xanthate (CX). CX has been first prepared already in the end of the 19th century and was since then used as a soluble cellulose derivative for the production of regenerated fibers. In a typical fiber producing process, the xanthates are regenerated by immersion in an acidic bath which in addition contains some additives to improve fiber properties. Nowadays the market for viscose based products is steadily increasing by ca 10% year whereas specialities become more and more attractive to manufactures. (Götze, 1951; Hämmerle, 2011)

For all these reasons, we became interested whether cellulose xanthate can be employed for the formation of thin cellulose films having film thicknesses below 100 nm. Cellulose thin films from

TMSC have shown potential for some applications but the use of CX as starting material may lead to new materials with interesting properties while being biobased and scalable to large quantities. The resulting films could then either be converted by simple immersion in an acidic bath to regenerate the cellulose or to expose them to an acidic atmosphere (e.g. HCl) similar to TMSC films. In the following, we report our approach to prepare such films starting from different concentrations of cellulose xanthate in aqueous alkaline solutions and their influence on film properties.

EXPERIMENTAL

Materials. A cellulose xanthate (CX) stock solution (10 wt.%) was provided by Lenzing AG (Lenzing, Austria) and used without any further treatment. CX solutions with 0.75, 1.0, 1.5, 2.0, 2.5, 3.0 and 4.0 wt.% were prepared by adding de-ionized water from an Elga PURELAB Prima (Bucks, United Kingdom) water treatment system to the stock solutions. Afterwards, the solutions were vigorously mixed using a vortex shaker over a period of 30 seconds, followed by a filtration step. The CX solutions were stored in a freezer at -18°C to prevent degradation. Sulfuric acid (95 wt.%) and hydrochloric acid (37 wt.%) were purchased from VWR Chemicals and hydrogen peroxide (30 wt.%) from Sigma-Aldrich. Silicon wafers, glass slides (Roth), Au-coated glass slides as substrate (SPR102-AU), Filter Chromafil Xtra PVDF-45/25 0.45 μm were used as obtained. BSA and fibrinogen were purchased from Sigma, Aldrich.

Cellulose thin film preparation. As substrates for the cellulose films, single side polished silicon wafers from Siegert Wafers (Aachen, Germany, wafer thickness: 675 ± 25 μm, 1 cm x 1 cm) and gold coated glass slides from BioNavis (Tampere, Finland, gold layer thickness: 50 nm, 1 cm x 2 cm) were used. The slides were cleaned by dipping them into piranha acid (H_2SO_4:H_2O_2 = 3:1 (v/v)) for 30 minutes (10 minutes for gold slides) and intensely washed with MilliQ water afterwards.

For spin coating, 80 μl of viscose solution (per square centimeter substrate) were deposited onto the surfaces and subjected to spin coating (a = 2500 rpm·s^{-1}, v = 4000 rpm, t = 60 s). Afterwards, the thin films were stored at room temperature overnight, followed by regeneration of the deposited CX layers in vaporous HCl atmosphere (created from concentrated hydrochloric acid). During the regeneration procedure, the HCl was deposited into a petri dish, and the substrates were positioned above the liquid HCl phase in another petri dish. A third petri dish was used as a lid to close the

system. After 20 minutes exposure to the gaseous HCl atmosphere, regeneration of the cellulose xanthates to cellulose is accomplished as proven by ATR-IR spectroscopy. Afterwards, the films were rinsed twice with water (3 ml) followed by drying in a stream of dry nitrogen.

Optical microscopy. Light microscopy investigations were carried out on an Olympus BX60 fitted with an Olympus E-520 camera. Prior to investigating the samples, carrier substrates were fixed on a glass layer.

Profilometry. The layer thickness was determined with a Bruker DekTak XT surface profiler. The scan length was set to 1000 µm over the time duration of 3 seconds with the hills and valleys scanning profile. The diamond stylus had a radius of 12.5 µm and the employed force was 3 mg. The measured profile was then used to determine the thickness. Each layer thickness has been determined by averaging 6 measurements on three different slides.

Attenuated total reflection – infrared spectroscopy. The infrared spectra were recorded with an ALPHA FT-IR spectrometer (Bruker; Billerica, MA, U.S.A.). For the measurement, an attenuated total reflection (ATR) attachment was used with 64 scans at a resolution of 4 cm^{-1} and a scan range between 4000 and 400 cm^{-1}. The samples were prepared on Au-coated glass slides (SPR102-AU). The data were analyzed with OPUS 4.0 software.

Atomic force microscopy. The atomic force microscopy (AFM) images were recorded in tapping mode with a Veeco Multimode Quadrax MM AFM (Bruker; Billerica, MA, USA). For the measurements silicon cantilevers (NCH-VS1-W from NanoWorld AG, Neuchatel, Switzerland; Coating: none) with a resonance frequency of 297 kHz were used. All measurements were performed under ambient atmosphere and at room temperature. The image processing and the calculation of the root mean square roughness (calculated from 2 µm × 2 µm an 10 µm x 10 µm images) were done with the Nanoscope software (V7.30r1sr3; Veeco).

Contact angle and surface free energy determination. For the calculation of the surface free energy (SFE) Milli-Q water (≥18 MΩcm-1) and diiodomethane were employed as test liquids. The drop shape analysis was done in the sessile drop modus at 25 °C with a DSA100 system (Krüss GmbH, Hamburg, Germany) equipped with a T1E CCD video camera (25 fps). The dispense rate of the 3 µL droplets was adjusted to 166 µL/min and the time before the image was captured was set to 2 seconds. Each sample was measured at least three times. The contact angle (CA) calculations (software: DSA1 v 1.90) were performed with the Young-Laplace equation and the surface free energy calculation with the Owens-Wendt-Rabel & Kaelble method.(Owens & Wendt, 1969)

Scanning electron microscopy - Energy-dispersive X-ray spectroscopy. An ESEM Quanta 600 FEG (FEI, Eindhoven, NL) scanning electron microscope was utilized to examine the surface structure during different steps of film preparation. To gain electrical conductivity a 15 nm thick carbon layer was vaporized on the film surface before. Images were recorded in the high vacuum mode either with secondary electrons (ETD Everhart Thornley detector, giving topographic contrast) or with backscattered electrons (SSD: Solid State Detector, delivering compositional contrast).

Multi parameter surface plasmon resonance spectroscopy. MP-SPR spectroscopy was accomplished with a SPR Navi 200 from Bionavis Ltd., Tampere, Finland, equipped with two different lasers (670 and 785 nm, respectively) in both measurement channels, using gold-coated glass slides as substrate (gold layer 50 nm). All measurements were performed using a full angular scan (39−78°, scan speed: $8° \cdot s^{-1}$). Protein adsorption was investigated with Bovine Serum Albumin (BSA) (1 mg·ml^{-1}) and fibrinogen (FIB) (1 mg·ml^{-1}) both in a 100 mM NaCl solution containing 10 mM PBS at pH 7.4. Flow was adjusted to 50 µl·min^{-1} for 5 minutes at 25 °C. Each measurement

was repeated 3 times at least. BioNavis Dataviewer software was used for processing all two wavelength SPR experiments.

Scheme 1. Cellulose thin film production based on aqueous viscose solutions.
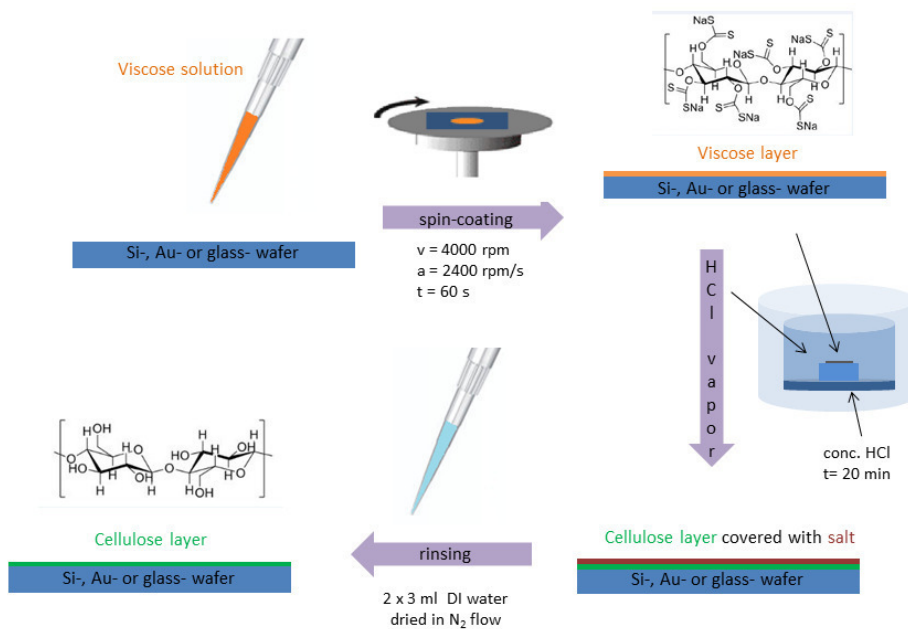
RESULTS AND DISCUSSION

In a first step, the film formation properties of CX solutions by spin coating were investigated as a function of the CX concentration. It turned out that the CX concentration must be in a range between 0.75 and 4.0 wt.% to obtain homogenous films on the different substrates (i.e. Si-wafer, glass slides, gold coated glass slides). Below concentrations of 0.75 wt.% CX incompletely covered films were obtained, whereas above 4.0 wt.% CX fully covered but inhomogeneous films having a wide range of defects were observed (data not shown). After deposition by spin coating, the CX films were regenerated using HCl. When the films were immersed in aqueous 3 M HCl, the films peeled off the substrate; therefore this method was not investigated in further detail. In contrast, the exposure to HCl vapors created from concentrated hydrochloric acid led to the regeneration of the CX to cellulose. The regeneration of the CX can be observed by naked eye, particularly when glass slides were employed as substrates. On these films, the yellow CX film steadily decolorizes with time concomitant with the formation of a white particle like coverage on the surface. This white material corresponds to the formation of salt crystals composed of NaCl (obtained as side product by reaction of the sodium xanthate and HCl) and can be easily removed by rinsing the films with water after regeneration (see AFM section). As expected, the higher the concentration of the CX solution used for film preparation was, the more pronounced the formation of this residue was.

The layer thickness of the CX films gradually increased with increasing CX concentration from 31 ± 3 (0.75 wt.%) to 688 ± 10 nm (4.0 wt.%). One would expect that the films significantly shrink during regeneration since the xanthate group is rather bulky and hydrogen bond formation would lead additionally to densification of the films as known for related cases involving other cellulose derivatives such as TMSC.(Eero Kontturi et al., 2011; T. Mohan et al., 2012) However, directly

10

after exposure of the films to HCl vapors, the opposite phenomenon was observed. Some films showed an increase in film thickness or did not change significantly which relates to the formation of NaCl, which certainly does not only form on the surface but also in the interior of the film. After removal of NaCl from the films by rinsing with water, the film thickness reduced significantly. Finally, pure cellulose films with film thicknesses between 21 ± 2 and 413 ± 11 nm were manufactured. It is of interest that the film with the smallest layer thickness showed just 23% of shrinking whereas for all the other films shrinkage was between 40 and 44% (Figure 1). Similar observations have been made when studying the film thickness reduction during regeneration of TMSC; obviously the substrate limits the shrinking and densification of the films to some extent.(Ehmann et al., 2015) Afterwards, the films were subjected to a drying procedure at 105 °C over a period of one hour. The films showed a slight shrinkage whereas here the thinnest films were affected to a larger extent than the thicker ones. An overview on the layer thickness data is provided in Table 1.

Table 1. Comparison of the layer thickness d [nm] of the films depending on initial CX concentration by stylus force profilometry.

	CX	after 20 min HCl	rinsed	dried 105°C
0.75 wt.%	31 ± 3	31 ± 3	24 ± 2	20 ± 2
1.0 wt.%	51 ± 3	58 ± 2	30 ± 3	29 ± 1
1.5 wt.%	103 ± 2	115 ± 3	58 ± 1	59 ± 1
2.0 wt.%	167 ± 2	205 ± 6	96 ± 3	93 ± 2
2.5 wt.%	243 ± 5	309 ± 6	138 ± 3	136 ± 2
3.0 wt.%	401 ± 4	463 ± 7	230 ± 3	229 ± 2
4.0 wt.%	688 ± 10	680 ± 8	413 ± 11	407 ± 10
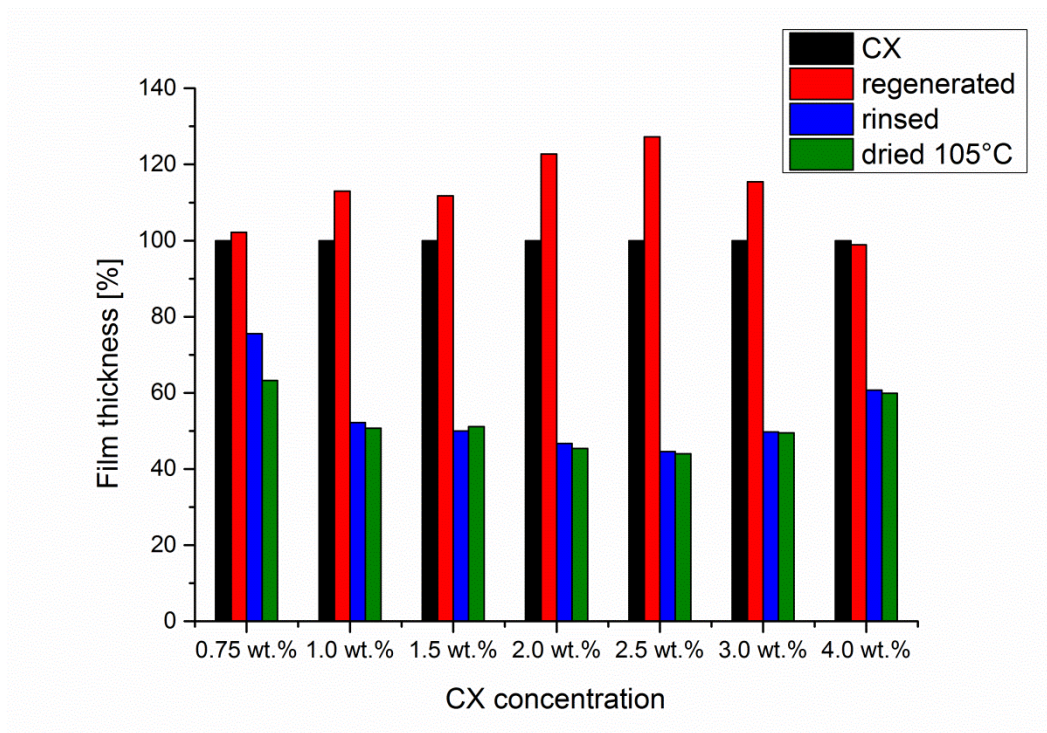
Figure 1. Film thickness changes [%] in dependence of process parameters.

A commonly used method to monitor chemical reactions of cellulose derivatives is IR spectroscopy. In the IR spectra (Figure 2), it is clearly visible that the non-regenerated films are not only composed of CX ($v_{C=S}$ at 1235 cm^{-1}, v_{C-S} at 925 cm^{-1}) but they do also contain significant amounts of CX decomposition products like sodium trithiocarbonate ($v_{C=S}$ at 1235 cm^{-1}), sodium thiocarbonate ($v_{C=O}$ at 1420 cm^{-1} (s)) and free CS_2 ($v_{C=S}$ at 1530 (s), v_{C-S} at 793 (w) cm^{-1}) as indicated by the overlapping bands in the region of 1520 to 1250 cm^{-1}.(Ogura & Sobue, 1968) During ongoing regeneration all bands related to the C=S and C-S vibrations disappear and a cellulose II spectrum is obtained. This is featured by broad bands from 3600 to 3100 cm^{-1}(v_{OH}) and from 3000 to 2850 cm^{-1} (C-H stretching vibrations), a series of small weak bands in the region of 1430 to 1150 cm^{-1} (C-O-H bending at 1430 cm^{-1}, C-H deformation at 1372 cm^{-1}, OH in plane deformation at 1330 and at 1200 cm^{-1}) , a strong and overlapping bands from 1160 to 950 cm^{-1}

(asym. C-O-C vibration at 1155 cm^{-1}, sym. C-O vibration at 1060 cm^{-1} and C-O stretching at 1035 cm^{-1}) and a small band at 899 cm^{-1} (C-O-C valence vibration).(Široký, Blackburn, Bechtold, Taylor, & White, 2010) Additionally, the spectra of the regenerated CX films show a small band at 1640 cm^{-1} indicating adsorbed water. When the CX films are stored over a period of 14 days, alterations in the intensity of the IR band appearing at 850 cm^{-1} (stretching vibrations of CS single bond) could be observed (Figure S2 supporting information). This observation is in consistency with the elimination and rearrangement of carbon disulfide groups during the aging process of cellulose xanthates described by Fink et al. and Woodings.(Fink, Stahn, & Matthes, 1934; Wilkes, 2001)
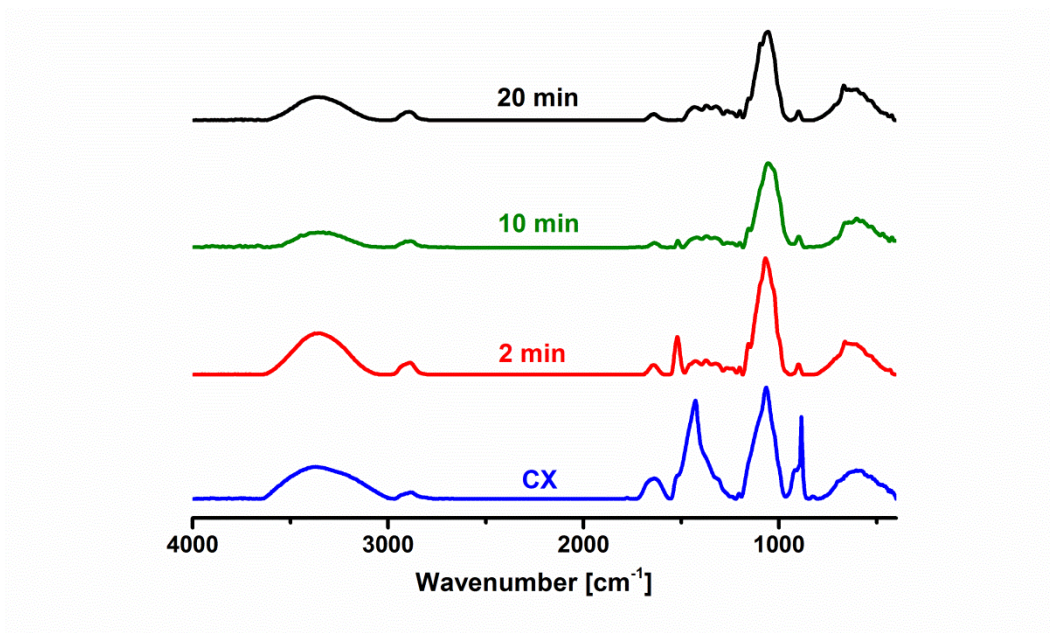
Figure 2. ATR-IR spectra of cellulose xanthate films (prepared from a 3 wt.% solution of CX) during the exposure to HCl vapors.

The morphology of the films shows a rather homogeneous surface structure, which is altered by the concentration used for film preparation. In general, an increase of the concentration of CX solutions used for the preparation of the films leads to surfaces with higher RMS roughness (R_q)

values. Figures 3 and 4 depict two different types of films, one prepared from 1.5 wt.% and the other from 2.5 wt.% CX solutions. It can be clearly seen that the surfaces feature much higher R_q values for the 2.5 wt.% films (6.9 nm) than for the 1.5 wt.% ones (3.0 nm). The exposure of the films to HCl vapors leads to a significant increase in roughness to 24 and 28 nm, respectively. However, this increase in roughness is not related to rough cellulose surfaces but to the formation of NaCl particles on the surfaces. As already indicated for the profilometry results, more particles are present on surfaces with increasing CX concentration in solutions prepared for film manufacturing and indeed this can also be observed in the AFM images. When the particles are removed by simply rinsing them with water, R_q values are reduced to their initial values (6.8 and 5.1 nm), a phenomenon which has been observed for cellulose thin films derived from TMSC as well. The films exhibit homogeneous surface morphology and a subsequent drying step slightly alters the structure, thereby further reducing the roughness values.
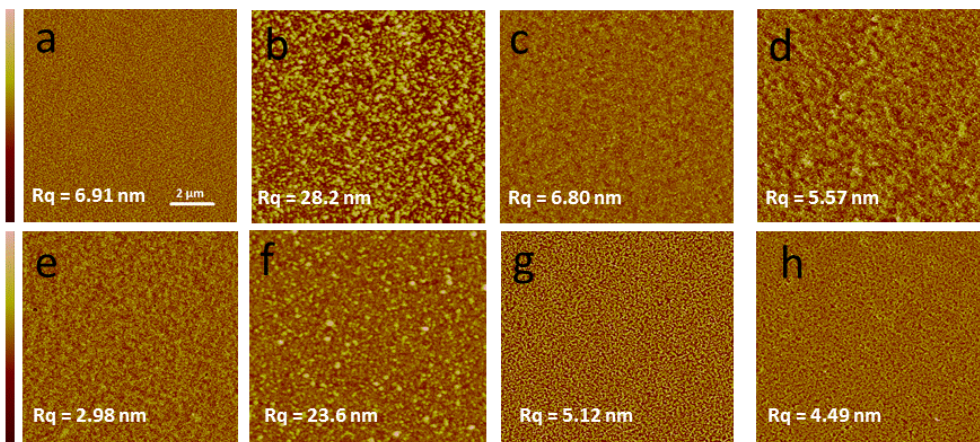
Figure 3. AFM images (10 x 10 μm²) and corresponding RMS roughness of different steps in cellulose thin film processing with a 2.5 wt.% (upper row) and a 1.5 wt.% (lower row) viscose solution. The images show the films directly after spin coating (a,e), after 20 minutes lasting

exposure to HCl atmosphere (b,f), after rinsing with de-ionized water (c,g) and after drying for 1 hour at 105°C (d,h). Z-scale is 100/200/50/50 nm for a,b,c,d and 30/300/30/50 nm for e,f,g,h.
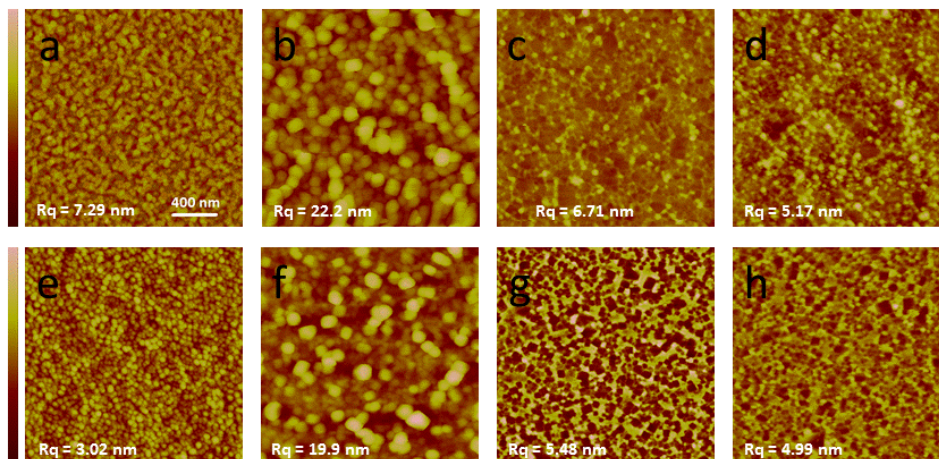
Figure 4. AFM images (2 x 2 µm²) and corresponding RMS roughness of different steps in cellulose thin film processing with a 2.5 wt.% (upper row) and a 1.5 wt.% (lower row) viscose solution. The images show the films directly after spin coating (a,e), after 20 minutes lasting exposure to HCl atmosphere (b,f), after rinsing with de-ionized water (c,g) and after drying for 1 hour at 105°C (d,h). Z-scale is 100/200/50/50 nm for a,b,c,d and 30/150/100/50 nm for e,f,g,h.

To validate the chemical reactions and the changes in surface morphology appearing in the different steps of cellulose thin film processing, SEM-EDX measurements were performed. The SEM images reveal flower like structures on the surface of CX films directly after the spin coating step (Figure 5a), which probably originate from sodium hydroxide. These structures are visible in the AFM images as well but since a smaller area was chosen, they could not be identified as separate phase. Further, the growth of crystallites during CX regeneration (Figure 5b) is visible, which disappear after rinsing with water (Figure 5c). EDX spectra clearly show that the crystals in Fig. 5b consist of sodium chloride. For the crystals present on the surface of untreated CX films,

EDX spectra (Fig. S3-S5, Supporting Information) show a small sulfur peak in addition to the common sodium and chloride peaks. The additional sulfur peak and the different crystalline structure indicate the presence of two different crystals (sodium hydroxide and probably sodium sulfide).
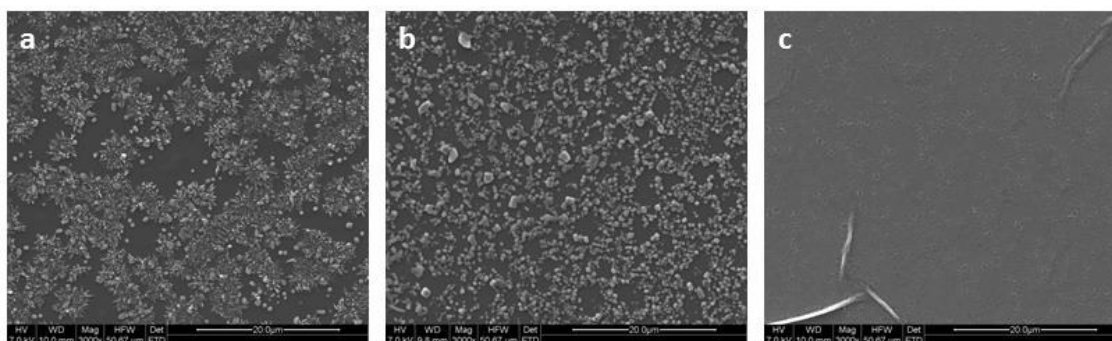
Figure 5. SEM images displaying the film surface after a) spin coating of 2.5 wt. % CX solution, b) regeneration of CX in HCl vapor and c) after rinsing the film with water.

An important parameter for the investigation of the surface properties of cellulose thin films is wettability. However, the determination of water contact angles on CX films could not be performed since the films were partially dissolved by water thereby giving no meaningful results while with CH_2I_2 contact angles ranging from 38 to 60° were obtained. After regeneration, the presence of NaCl particles on the surfaces prevented the measurement of the contact angles for both liquids. After rinsing the films with water, static water contact angles between 27 and 38° were determined. The drying of the films did not change the wettability with both liquids significantly. In general, these cellulose surfaces are a bit more hydrophobic than those prepared from TMSC where usually static water contact angles between 24 to 33° have been reported.

Based on this data, the surface free energies (SFE) of the surfaces were determined according to the Owens–Wendt–Rabel and Kaelble method.(Kaelble, 1970; Owens & Wendt, 1969; Rabel, 1971) This method exploits the wettability behavior of two different liquids in order to calculate the total surface free energy as well as the dispersive and polar components. In this paper, water and diiodomethane were chosen as test liquids. Figure 6 illustrates that the surface free energy decreases significantly after rinsing the films with de-ionized water. However, the following heat treatment did not have any substantial impact on the surface free energy. Taking a closer look at the decrease in SFE after the washing step reveals that the polar part of SFE energy stays constant over all process steps and only the disperse part of SFE is slightly changing.

Table 2. Static contact angle for viscose thin films in different concentrations and various steps of film production

	0.75 wt.%		1.50 wt.%		3.0 wt.%	
	H_2O	CH_2I_2	H_2O	CH_2I_2	H_2O	CH_2I_2
CX	n. d	38 ± 1	n. d.	60 ± 2	n. d.	48 ± 2
regenerated	25 ± 1	34 ± 1	21 ± 1	36 ± 1	15 ± 1	40 ± 2
rinsed	34 ± 1	31 ± 1	38 ± 1	33 ± 1	27 ± 1	28 ± 1
dried 105°C	33 ± 1	34 ± 1	37 ± 1	32 ± 1	30 ± 1	32 ± 1
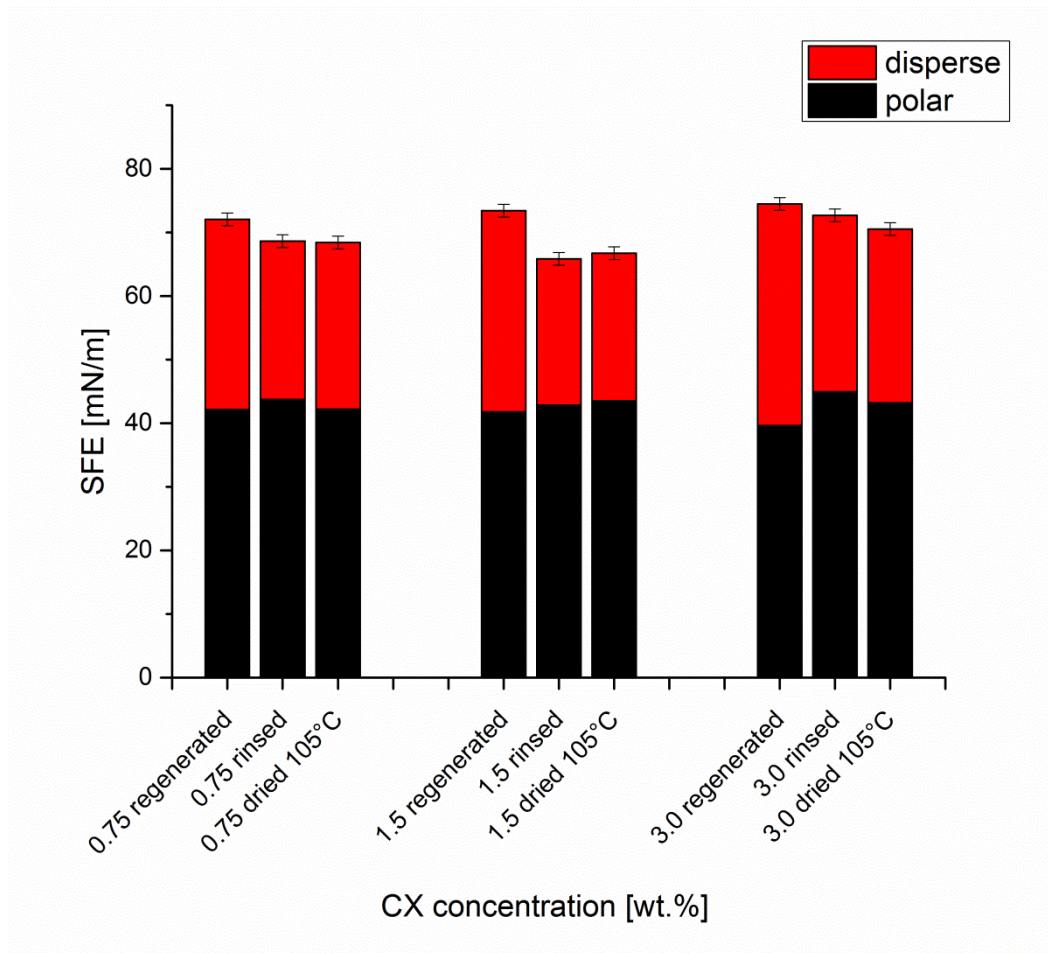
Figure 6. Surface free energy of cellulose layers prepared from different concentrations, determined directly after film regeneration, rinsing and heat treatment.

SPR spectroscopy is one of the methods of choice to investigate protein adsorption on thin films allowing for the evaluation of the dry adsorbed mass (adsorbed mass without coupled water) as well as the adsorption kinetics. Protein adsorption was tested using bovine serum albumin (BSA), a widely accepted marker for nonspecific protein interaction, and fibrinogen (FIB), a serum protein which plays an important role in the blood coagulation cascade.(Pallister & Watson, 2010) Since the herein investigated cellulose thin films are potential materials for the usage in life science applications, SPR experiments were accomplished at a pH value of 7.4 which corresponds to the pH value of human blood. The adsorption experiments were designed in a way that the films were

first equilibrated for 45 minutes using buffer, followed by injection of the protein solutions over a period of 5 minutes and finalized by a subsequent rinsing step. At these conditions, the protein amount deposited (Figure 7) on regenerated and washed films was determined to be 1.11 ± 0.18 mg·m^{-2} and 0.22 ± 0.08 mg·m^{-2} for FIB and BSA, respectively.(Tamilselvan Mohan et al., 2017) The preferred adsorption behavior for FIB in contrast to BSA is observed for other surfaces as well and can be attributed to the size of FIB. FIB (340 kDa) is a larger protein than BSA (66.5 kDa) and displays a larger contact area hereby increasing the extent of adsorption. Heat treatment of the cellulose films led to a decrease in the change of the SPR angle by the half which corresponds to lower protein adsorption (0.55 ± 0.07 mg·m^{-2} for FIB and 0.11 ± 0.04 mg·m^{-2} for BSA). The reduction in the adsorbed protein amount is accompanied with a change in surface morphology of the thin films since the wettability, another factor potentially playing a role, remains nearly constant after drying. A decrease in roughness minimizes the available surface area therefore leading to reduced interaction. There is not any noteworthy difference in adsorption kinetics (see sensograms, Figure 7b) for all of the experiments, however it seems that proteins start to desorb even before the rinsing step is initiated (after 10 min) at the heat treated surfaces, whereas on the washed films non-bound material is only removed upon rinsing. This could be also related to the overshooting effect as described recently.(Rabe, Verdes, & Seeger, 2011) Different phenomena have been described in literature to explain this effect such as the Vroman effect (competition of high affinity species with low adsorption speed vs low affinity species with high adsorption rate), and the Daly and Wertz effect (change of protein conformation after adsorption). In our case it is obvious that reorientation takes place on the surfaces since both proteins under investigation can adsorb in different conformations.

Compared to other cellulosic surfaces, for instance cellulose thin films prepared from TMSC, cellulose films made from viscose offer similar protein adsorption behavior. Depending on the adsorption parameters, e.g. adsorption time, flow rate, ionic strength and others, values in the range of 0.3-0.6 mg BSA·m^{-2} determined by SPR are reported in literature.
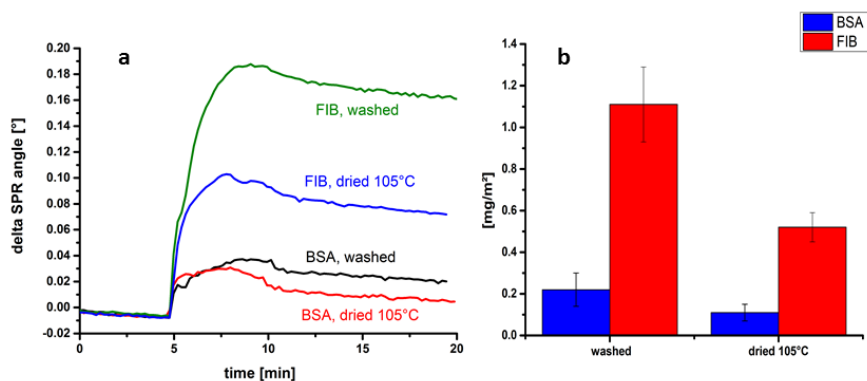
Figure 7. 670 nm sensogram recorded during the adsorption of FIB and BSA on washed and heat treated films (a, prepared from 1 wt.% CX solutions). (b) the amount of protein adsorbed on differently treated films, calculated through the change in the SPR angle via the de Feijter equation. (De Feijter, Benjamins, & Veer, 1978)

CONCLUSION

In summary, the manufacturing and properties of cellulose thin films derived from CX have been presented. These films, which may be best described as two-dimensional model systems for viscose based materials, display similar properties as other cellulosic materials in terms of wettability/surface free energy and protein interaction behavior. The use of CX as starting material offers the possibility to prepare thin films in the nanometer range from aqueous solutions in large scale whereas regeneration can be performed via the gas phase. During this reaction, volatile side products are generated and NaCl particles are formed which are easily removed by simply rinsing the films with water. Afterwards, homogenous films are obtained which show a regular but rougher and more porous surface compared to those derived from TMSC for instance. The films show similar behavior towards proteins as other cellulose matrices. In future work, we will focus how these films perform in other areas compared to those derived from other sources such as TMSC.

REFERENCES

Blomstedt, M., Kontturi, E., & Vuorinen, T. (2007). Optimising CMC sorption in order to improve tensile stiffness of hardwood pulp sheets. *Nord. Pulp Paper Res. J.,* 22, 336-342.

De Feijter, J. A., Benjamins, J., & Veer, F. A. (1978). Ellipsometry as a tool to study the adsorption behavior of synthetic and biopolymers at the air–water interface. *Biopolymers,* 17(7), 1759-1772.

Ehmann, H. M. A., Werzer, O., Pachmajer, S., Mohan, T., Amenitsch, H., Resel, R., Kornherr, A., Stana-Kleinschek, K., Kontturi, E., & Spirk, S. (2015). Surface-Sensitive Approach to

Interpreting Supramolecular Rearrangements in Cellulose by Synchrotron Grazing Incidence Small-Angle X-ray Scattering. *ACS Macro Letters*, 713-716.

Filpponen, I., Kontturi, E., Nummelin, S., Rosilo, H., Kolehmainen, E., Ikkala, O., & Laine, J. (2012). Generic Method for Modular Surface Modification of Cellulosic Materials in Aqueous Medium by Sequential "Click" Reaction and Adsorption. *Biomacromolecules, 13*, 736−742.

Fink, H., Stahn, R., & Matthes, A. (1934). Reifebestimmung und Ultrafiltration von Viscose. *Angewandte Chemie, 47*(34), 602-607.

Götze, K. (1951). *Chemiefasern nach dem Viskoseverfahren*. (2nd ed.). Heidelberg, Germany: Springer Verlag.

Hämmerle, F. M. (2011). The cellulose gap. *Lenzinger Berichte, 89*, 12-21.

Kaelble, D. H. (1970). Dispersion-Polar Surface Tension Properties of Organic Solids. *J. Adhes. , 2*, 66-81.

Kargl, R., Mohan, T., Ribitsch, V., Saake, B., Puls, J., & Kleinschek, K. S. (2015). Cellulose thin films from ionic liquid solutions. *Nordic Pulp & Paper Research Journal, 30*(1), 6-13.

Kontturi, E., Suchy, M., Penttila, P., Jean, B., Pirkkalainen, K., Torkkeli, M., & Serimaa, R. (2011). Amorphous Characteristics of an Ultrathin Cellulose Film. *Biomacromolecules, 12*(3), 770-777.

Kontturi, E., Tammelin, T., & Österberg, M. (2006). Cellulose model films and the fundamental approach. *Chem. Soc. Rev., 35*, 1287-1304.

Kontturi, E., Thüne, P. C., & Niemantsverdriet, J. W. (2003). Cellulose Model Surfaces Simplified Preparation by Spin Coating and Characterization by X-ray Photoelectron Spectroscopy, Infrared Spectroscopy, and Atomic Force Microscopy. *Langmuir,* 19(14), 5735-5741.

Kontturi, K. S., Kontturi, E., & Laine, J. (2013). Specific water uptake of thin films from nanofibrillar cellulose. *J. Mater. Chem. A,* 1, 13655-13663.

Mohan, T., Niegelhell, K., Nagaraj, C., Reishofer, D., Spirk, S., Olschewski, A., Stana Kleinschek, K., & Kargl, R. (2017). Interaction of Tissue Engineering Substrates with Serum Proteins and Its Influence on Human Primary Endothelial Cells. *Biomacromolecules,* 18(2), 413-421.

Mohan, T., Spirk, S., Kargl, R., Doliska, A., Vesel, A., Salzmann, I., Resel, R., Ribitsch, V., & Stana-Kleinschek, K. (2012). Exploring the rearrangement of amorphous cellulose model thin films upon heat treatment. *Soft Matter,* 8, 9807-9815.

Niegelhell, K., Süßenbacher, M., Jammernegg, K., Ganner, T., Schwendenwein, D., Schwab, H., Stelzer, F., Plank, H., & Spirk, S. (2016). Enzymes as Biodevelopers for Nano- And Micropatterned Bicomponent Biopolymer Thin Films. *Biomacromolecules,* 17(11), 3743-3749.

Niinivaara, E., Faustini, M., Tammelin, T., & Kontturi, E. (2016). Mimicking the Humidity Response of the Plant Cell Wall by Using Two-Dimensional Systems: The Critical Role of Amorphous and Crystalline Polysaccharides. *Langmuir,* 32(8), 2032-2040.

Niinivaara, E., Faustini, M., Tanunelin, T., & Kontturi, E. (2015). Water Vapor Uptake of Ultrathin Films of Biologically Derived Nanocrystals: Quantitative Assessment with Quartz Crystal Microbalance and Spectroscopic Ellipsometry. *Langmuir,* 31(44), 12170-12176.

Ogura, K., & Sobue, H. (1968). Studies on the derivatives of sodium cellulose xanthate. Part I. Infrared absorption spectra and characteristic frequencies of C□S and C□S groups in sodium cellulose xanthate and its stable derivatives. *Journal of Polymer Science Part B: Polymer Letters,* 6(1), 63-67.

Orelma, H., Filpponen, I., Johansson, L.-S., Laine, J., & Rojas, O. J. (2011). Modification of Cellulose Films by Adsorption of CMC and Chitosan for Controlled Attachment of Biomolecules. *Biomacromolecules,* 12(12), 4311-4318.

Orelma, H., Johansson, L.-S., Filpponen, I., Rojas, O. J., & Laine, J. (2012). Generic Method for Attaching Biomolecules via Avidin-Biotin Complexes Immobilized on Films of Regenerated and Nanofibrillar Cellulose. *Biomacromolecules,* 13, 2802-2810.

Owens, D. K., & Wendt, R. C. (1969). Estimation of the surface free energy of polymers. *Journal of Applied Polymer Science,* 13(8), 1741-1747.

Pallister, C. J., & Watson, M. S. (2010). *Haematology*: Scion Publishing.

Rabe, M., Verdes, D., & Seeger, S. (2011). Understanding protein adsorption phenomena at solid surfaces. *Advances in Colloid and Interface Science,* 162(1), 87-106.

Rabel, W. (1971). Einige Aspekte Der Benetzungstheorie Und Ihre Anwendung Auf Die Untersuchung Und Veränderung Der Oberflächeneigenschaften von Polymeren. *Farbe und Lack,* 77, 997-1005.

Reishofer, D., Rath, T., Ehmann, H. M., Gspan, C., Dunst, S., Amenitsch, H., Plank, H., Alonso, B., Belamie, E., Trimmel, G., & Spirk, S. (2017). Biobased Cellulosic–CuInS2 Nanocomposites for Optoelectronic Applications. *ACS Sustainable Chemistry & Engineering*.

Schaub, M., Wenz, G., Wegner, G., Stein, A., & Klemm, D. (1993). Ultrathin films of cellulose on silicon wafers. *Advanced Materials, 5*(12), 919-922.

Široký, J., Blackburn, R. S., Bechtold, T., Taylor, J., & White, P. (2010). Attenuated total reflectance Fourier-transform Infrared spectroscopy analysis of crystallinity changes in lyocell following continuous treatment with sodium hydroxide. *Cellulose, 17*(1), 103-115.

Taajamaa, L., Rojas, O. J., Laine, J., Yliniemi, K., & Kontturi, E. (2013). Protein-assisted 2D assembly of gold nanoparticles on a polysaccharide surface. *Chemical Communications, 49*(13), 1318-1320.

Wilkes, A. G. (2001). *3 - The viscose process A2 - Woodings, Calvin*. In *Regenerated Cellulose Fibres* (pp. 37-61): Woodhead Publishing

Wolfberger, A., Kargl, R., Griesser, T., & Spirk, S. (2014). Photoregeneration of Trimethylsilyl Cellulose as a Tool for Microstructuring Ultrathin Cellulose Supports. *Molecules, 19*(10), 16266-16273.

Wolfberger, A., Petritz, A., Fian, A., Herka, J., Schmidt, V., Stadlober, B., Kargl, R., Spirk, S., & Griesser, T. (2015). Photolithographic patterning of cellulose: a versatile dual-tone photoresist for advanced applications. *Cellulose, 22*, 717-727.

Supporting Information #6

Homogeneous Cellulose Thin Films by Regeneration of Cellulose Xanthate – Properties and Characterization

submitted to Cellulose
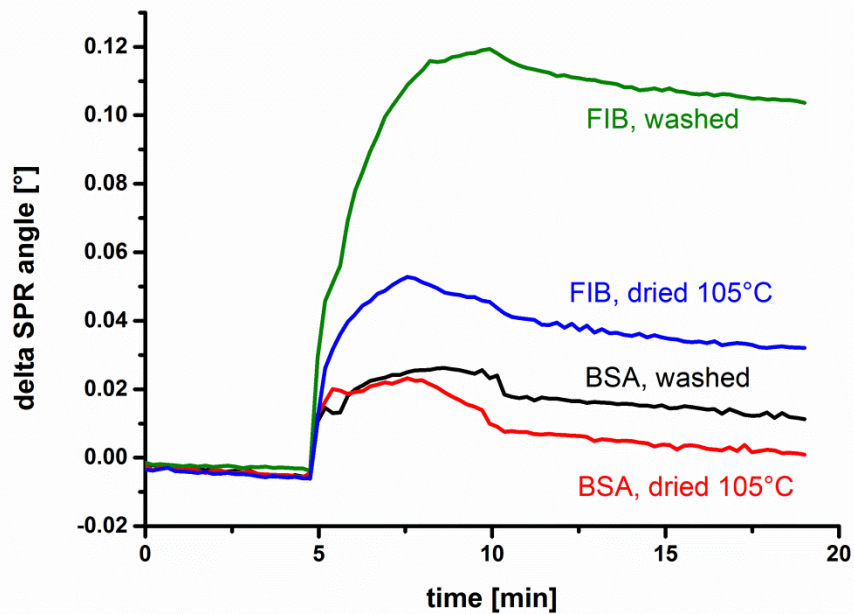
Figure S1. 785 nm sensogram recorded during the adsorption of FIB and BSA on washed and heat treated films.

Table S1. Surface roughness of cellulose thin films in different stages of processing and with variation in CX concentration during spin coating, calculated via AFM images.

	10x10 µm² images			2x2 µm² images		
	0.75 wt.%	1.50 wt.%	2.50 wt.%	0.75 wt.%	1.50 wt.%	2.50 wt.%
CX	1.5	3.0	6.9	2.0	3.0	7.3
regenerated	16.0	23.6	28.2	14.9	19.9	22.2
washed	3.8	5.1	6.8	4.1	6.9	6.7
dried at 105°C	2.9	4.5	5.6	3.0	5.0	5.2
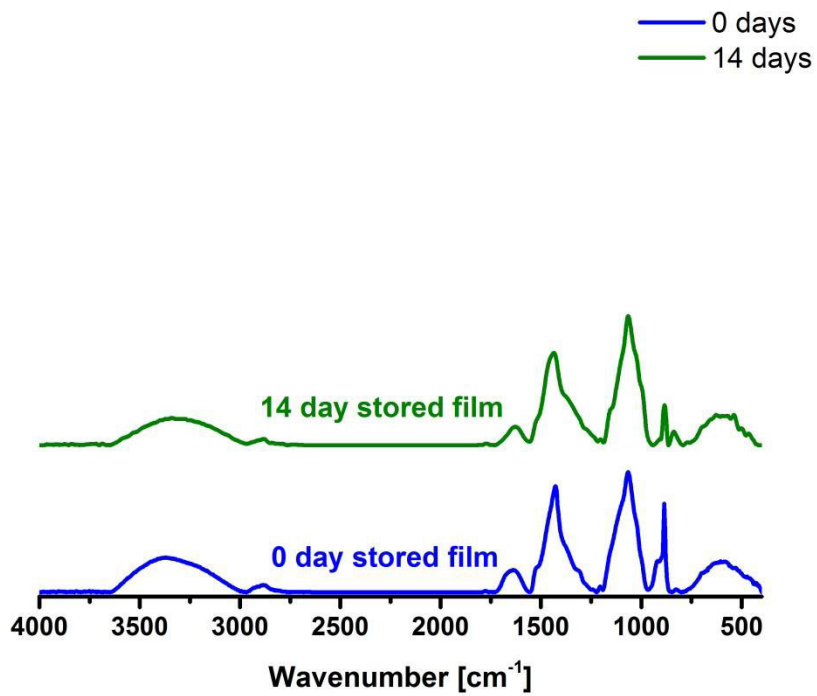
Figure S2. ATR-IR spectra of untreated viscose solutions, stored for 0 and 14 days under the influence of atmosphere and sun light.
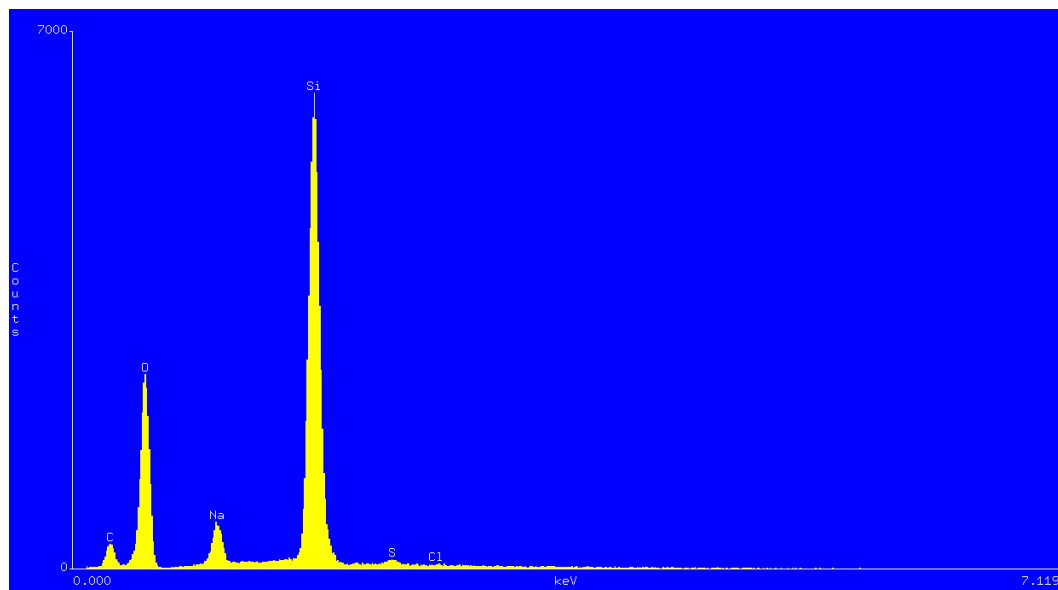
Figure S3. SEM-EDX spectrum of the salt crystals present on the films after spin coating of the CX solutions.
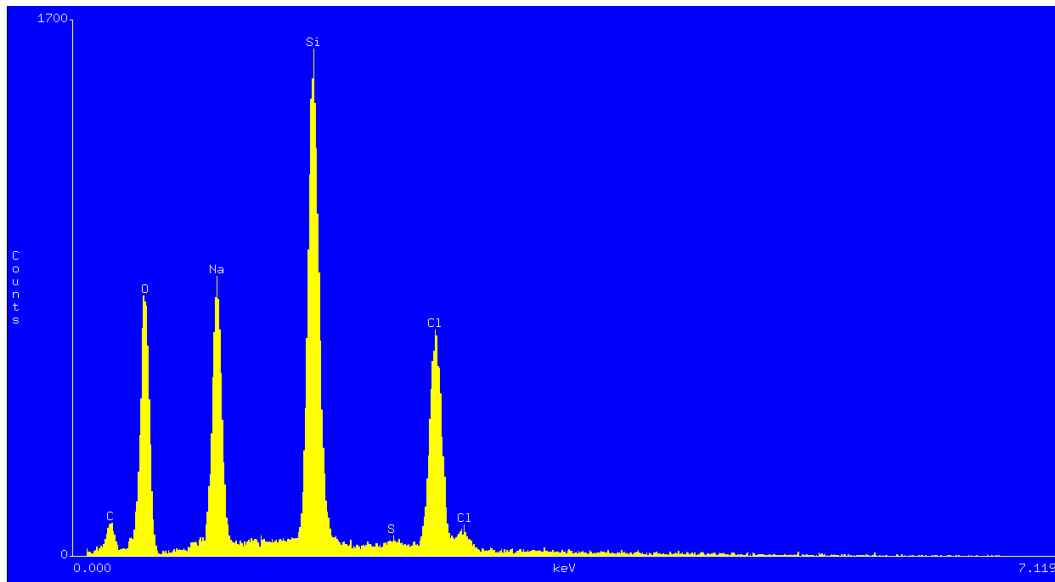
Figure S4. SEM-EDX spectrum of the salt crystals present in the films after regerneration with

HCl vapors.
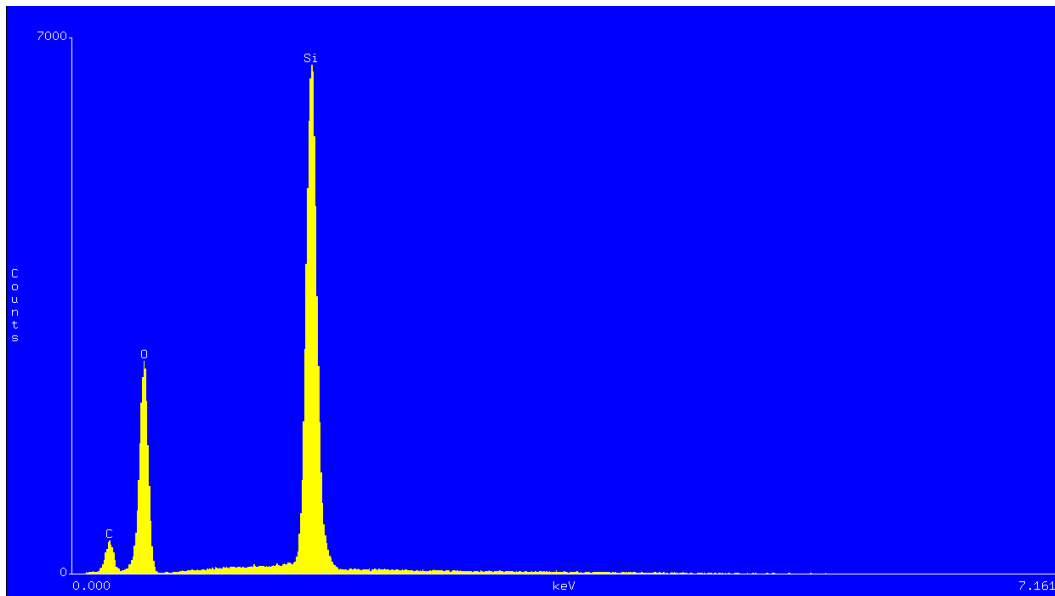
Figure S5. SEM-EDX spectrum of the films after rinsing with water.

PAPER #7

Interaction of Industrially Relevant Cationic Starches with Cellulose

submitted to Carbohydrate Polymers

For this paper, I conducted the sample preparations, AFM and MP-SPR spectroscopy experiments and contact angle measurements. I interpreted the data and wrote a significant part of the manuscript.

Interaction of Industrially Relevant Cationic Starches with Cellulose

Katrin Niegelhell[1,2], Angela Chemelli[3], Josefine Hobisch[4], Thomas Griesser[5], Heidemarie Reiter[6,2], Ulrich Hirn[1,2], Stefan Spirk[1,2]*

[1] Graz University of Technology, Institute for Paper, Pulp and Fiber Technology, Inffeldgasse 23A, 8010 Graz, Austria

[2]CD-Laboratory for Fibre Swelling and Paper Performance, Inffeldgasse 23A, 8010 Graz, Austria

[3]Graz University of Technology, Institute for Inorganic Chemistry, Stremayrgasse 9, 8010 Graz, Austria

[4]Graz University of Technology, Institute for Chemistry and Technology of Materials, Stremayrgasse 9, 8010 Graz, Austria

[5]University of Leoben, Chair of Polymeric Materials, Otto-Glöckl-Strasse 9, 8700 Leoben, Austria

[6]Mondi Uncoated Fine & Kraft Paper GmbH, Marxergasse 4A, 1030 Wien, Austria

To whom correspondence should be addressed:

* E-Mail: stefan.spirk@tugraz.at, Tel.:+43 316 873 32284.

ABSTRACT

Industrially relevant, commercially available cationic starches have been investigated towards their interaction capacity with cellulose thin films derived from trimethylsilyl cellulose (TMSC). The starches used in this study stem from different sources (potato, pea, corn) and featured rather low degrees of substitution ranging from 0.030 to 0.062. The interaction of those starches with cellulose thin films was studied by surface plasmon resonance spectroscopy under flow conditions using concentrations of 1.0 mg·ml^{-1} and a flow rate of 25 μl·min^{-1}. All the investigated starches employed in this study were capable to efficiently interact with the slightly negatively charged cellulose surface leading to irreversible deposition on the surface. As complementary techniques atomic force microscopy and x-ray photoelectron spectroscopy were used to confirm the presence of the starches on the cellulose film surface. Further, dynamic light scattering and size exclusion chromatography measurements were performed to correlate adsorbed amount, particle size and molecular weight of the starches to their interaction behavior.

INTRODUCTION

Cationic polymers are important materials for tailoring the properties of cellulosic substrates such as fibers and pulps. These polyelectrolytes carry a large amount of positive charges on their backbone and are capable to efficiently interact with negatively charged polymers. (Dobrynin, Deshkovski, & Rubinstein, 2001) The cationic polymers very often take the role of adhesion promoters, thereby triggering or enhancing the adsorption of other functional molecules/particles. Consequently, the interaction of many cationic polymers with a variety of cellulosic substrates has been extensively studied in the past. (Geffroy, Labeau, Wong, Cabane, & Cohen Stuart, 2000; Guan, Qian, Xiao, Zheng, & He, 2008; Hasani, Cranston, Westman, & Gray, 2008; K. S. Kontturi et al., 2009; K. S. Kontturi, Tammelin, Johansson, & Stenius, 2008; Lee, Lee, & Youn, 2014; Tamilselvan Mohan et al., 2014; T. Mohan, Ristic, et al., 2013; T. Mohan, Zarth, et al., 2013; Petersen, Radosta, Vorwerg, & Kießler, 2013; Schwikal et al., 2011; Terada, Samoshina, Nylander, & Lindman, 2004a, 2004b; Yokota, Kitaoka, & Wariishi, 2007) This originates from the importance of cationic polymers in fiber manufacturing processes as well as in papermaking. For instance, cationization of cellulosic textile fibers is often employed to increase anionic dye uptake on and into the fiber matrix. (Nechwatal, Michels, Kosan, & Nicolai, 2004) Further, the deposition of cationic starches has also been proposed to induce antimicrobial action against several microorganisms. (Guan, Qian, Xiao, & Zheng, 2008) In contrast, in paper industry the addition of cationic polymers and here in particular of cationic starches is pivotal to produce papers with better retention properties and higher dry strength.(Nachtergaele, 1989) A major issue to unravel the interaction of such cationic starches with cellulosic materials is their intrinsic inhomogeneity (e.g. diameter, morphology, accessibility, composition etc.) which makes it difficult to extract fundamental parameters governing their interaction behavior in real time.

Although there are some methods available which can track changes on e.g. fiber matrices such as isothermal titration calorimetry (thermodynamics) and zeta potential (charge) measurements, an elegant way to overcome problems associated with inhomogeneity is to use materials with a well-defined morphology, chemistry and charge.(Rohm, Hirn, Ganser, Teichert, & Schennach, 2014) A particularly well established system has been introduced by Klemm in 1993 and further developed by Kontturi which is based on mostly amorphous cellulose thin films. (E. Kontturi, Thüne, & Niemantsverdriet, 2003; Schaub, Wenz, Wegner, Stein, & Klemm, 1993) These two-dimensionally constrained films can be easily prepared by depositing solutions of a precursor (trimethylsilyl cellulose, TMSC) on a flat surface and by a subsequent spin coating step smooth films are obtained. These silylated cellulose films can be simply converted to cellulose thin films by exposing them to hydrochloric acid vapors over a period of several minutes. Their defined morphology, chemical composition and the homogenous surface allow for a detailed investigation of the surface properties and their interaction with other biomolecules such as proteins, or other polysaccharides. (Niegelhell et al., 2016; Hannes; Orelma, Johansson, Filpponen, Rojas, & Laine, 2012; Strasser et al., 2016) In this context, just a few studies focus on how cationic polysaccharides interact with cellulose thin films. Examples include different types of chitosans, cationic celluloses, cationic xylans and also cationic starches. (Lee et al., 2014; Tamilselvan Mohan et al., 2014; T. Mohan, Ristic, et al., 2013; T. Mohan, Zarth, et al., 2013; Hannes Orelma, Filpponen, Johansson, Laine, & Rojas, 2011) In these studies researchers employ cationic starches with different degrees of substitution (0.2-0.75) and focus on whether and to which extent the presence of electrolytes change the interaction capacity with cellulose and as comparison to silica. (K. S. Kontturi et al., 2009; K. S. Kontturi et al., 2008) As for other charged polymers (Geffroy et al., 2000; Hasani et al., 2008; Tammelin, Saarinen, Österberg, & Laine, 2006; Yokota et al., 2007) it

was demonstrated that the degree of coiling strongly determines the adsorption of the starches onto the surfaces. (Tammelin, Merta, Johansson, & Stenius, 2004) The degree of coiling in turn strongly correlates with the amount of electrolyte in the solutions since it prevents repulsion between individually charged segments by charge screening. Without such a screening the cationic polymers adopt a flat-like, extended conformation usually leading to the formation of thin layers. (Dobrynin et al., 2001; Dobrynin & Rubinstein, 2005) However, the use of starches directly employed for papermaking processes do often have rather low degrees of substitution DS (<0.08). Therefore, the repulsion between the substituted segments is small and can become at a certain point negligible leading to coiled conformations even in the absence of electrolytes. In this study, we aim at a deeper understanding on how such lowly substituted starches interact with cellulose thin films in real time using surface plasmon resonance spectroscopy (SPR). The employed cationic starches are manufactured in large quantities and are intended for papermaking issues. They feature DSs ranging from 0.030 to 0.062.

EXPERIMENTAL

Materials. Trimethylsilyl cellulose (TMSC, Avicel, M_w = 185,000 g·mol^{-1}, M_n = 30,400 g·mol^{-1}, PDI = 6.1 determined by SEC in chloroform) with a DS_{Si} value of 2.8-2.9 was purchased from TITK (Rudolstadt, Germany). SPR gold sensor slides (CEN102AU) were purchased from Cenibra, Germany. Milli-Q water (resistivity = 18.2 MΩ^{-1}·cm^{-1}) from a Millipore water purification system (Millipore, USA) was used for contact angle determinations and SPR experiments. Chloroform (99.3%), hydrochloric acid (37%), hydrogen peroxide (30% in water) and sulfuric acid (95%) were purchased from Sigma Aldrich and used as received. Wet end starches commonly used in paper

production were used without further purification. Cationic starches were cooked at appropriate temperatures (95-125°C).

Substrate Cleaning and Film Preparation. Prior to spin coating, SPR gold sensor slides/silicon wafers were immersed in a "piranha" solution containing H_2O_2 (30 wt.%)/H_2SO_4 (1:3 v/v) for 10 min, then extensively rinsed with MilliQ water and blow dried with N_2 gas. 100 µl of a TMSC solution (0.75 wt% in chloroform) were deposited onto the substrate and then rotated for 60 s at a spinning speed of 4000 rpm and an acceleration of 2500 rpm·s^{-1}. To convert TMSC into pure cellulose, the sensors/wafers were placed in a polystyrene petri-dish (5 cm in diameter) containing 3 ml of 10 wt.% hydrochloric acid (HCl). The dish was covered with its cap and the films were exposed to the vapors of HCl for 12 min. The regeneration of cellulose from TMSC was verified by water contact angle (**Figure S1**) and ATR-IR (**Figure S2**) measurements as reported elsewhere. (Tamilselvan Mohan et al., 2012; T. Mohan et al., 2012)

Multi Parameter Surface Plasmon Resonance Spectroscopy – MP-SPR. MP-SPR spectroscopy was accomplished with a SPR Navi 200 from Bionavis Ltd., Tampere, Finland, equipped with two different lasers (670 and 785 nm) in both measurement channels, using gold coated glass slides as substrate (gold layer 50 nm, chromium adhesion layer 10 nm). All measurements were performed using a full angular scan (39–78°, scan speed: 8°·s^{-1}).

For the adsorption experiments, solutions of cationic starches have been prepared by heating dispersions with a concentration of 1 mg·ml^{-1} (bone-dry substance) over a period of one hour at 95°C. The resulting clear solutions were then directly used for the adsorption experiments. For the adsorption experiments, the cellulose thin films were allowed to equilibrate for 45 minutes before a continuous flow of the starch solutions was pumped through. The starches were allowed to adsorb

for 10 minutes (flow rate 25 µl·min⁻¹). Afterward, the surfaces have been rinsed with MilliQ water to remove loosely bound material.

The adsorption of cationic starches onto the cellulose surfaces was quantified according to equation 1, which considers the dependence of the angular response of the surface plasmon resonance in dependence of the refractive index increment (dn/dc) of the adsorbing layer.

$$\Gamma = \frac{\Delta\Theta \times k \times d_p}{dn/dc}$$

(1)

For thin layers (<100 nm), k×d$_p$ can be considered constant and can be obtained by calibration of the instrument by determination of the decay wave length λ$_d$. For the SPR Navi 200 used in this study, k×d$_p$ values are approximately $1.09 \cdot 10^{-7}$ cm/° (at 670 nm) and $1.9 \cdot 10^{-7}$ cm/° (at 785 nm) in aqueous systems. Since the degree of substitution of the starches is very low, dn/dc values for native starches have been used (0.150 cm³·g⁻¹) to determine the amount of adsorbed masses. (Theisen, Johann, Deacon, & Harding, 2000)

Dynamic Light Scattering – DLS. The DLS equipment consisted of a diode laser (Coherent Verdi V5, λ= 532 nm) and a goniometer with single-mode fiber detection optics (OZ from GMP, Zürich, Switzerland). The data was acquired by an ALV/SO-SIPD/DUAL photomultiplier with pseudo-cross correlation and an ALV 7004 Digital Multiple Tau Real Time Correlator (ALV, Langen, Germany). The correlation functions were determined and stored by the ALV software package. The light scattering (LS) was measured ten times 30 s at a scattering angle of 90° at 25°C and the resulting correlation functions were averaged. The hydrodynamic radius was calculated by the optimized regulation technique software (Schnablegger & Glatter, 1991) by means of the cumulant method. (Koppel, 1972) All cationic starch solutions have been centrifuged at 4000 rpm for 30 s prior to measurements.

Atomic Force Microscopy – AFM. Surface morphology and roughness of the N_2-dried films were obtained in tapping mode in ambient atmosphere at room temperature by a Veeco Multimode Quadrax MM scanning probe microscope (Bruker; Billerica, MA, USA) using Si-cantilevers (NCH-VS1-W from NanoWorld AG, Neuchatel, Switzerland) with a resonance frequency of 320 kHz and a force constant of 42 $N \cdot m^{-1}$. Root mean square (RMS) roughness calculation and image processing was performed with the Nanoscope software (V7.30r1sr3, Veeco).

X-ray photoelectron spectroscopy: XPS spectra were recorded using a Thermo Scientific instrument equipped with a monochromatic Al-Kα X-ray source (1486.6 eV). High resolution scans were acquired at a pass energy of 50 eV and a step size (resolution) of 0.1 eV. Wide scans were acquired with a pass energy of 100 eV and a step size of 1.0 eV. Photo-electrons were collected using a take-off angle of 90 ° relative to the sample surface. Charge compensation was performed with an argon flood gun. All analyses were performed at room temperature.

Size Exclusion Chromatography (SEC). Size exclusion chromatography was performed on a SEC-3010 equipped with an autosampler, a pump with degasser and a refractive index detector from WGE Dr. Bures (Dallgow, Germany). Two analytical columns from AppliChrom (ABOA CatPhil P-350 300 mm × 8 mm) were used at a flow rate of 1 $ml \cdot min^{-1}$. The temperature of the column oven was set to 30 °C. 0.1 M $NaNO_3$ was used as eluent. The calibration curve was made with pullulan standards purchased from PSS (Mainz, Germany) with molar masses ranging from 1,080 $g \cdot mol^{-1}$ to 708,000 $g \cdot mol^{-1}$.

Contact Angle (CA) and Surface Free Energy (SFE) Determination. Static contact angle measurements were performed with a Drop Shape Analysis System DSA100 (Krüss GmbH, Hamburg, Germany) with a T1E CCD video camera (25 fps) and the DSA1 v 1.90 software. Measurements were done with MilliQ water and di-iodomethane using a droplet size of 3 μl and a

dispense rate of 400 µl·min^{-1}. For these experiments ex-situ coated silicon wafers have been used since the adsorption slot of the SPR slides is just a few mm^2. The ex-situ adsorption was performed in a similar manner as the in situ experiments using SPR. This involved the swelling of the films in water for 45 minutes (deposition of ca 500 µl MilliQ water on a 1 cm × 2 cm cellulose coated silicon wafer), then the water was exchanged by the cationic starch solutions (1 mg·ml^{-1}) and allowed to adsorb for 10 minutes. Afterwards, the samples were rinsed with 500 ml of MilliQ water and dried in air overnight at ambient temperatures. All measurements were performed at least 3 times. SCA were calculated with the Young-Laplace equation and the SFE was determined with the Owen-Wendt-Rabel-Kaelble (OWRK) method. (Kaelble, 1970; Owens & Wendt, 1969; Rabel, 1971)

RESULTS AND DISCUSSION

For the determination of the interaction capacity with cellulose thin films, different industrially relevant cationic starches (CS) were selected which feature very low degrees of substitution (0.030-0.062). As samples four different starches from different origins as well as a blend of two starches have been chosen for this study (**Table 1**).

Table 1. List of cationic starches used in this study including information on source, dry solids content, degree of substitution (DS) and molecular weight.

Source	Label	Dry Solids Content [%]	DS^a	M_n [g·mol^{-1}]	M_w [g·mol^{-1}]	PDI
corn	A	87.3	0.058	7.7×10^4	1.7×10^5	2.18
potato	B	83.9	0.030-0.036	4.3×10^5	1.4×10^6	3.20

corn, potato	Blend A:B 80:20	85.2	0.050-0.056	n.d.	n.d.	n.d.
pea	C	81.9	0.047	3.7×10^5	7.4×10^5	1.99
waxy corn	D	86.9	0.062	1.3×10^6	2.4×10^6	1.94

[a] According to the manufacturer. (n.d. non determined)

Since the investigated starches do not completely dissolve at room temperature in water, they were cooked at appropriate temperatures (95-125°C, 1 mg·ml^{-1} bone-dry substance) over a period of 60 minutes to obtain macroscopically clear solutions suitable for adsorption experiments. It should be noted here that all the starches have been used at their native pH values (5.0-5.8) (**Table S1**); any adjustment of pH value or addition of electrolytes was intentionally avoided for this study. These macroscopically clear solutions were investigated by size exclusion chromatography and dynamic light scattering after cooling to room temperature. Size exclusion chromatography results are in agreement with literature, where molar masses of approximately 10^5-10^6 g·mol^{-1} and 10^7-10^8 g·mol^{-1}, have been determined for amylose and amylopectin respectively. (Banks & Greenwood, 1975) In general, waxy corn starches feature amylose contents of maximum 1% (Pérez & Bertoft, 2010) and therefore CS D displays the highest molar mass of the herein studied starches concomitant with a small polydispersity index. Starches containing relatively high amylose contents, such as pea starch (40-70%) and corn starch (30 %) feature lower molar masses compared to starches derived from waxy corn or potato (20% amylose content). (McCready, Guggolz, Silviera, & Owens, 1950; Rosin, Lajolo, & Menezes, 2002)

As depicted in **Figure 1**, all of the investigated starches form particles with a size (median hydrodynamic diameter) ranging from 57 (CS D) to 100 nm (Blend, CS C). However, the size distribution is at least of bimodal nature and shows larger particles (micron range) as well as very small particles with a size of ca 10 nm. It is important to point out that particles with larger size

lead to a response with higher intensity than smaller particles. Interestingly, there are not any particles in the micron range size present for the starch solutions consisting mostly of amylopectin (CS D). It could be concluded that the large particles present in solutions of the other compounds (CS A, B, and C) are composed of starch clusters formed by aggregation of amylose and amylopectin. (Shirazi, van de Ven, & Garnier, 2003a) Although amylopectin is the starch component with higher molecular weight, it is of branched nature and therefore the hydrodynamic radius is smaller for CS D than for the other starches containing non-branched amylose.
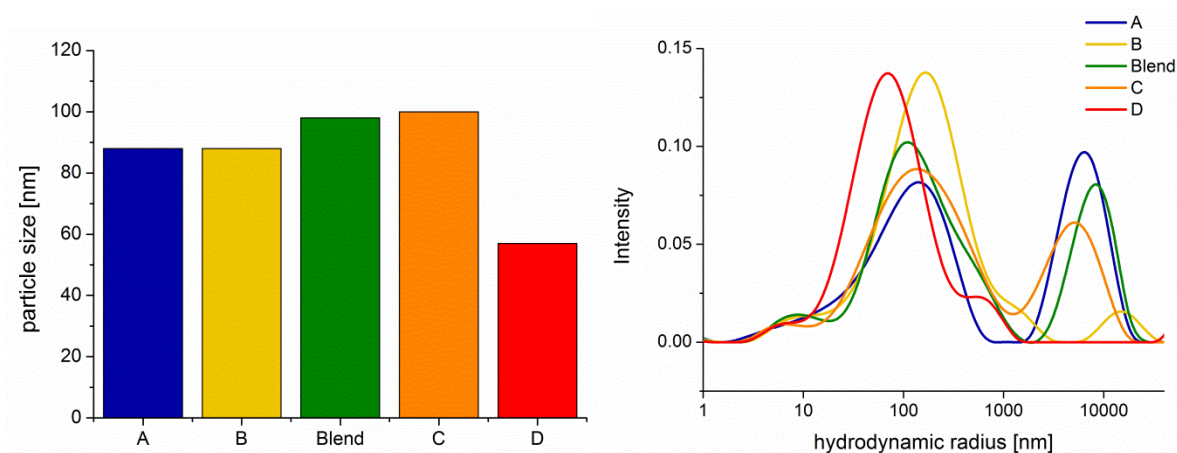
Figure 1. Left: Comparison of the median particle size of the different cationic starches in aqueous solution (c = 1 mg·ml^{-1}) determined by DLS in the 57-100 nm regime. Right: Intensity weighted size distribution of the cationic starch solutions obtained by DLS.

For adsorption experiments using surface plasmon resonance spectroscopy, the same dissolution procedure was applied as for the samples used in SEC and DLS experiments. These adsorption experiments were designed in way that after equilibration of the cellulose thin films over a period of 45 minutes in water, the cationic starches were pumped through the microfluidic channel and allowed to interact until a plateau was reached (i.e. after 10 minutes). Afterwards, the samples were rinsed with water in order to remove loosely bound materials from the cellulose thin films.

The change in the surface plasmon resonance angle is then used to determine the amount of deposited cationic starches onto the surfaces according to equation (1).

As depicted in **Figure 2**, the cationic starches irreversibly adsorb onto the cellulose thin films and a final rinsing step did not remove a significant amount of material from any of the films. This can be attributed to reorientation of the adsorbed molecules as well, since SPR detects changes in refractive index which is traceable to adsorption, desorption or density variations. Furthermore, adsorption occurs spontaneously and kinetics is fast, demonstrating a high affinity of the CS to the cellulose films. However, the extent of adsorption strongly varies for all the investigated samples ranging from 0.74 ± 0.15 (CS D) to ca. 3.94 ± 0.13 mg·m^{-2} (CS A). An exception in terms of kinetics is the starch B sample whose adsorption profile is much slower than for all the other investigated samples. Factors governing the kinetics in the adsorption of polymers can be related to molecular weight and to the PDI, to mention just two parameters. It is known from literature that a polymer with higher PDI is prone to slower adsorption than the same polymer with a smaller PDI. Interestingly, the PDI is the highest for CS B sample which could be the reason for the rather slow adsorption on cellulose thin films. (Kronberg, Holmberg, & Lindman, 2014) This phenomenon initially proven for proteins and often recalled the Vroman effect, relates to species with a lower molar mass which are slowly replaced by those with a higher mass, thereby causing much slower kinetics.
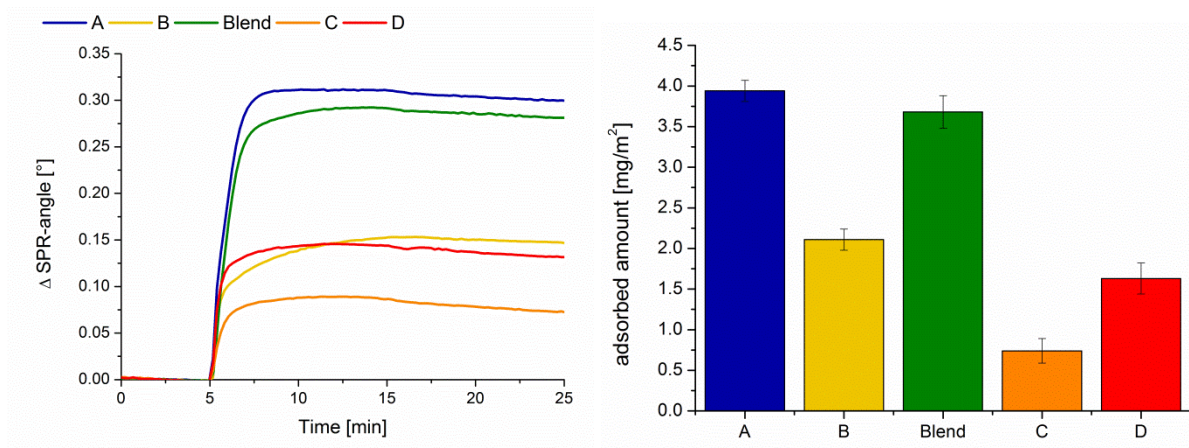
Figure 2. Comparison of the adsorption behavior of the different starches (c= 1 mg·ml^{-1}, flow rate 25 µl·min^{-1}) as a function of the SPR angle (left) and corresponding adsorbed masses (right).

A similar behavior is observed for the blend of CS A and CS B (80:20). Here, the extent of adsorbed material (3.68 ± 0.2 mg·m^{-2}) matches the calculated value of the individual components (3.57 ± 0.13 mg·m^{-2}) but the adsorption kinetics is rather different. In the beginning of the adsorption experiment, the blend behaves like CS A (same slope) with a very fast adsorption rate. However, after 2 minutes the slope of the curve becomes less steep i.e. the adsorption is slower and proceeds in a similar fashion as the curve of CS B. As for the CS B adsorption, the fraction with higher molar mass slowly replaces those with lower molar mass as mentioned in literature for other polymer blends having different molar masses. (Dijt, Cohen Stuart, & Fleer, 1994; Fu & Santore, 1998)

After drying in air at room temperature, the same films from SPR experiments were subjected to XPS measurements to confirm the presence of nitrogen stemming from the cationically charged groups (i.e. ammonium groups) in CS on the cellulose films. The XPS results are shown in **Table 2** and clearly show the presence of the cationic species on those films exposed to CS solutions whereas the neat cellulose films do not contain any nitrogen. However, a quantitative assessment

13

using XPS is not always straightforward since the recorded intensities depend on several parameters e.g. the homogeneous distribution of starch particles throughout the sample. Besides the N_{1s} also the Cl_{2p} signal is observed, which relates to the chloride counterion and matches the nitrogen content. Carbon and oxygen signals arise from the backbone of starch and the underlying cellulose layer, which is plausible since even some signal originating from the gold substrate is detectable to a minor extent. The full survey scans are available in the Supporting Materials (**Figure S1-S6**).

Table 2. Elemental composition (atom%) of the pure and cationically modified cellulose films determined by XPS.

	atom%					
	Cellulose	A	B	blend	C	D
C_{1s}	58.1	59.4	58.9	59.2	59.1	59.2
O_{1s}	38.0	36.8	38.5	37.9	39.0	38.9
N_{1s}	**<LOD**	**0.8**	**1.1**	**1.1**	**0.9**	**1.0**
Cl_{2p}	<0.5	1.0	0.9	0.9	0.8	1.0

Further, the SPR samples were subjected to atomic force microscopy. The topography images (**Figure 3**) do not exhibit large differences between the different samples before and after adsorption, albeit a decrease in surface roughness is observed after CS adsorption. This can be explained by cationic starch particles filling the pores and holes present on the cellulose thin film. Despite the similar chemical nature of adsorbens and the cellulose surface, the amplitude images provide (**Figure 4**) better insights. In those images, it can be clearly seen that larger particulates are present for CS A and the blend, whereas for the other samples rather small features are present. The size of these features is in good agreement with the results obtained by DLS, where both, CS

A and the blend, feature a bimodal size distribution with some large particles. CS C displays aggregates with large particles size too, however, the amount deposited on the cellulose films is rather low to be detected by AFM.
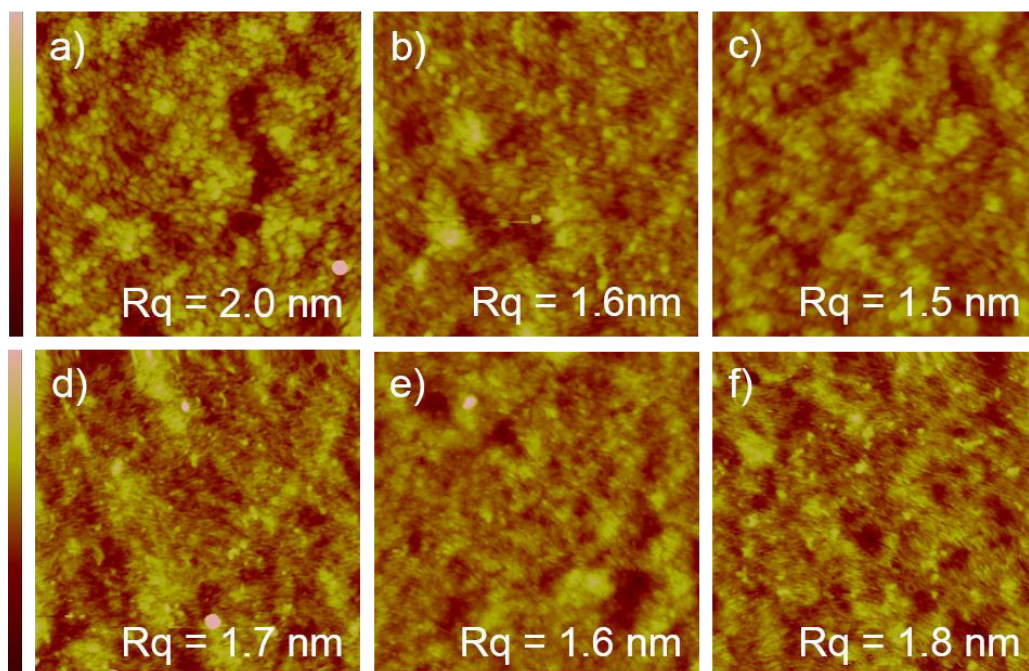
Figure 3. Comparison of AFM topography images (1x1 μm^2, z-scale 20 nm) of the different samples before (a) and after adsorption (b-f). b: CS A, c: CS B, d: blend, e: CS C, f: CS D. All samples have been measured in air at ambient atmosphere.
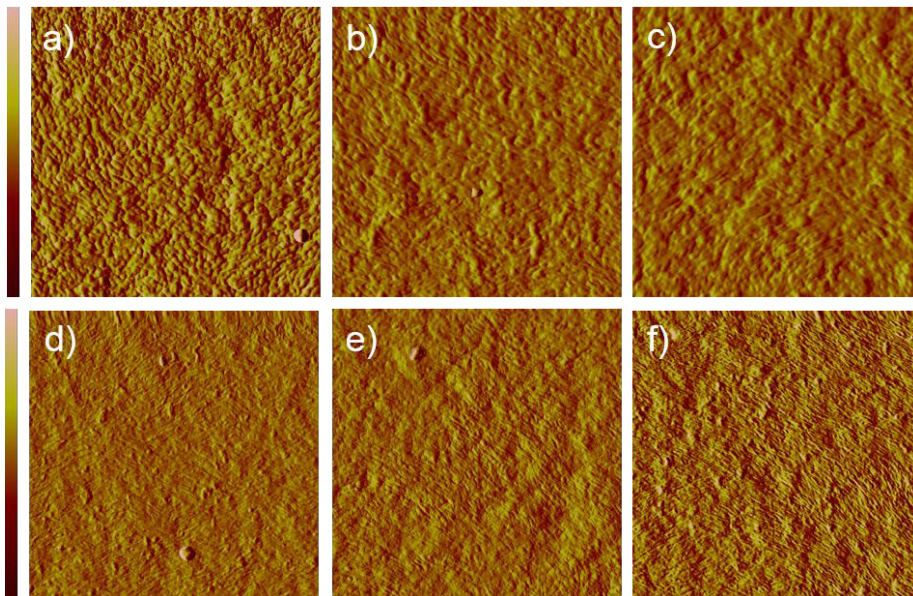
Figure 4. Comparison of AFM amplitude images (1x1 μm^2, z-scale 10mV) of the different samples before (a) and after adsorption (b-f). b: CS A, c: CS B, d: blend, e: CS C, f: CS D. All samples have been measured in air at ambient atmosphere.

The modification of a surface by a charged polymer should impact the hydrophilicity of the surface to some extent as well. The surface free energies of the films, determined by wettability studies using water and diiodomethane, increased after the deposition of the cationic starches on the surfaces (**Figure 5**). However, the increase in SFE does not significantly relate to the amount of cationic starch deposited on the surface and SFEs in the range of 70 mJ·m^{-2} have been determined. Only for the sample with the lowest affinity, a slightly lower SFE was observed. However, even for the CS with a rather low affinity to the surface, the SFE increased compared to cellulose (67 mJ·m^{-2} for CS D vs. 62 mJ·m^{-2} for cellulose). The increase in SFE can be mainly attributed to higher polar contributions to SFE in the case of CS compared to cellulose.
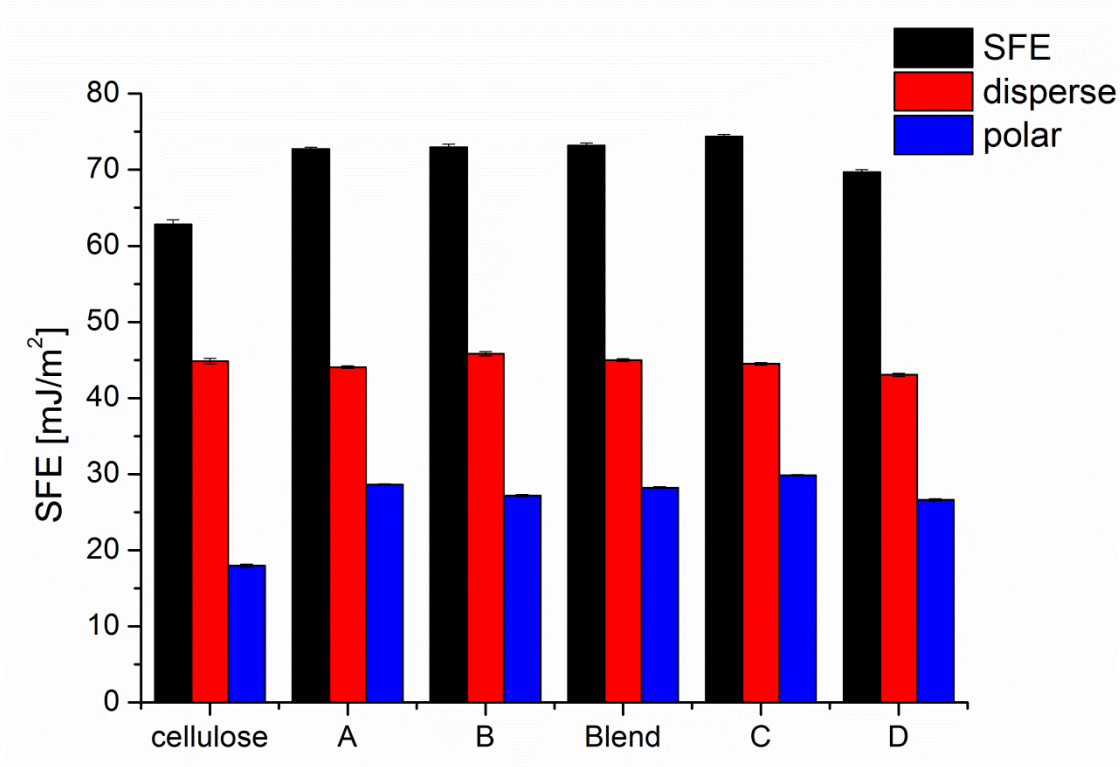
Figure 5. Comparison of the SFE of non-modified cellulose thin films and those modified with CS.

The results can be rationalized in following respects. The interaction of any type of polymer with a surface is governed by the properties of the individual components (e.g. charge density), the conformation of the adsorbens (flat vs. coiled) and the solubility of the polymer at the interface.(Dobrynin & Rubinstein, 2005) The SPR data shows significant differences in the interaction capacity of cellulose thin films with different cationic starches. These differences depend partially on the charge of the substrate and the adsorbens. However, for the industrially relevant CS, the amount of cationic groups is rather low. When considering an average length of 0.5 nm of an anhydrous glucose unit (AGU), the mean distance between the charges ranges from 8 to 15 nm for the CS with the lowest and highest DS, respectively. Considering the molecular weights of the different compounds employed in this study, the amount of charged groups that are

present on the polymer backbone were calculated and are shown in **Table 3**. The calculations assume perfectly flat, non aggregated starch molecules and neither take into account the uneven distribution of the cationic groups within the starch molecules nor the difference in cationization of amylose and amylopectin within the type of CS. In general, amylose is better accessible for cationic modification than amylopectin leading to a higher DS. (Steeneken & Smith, 1991) Despite the low mean number of charges per molecule compared to cationic starches with higher degree of substitution, a relatively high interaction capacity is found for the starches applied in this study. In terms of nitrogen content determined by XPS, all the modified cellulose featured higher N contents than those reported in literature where many CS with higher DS had been used (0.2 and 0.75). (K. S. Kontturi et al., 2008)

Table 3. Mean distance between charges, mean length of starch molecules and number of cationic charges present on the polymer backbone in an extended flat conformation of different CS calculated from molecular weights and DS.

	mean distance charges [nm]	mean length molecule [nm]	mean number of charges
A	8.6	376	44
B	15.2	2810	185
Blend	9.4	3514	372
C	10.6	1715	161
D	8.1	5690	706

Results from cationic starches with the same particle size reveal the influence of the DS and the amount of cationic charges at the polymer backbone. For instance, CS A (3.94 ± 0.13 mg·m^{-2}) and CS B (2.11 ± 0.13 mg·m^{-2}) features the same particle size, but a different DS. Higher DS basically

leads to more electrostatic attraction between the cellulosic substrate and the compound leading to more pronounced interaction and finally adsorption. Additionally, CS A and CS B have a similar content of amylose, therefore the uneven distribution of cationic charges between amylose and amylopectin can be considered negligible. This effect is observed for the blend (3.68 ± 0.2 mg·m^{-2}) and CS C (0.74 ± 0.15 mg·m^{-2}) as well. In this case, the amylose content differs, which may have an effect in the adsorption behavior.

CS B and CS C (**Table 3**) exhibit different adsorption capacities on the cellulose films, even though they contain a similar amount of cationic charges. Interestingly, the compound with the higher DS (CS C) adsorbs to a lesser extent, whereby the adsorbed amount of the CS that forms the smaller aggregates (CS B) is more than twice as high. This indicates that besides the DS, additional factors influence the adsorption behavior of the cationic starches. One of these factors is the solubility of the polymers which is dependent on molecular weight, the amylose/amylopectin ratio and the charge. (Kronberg et al., 2014) Polymer solubility increases with the amount of charges on a polyelectrolyte leading to lower adsorption. However, this is in contradiction with the electrostatic interaction between adsorbens and substrate, since a high DS favors electrostatic attraction to the negatively charged cellulose substrate. This phenomenon is observed for compounds with the same particle size, such as CS A and CS B or the blend and CS C, where electrostatic attraction is overruled by solubility. Besides charge, molecular weight and particle size control the solubility. In principle, low molecular weight polymers are better soluble than those with high molecular weight, therefore large molecules tend to adsorb in larger amounts but - as already discussed above - slower. The same effect applies for particle sizes. Different observations have been made by Shirazi and coworkers, who investigated the adsorption of cationic starches on pulp fibers. (Shirazi, van de Ven, & Garnier, 2003b) They proposed an initial

adsorption step of starch aggregates followed by a deposition of individual macromolecules onto the cellulose fiber surface.

The influence of particle hydrodynamic radius can be illustrated by comparing CS A (88 nm), the blend (98 nm) and CS D (57 nm), all having a similar DS. Compared to CS D for instance, larger amounts of CS A and the blend (compared to CS D) adsorb onto the cellulose films since larger particles are less soluble and tend to adsorb to a higher extent. Moreover, conformation and the resulting availability of attachment sites are decisive factors as well. As seen in the above mentioned case of CS C and CS B, this parameter is important and can be ascribed to the amylose content of the starches. Since amylose is the low molecular polymer in starch and is better accessible to the cationization procedure than amylopectin, therefore featuring a higher DS, the amylose proportion of the cationic starch keeps dissolved while larger starch clusters adsorb. CS D, the cationic starch with the highest molecular weight and amylopectin content, displays theoretically the highest amount of charges (~706) present on the polymer backbone. However, due to the conformation of amylopectin, fewer charges are accessible for interaction with the surface. (Shirazi et al., 2003b; Swerin & Wågberg, 1994) The branched structure of amylopectin permits less freedom in chain movement and does not easily rearrange compared to amylose. In addition to that, CS D forms rather small particles, thereby increasing their solubility.

Of course ionic strength is an essential parameter in the interaction of oppositely charged materials, because it impacts conformation by charge screening. Although the investigation of the influence of ionic strength on the adsorption behavior was not the main focus of this work, for the sake of comparison one sample (CS B) was selected and adsorbed at different electrolyte concentrations (1 mM, 10mM, 100 mM NaCl) in the same SPR setup as for the other samples. The results are summarized in **Figure S8-S12**. Results follow the expected trends and fit to data

reported in literature. (Shirazi et al., 2003b) The particle size of CS B decreases upon addition of salt to the CS solution from 88 nm (pure water) to approximately 75 nm due to screening of the positive charges and reduction of electrostatic repulsion in the polymer. The increase of the ionic strength to 1 mM NaCl leads to a higher extent of adsorption. However, a further increase in salt concentration does not only decrease intramolecular repulsion but the surface-starch interactions are screened too, leading to even smaller adsorbed amounts of CS B than in pure water.

CONCLUSION

In summary, the adsorption behavior of industrially relevant cationic starches with low degrees of substitution (0.03-0.06) on cellulose thin films was investigated in the absence of any electrolytes and at native pH value of the starches. It turned out that all the investigated starches irreversibly adsorb onto cellulose, whereas the extent of mass deposited on the surfaces varies from ca 0.7 to ca 4.0 mg·m^{-2}. For CS with the same size, the adsorption capacity is mainly influenced by the DS. For those CS, a high DS leads to higher deposition on the surface. In these cases, electrostatic interactions overcome solubility of the polymers. When it comes to starches with very similar DS, the particle size dominates adsorption, since smaller particles are better soluble and therefore adsorb to a lesser extent. Another crucial factor is the conformation of the polymer and concomitant the availability of attachment sites, which is among others dependent on the amylose-amylopectin ratio of the starch. In conclusion, cationic starch adsorption behavior is primarily governed by the interplay of solubility and electrostatic interaction which are both influenced by different parameters such as particle size, molecular weight, conformation and DS. Currently, we are investigating whether these results are transferable to industrially manufactured materials such as fibers and papers.

REFERENCES

Banks, W., & Greenwood, C. T. (1975). *Starch and its Components*. New York: Wiley.

Dijt, J. C., Cohen Stuart, M. A., & Fleer, G. J. (1994). Competitive Adsorption Kinetics of Polymers Differing in Length Only. *Macromolecules,* 27(12), 3219-3228.

Dobrynin, A. V., Deshkovski, A., & Rubinstein, M. (2001). Adsorption of Polyelectrolytes at Oppositely Charged Surfaces. *Macromolecules,* 34(10), 3421-3436.

Dobrynin, A. V., & Rubinstein, M. (2005). Theory of polyelectrolytes in solutions and at surfaces. *Progress in Polymer Science,* 30(11), 1049-1118.

Fu, Z., & Santore, M. M. (1998). Competitive Adsorption of Poly(ethylene oxide) Chains with and without Charged End Groups. *Langmuir,* 14(15), 4300-4307.

Geffroy, C., Labeau, M. P., Wong, K., Cabane, B., & Cohen Stuart, M. A. (2000). Kinetics of adsorption of polyvinylamine onto cellulose. *Colloids and Surfaces A: Physicochemical and Engineering Aspects,* 172(1–3), 47-56.

Guan, Y., Qian, L., Xiao, H., & Zheng, A. (2008). Preparation of novel antimicrobial-modified starch and its adsorption on cellulose fibers: Part I. Optimization of synthetic conditions and antimicrobial activities. *Cellulose,* 15(4), 609-618.

Guan, Y., Qian, L., Xiao, H., Zheng, A., & He, B. (2008). Synthesis of a novel antimicrobial-modified starch and its adsorption on cellulose fibers: part II—adsorption behaviors of cationic starch on cellulose fibers. *Cellulose,* 15(4), 619-629.

Hasani, M., Cranston, E. D., Westman, G., & Gray, D. G. (2008). Cationic Surface Functionalization of Cellulose Nanocrystals. *Soft Matter,* 4, 2238-2244.

Kaelble, D. H. (1970). Dispersion-Polar Surface Tension Properties of Organic Solids. *J. Adhes. ,* 2, 66-81.

Kontturi, E., Thüne, P. C., & Niemantsverdriet, J. W. (2003). Cellulose Model Surfaces Simplified Preparation by Spin Coating and Characterization by X-ray Photoelectron Spectroscopy, Infrared Spectroscopy, and Atomic Force Microscopy. *Langmuir,* 19(14), 5735-5741.

Kontturi, K. S., Holappa, S., Kontturi, E., Johansson, L.-S., Hyvärinen, S., Peltonen, S., & Laine, J. (2009). Arrangements of cationic starch of varying hydrophobicity on hydrophilic and hydrophobic surfaces. *Journal of Colloid and Interface Science,* 336(1), 21-29.

Kontturi, K. S., Tammelin, T., Johansson, L.-S., & Stenius, P. (2008). Adsorption of Cationic Starch on Cellulose Studied by QCM-D. *Langmuir,* 24(9), 4743-4749.

Koppel, D. E. (1972). Analysis of Macromolecular Polydispersity in Intensity Correlation Spectroscopy: The Method of Cumulants. *The Journal of Chemical Physics,* 57(11), 4814-4820.

Kronberg, B., Holmberg, K., & Lindman, B. (2014). *Adsorption of Polymers at Solid Surfaces*. In *Surface Chemistry of Surfactants and Polymers* (pp. 211-229): John Wiley & Sons, Ltd

Lee, S. H., Lee, H. L., & Youn, H. J. (2014). Adsorption and viscoelastic properties of cationic xylan on cellulose film using QCM-D. *Cellulose,* 21(3), 1251-1260.

McCready, R. M., Guggolz, J., Silviera, V., & Owens, H. S. (1950). Determination of Starch and Amylose in Vegetables. *Analytical Chemistry,* 22(9), 1156-1158.

Mohan, T., Niegelhell, K., Zarth, C. S. P., Kargl, R., Köstler, S., Ribitsch, V., Heinze, T., Spirk, S., & Stana-Kleinschek, K. (2014). Triggering Protein Adsorption on Tailored Cationic Cellulose Surfaces. *Biomacromolecules,* 15(11), 3931-3941.

Mohan, T., Ristic, T., Kargl, R., Doliska, A., Köstler, S., Ribitsch, V., Marn, J., Spirk, S., & Stana-Kleinschek, K. (2013). Cationically rendered biopolymer surfaces for high protein affinity support matrices. *Chem. Comm.,* 49, 11530-11532.

Mohan, T., Spirk, S., Kargl, R., Doliška, A., Ehmann, H. M. A., Köstler, S., Ribitsch, V., & Stana-Kleinschek, K. (2012). Watching cellulose grow – Kinetic investigations on cellulose thin film formation at the gas–solid interface using a quartz crystal microbalance with dissipation (QCM-D). *Colloids and Surfaces A: Physicochemical and Engineering Aspects,* 400, 67-72.

Mohan, T., Spirk, S., Kargl, R., Doliska, A., Vesel, A., Salzmann, I., Resel, R., Ribitsch, V., & Stana-Kleinschek, K. (2012). Exploring the rearrangement of amorphous cellulose model thin films upon heat treatment. *Soft Matter,* 8, 9807-9815.

Mohan, T., Zarth, C., Doliska, A., Kargl, R., Grießer, T., Spirk, S., Heinze, T., & Stana-Kleinschek, K. (2013). Interactions of a cationic cellulose derivative with an ultrathin cellulose support. *Carbohydr. Polym.,* 92, 1046-1053.

Nachtergaele, W. (1989). The Benefits of Cationic Starches for the Paper Industry. *Starch - Stärke,* 41(1), 27-31.

Nechwatal, A., Michels, C., Kosan, B., & Nicolai, M. (2004). Lyocell blend fibers with cationic starch: potential and properties. *Cellulose (Dordrecht, Neth.),* 11(2), 265-272.

Niegelhell, K., Süßenbacher, M., Jammernegg, K., Ganner, T., Schwendenwein, D., Schwab, H., Stelzer, F., Plank, H., & Spirk, S. (2016). Enzymes as Biodevelopers for Nano- And Micropatterned Bicomponent Biopolymer Thin Films. *Biomacromolecules,* 17(11), 3743-3749.

Orelma, H., Filpponen, I., Johansson, L.-S., Laine, J., & Rojas, O. J. (2011). Modification of Cellulose Films by Adsorption of CMC and Chitosan for Controlled Attachment of Biomolecules. *Biomacromolecules,* 12(12), 4311-4318.

Orelma, H., Johansson, L.-S., Filpponen, I., Rojas, O. J., & Laine, J. (2012). Generic Method for Attaching Biomolecules via Avidin-Biotin Complexes Immobilized on Films of Regenerated and Nanofibrillar Cellulose. *Biomacromolecules,* 13, 2802-2810.

Owens, D. K., & Wendt, R. C. (1969). Estimation of the surface free energy of polymers. *Journal of Applied Polymer Science,* 13(8), 1741-1747.

Pérez, S., & Bertoft, E. (2010). The molecular structures of starch components and their contribution to the architecture of starch granules: A comprehensive review. *Starch - Stärke,* 62(8), 389-420.

Petersen, H., Radosta, S., Vorwerg, W., & Kießler, B. (2013). Cationic starch adsorption onto cellulosic pulp in the presence of other cationic synthetic additives. *Colloids and Surfaces A: Physicochemical and Engineering Aspects,* 433, 1-8.

Rabel, W. (1971). Einige Aspekte Der Benetzungstheorie Und Ihre Anwendung Auf Die Untersuchung Und Veränderung Der Oberflächeneigenschaften von Polymeren. *Farbe und Lack,* 77, 997-1005.

Rohm, S., Hirn, U., Ganser, C., Teichert, C., & Schennach, R. (2014). Thin cellulose films as a model system for paper fibre bonds. *Cellulose,* 21(1), 237-249.

Rosin, P. M., Lajolo, F. M., & Menezes, E. W. (2002). Measurement and Characterization of Dietary Starches. *Journal of Food Composition and Analysis,* 15(4), 367-377.

Schaub, M., Wenz, G., Wegner, G., Stein, A., & Klemm, D. (1993). Ultrathin films of cellulose on silicon wafers. *Advanced Materials,* 5(12), 919-922.

Schnablegger, H., & Glatter, O. (1991). Optical sizing of small colloidal particles: an optimized regularization technique. *Applied Optics,* 30(33), 4889-4896.

Schwikal, K., Heinze, T., Saake, B., Puls, J., Kaya, A., & Esker, A. R. (2011). Properties of spruce sulfite pulp and birch kraft pulp after sorption of cationic birch xylan. *Cellulose,* 18, 727–737.

Shirazi, M., van de Ven, T. G. M., & Garnier, G. (2003a). Adsorption of Modified Starches on Porous Glass. *Langmuir,* 19(26), 10829-10834.

Shirazi, M., van de Ven, T. G. M., & Garnier, G. (2003b). Adsorption of Modified Starches on Pulp Fibers. *Langmuir,* 19(26), 10835-10842.

Steeneken, P. A. M., & Smith, E. (1991). Topochemical effects in the methylation of starch. *Carbohydrate Research,* 209, 239-249.

Strasser, S., Niegelhell, K., Kaschowitz, M., Markus, S., Kargl, R., Stana-Kleinschek, K., Slugovc, C., Mohan, T., & Spirk, S. (2016). Exploring Nonspecific Protein Adsorption on Lignocellulosic Amphiphilic Bicomponent Films. *Biomacromolecules,* 17(3), 1083-1092.

Swerin, A., & Wågberg, L. (1994). Size-exclusion chromatography for characterization of cationic polyelectrolytes used in papermaking. *Nordic Pulp & Paper Research Journal,* 09(1), 018-025.

Tammelin, T., Merta, J., Johansson, L.-S., & Stenius, P. (2004). Viscoelastic Properties of Cationic Starch Adsorbed on Quartz Studied by QCM-D. *Langmuir,* 20, 10900-10909.

Tammelin, T., Saarinen, T., Österberg, M., & Laine, J. (2006). Preparation of Langmuir/Blodgett-cellulose Surfaces by Using Horizontal Dipping Procedure. Application for Polyelectrolyte Adsorption Studies Performed with QCM-D. *Cellulose,* 13(5), 519.

Terada, E., Samoshina, Y., Nylander, T., & Lindman, B. (2004a). Adsorption of Cationic Cellulose Derivative/Anionic Surfactant Complexes onto Solid Surfaces. II. Hydrophobized Silica Surfaces. *Langmuir,* 20, 6692-6701.

Terada, E., Samoshina, Y., Nylander, T., & Lindman, B. (2004b). Adsorption of Cationic Cellulose Derivatives/Anionic Surfactant Complexes onto Solid Surfaces. I. Silica Surfaces. *Langmuir,* 20, 1753-1762.

Theisen, A., Johann, C., Deacon, M., & Harding, S. (2000). *Refractive Increment Data-Book for Polymer and Biomolecular Scientists*: Nottingham University Press.

Yokota, S., Kitaoka, T., & Wariishi, H. (2007). Surface morphology of cellulose films prepared by spin coating on silicon oxide substrates pretreated with cationic polyelectrolyte. *Applied Surface Science,* 253(9), 4208-4214.
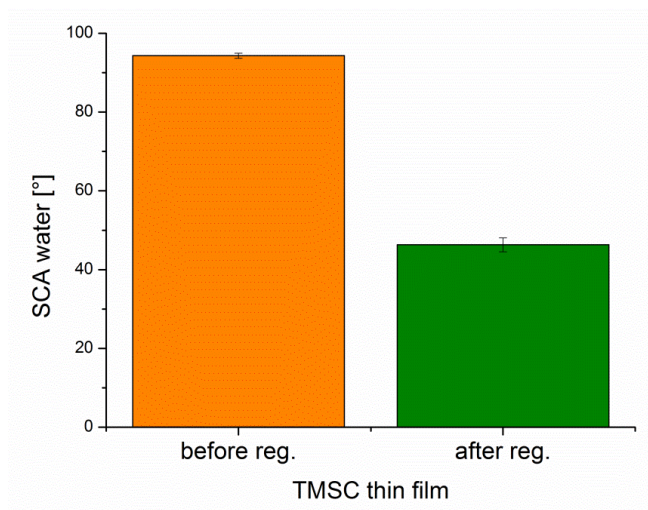
Supporting Information #7

Interaction of Industrially Relevant Cationic Starches with Cellulose

submitted to Carbohydrate Polymers
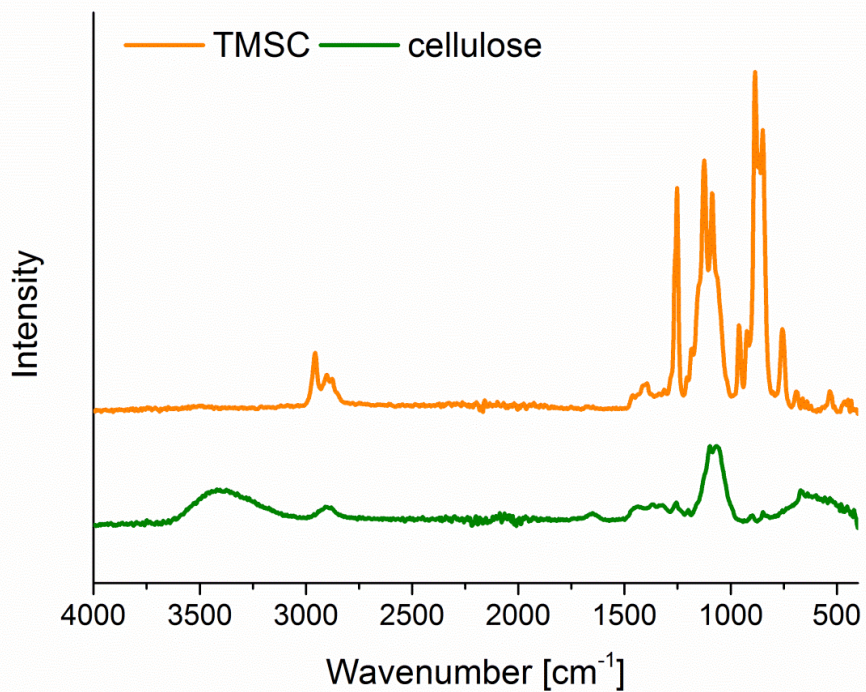
Figure S1. ATR-IR spectra of a TMSC film deposited on a gold substrate and a regenerated TMSC film confirm the regeneration of TMSC to cellulose.


Figure S2. Comparison of contact angles of TMSC thin films before and after regeneration. Contact angles show typical values for TMSC and cellulose before and after treatment with HCl vapors, respectively.

XPS.

XPS survey scans of all samples show signals for O_{1s}, C_{1s}, Cl_{2p}, Au_{4f}, N_{1s}, Si_{2p} and Na_{1s} at binding energies of 533 eV, 286-287 eV, 198-199 eV, 85 eV, 402 eV, 102 eV and 1071-1072 eV respectively. The blank displays signals for O_{1s}, C_{1s} and Si_{2p}.
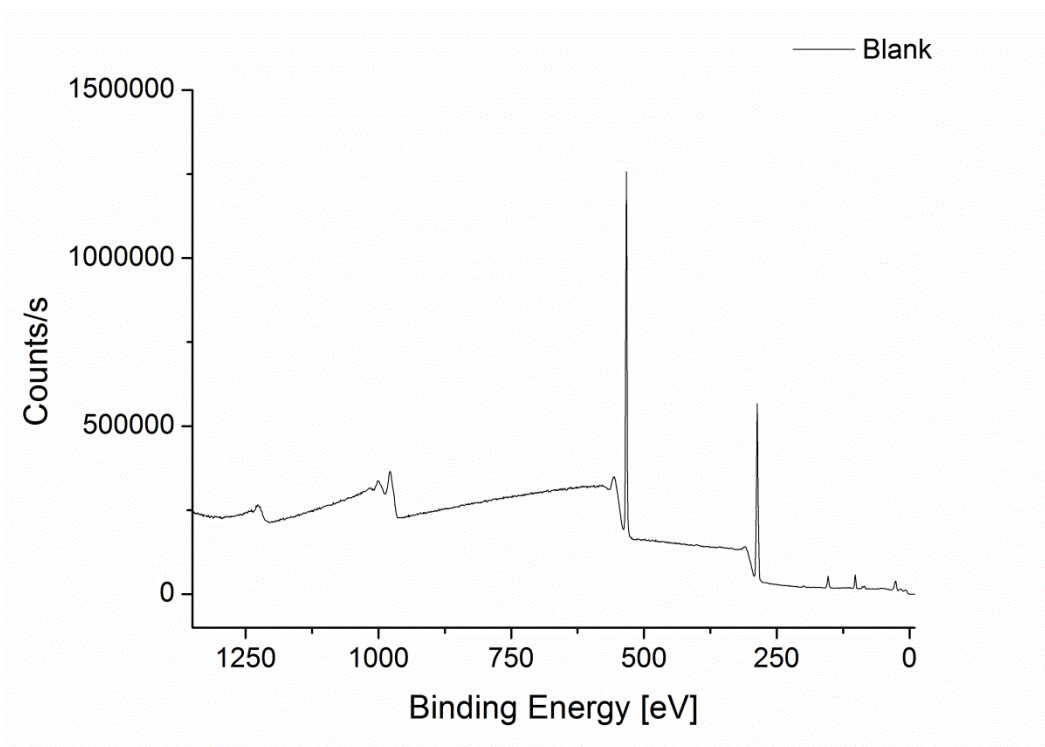
Figure S3. XPS survey scan blank (cellulose thin film on gold sensor slide).
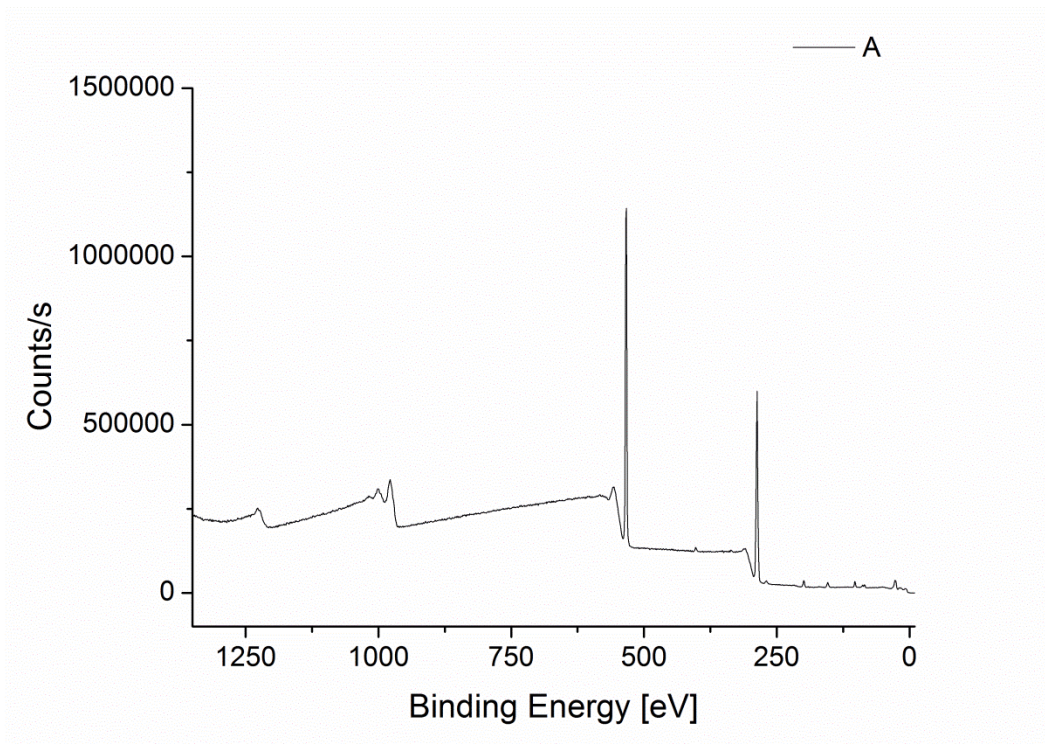
Figure S4. XPS survey scan of cationic starch A adsorbed onto a cellulose thin film.
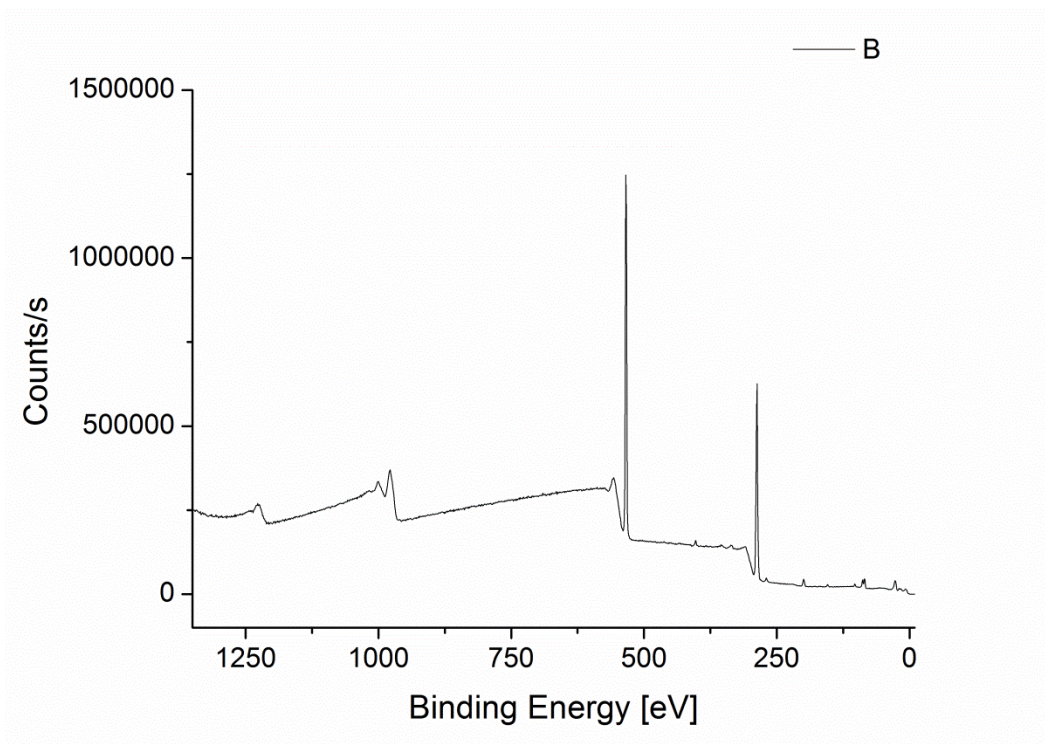
Figure S5. XPS survey scan of cationic starch B adsorbed onto a cellulose thin film.
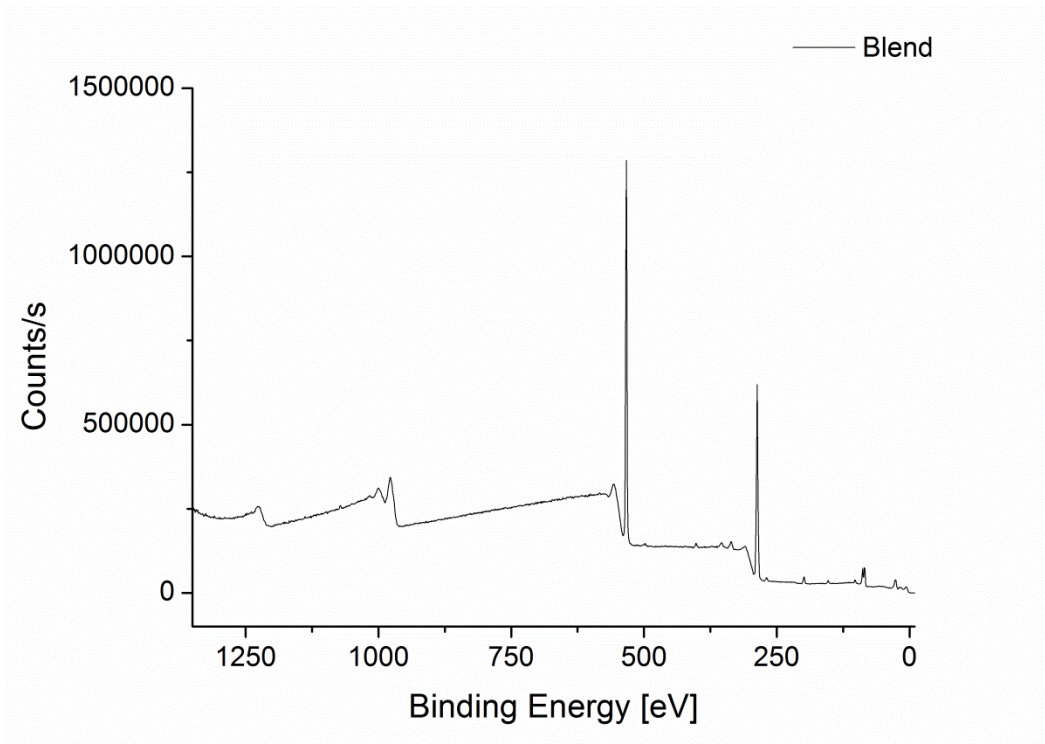
Figure S6. XPS survey scan of cationic starch blend adsorbed onto a cellulose thin film.
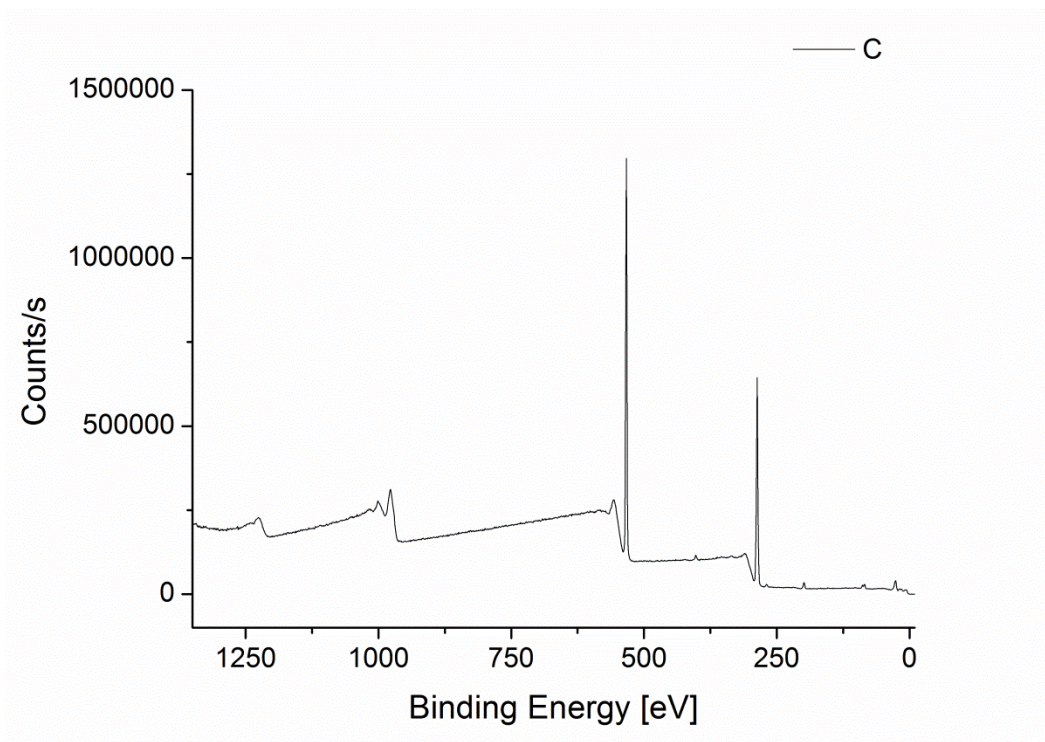
Figure S7. XPS survey scan of cationic starch C adsorbed onto a cellulose thin film.
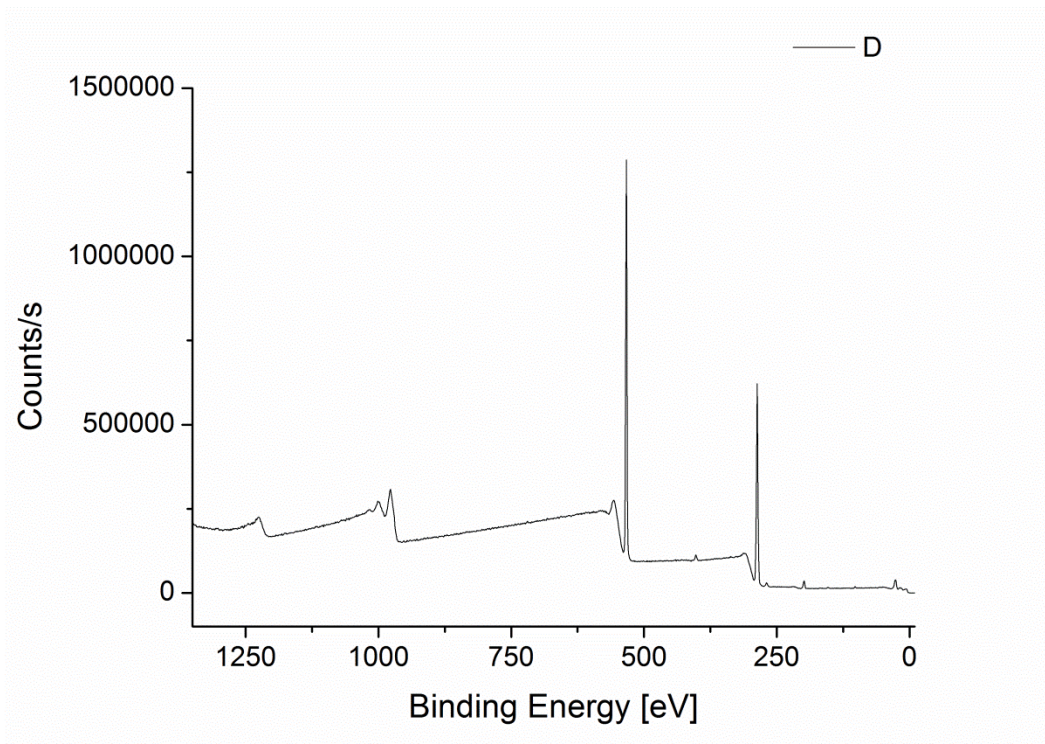
Figure S8. XPS survey scan of cationic starch D adsorbed onto a cellulose thin film.

Table S1. pH values of different cationic starch solutions after cooking at a concentration of 1 mg·ml^{-1} in water.

Starch	pH value
A	5.7
B	5.6
Blend	5.8
C	5.5
D	5.0
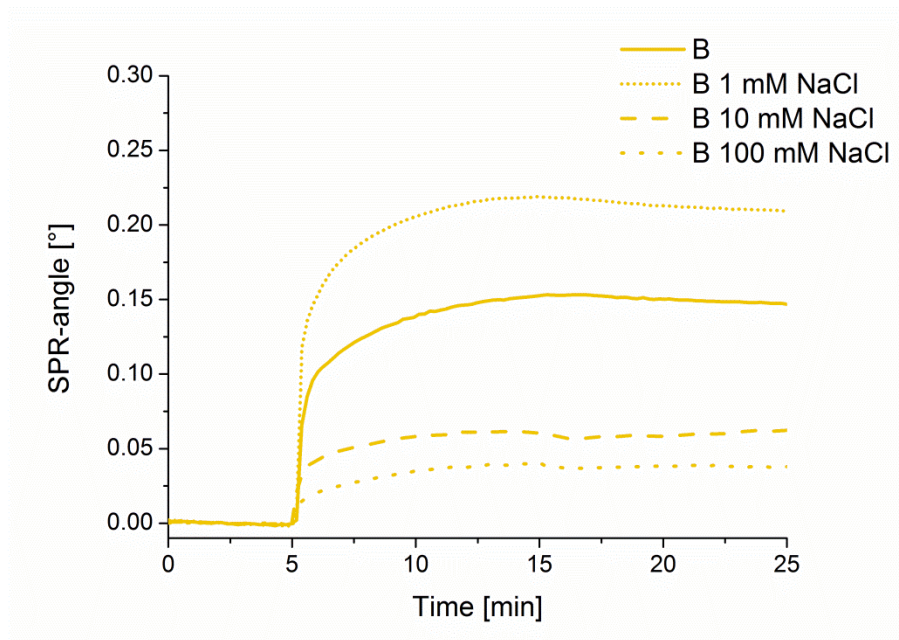
Figure S9. Comparison of the adsorption behavior of cationic starch B at different ionic strengths measured at 785 nm.
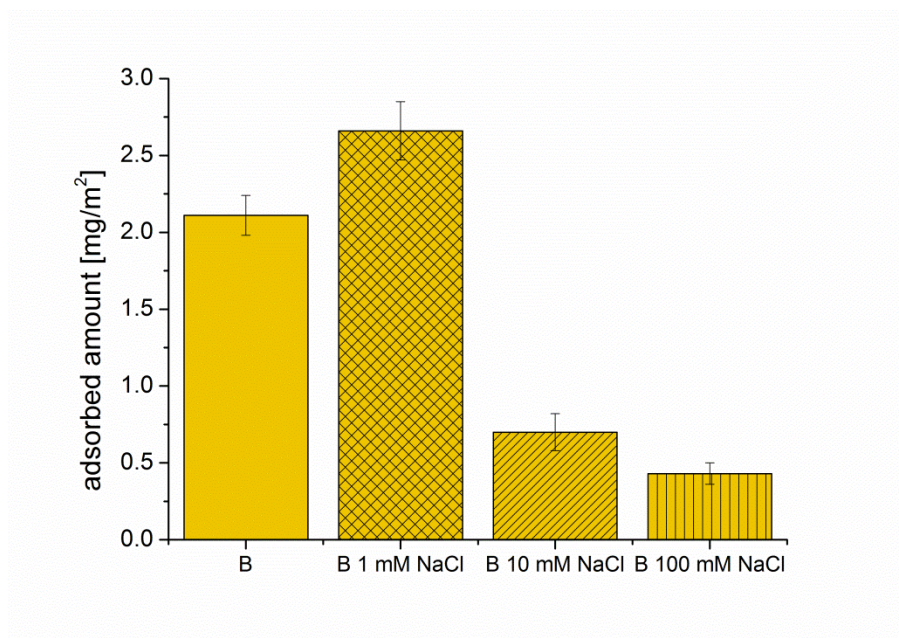
Figure S10. Comparison of adsorbed amounts (calculated from change in SPR angle) of cationic starch B at different ionic strengths.
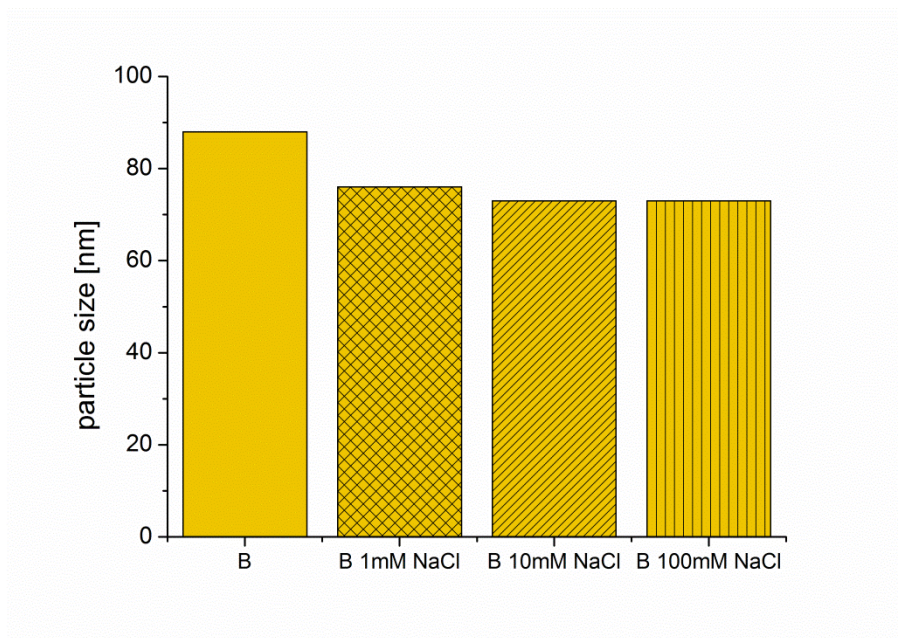
Figure S11. Comparison of the particle sizes of cationic starch B determined by DLS at different ionic strengths.
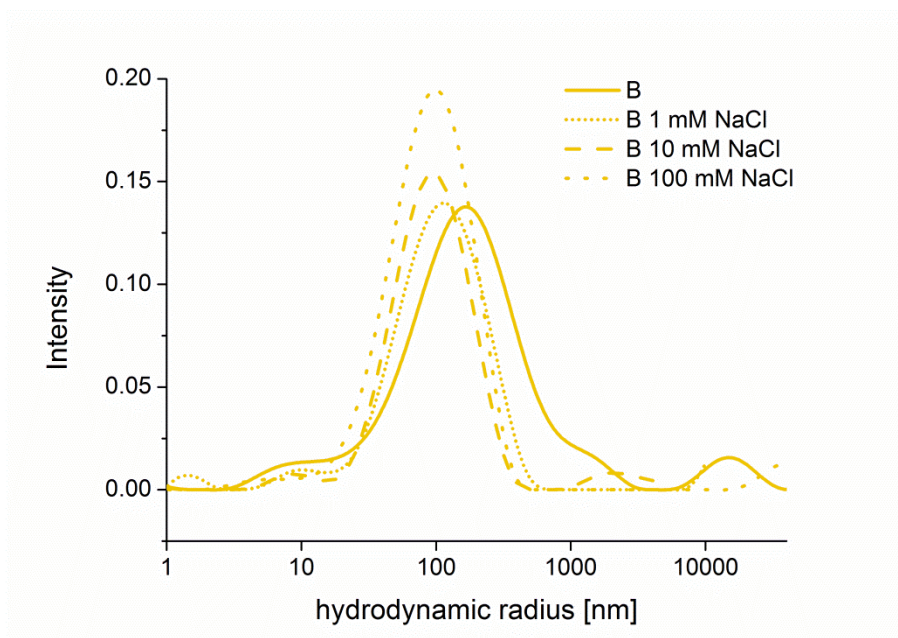
Figure S12. Comparison of intensity weighted size distribution of cationic starch B at different ionic strengths measured by means of DLS.

Calculation of charged numbers present on the polymer backbone.

All values were calculated from M_n and M_w and a mean value was determined.

Length AGU = 0.5 nm

Molecular mass AGU = 162.14 g/mol

$$distance\ charges = \frac{length\ AGU}{DC}$$

$$number\ AGU = \frac{molecular\ weight\ polymer}{162.14\ g/mol}$$

$$length\ molecule = \ number\ AGU \times length\ AGU$$

$$number\ of\ charges = \frac{length\ molecule}{distance\ charges}$$
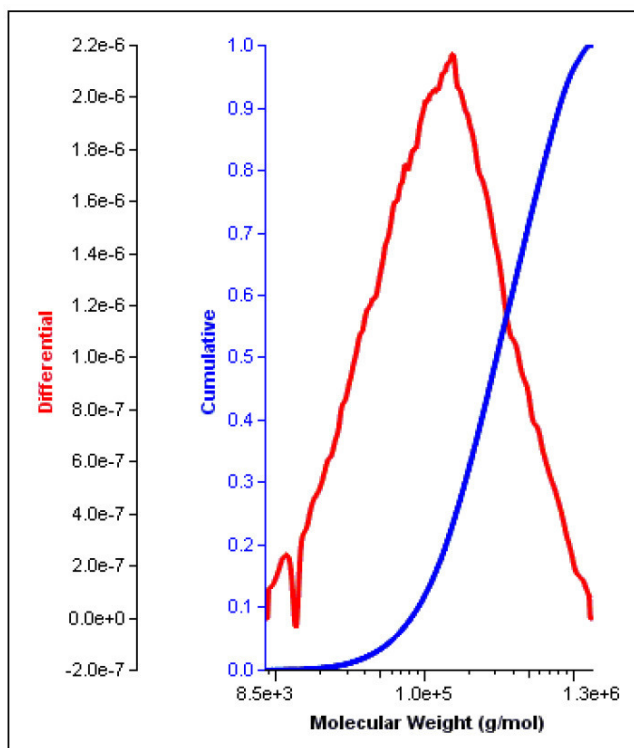
Figure S13. Molecular weight distribution of CS A measured by GPC.
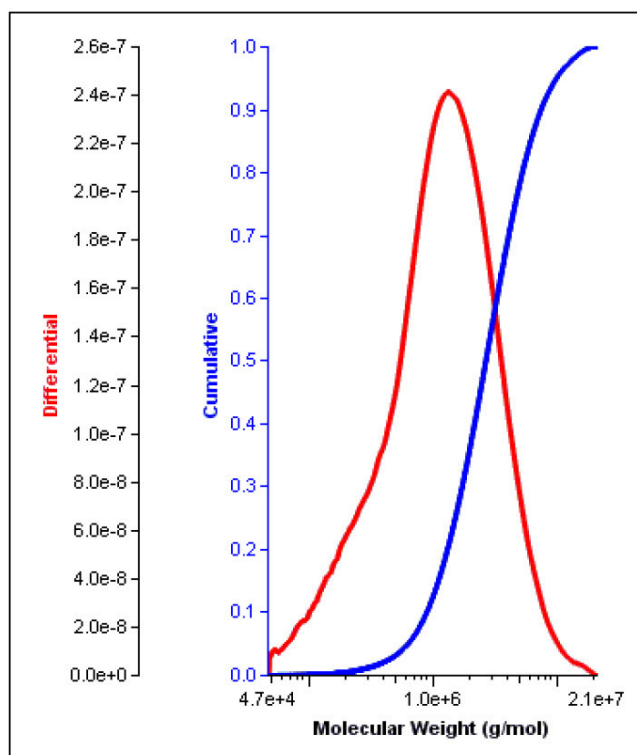
Figure S14. Molecular weight distribution of CS B measured by GPC.
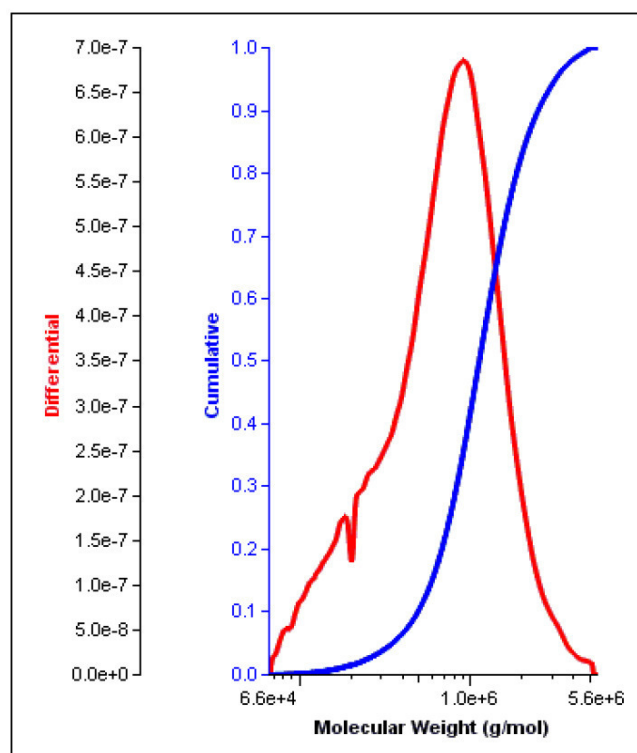
Figure S15. Molecular weight distribution of CS C measured by GPC.
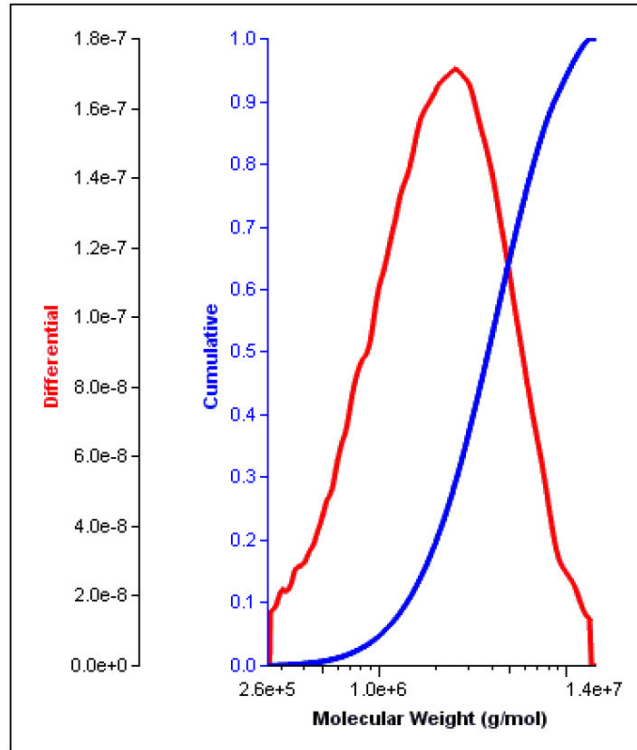
Figure S16. Molecular weight distribution of CS D measured by GPC.

PAPER #8

Topography Effects in AFM Force Mapping Experiments on Xylan-Decorated Cellulose Thin Films

For this paper, I conducted the MP-SPR spectroscopy experiments and interpreted the corresponding data.

Christian Ganser[a], Katrin Niegelhell[a], Caterina Czibula[a], Angela Chemelli[a], Christian Teichert[a], Robert Schennach[a] and Stefan Spirk[a,*]

Topography effects in AFM force mapping experiments on xylan-decorated cellulose thin films

Abstract: Xylan-coated cellulose thin films has been investigated by means of atomic force microscopy (AFM) and force mapping experiments. The birch xylan deposition on the film was performed under control by means of a multiple parameter surface plasmon resonance spectroscopy (MP-SPR) under dynamic conditions. The coated films were submitted to AFM in phase imaging mode to force mapping with modified AFM tips (sensitive to hydrophilic OH and hydrophobic CH_3 groups) in order to characterize and localize the xylan on the surfaces. At the first glance, a clear difference in the adhesion force between xylan-coated areas and cellulose has been observed. However, these different adhesion forces originate from topography effects, which prevent an unambiguous identification and subsequent localization of the xylan on the cellulosic surfaces.

Introduction

In pioneering times of cellulose research its main directions have been dominated by large cellulose processing industries, while more recently diverse nanocelluloses such as cellulose nanocrystals (CNC), cellulose nanofibers (CNF), and cellulose films have been the focus. The latter serve to design new platforms for sensing, transistors, catalysts, but also to get better insights in the basic fundamental phenomena of cellulosic substrates. The interaction capacity of films with polysaccharides, proteins, and DNA are also essential research topics (Orelma et al. 2011; Hoeger et al. 2012; Orelma et al. 2012; Martín-Sampedro et al. 2013; Mohan et al. 2013; Mohan et al. 2014; Ehmann et al. 2015; Wolfberger et al. 2015). Particularly, the interaction with xylans have attracted considerable interest, both from basic and applied research point of view. Xylan is often observed in particle- like aggregates on the cellulosic surfaces (Henriksson and Gatenholm 2001, 2002; Linder et al. 2003; Coleho dos Santos Muguet et al. 2011; Silva et al. 2011). The equilibrium of individually solvated macromolecules and their corresponding aggregates on the solid surface are important in this context. For example, hydrophobic interactions, mainly via 4-OMe-Glc units, govern the coiling of xylans as demonstrated for interaction with bacterial cellulose surfaces (Linder et al. 2003). The coiling and the interaction of aggregates with cellulosic surfaces is influenced by the substitution patterns, molecular weight, and chemistry of the side chains (Kabel et al. 2007). The interactions of carbohydrates (including xylans) was studied on mica surfaces (Neuman et al. 1993; Claesson et al. 1995). Österberg et al. (2001) studied in detail the influence of xylans' charge density in terms of their adhesion force towards other materials. The potential of atomic force microscopy (AFM) was also evaluated for visualizing xylan-coated

[a]All authors are members of the European Polysaccharide Network of Excellence

*Corresponding author: Stefan Spirk, Graz University of Technology, Institute for Chemistry and Technology of Materials, Stremayrgasse 9, 8010 Graz, Austria; and University of Maribor, Institute for the Engineering and Design of Materials, Smetanova Ulica 17, 2000 Maribor, Slovenia, Phone: +43-316-873-32284,
e-mail: stefan.spirk@tugraz.at
Christian Ganser: University of Leoben, Institute for Physics, Franz-Josef-Str. 18, 8700 Leoben, Austria; Graz University of Technology, Institute for Paper, Pulp and Fibre Technology, Innfeldgasse 23, 8010 Graz, Austria; and CD-Laboratory for surface chemical and physical fundamentals of paper strength, Petersgasse 16/2, 8010 Graz, Austria
Katrin Niegelhell: Graz University of Technology, Institute for Chemistry and Technology of Materials, Stremayrgasse 9, 8010 Graz, Austria
Caterina Czibula and Christian Teichert: University of Leoben, Institute for Physics, Franz-Josef-Str. 18, 8700 Leoben, Austria; and CD-Laboratory for surface chemical and physical fundamentals of paper strength, Petersgasse 16/2, 8010 Graz, Austria
Angela Chemelli: Graz University of Technology, Institute for Inorganic Chemistry, Innfeldgasse 23, 8010 Graz, Austria
Robert Schennach: Graz University of Technology, Institute for Solid State Physics, Petersgasse 16/2, 8010 Graz, Austria; and CD-Laboratory for surface chemical and physical fundamentals of paper strength, Petersgasse 16/2, 8010 Graz, Austria

areas and to correlate these observations with water uptake properties (Miletzky et al. 2015). However, the potential of AFM force mapping had not yet been investigated. This technique allows for observation of locally resolved adhesion forces in biomaterials (Gad et al. 1997; Heinz and Hoh 1999; Touhami et al. 2003) with a better spatial resolution of adsorbates on cellulose compared to common AFM topography imaging. However, the challenge is to differentiate between force mapping and topographic effects.

The bonding between paper fibers depends to a large degree on the surface chemistry (Hirn and Schennach 2015). Thus, it is of great interest to know the interrelation between cellulose, hemicelluloses, and lignin on fiber surfaces with a lateral resolution on the nanometer scale. Pulp fibers are rather difficult to explore by AFM, while studies based on model systems offer some advantages. Thin cellulose films can be prepared rather easily from a variety of precursors and their defined and flat morphology facilitates AFM analysis (Rohm et al. 2014). It was also demonstrated that results obtained on such model systems can be interpreted in terms of fiber adsorption (Delgado-Fornué et al. 2011; Ganser et al. 2014).

In the present paper, the focus will be on topography effects in the localization of xylan on the surface of cellulose thin films. Force mapping experiments will be performed and the extent of topography effects on the results should be evaluated. The xylan particle size will be characterized in the xylan solutions and the cellulose thin films will be observed in a device called "multiple parameter surface plasmon resonance spectroscopy (MP-SPR)" under flow conditions. Then these surfaces will be subjected to AFM phase imaging and force mapping. The force mapping results are influenced by the surface roughness.

Materials and methods

Trimethylsilyl cellulose (TMSC, Avicel) with a DS_{Si} value of 2.8 was purchased from TITK (Rudolstadt, Germany) and used as starting material for cellulose film preparation. Birch xylan (extracted from a birch dissolving pulp) was obtained from Lenzing AG, Austria and used without further purification. The zeta potential of the xylan was determined to be -28 mV at pH 7. Milli-Q (MQ) water from a Millipore water purification system (Millipore, USA, resistivity=18.2 Ω^1 cm^{-1}) was used for SPR investigations.

The DLS equipment consisted of a diode laser (Coherent Verdi V5, λ=532 nm) and a goniometer with single-mode fiber detection optics (OZ from GMP, Zürich, Switzerland). The data was acquired by a photon counting module (Perkin Elmer, Voudreuil, Canada) and an ALV 7002/USB digital multiple tau real time correlator (ALV, Langen, Germany). The correlation functions were determined and stored by the ALV software package. The light scattering (LS) was measured five times for 30 s at a scattering angle of 90° at 25°C and the resulting correlation functions were averaged. The hydrodynamic radius was calculated by the optimized regulation technique software (Schnablegger and Glatter 1991).

Multi-parameter surface plasmon resonance (MP-SPR) was done on a SPR Navi 200 from Bionavis Ltd, Tampere, Finland on Au-coated glass slides as substrates (SPR102-AU) equipped with two different lasers (670 and 785 nm, respectively) in both measurement channels (Figure 1).

All measurements are based on a full angular scan (39–78°, scan speed of 8 s^{-1}). SPR sensors (gold-coated sensors (d~50 nm) with a chromium adhesion layer, ~2 nm) were obtained from BioNavis Ltd. To remove carbon impurities, SPR sensors were cleaned using piranha solution (freshly prepared from H_2SO_4/H_2O_2 (3/1, v/v) over a period of 15 min). Afterwards, the SPR slides were rinsed with Milli-Q water, dried in an N_2 stream. Then, a cellulose film (25 nm) from TMSC was prepared according to the literature (Kontturi et al. 2003; Kontturi and Lankinen 2010; Mohan et al. 2012a; Mohan et al. 2012b), and the slide was mounted in the sample holder. After equilibration in air for ca 20 min, first water and then buffer was injected and the cellulose film was allowed to equilibrate for another 20 min at each step. Then xylan solution was pumped over the gold surfaces (c=1 g·l^{-1}, flow rate 0.1 ml·min^{-1}) and allowed to adsorb for a period of 7 min. Afterwards, the slides were rinsed with buffer and water
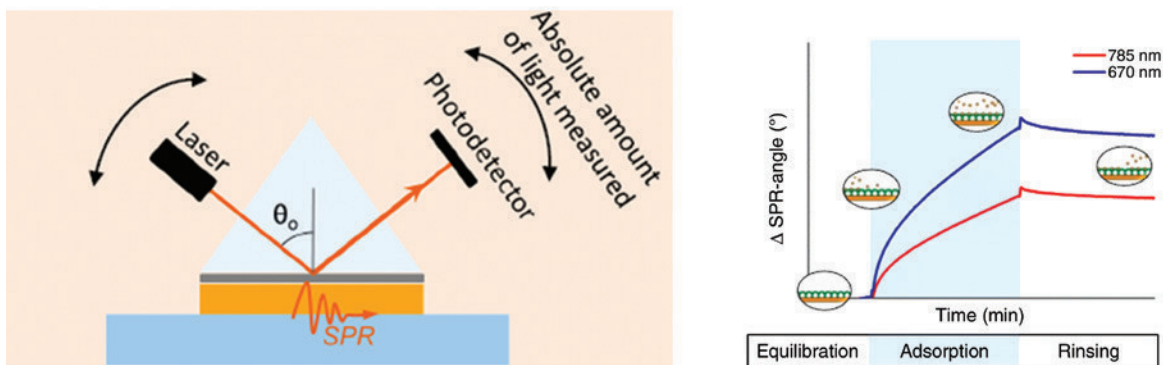
Figure 1: Setup of the SPR instrument (Kretschmann configuration, left) and a resulting sensogram obtained from such a measurement (right).

(each 30 min) in order to remove loosely bound material followed by drying in N_2 stream. Full angular scans were acquired and the shifts in the SPR angle served for modeling the data based on multilayer models via the Winspall 3.02 software. The two wavelengths and two-medium cross point analyses were performed by means of microsoft office excel 2010. All two-wavelength SPR experiments were processed by the BioNavis dataviewer software.

For studying of adsorption processes in-situ, the microfluidic cells allows to pump an adsorbate with a defined flow rate over the surfaces of interest. During the adsorption, the SPR angle is shifted and the SPR curves before and after adsorption permit a conclusion to the layer thickness and refractive index (RI) of the attached layer by fitting procedures (Geddes et al. 1994). However, it is often difficult to determine the layer thickness precisely with a single light source as it also highly dependent on the RI. If the RI of the adsorbed layer is not known, a continuum of minima for the surface plasmon wave vector k_{SP} are obtained during fitting, resulting in similar goodness (Eq. 1)

$$k_{SP} \propto n*d \tag{1}$$

To solve this problem, the two-media and the two/three wavelength approaches were proposed (Peterlinz and Georgiadis 1996). The two-media approach acquires SPR curves in different environments, e.g. in water and air. If the differences in n are large enough, then a unique solution can be easily derived for the final layer by plotting the continuum solutions of measurements in different media in a single graph. The intersection point of the two continuum solutions yields the RI at a certain wavelength as well as the unique layer thickness d of the film ($d_1 = d_2 = d$):

$$k_{SP1} = n_1 * d_1 \tag{2}$$

and

$$k_{SP2} = n_2 * d_2 \tag{3}$$

The second approach is to perform the measurements at different wavelengths, while a set of continuum solutions for k_{SP} is obtained for each wavelength. As the RI is a function of the wavelength, a shifting of the curves by the chromatic dispersion $dn/d\lambda$ yields unique solutions for n and d at the intersection point of the continuum solutions:

$$k_{sp1} = n_{\lambda 1} * d \tag{4}$$

and

$$k_{sp2} = n_{\lambda 2} * d, \tag{5}$$

where

$$n_{\lambda 2} = \left(n_{\lambda 1} + \frac{dn}{d\lambda}(\lambda_2 - \lambda_1) \right) \tag{6}$$

and

$$k_{SP1} = n_{\lambda 1} * d \tag{7}$$

and

$$k_{SP2} = \left(n_{\lambda 1} + \frac{dn}{d\lambda}(\lambda_2 - \lambda_1) \right) * d \tag{8}$$

The disadvantage of this approach is that $dn/d\lambda$ is often unknown and must be determined either by other methods, e.g. the two-media approach or by ellipsometry. In fact, the multiple wavelengths approach would also allow for the determination of

Cauchy parameters, instead of the linear approximations of $dn/d\lambda$. It should be noted here that the evaluation of data based on these approaches only makes sense if the layers do not absorb light at the wavelengths used for the SPR evaluations, i.e. if $k=0$ (which is true for most organic compounds). If $k \neq 0$, a unique solution of k_{SP} does exist and makes the above-mentioned approaches unnecessary.

AFM instrument: Asylum Research MFP-3D AFM (Santa Barbara, CA, USA) system was equipped with a closed-loop planar x-y-scanner with a scanning range of 85×85 μm². Standard topography measurements were conducted in tapping mode (Olympus AC240-TS, Japan, silicon cantilevers) with a spring constant of ca. 2 N m^{-1} and the tip attached at the very end has a nominal apex radius of 7 nm.

For the detection of xylan on the cellulose surfaces, Nanocraft AFM tips (Germany) functionalized with OH- and CH_3-groups by the manufacturer were used. The tip apex radius is ca. 40 nm, estimated by employing an NT-MDT TGT1 tip characterization grid (Russia). The cantilevers have a spring constant of 9–11 N m^{-1} and were calibrated by a combination (Sader et al. 2012) of the thermal sweep method (Hutter and Bechhoefer 1993), and the method of Sader et al. (1999). In force mapping, at each point of a 32×32 square grid, force-vs.-distance curves are recorded. The maximum applied force was approximately 50 nN and the approach and retract velocities were 2 μm s^{-1}.

The RMS roughness (R_q) values were calculated via the Gwyddion software (Nečas and Klapetek 2011). All R_q values were calculated from the images to which they are referred to in the text. In the case of the R_q values corresponding to Figure 7, it should be noted that these values were calculated from low resolution images (32×32 pixel).

Results and discussion

Characterization of the xylan solution by DLS

Dynamic light scattering (DLS) provides access to the hydrodynamic radius of colloidal particles in solution, and it is a very versatile tool for determination of particle sizes. This approach was employed to characterize the xylan aggregates prior to adsorption on the surfaces.
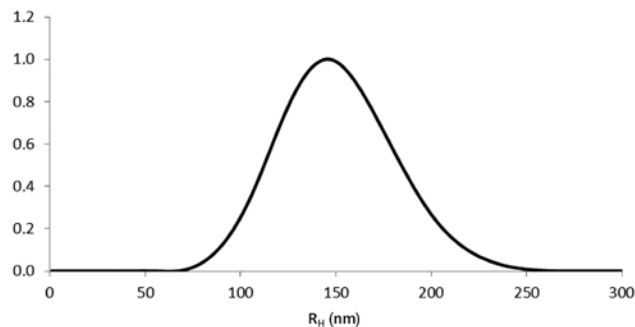
Figure 2: Size distribution of xylan particles in aqueous solution at pH 8 (c=1 g·l^{-1}) obtained by DLS.

As depicted in Figure 2, the size distribution of the xylan aggregates (pH 8, 1 mM NaCl) span a range of the hydrodynamic radius from ca. 50 to 250 nm, with a maximum at ca. 150 nm.

Cellulose film preparation and xylan adsorption

For the preparation of amorphous cellulose thin films, organosoluble trimethylsilyl cellulose (TMSC) was deposited on a silicon wafer by spin-coating, followed by exposure to acidic vapors of HCl (Kontturi et al. 2003). The original intention was to deposit xylans on the cellulose thin films at different pH values and ionic strength. However, the solutions are difficult to handle for a longer period of time, and particularly at low pH values (3–6) the aggregates tend to precipitate after 0.5 h, which makes the SPR studies less reliable and reproducible. Therefore, the experiments were performed only at pH 8, which is a compromise between the thin films' stability and the solubility of xylans. The SPR data clearly show that irreversible adsorption of the xylan takes place, with an average shift of the plasmon resonance angle $\Delta\theta$ of $0.41\pm0.03°$ (785 nm) and $0.65\pm0.05°$ (670 nm) after rinsing (Figure 3a). This can be related to a change in RI, which is in turn directly dependent on the film thickness. Therefore, for each adsorption data set, experiments need to be performed either at two wavelengths (here at 670 and 785 nm) or in different media to obtain a unique solution of the layer thickness/RI data. The obtained layer thickness can be easily converted to the surface concentration Γ, given the known density of the film. In contrast to quartz crystal microbalance with dissipation (QCM-D) technique, which is widely used for surface characterization (e.g. Hong et al. 2016), SPR yields the dry mass of the material, which is more straightforward because AFM images have been acquired under dry conditions as well. The determined mass of the xylan in the course of the two-media and the two-wavelength approaches are in very good agreement. In both cases, the determined layer thickness ranges from 5.1 to 5.6 nm in all measurements (Figure 3b and c). The surface concentration Γ can be determined based on the density of xylan (1.2 g cm^{-3}) leading to masses in a range from 6.0 to 6.7 mg·m^{-2}. However, it has to be emphasized that the layer thickness determined by SPR is significantly smaller than the average particle size. One reason for this phenomenon is that DLS yields the hydrodynamic radius of aggregated particles in solution, whereas the SPR technique just related to the dry material. It is obvious that xylans
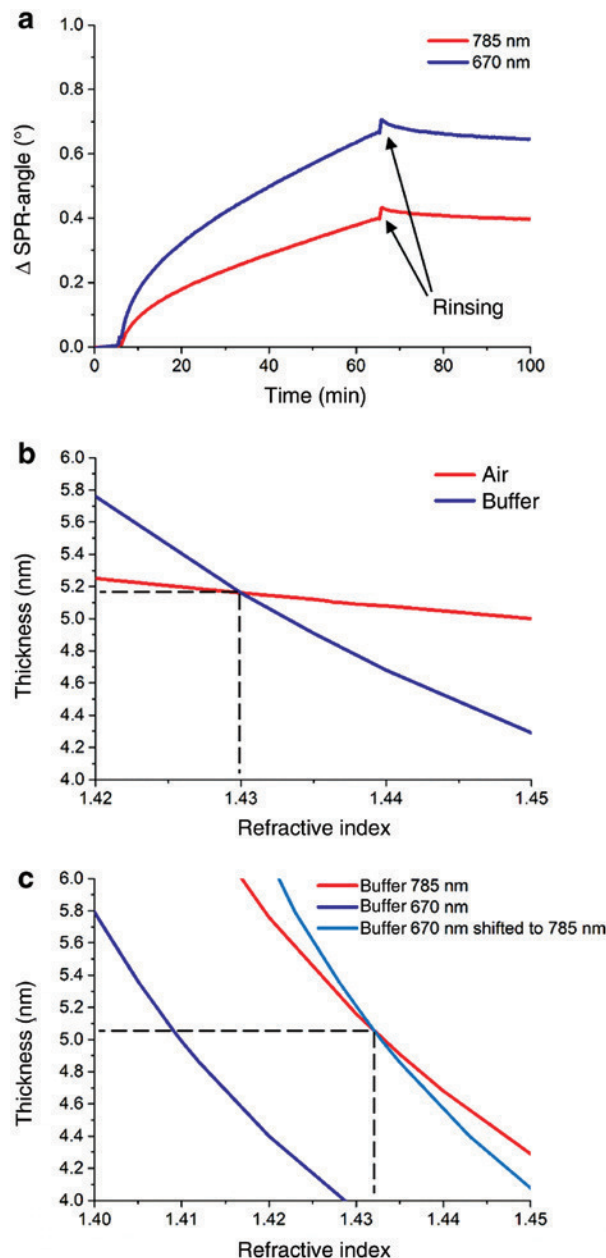
Figure 3: Adsorption of xylan (pH 8, c=1 g·l^{-1}, flow rate 0.1 ml·min^{-1}) on cellulose thin films in dependence of the surface plasmon resonance angle (a) and data evaluation according to the two-media (b) and two-wavelength approach (c) (dashed lines in b,c).

featuring a low degree of order are very prone to swelling, which leads in dry state to a drastic reduction of film thickness as well as to a potential distortion of the geometry from round-like to disk-shaped upon drying. The second reason is that SPR is an averaging technique over the measured area; the result is therefore a homogeneous layer thickness accounting for all the different hills and valleys caused by the different particles present on the surface.
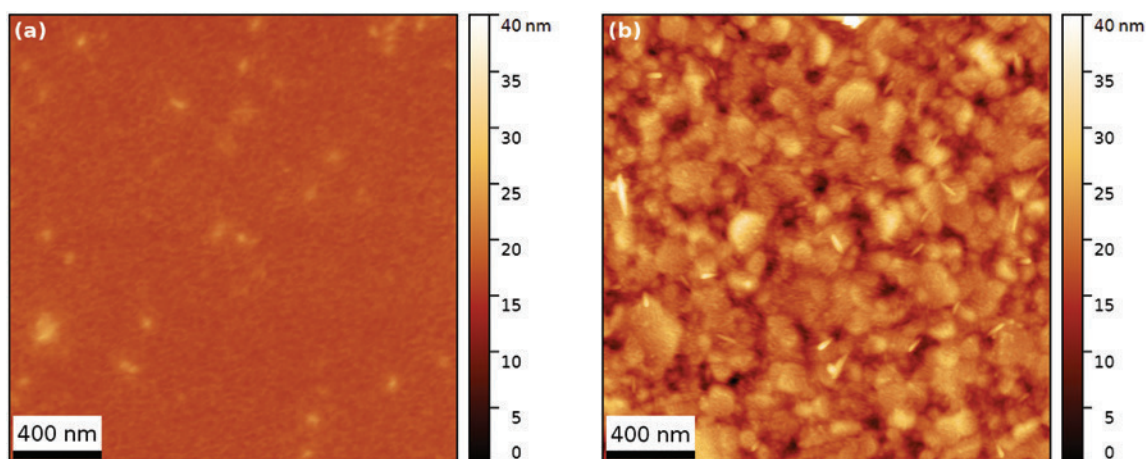
AFM topography

Figure 4 permits a comparison of AFM topography images of a pure spin-coated cellulose and a cellulose surface after xylan adsorption via the SPR experiment. It can be clearly seen that the cellulose surface does not exhibit any distinct surface features (root mean square roughness: $R_q = 0.7$ nm), whereas the xylan-coated cellulose films show a "hilly" structure ($R_q = 3.9$ nm). These hills have an average lateral dimension of 240±10 nm (determined from three independent $2 \times 2\ \mu m^2$ AFM topography images) and are slightly smaller than those determined by DLS (300 nm diameter), because the particles in solution are highly swollen and more extended than in the dry state. The geometry of these former round-shaped particles seems to have changed. It is likely that a distortion of the particles to an ellipsoid-like structure occurs already during adsorption, and this is further triggered by drying, resulting in disc-like particles. This can be also seen for some smaller particles that are oriented perpendicular to the surface having a lateral size of 30 nm and appearing as rods at the first glance in the AFM images. Although there are a few holes in the coated films, the surface is mostly covered by hilly structures which are in turn composed of xylan aggregates.

Localization of xylan on the cellulose thin films

To distinguish between xylan-enriched domains and the substrate, functionalized hydrophilic and hydrophobic AFM tips (-OH and -CH_3 terminated, respectively) were employed. AFM topography and phase images recorded with these tips are presented in Figure 5. It is visible that the phase images exhibit regions with a high phase shift, which usually indicates the presence of two different materials on the surface. Thus the first impression was that the cellulose regions can be clearly distinguished from the xylan-coated areas. A similar result is obtained by analysis of the adhesion force maps of the functionalized tips on the xylan/cellulose surface (Figure 6). However, for the AFM images recorded with OH tips, the adhesion force is high between the xylan particles and low at their apex. For hydrophobically modified tips, this effect is in place but less pronounced, which is an indication that the observed differences in adhesion forces are induced by the sample's topography. The regions marked yellow in the adhesion force maps exhibit an especially low adhesion force which always coincide with maxima in the topography. These regions have a diameter of about 50 nm, which is much lower than the particle size from the DLS analysis. In the light of these findings, the observed phase shift (Figure 5) is probably highly correlated with topographical features because elevated structures exhibit a lower phase shift compared to flat areas and, as for the force mapping experiments, the effect is more pronounced for the hydrophilically modified AFM tips due to the larger interaction capacity of the surface with hydrophilic OH groups. Obviously, a topography effect was tracked during these measurements.

A neat cellulose surface and a neat xylan surface were both mapped by OH functionalized tips (Figure 7). Evaluation of the adhesion force maps from Figure 7 yields an average adhesion force for cellulose of 8.1±0.7 nN and 8.0±1.2 nN for xylan. Evidently, any

Figure 4: Representative $2 \times 2\ \mu m^2$ AFM topography images of (a) a pure cellulose surface and (b) xylan deposited on a cellulose surface at pH 8 and 1 mM NaCl. The hills' lateral extent was determined by locating the maximum of the power spectral density functions of five independent $2 \times 2\ \mu m^2$ AFM images.
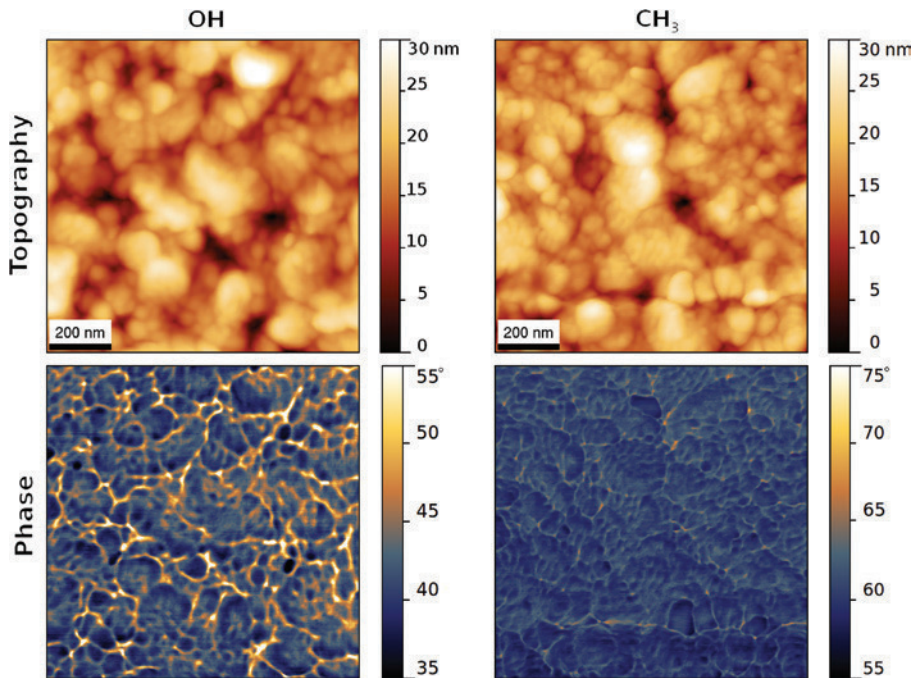
Figure 5: Representative $1{\times}1\ \mu m^2$ AFM topography and corresponding phase images of xylan-coated cellulose thin films, acquired by OH and CH_3 functionalized tips, as indicated.
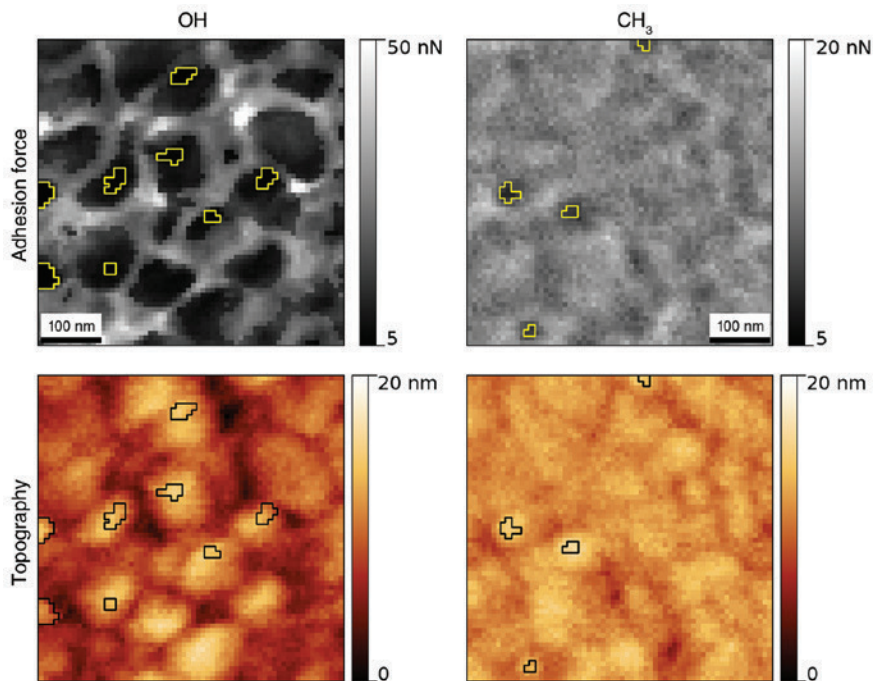
Figure 6: $500{\times}500\ nm^2$ adhesion force maps and the corresponding AFM topography images, recorded with OH and CH_3 functionalized tips. Regions with an adhesion force below 10 nN are marked yellow in the adhesion force maps and black in the topography maps.

differences in adhesion force between cellulose and xylan were not observed with OH functionalized tips. By comparing the adhesion maps to the topography, it becomes clear that the only difference between cellulose and xylan in the force maps is the slightly larger data spread (contrast) for xylan, which is due to the higher roughness of this film (R_q=0.7 nm for cellulose and R_q=3.7 nm for xylan). Apparently, a further
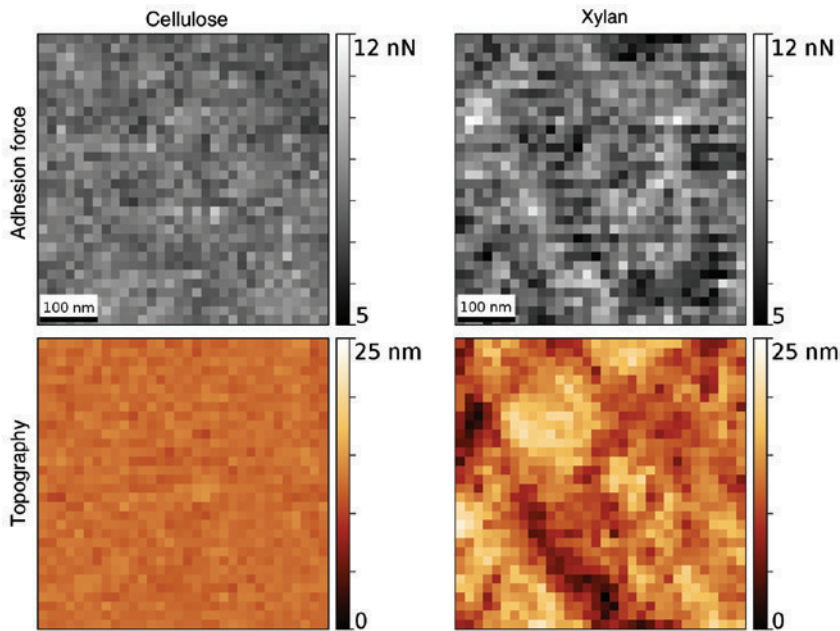
Figure 7: 500×500 nm² AFM force maps of a pure cellulose surface and of a pure xylan surface recorded by OH functionalized tips.
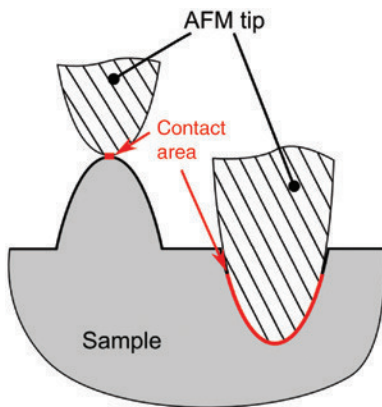
Figure 8: Sketch of the contact area between AFM tip and sample on a hill and in a hole.

localization by force mapping is not feasible, because xylan and cellulose are chemically too similar to be differentiable by this method. It can be safely concluded that the contrast obtained in the adhesion force maps is solely due to topographic artifacts.

This effect is explained in Figure 8. On the top of a hill the contact area between tip and sample is low, whereas on the bottom of a hole a high contact area is established. The adhesion force will be high in case of a large tip area in contact and low in the opposite case. This is in accordance with all adhesion maps shown here, where a low adhesion force was found on top of hills, whereas in holes or trenches a high adhesion was determined.

Conclusions

Xylan particles were deposited on a cellulose thin film via an SPR setup. The particle sizes determined by AFM topography images and DLS are in good agreement, considering that DLS measures swollen particles in suspension and AFM the dried, dehydrated, and distorted particles. The expectation that functionalized tips would allow for distinguishing xylan particles from the cellulose substrate was not fulfilled. A further localization of the xylan particles by AFM force mapping experiments is not feasible due to chemical similarity between xylan and cellulose. The adhesion forces of functionalized AFM tips on cellulose are indistinguishable from those on xylan. Moreover, the topography itself may contribute 5 nN and 50 nN to the adhesion forces, whereas the adhesion between the tip and cellulose/xylan is just in the range of 8 nN. It can be concluded that an AFM approach based on functionalized tips is not suitable to distinguish between xylan and cellulose, even in case of rather smooth samples, which were in focus of the present study.

References

Claesson, P.M., Christenson, H.K., Berg, J.M., Neuman, R.D. (1995) Interactions between mica surfaces in the presence of carbohydrates. J. Colloid. Interface Sci. 172:415–424.

Coleho dos Santos Muguet, M., Pedrazzi, C., Colodette, J. (2011) Xylan deposition onto eucalyptus pulp fibers during oxygen delignification. Holzforschung 65:605–612.

Delgado-Fornué, E., Contreras, H.J., Toriz, G., Allan, G.G. (2011) Adhesion between cellulosic fibers in paper. J. Adh. Sci. Techn. 25:597–614.

Ehmann, H.M.A., Werzer, O., Pachmajer, S., Mohan, T., Amenitsch, H., Resel, R., Kornherr, A., Stana-Kleinschek, K., Kontturi, E., Spirk, S. (2015) Surface-sensitive approach to interpreting supramolecular rearrangements in cellulose by synchrotron grazing incidence small-angle X-ray scattering. ACS Macro. Lett. 4:713–716.

Gad, M., Itoh, A., Ikai, A. (1997) Mapping cell wall polysaccharides of living microbial cells using atomic force microscopy. Cell Biol. Intern. 21:697–706.

Ganser, C., Weber, F., Czibula, C., Bernt, I., Schennach, R., Teichert, C. (2014) Tuning hardness of swollen viscose fibers. Bioinspir. Biomim. Nan. 3:131–138.

Geddes, N.J., Martin, A.S., Caruso, F., Urquhart, R.S., Furlong, D.N., Sambles, J.R., Than, K.A., Edgar, J.A. (1994) Immobilisation of IgG onto gold surfaces and its interaction with anti-IgG studied by surface plasmon resonance. J. Immunol. Methods 175:149–160.

Heinz, W.F., Hoh, J.H. (1999) Spatially resolved force spectroscopy of biological surfaces using the atomic force microscope. Trends Biotechnol. 17:143–150.

Henriksson, A., Gatenholm, P. (2001) Controlled assembly of glucuronoxylans onto cellulose fibers. Holzforschung 55:494–502.

Henriksson, A., Gatenholm, P. (2002) Surface properties of CTMP fibres modified with xylans. Cellulose 9:55–64.

Hirn, U., Schennach, R. (2015) Comprehensive analysis of individual pulp fiber bonds quantifies the mechanisms of fiber bonding in paper. Sci. Rep. 5:10503.

Hoeger, I.C., Filpponen, I., Martin-Sampedro, R., Johansson, L.-S., Österberg, M., Laine, J., Kelley, S., Rojas, O.J. (2012) Bicomponent lignocellulose thin films to study the role of surface lignin in cellulolytic reactions. Biomacromolecules 13:3228–3240.

Hong, N., Yu, W., Xue, Y., Zeng, W., Huang, J., Xie, W., Qiu, X., Li, Y. (2016) A novel and highly efficient polymerization of sulfomethylated alkaline lignins via alkyl chain cross-linking method. Holzforschung 70:297–304.

Hutter, J.L., Bechhoefer, J. (1993) Calibration of AFM tips. Rev. Sci. Instrum. 64:1868–1873.

Kabel, M.A., Borne, H.V.D., Vincken, J.-P., Voragen, A.G.J., Schols, H.A. (2007) Structural differences of xylans affect their interaction with cellulose. Carbohydr. Polym. 69:94–105.

Kontturi, E., Lankinen, A. (2010) Following the kinetics of a chemical reaction in ultrathin supported polymer films by reliable mass density determination with X-ray reflectivity. J. Am. Chem. Soc. 132:3678–3679.

Kontturi, E., Thüne, P.C., Niemantsverdriet, J.W. (2003) Cellulose model surfaces simplified preparation by spin coating and characterization by X-ray photoelectron spectroscopy, infrared spectroscopy, and atomic force microscopy. Langmuir 19:5735–5741.

Linder, Å., Bergman, R., Bodin, A., Gatenholm, P. (2003) Mechanism of assembly of xylan onto cellulose surfaces. Langmuir 19:5072–5077.

Martín-Sampedro, R., Rahikainen, J.L., Johansson, L.-S., Marjamaa, K., Laine, J., Kruus, K., Rojas, O.J. (2013) Preferential adsorption and activity of monocomponent cellulases on lignocellulose thin films with varying lignin content. Biomacromolecules 14:1231–1239.

Miletzky, A., Punz, M., Zankel, A., Schlader, S., Czibula, C., Ganser, C., Teichert, C., Spirk, S., Zöhrer, S., Bauer, W., Schennach, R. (2015) Modifying cellulose fibers by adsorption/precipitation of xylan. Cellulose 22:189–201.

Mohan, T., Spirk, S., Kargl, R., Doliška, A., Ehmann, H.M.A., Köstler, S., Ribitsch, V., Stana-Kleinschek, K. (2012a) Watching cellulose grow – kinetic investigations on cellulose thin film formation at the gas–solid interface using a quartz crystal microbalance with dissipation (QCM-D). Coll. Surf. A Physicochem. Eng. Asp. 400:67–72.

Mohan, T., Spirk, S., Kargl, R., Doliska, A., Vesel, A., Salzmann, I., Resel, R., Ribitsch, V., Stana-Kleinschek, K. (2012b) Exploring the rearrangement of amorphous cellulose model thin films upon heat treatment. Soft. Matter 8:9807–9815.

Mohan, T., Ristic, T., Kargl, R., Doliska A., Köstler, S., Ribitsch, V., Marn, J., Spirk, S., Stana-Kleinschek, K. (2013) Cationically rendered biopolymer surfaces for high protein affinity support matrices. Chem. Comm. 49:11530–11532.

Mohan, T., Niegelhell, K., Zarth, C., Kargl, R., Köstler, S., Ribitsch, V., Heinze, T., Spirk, S., Stana-Kleinschek, K. (2014) Triggering protein adsorption on cationically rendered cellulose surfaces. Biomacromolecules 15:3931–3941.

Nečas, D., Klapetek, P. (2011) Gwyddion: an open-source software for SPM data analysis. Central European J. Phys. 10:181–188.

Neuman, R.D., Berg, J.M., Claesson, P.M. (1993) Direct measurement of surface forces in papermaking and paper coating systems Nord. Pulp. Paper Res. J. 8:96–104.

Orelma, H., Filpponen, I., Johansson, L.-S., Laine, J., Rojas, O.J. (2011) Modification of cellulose films by adsorption of CMC and Chitosan for controlled attachment of biomolecules. Biomacromolecules 12:4311–4318.

Orelma, H., Johansson, L.-S., Filpponen, I., Rojas, O.J., Laine, J. (2012) Generic method for attaching biomolecules via avidin-biotin complexes immobilized on films of regenerated and nanofibrillar cellulose. Biomacromolecules 13:2802–2810.

Österberg, M., Laine, J., Stenius, P., Kumpulainen, A., Claesson, P.M. (2001) Forces between xylan-coated surfaces: effect of polymer charge density and background electrolyte. J. Colloid Interface Sci. 242:59–66.

Peterlinz, K.A., Georgiadis, R. (1996) Two-color approach for determination of thickness and dielectric constant of thin films using surface plasmon resonance spectroscopy. Opt. Comm. 130:260–266.

Rohm, S., Hirn, U., Ganser, C., Teichert, C., Schennach, R. (2014) Thin cellulose films as a model system for paper fibre bonds. Cellulose 21:237–249.

Sader, J.E., Chon, J.W.M., Mulvaney, P. (1999) Calibration of rectangular atomic force microscope cantilevers. Rev. Sci. Instrum. 70:3967–3969.

Sader, J.E., Sanelli, J.A., Adamson, B.D., Monty, J.P., Wei, X., Crawford, S.A., Friend, J.R., Marusic, I., Mulvaney, P., Bieske, E.J. (2012) Spring constant calibration of atomic force microscope cantilevers of arbitrary shape. Rev. Sci. Instrum. 83:103705.

Schnablegger, H., Glatter, O. (1991) Optical sizing of small colloidal particles: an optimized regularization technique. Appl. Opt. 30:4889–4896.

Silva, T., Colodetta, J.L., Lucia, L., de Oliveira, R., Oliveira, F., Silva, L. (2011) Adsorption of chemically modified xylans on eucalyptus pulp and its effect on the pulp physical properties. Ind. Eng. Chem. Res. 50:1138–1145.

Touhami, A., Nysten, B., Dufrêne, Y.F. (2003) Nanoscale mapping of the elasticity of microbial cells by atomic force microscopy. Langmuir 19:4539–4543.

Wolfberger, A., Petritz, A., Fian, A., Herka, J., Schmidt, V., Stadlober, B., Kargl, R., Spirk, S., Griesser, T. (2015) Photolithographic patterning of cellulose: a versatile dual-tone photoresist for advanced applications. Cellulose 22:717–727.

PAPER #9

Multilayer Density Analysis of Thin Films

submitted to Langmuir

For this paper, I conducted the stylus profilometry, AFM and MP-SPR spectroscopy measurements, interpreted the data and wrote a significant part of the manuscript.

Multilayer Density Analysis of Thin Films

Katrin Niegelhell[†,‡], Katri Kontturi[#], Ulrich Hirn[†,‡], Stefan Spirk[†,‡]*

[†]Graz University of Technology, Institute for Paper, Pulp and Fibre Technology, Inffeldgasse 23, 8010 Graz, Austria

[‡]CD-Laboratory for Fibre Swelling and Paper Performance, Inffeldgasse 23A, 8010 Graz, Austria

[#]VTT Technical Research Centre of Finland, Espoo, Finland

Members of NAWI Graz and the European Polysaccharide Network of Excellence (EPNOE)

KEYWORDS

Multilayer Analysis; Surface Plasmon Resonance; Atomic Force Microscopy; Roughness; Density; Cellulose Thin Films

ABSTRACT

An approach for the multilayer density analysis of thin film samples at the example of cellulose is presented. By the combination of atomic force microscopy (AFM) and multi-parameter surface plasmon resonance (MP-SPR) spectroscopy it is possible to determine the density in different layers of the sample, which is particularly interesting for processes occurring at the interface such as surface modification or water interaction. Cellulose thin films with and low (R_q = 1.6 nm) and high (R_q = 4.5 nm) roughness displayed densities of 1.20 g·cm^{-3} and 1.11 g·cm^{-3}, respectively. A multilayer model was developed for the evaluation of the films, wherein the cellulose film was split into a so-called roughness layer occurring at the surface and a bulk layer. Higher porosity of the films in the surface regions is shown by a lower density of the outermost layers (smooth film 0.78 g·cm^{-3}, rough film 0.74 g·cm^{-3}) compared to the bulk (smooth film 1.22 g·cm^{-3}, rough film 1.14 g·cm^{-3}). Calculations for comparison of data obtained by the two techniques were performed. The results thereof are in good agreement, supporting the accuracy of the presented strategy to analyze with spatial resolution in z-axis.

INTRODUCTION

In the past few decades, the desire to explore the vast number of processes occurring at the surface of materials lead to the development of a variety of surface sensitive techniques. These techniques are either capable of determining surface properties, such as physical topography or chemical structure and composition, or they are utilized to monitor phenomena taking place at interfaces, such as adsorption, modification or wetting, just to name a few.[1,2]

Atomic force microscopy, for instance, is an imaging technique for the investigation of surfaces on an atomic scale by simply scanning the surface with a cantilever with a sharp tip while it is maintained at constant force or constant height above the sample. As the tip scans the surface it is moving along the features of the surface leading to a deflection of the cantilever, which is monitoring an beam of laser light is reflected from the cantilever onto a photodiode. Then either the height deviation (in constant force mode) or the deflection force on the sample (in constant height mode) is recorded. Since the method was first reported in 1986[3], it has gained high importance in the field of surface science. The technique was further enhanced e.g. to determine mechanical properties of surfaces, or to measure in different liquids enabling the examination of biological samples, just to name a few applications. Nowadays, the observation of surfaces in real-time, for example, during enzymatic degradation or adsorption, and the production of videos thereof is possible.[4-6]

Surface plasmon resonance (SPR) spectroscopy is a surface sensitive technique that is able to monitor processes in real-time as well. In contrast to atomic force microscopy, it detects changes in the chemical environment, i.e. the refractive index, near a metal surface (ca. 100 nm).[7] The technique is based on the resonance of surface plasmons, which originate from the oscillation of charge densities on the metal surface caused by freely moving electron gas.[8] Acquisition of SPR

spectra is accomplished by focusing a p-polarized light source onto a metal surface (*e.g.* a glass slide coated with a thin gold layer) and recording the intensity of the reflected light by a detection system (*e.g.* photodiodes). Modern, so-called multi parameter, SPR devices enable the detection of spectra in dependence of the incidence angle of the light, which allows the investigation of processes in real-time and in varying ambient media (*i.e.* gas or liquid) in a single experiment. The resulting curves are evaluated by a multilayer fitting procedure, whereby thickness and refractive index of the examined layer are derived.[9] In a standard SPR spectrometer, where the measurement is performed with only a single wavelength, determination of both layer thickness and refractive index without assuming or knowing one of the values is not possible. However, multi-parameter SPR systems measuring at two or more wavelengths overcome this problem.[10,11]

When observing phenomena with SPR spectroscopy in real-time, the change in refractive index related of the whole sample is detected. Nevertheless, in the case of processes such as adsorption or chemical surface modification, it is desirable to differentiate between the surface regions and the bulk. Up to now, the multilayer fitting procedure used in SPR data evaluation has only been used to describe the examined film as one layer. When splitting the film into more than one layer, more information is required for the fitting procedure. Therefore, the combination of AFM, giving information about the surface topography, and multi-parameter SPR spectroscopy could lead to a new method enabling the examination of changes in the bulk material and surface regions separately. The refractive index obtained from SPR spectroscopy can be used to calculate the composition i.e. the density of the different layers. Thereby, variations in direction of the z-axis could be detected inside a material.

Herein, the investigation of such an approach to evaluate densities of different layers in thin films at the example of cellulose is reported. A model describing the thin films as a multilayer

system for this particular analysis approach was developed. The implementation of AFM data into the multilayer fitting model used in the MP-SPR spectroscopy method yields spatial resolution along z-axis of the examined films. Compositions of the entire films as well as differences between the surface regions and the bulk were evaluated. Furthermore, validation of the approach was accomplished by comparison of the techniques in terms of material fraction, density and thickness of the surface regions.

EXPERIMENTAL

Materials. Trimethylsilyl cellulose (TMSC, DS_{Si} = 2.8, Avicel, M_w=185,000 $g \cdot mol^{-1}$, M_n=30,400 $g \cdot mol^{-1}$, PDI=6.1 determined by SEC in chloroform) was purchased from TITK (Rudolfstadt, Germany). Chloroform (99.3%), tetrahydrofuran (99.9%), hydrochloric acid (37%), hydrogen peroxide (30% in water) and sulfuric acid (95%) were purchased from Sigma Aldrich and used as received. MilliQ water (resistivity = 18 $M\Omega \cdot cm$) from a Millipore water purification system (Millipore, USA) was used for all experiments.

Substrate Cleaning and Film Preparation. SPR sensors (glass sensors with gold coating (~50 nm) and chromium adhesion layer (~2 nm), (CEN102Au)) were obtained from Cenibra, (Bramsche, Germany). In order to remove adventitious carbon, SPR sensors were cleaned before use by treatment with piranha solution (freshly prepared from sulfuric acid and hydrogen peroxide in a 3:1 ratio (v/v)) over a period of 10 minutes. Afterwards the SPR slides were extensively rinsed with MilliQ water and dried in a stream of nitrogen. Cellulose thin films were prepared by spin coating trimethylsilyl cellulose (0.75 wt.% in either chloroform or tetrahydrofuran). 100 μl of solution were deposited on the substrate and then rotated for 60 s at a spinning speed of 4000 rpm and an acceleration of 2500 $rpm \cdot s^{-1}$. TMSC was converted to cellulose by treatment with hydrochloric acid (HCl) vapor. The TMSC films were placed into a petri dish (diameter 5 cm)

containing 3 ml of 10 wt.% HCl. The dish was covered with its cap and the films were exposed to the HCl vapors for 15 min. The regeneration was verified by water contact angle and ATR-IR measurements as reported elsewhere.[12–14]

Profilometry. Film thicknesses were attained by a DETAK 150 Stylus Profiler from Veeco using a diamond stylus with a radius of 12.5 μm. The scan length was adjusted to 1000 μm over a duration of 3 s. Measurements were performed with a force of 3 mg, a resolution of 0.333 μm per sample and a measurement range of 6.5 μm. Samples were measured after scratching the film (deposited on a silicon wafer).The resulting profile was used to determine the film thicknesses. All samples were measured in three parallels.

Atomic Force Microscopy (AFM). AFM imaging was performed in atomic force microscopy tapping mode with a Veeco multimode scanning probe microscope (Bruker, USA). The images were scanned using silicon cantilevers (NCH-VS1-W, Nanoworld, Switzerland) with a resonance frequency of 320 kHz and a force constant of 42 N·m^{-1}. All images were processed using Nanoscope software package (V7.30r1sr3, Veeco).

The thickness of the roughness layer is evaluated from the topography images measured by AFM. The roughness layer is the region of the cellulose film where both, material and ambient medium (water or air) are found, i.e. the region containing the boundary between cellulose film and surrounding. The thickness of this region depends on the roughness of the film. We have defined the roughness layer as the z-directional layer containing 95% of the surface roughness. For calculation, the histogram of the topography distribution is evaluated. From each edge of the histogram, 2.5% of the topography values are clipped off, the topography range comprising the remaining 95% of height values is defined as the roughness layer thickness. We are not using 100% of the values because the topography distribution is close to normally distributed which

means there are always some far outliers which would bloat the roughness layer beyond the true surface interaction range.

Multi-Parameter Surface Plasmon Resonance (MP-SPR). Two-wavelength MP-SPR spectroscopy experiments were performed with an MP-SPR Navi™ 210A Vasa instrument (by BioNavis Ltd., Tampere, Finland) equipped with two light source pairs providing 670 and 785 nm in each of the two measurement channels. All measurements were performed using a full angular scan (39-78°, scan speed: $8° \cdot s^{-1}$) in three parallels. SPR data was processed with BioNavis Dataviewer software. The full angular scans were simulated with the optical fitting software Winspall 3.01 (which is freely available from the Max-Planck Institute for Polymer Research (Mainz, Germany), http://www2.mpip-mainz.mpg.de/groups/knoll/software, 12.6.2013). The multilayer fitting approach is based on the Fresnel equations and the recursion formalism. The SPR signal of the pure sensor surface was simulated first in order to obtain the background for the subsequent evaluation of the cellulose thin film. The two wavelengths cross point analyses were performed by using Microsoft Office Excel 2010.

THEORETICAL BASIS

Determination of Thickness and Refractive Index of Cellulose Thin Films. The simulation of a sample measured at a single wavelength provides a refractive index (n) − thickness (d) continuum (n decreasing when d increasing) without a unique solution. In order to determine a unique solution, measurements at two wavelengths resulting in two different sets of $n - d$ continua are required. Since the refractive index is dependent on the wavelength, the $n - d$ continuum measured at one wavelength can be shifted to the other wavelength. The dependence of refractive index on the wavelength, i.e. chromatic dispersion ($dn/d\lambda$), is approximated to be linear for relatively small wavelength changes (a few hundred nm). For cellulose, the $dn/d\lambda$ at 670 nm and

785 nm is -0.0338 µm⁻¹ and -0.0204 µm⁻¹, respectively.[15] The average, -0.0271 µm⁻¹, was used in the calculations as a chromatic dispersion value of pure cellulose. The corresponding value for air is -0.00000856 µm⁻¹.[16] The *n - d* curves of the cellulose thin film obtained with both wavelengths were plotted in the same graph. The *n - d* curve of the measurement performed at 785 nm was shifted by the *dn/dλ* value of cellulose and by the *dn/dλ* value of the medium (air). The intersection points of the shifted curves measured at 785 nm with the curve measured at 670 nm results in two unique solutions. An average (n_{film}) of the *n* values obtained by the intersection points was calculated. The proportion of cellulose of the volume of the film, *a*, corresponding to the obtained n_{film} value, was calculated according to equation 1:

$$n_{film} = a\, n_{cellulose} + (1 - a)n_{medium} \qquad\qquad \text{Eq.1}$$

where $n_{cellulose}$ is 1.46650[15] and n_{medium} is 1.00028 for air.[16] Based on *a*, the value of dn/dλ was corrected by equation 2.

$$dn/d\lambda_{film} = a\, dn/d\lambda_{cellulose} + (1 - a)\, dn/d\lambda_{medium} \qquad\qquad \text{Eq.2}$$

Then, the intersection point of the *n - d* curve measured at 670 nm and the *n - d* curve shifted from 785 nm to 670 nm with the new dn/dλ results in the unique solution (*n* and *d*) of the cellulose thin film. The composition of the film was determined by equation. 1. The densities of the films were calculated from the composition and the density values of pure cellulose and air (see SI).

Multilayer Analysis of Cellulose Thin Films. In the evaluation model, the cellulose thin films displaying a certain thickness d_{SPR} and refractive index n_{SPR} were split into a top and a bottom layer. The starting thickness values for the top layer d_t^0 were taken from AFM data (half the thickness of roughness layer thickness, *RLT*). The initial bottom layer thickness d_b^0 was recalculated from the thickness of the entire cellulose thin film d_{SPR}. The refractive index of the entire cellulose thin film n_{SPR} was chosen as starting refractive index value for both layers. Then

the iteration was performed in the simulation program leading to lower refractive indices for the top layer n_t^0 than for the bottom layer n_b^0. After this first iteration, the bottom layer was evaluated with the 2-wavelength method (in the same fashion as the entire cellulose films), while keeping the values for the top layer (d_t^0, n_t^0) constant. Afterwards, the roughness layer thickness obtained from AFM data (RLT_{AFM}) was implemented into the model as new thickness value for the top layer. The corresponding refractive index was iterated in the simulation program and the top layer was evaluated with the 2-wavelength method while the bottom layer values (d_b^1, n_b^1) were kept constant. In a last step, the bottom layer was evaluated with the 2-wavelength method again using the new values for the top layer (d_t^1, n_t^2), in order to validate the simulations.

Scheme 1. Steps of multilayer analysis of cellulose thin films performed by means of MP-SPR spectroscopy.[a]

d_{SPR}, n_{SPR}

medium
material

material

RLT_{AFM}, mf_{AFM}

d_t^0, n_{SPR}
d_b^0, n_{SPR}

$$d_t^0 = \frac{RLT}{2}$$
$$d_b^0 = d_{SPR} - \frac{RLT}{2}$$

Iteration of n_{SPR} values in the simulation program

d_t^0, n_t^0
d_b^0, n_b^0

2-λ-method evaluation of bottom layer while d_t^0 and n_t^0 are kept constant

d_t^0, n_t^0
d_b^1, n_b^1

Implementation of RLT_{AFM}

RLT_{AFM}, n_t^0
d_b^1, n_b^1

Iteration of n_t^0
2-λ-method evaluation of top layer while d_b^1 and n_b^1 are kept constant

d_t^1, n_t^1
d_b^1, n_b^1

2-λ-method evaluation of bottom layer while d_t^1 and n_t^1 are kept constant

d_t^1, n_t^1
d_b^2, n_b^2

Calculations according to equations 3 -6

RLT_{AFM}
ρ_{RL}^{AFM}
mf_{AFM}

material

RLT_{SPR}
ρ_{RL}^{SPR}
mf_{SPR}

$BLT = d_b$
$\rho_{BL} = \rho_b$
$mf = 100\%$

[a]Where *d* is the thickness, *n* is the refractive index, *RL* is the roughness layer, R*LT* is the roughness layer thickness, *mf* is the material fraction, *BL* is the bulk layer, *BLT* is the bulk layer

thickness and ρ is the density. The indices *t, b, AFM* and *SPR* stand for top layer, bottom layer, derived from AFM data and MP-SPR spectroscopy data, respectively.

Calculations for comparison of AFM and MP-SPR spectroscopy results. Calculations according to the following equations were made to enable a comparison of results from both methods used in this study.

$$\rho_{RL}^{AFM} = mf_{AFM} \times \rho_m^t \qquad \text{Eq. 3}$$

$$RLT_{SPR} = \frac{d_t}{\rho_m^t} \qquad \text{Eq.4}$$

$$\rho_{RL}^{SPR} = mf_{SPR} \times \rho_m^t \qquad \text{Eq.5}$$

$$mf_{SPR} = \frac{d_t}{RLT_{AFM}} \qquad \text{Eq.6}$$

where $\rho_{RL}^{AFM/SPR}$ is the density of the roughness layer and $mf^{AFM/SPR}$ is the material fraction calculated from AFM or MP-SPR data, *RLT* is the roughness layer thickness, d_t is the thickness of the top layer and ρ_m^t is the density of the top layer from MP-SPR multilayer evaluation.

RESULTS AND DISCUSSION

Characterization of Cellulose Thin Films. Cellulose thin films were prepared by spin coating of trimethylsilyl cellulose (TMSC), dissolved in tetrahydrofuran (THF) or chloroform (CHCl$_3$), and subsequent conversion to cellulose by a regeneration step completed with HCl vapors, cleaving off the TMS groups.[17] Atomic force microscopy (AFM) images display smooth or rough films depending on the solvent used for the preparation (Figure 1). Films with low RMS roughness arise from spin coating with CHCl$_3$ and ones with higher RMS roughness are obtained by using THF. In both cases, the cellulose thin films feature very homogenous surfaces.
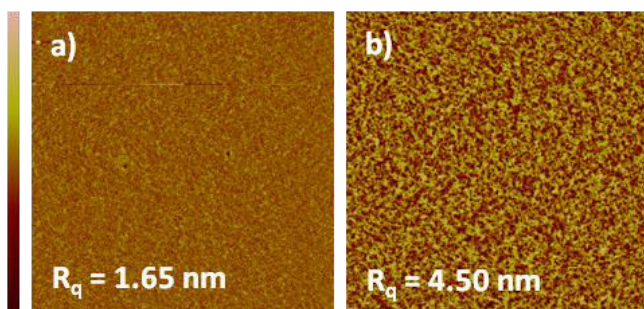
Figure 1. AFM images (10×10 µm2) and RMS roughness (Rq) of cellulose thin films spin coated from CHCl3 (a) or THF (b) solution, z-scale 30 nm.

The thicknesses and refractive indices of the cellulose thin films were determined by the 2-wavelength method (Figure 2) as described in the experimental section. The thickness values from profilometry, 31 ± 2 nm and 30 ± 2 nm for the smooth and rough surfaces, deviate from the values obtained by multi-parameter surface plasmon resonance (MP-SPR) spectroscopy measurements, 35.0 ± 0.4 nm and 39.0 ± 1.1 nm, respectively. The discrepancy might be traced back to the fact that the profilometry measurements were performed on different substrates than MP-SPR spectroscopy experiments. Scratching of the films is necessary prior to thickness determination. Therefore, profilometry was performed on hard silicon wafers instead of the soft gold surfaces. Additionally, the profilometry data gives an average value of different samples detected at varying spots, whereas MP-SPR spectroscopy records at one single spot. Although the samples look very homogenous in the AFM images, small variations in film thickness throughout the substrate are possible.

The refractive indices of the films indicate a slightly higher density of the smooth films (ρ_{SPR} = 1.20 g·cm^{-3}) compared to the rough films (ρ_{SPR} = 1.11 g·cm^{-3}). Both types of films are of porous nature, since they are less dense than pure cellulose (ρ = 1.5 g·cm^{-3})[18] The porosity originates from the regeneration step, where the TMS groups are removed as volatile compound, leaving behind

pores. The difference in porosity of the two types of films is explainable by the orientation of cellulose molecules stemming from the spin coating behavior of TMSC. Whereat, the solubility of TMSC in the solvents and the difference in volatility of the solvents play a major role.[19]
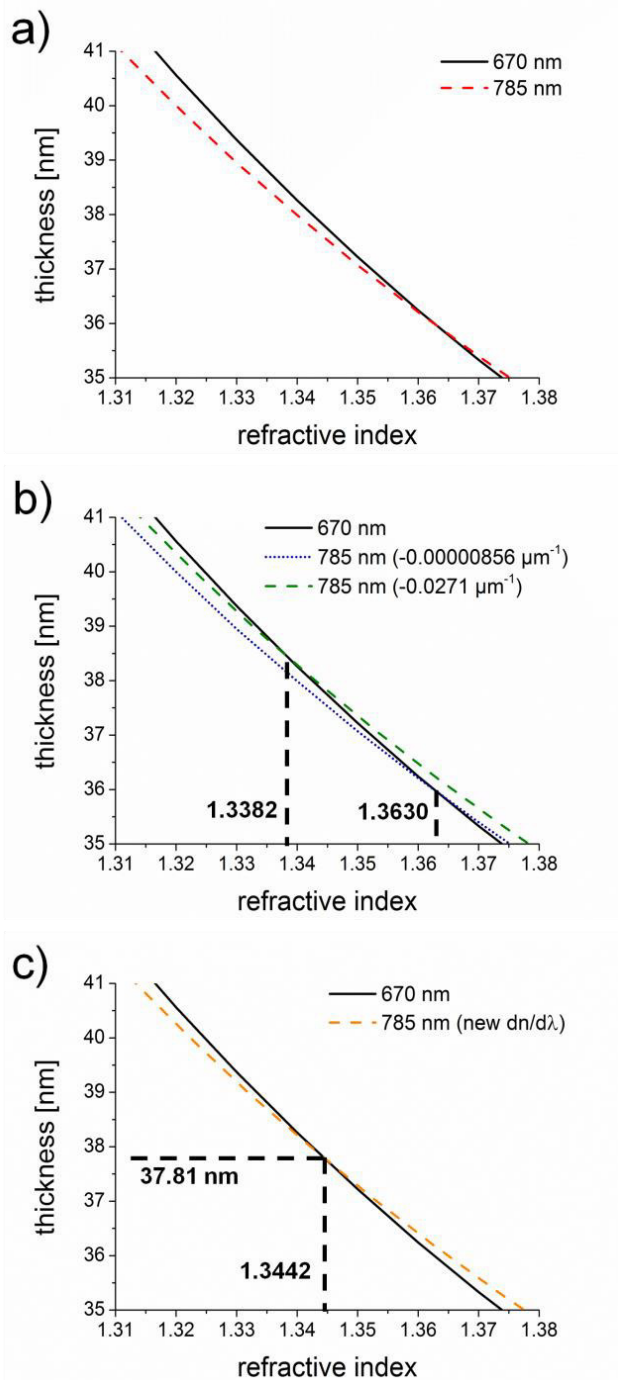
Figure 2. Continuous solutions ($n - d$ curves) obtained at 670 nm and 785 nm for a dry cellulose thin film spin coated from THF (a). The curve measured at 785 nm was shifted with the $dn/d\lambda$ of air (-0.00000856 μm^{-1}) and cellulose (-0.0271 μm^{-1}) in order to determine the composition of the film (b). The new dn/dλ value for the film consisting of air and cellulose was re-estimated from the composition (average of refractive indices at both intersection points) with equation 2. The n $- d$ curve recorded at 785 nm was shifted with the resulting $dn/d\lambda$ to obtain the unique solution (d $= 37.81$ nm, $n = 1.3442$, $a = 74\%$ cellulose) for the investigated film (c).

Multilayer Analysis of Cellulose Thin Films. In the model, which was developed for the multilayer analysis of thin film samples (Figure 3), the investigated film is described by two layers, namely the roughness layer (*RL*) and the bulk layer (*BL*). The *RL* describes the layer that contains the boundary between the film and the ambient medium i.e. the roughness of the film. The material fraction (*mf*) refers to the material inside the *RL*, which consist of a porous film, which in turn is composed of cellulose and air. It is important to note, that the density of the *RL* (ρ_{RL}) and the density of the material (ρ_m^t) are not to be confused.
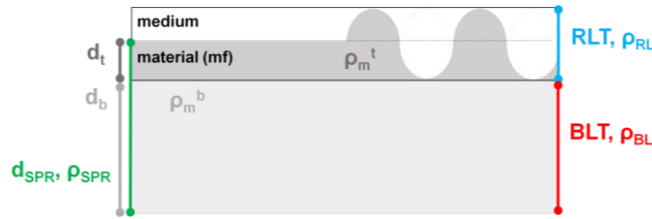
Figure 3. Graphic description of the multilayer analysis model. The film consist of a roughness layer *RL* and a bulk layer *BL* with certain thickness *T* and density ρ. The thickness d_{SPR} and density ρ_{SPR} of the film are obtained via MP-SPR spectroscopy. The film is then split into a top (d_t, ρ_m^t) and a bottom (d_b, ρ_m^b) layer. The top layer gives information about the material fraction (*mf*) inside the *RL*, whereas the bottom layer refers to the *BL*.

The thickness of the roughness layer (*RLT*) was acquired from AFM experiments. AFM data was evaluated as summarized in Figure 4 and implemented into simulations. A detailed description of the AFM evaluations is shown in the experimental section. Additional data required for the model is attained by MP-SPR spectroscopy. This optical technique is sensitive to changes in the refractive index of a material, therefore it detects the material inside the *RL* as a flat layer with a certain thickness and density (d_t, ρ_m^t), neglecting the surrounding medium of the material inside the *RL*. d_t is the thickness of the material inside the *RL*, whereas *RLT* is the thickness of the area containing the material and the medium. Therefore, the d_t values are smaller than the *RLT* values.

In order to achieve multilayer analysis, the films of interest are split into a top and a bottom layer. MP-SPR spectroscopy gives data regarding the bulk layer (*BL*) from the evaluation of the bottom layer and data corresponding to the material inside the *RL* from evaluation of the top layer. Thereby, the model enables the determination of thickness and refractive index i.e. density of different layers in a thin film. The procedure is described in detail in the experimental section.
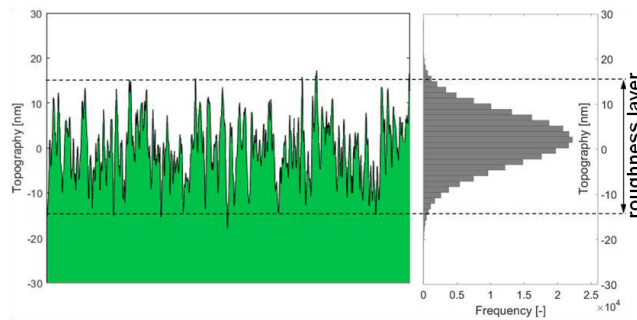
Figure 4. Graphic description of AFM data evaluation: the thickness of the roughness layer comprises 95% of the topography range measured with the AFM.

The results attained from AFM and MP-SPR spectroscopy experiments are collated in Figure 5. The thicknesses of the films and the sum of the top and bottom layer thicknesses obtained by multilayer analysis are consistent. The densities of the top and bottom layers match the densities

of the entire film. Densities in the top layer of both low and high RMS films indicate a higher porosity at the surface than in the bulk. This trend was recently reported in literature for other cellulose thin films. It cannot be ruled out that a porosity gradient is present throughout the film, with decreasing porosity towards the substrate-cellulose interface. Since the film was only split into two layers, we were not able to detect such a gradient.
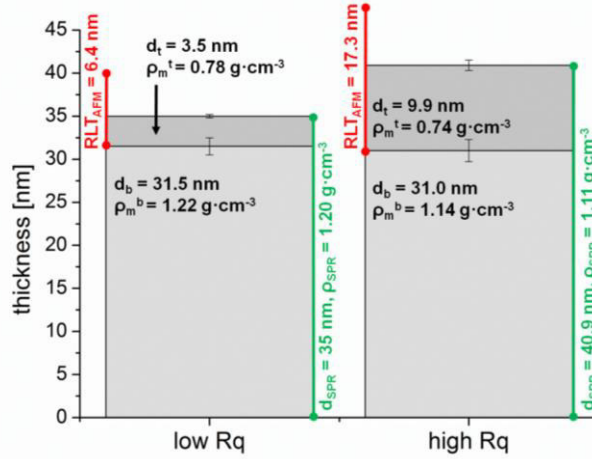
Figure 5. Comparison of results from the 2-wavelength evaluation the cellulose thin films (d_{SPR}, ρ_{SPR})), AFM evaluation (RLT_{AFM}) and multilayer analysis (d_t, $\rho_m{}^t$, d_b, $\rho_m{}^b$).

Due to the aforementioned differences in measurement principles of the applied techniques, the resulting data from AFM and MP-SPR spectroscopy was compared by the following considerations to validate the employed strategy for multilayer analysis. The material fraction (mf, composed of cellulose and air) and RLT were acquired by AFM. The cellulose content, i.e. the density in the material ($\rho_m{}^t$), and the thickness of the layer consisting of material, i.e. the top layer (d^t), were obtained from MP-SPR spectroscopy. For each technique, values which correspond to the same parameter determined by the other technique ($\rho_{RL}{}^{AFM}$, $\rho_{RL}{}^{SPR}$, RLT_{SPR} and mf_{SPR} were calculated from the measured results mf_{AFM}, RLT_{AFM}, d_t and $\rho_m{}^t$). The outcome of these calculations are summarized in Table 1. The results from both techniques are in good agreement for the low

and high RMS roughness films. Deviations can be attributed to the different measurement areas of the applied techniques and small variations in the cellulose thin films. AFM covers an area of 10 × 10 µm^2, whereas the area of the MP-SPR spectroscopy lasers (Ø = 0.6 mm) is approximately 0.28 mm^2.

Table 1. Comparison of results determined by MP-SPR spectroscopy and AFM of cellulose thin films measured in air. The boxes shaded in grey display values which were calculated from results shown in Figure 5.[a]

	low R$_q$		high R$_q$	
	AFM	MP-SPR	AFM	MP-SPR
d$_t$	-	3.5 nm	-	9.9 nm
ρ$_m^t$	-	0.78 g·cm^{-3} (52%)	-	0.74 g·cm^{-3} (49%)
d$_b$	-	31.5 nm	-	31.0 nm
ρ$_m^b$	-	1.22 g·cm^{-3} (81%)	-	1.14 g·cm^{-3} (76%)
RLT	**6.4 nm**	**6.7 nm**	**17.3 nm**	**19.6 nm**
ρ$_{RL}$	**0.38 g·cm^{-3} (25%)**	**0.42 g·cm^{-3} (28%)**	**0.36 g·cm^{-3} (24%)**	**0.41 g·cm^{-3} (27%)**
mf	**48%**	**55%**	**49%**	**57%**
BLT	**-**	**d$_b$**	**-**	**d$_b$**
ρ$_{BL}$	**-**	**ρ$_m^b$**	**-**	**ρ$_m^b$**
mf	**-**	**100%**	**-**	**100%**

[a]The shown percentages refer to the cellulose content.

The values chosen for the simulations in the beginning of the multilayer analysis are of high importance. Therefore, additional experiments with varying starting values were performed (see SI). Of course, when the refractive index values in the first evaluation step are chosen manually and not by iteration, various results are obtained. However, a result was only attained when the starting values for the refractive index were in the range between n_{SPR} and the value from iteration

of the simulation program (n_t^0). Experiments with values outside this range did not yield intersections of $n - d$ curves. As for starting values for the thickness (d_t^0) with assumed *RLT*, results are obtained, but cannot be trusted. The thicker the *RLT* was chosen, the higher the density of this *RL* was. Indicating a porosity gradient in the cellulose thin films. Additionally, the first bottom layer result in the multilayer analysis is achieved by keeping the values of the top layer constant, thereby influencing the outcome of the simulation. A randomly chosen starting value for the *RLT* does not lead to a result corresponding to the real *RLT* of the thin film. As a result, proper starting values are required. The implementation of AFM data is necessary for the presented multilayer analysis method and evaluation cannot be achieved by MP-SPR spectroscopy alone.

CONCLUSION

A strategy to determine the density of different layers in thin film samples by means of AFM and MP-SPR spectroscopy was presented. Cellulose thin films with low and high RMS roughness were examined. Compositions obtained from MP-SPR spectroscopy reveal the porous nature of the cellulose films. Results of the whole films match the thickness and densities of the layers present inside those films, indicating the integrity of the approach. Spatially resolved analysis of the cellulose films reports an even higher porosity in the surface regions than for the bulk material. Calculations in order to compare the results from the employed surface sensitive techniques were made. Conformity of material fraction, density and thickness of the roughness layer attained from both methods validates the approach. The herein presented multilayer analysis method serves as basis for investigations concerning processes occurring at interfaces. The method is able to monitor phenomena such as adsorption, surface modification or swelling, and therefore can act as an important tool in surface and interface science.

ASSOCIATED CONTENT

Supporting information available including AFM topography evaluation, Background MP-SPR curves, additional simulation experiments for multilayer analysis

AUTHOR INFORMATION

Corresponding Author

*E-mail stefan.spirk@tugraz.at, Tel +43 316 873 32284

Author Contributions

The manuscript was written through contributions of all authors. All authors have given approval to the final version of the manuscript.

ACKNOWLEDGEMENT

REFERENCES

(1)   Zaera, F. Surface Chemistry at the Liquid/solid Interface. *Surf. Sci.* **2011**, *605* (13-14), 1141–1145.

(2)   *Surface Analysis - The Principle Techniques*; Vickerman, J. C., Gilmore, I. S., Eds.; Wiley, 2009.

(3)   Binnig, G.; Quate, C. F. Atomic Force Microscope. *Phys. Rev. Lett.* **1986**, *56* (9), 930–933.

(4)   Giessibl, F. J. Advances in Atomic Force Microscopy. *Rev. Mod. Phys.* **2003**, *75* (3), 949–983.

(5)   Jalili, N.; Laxminarayana, K. A Review of Atomic Force Microscopy Imaging Systems: Application to Molecular Metrology and Biological Sciences. *Mechatronics* **2004**, *14* (8), 907–945.

(6)   Eibinger, M.; Ganner, T.; Bubner, P.; Ro??ker, S.; Kracher, D.; Haltrich, D.; Ludwig, R.; Plank, H.; Nidetzky, B. Cellulose Surface Degradation by a Lytic Polysaccharide Monooxygenase and Its Effect on Cellulase Hydrolytic Efficiency. *J. Biol. Chem.* **2014**, *289* (52), 35929–35938.

(7)   Raether, H. Surface Plasma Oscillations and Their Applications. *Phys. Thin Film.* **1977**, *9*, 145–261.

(8)   Ritchie, R. H. Plasma Losses by Fast Electrons in Thin Films. *Phys. Rev.* **1957**, *106* (5), 874–881.

(9)   Geddes, N. J.; Martin, A. S.; Caruso, F.; Urquhart, R. S.; Furlong, D. N.; Sambles, J. R.; Than, K. A.; Edgar, J. A. Immobilisation of IgG onto Gold Surfaces and Its Interaction with Anti-IgG Studied by Surface Plasmon Resonance. *J. Immunol. Methods* **1994**, *175*, 149–160.

(10)   Peterlinz, K. a; Georgiadis, R. Two-Color Approach for Determination of Thickness and Dielectric Constant of Thin Films Using Surface Plasmon Resonance Spectroscopy. *Opt. Commun.* **1996**, *130* (4-6), 260–266.

(11) Liang, H.; Miranto, H.; Granqvist, N.; Sadowski, J. W.; Viitala, T.; Wang, B.; Yliperttula, M. Surface Plasmon Resonance Instrument as a Refractometer for Liquids and Ultrathin Films. *Sensors Actuators, B Chem.* **2010**, *149* (1), 212–220.

(12) Mohan, T.; Spirk, S.; Kargl, R.; Doliška, A.; Vesel, A.; Salzmann, I.; Resel, R.; Ribitsch, V.; Stana-Kleinschek, K. Exploring the Rearrangement of Amorphous Cellulose Model Thin Films upon Heat Treatment. *Soft Matter* **2012**, *8* (38), 9807.

(13) Mohan, T.; Spirk, S.; Kargl, R.; Doliška, A.; Ehmann, H. M. a; Köstler, S.; Ribitsch, V.; Stana-Kleinschek, K. Watching Cellulose Grow - Kinetic Investigations on Cellulose Thin Film Formation at the Gas-Solid Interface Using a Quartz Crystal Microbalance with Dissipation (QCM-D). *Colloids Surfaces A Physicochem. Eng. Asp.* **2012**, *400*, 67–72.

(14) Mohan, T.; Kargl, R.; Doliška, A.; Vesel, A.; Köstler, S.; Ribitsch, V.; Stana-Kleinschek, K. Wettability and Surface Composition of Partly and Fully Regenerated Cellulose Thin Films from Trimethylsilyl Cellulose. *J. Colloid Interface Sci.* **2011**, *358* (2), 604–610.

(15) Kasarova, S. N.; Sultanova, N. G.; Ivanov, C. D.; Nikolov, I. D. Analysis of the Dispersion of Optical Plastic Materials. *Opt. Mater. (Amst).* **2007**, *29* (11), 1481–1490.

(16) Ciddor, P. E. Refractive Index of Air: New Equations for the Visible and near Infrared. *Appl. Opt.* **1996**, *35* (9), 1566–1573.

(17) Kontturi, E.; Thüne, P. C.; Niemantsverdriet, J. W. Cellulose Model Surfaces-Simplified Preparation by Spin Coating and Characterization by X-Ray Photoelectron Spectroscopy, Infrared Spectroscopy, and Atomic Force Microscopy. *Langmuir* **2003**, *19* (14), 5735–5741.

(18) Mwaikambo, L. Y.; Ansell, M. P. The Determination of Porosity and Cellulose Content of Plant Fibers by Density Methods. *J. Mater. Sci. Lett.* **2001**, *20* (23), 2095–2096.

(19) Hall, D. B.; Underhill, P.; Torkelson, J. M. Spin Coating of Thin and Ultrathin Polymer Films. *Polym. Eng. Sci.* **1998**, *38* (12), 2039–2045.

Supporting Information #9

Multilayer Density Analysis of Thin Films

submitted to Langmuir

AFM topography evaluation.
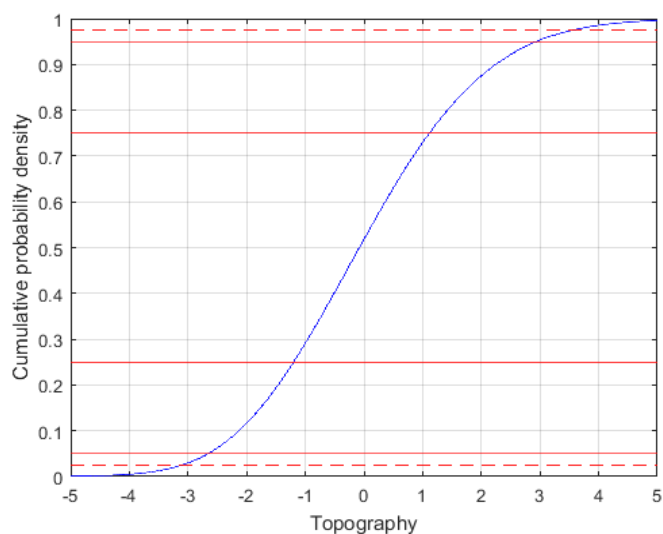
Figure S1. AFM topography evaluation (cumulative probability density vs. topography [nm]) for cellulose thin films spin coated from $CHCl_3$. Calculated roughness layer thickness = 6.4 nm and material fraction = 47.9%.
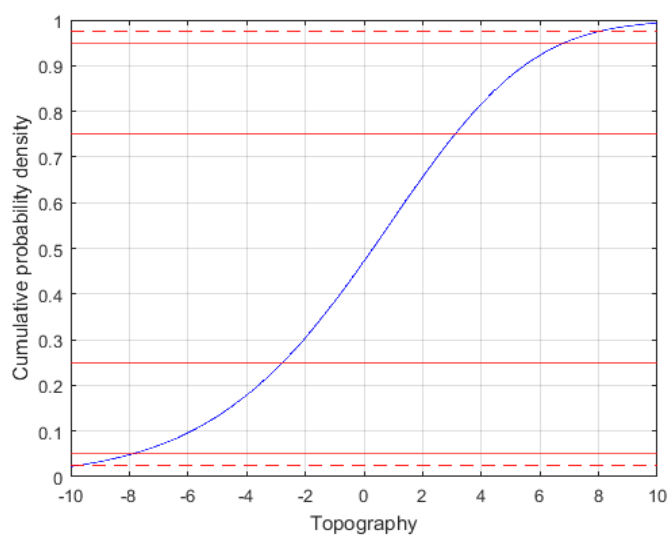
Figure S2. AFM topography evaluation (cumulative probability density vs. topography [nm]) for cellulose thin films spin coated from THF. Calculated roughness layer thickness = 17.3 nm and material fraction = 49.3%.

MP-SPR spectroscopy evaluation.
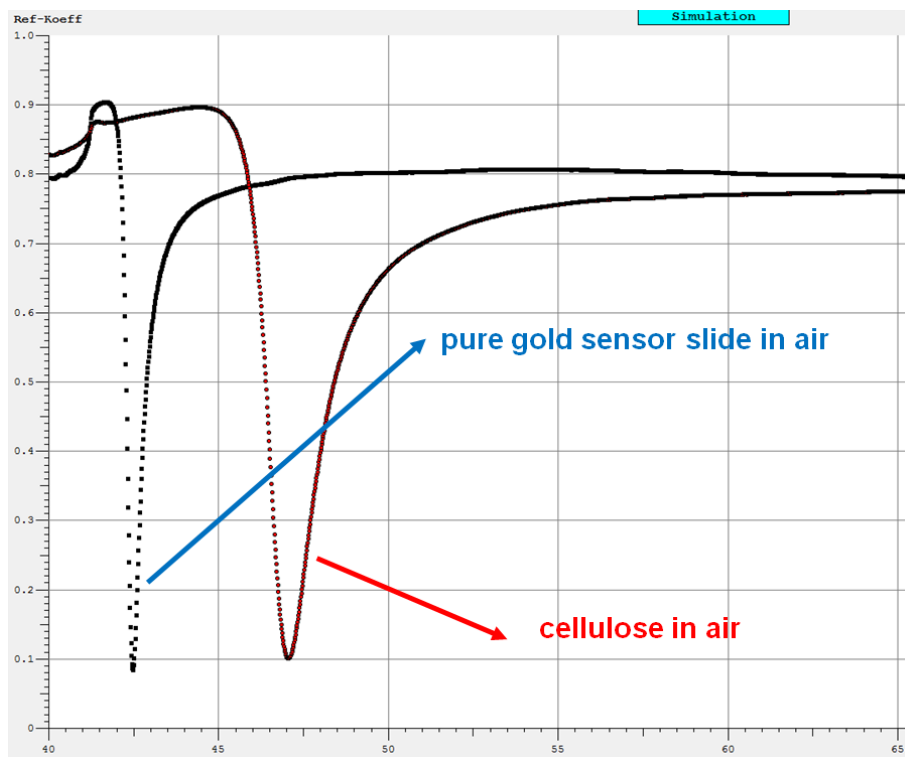
Figure S3. Pure gold sensor slide (background) and cellulose thin film spin coated from CHCl$_3$ measured in air.

Calculation of film/layer density.

Densities of the films/layers in the film were calculated from the content of cellulose (% cellulose) obtained from MP-SPR spectroscopy measurements according to the following equations.

$$\rho_{film/layer} = \frac{\%_{cellulose} \times \rho_{cellulose} + \%_{air} \times \rho_{air}}{100}$$

$$\rho_{cellulose} = 1.5 \; g \cdot cm^{-3}$$

$$\rho_{air} = 0.00118 \; g \cdot cm^{-3}$$

Table 1. MP-SPR simulation values at the example of a cellulose thin film spin coated from CHCl$_3$.[a]

evaluation whole film	670 nm			785 nm		
	d [nm]	RI	kappa	d [nm]	RI	kappa
Cr	5.16	0.7547	6.8748	5.50	0.7312	8.9008
Au	54.04	0.0451	2.2156	55.88	0.0333	2.5363
Cellulose	35.10	1.3680	/	35.10	1.3655	/
splitting of the cellulose film						
Cr	5.16	0.7547	6.8748	5.50	0.7312	8.9008
Au	54.04	0.0451	2.2156	55.88	0.0333	2.5363
bottom	31.90	1.3760	/	31.90	1.3735	/
top	3.20	1.2778	/	3.20	1.2771	/
evaluation of bottom layer + implementation of RLT$_{AFM}$ + iteration of RI top layer						
Cr	5.16	0.7547	6.8748	5.50	0.7312	8.9008
Au	54.04	0.0451	2.2156	55.88	0.0333	2.5363
bottom	31.92	1.3752	/	31.92	1.3726	/
top	6.40	1.2991	/	6.40	1.1267	/
evaluation of top layer						
Cr	5.16	0.7547	6.8748	5.50	0.7312	8.9008
Au	54.04	0.0451	2.2156	55.88	0.0333	2.5363
bottom	31.92	1.3752	/	31.92	1.3726	/
top	3.68	1.2400	/	3.68	1.2399	/
re-evaluation of bottom layer (not shown)						

[a]values for Cr and Au remain constant during the analysis.

Table 2. Influence of starting values for the refractive index on the outcome of the multilayer analysis shown for the case of a cellulose thin film spin coated from THF.[a]

evaluation whole film	670 nm			785 nm		
	d [nm]	RI	kappa	d [nm]	RI	kappa
Cr	4.58	0.6837	5.6774	4.45	0.9197	11.7096
Au	53.75	0.0597	2.71	54.59	0.1121	3.1604
Cellulose	37.81	1.3442	/	37.81	1.3419	/
evaluation with RI from iteration in the program (n_t^0)						
splitting the film + iteration of n_{SPR} values						
bottom	29.16	1.3710	/	29.16	1.3695	/
top	8.65	1.2506	/	8.65	1.2521	/
results bottom and top layer						
bottom	29.47	1.3620	/	29.47	1.3595	/
top	10.61	1.2090	/	10.61	1.2077	/
evaluation with RI $= n_{SPR}$						
splitting the film + keeping n_{SPR} as starting value						
bottom	29.16	1.3442	/	29.16	1.3419	/
top	8.65	1.3442	/	8.65	1.3419	/
results bottom and top layer						
bottom	28.67	1.3460	/	28.67	1.3437	/
top	8.90	1.3490	/	8.90	1.3467	/
evaluation with higher RI for top layer than from iteration (RI $> n_t^0$)						
splitting the film + iteration + manually choosing a higher RI for top layer						
bottom	29.16	1.3576	/	29.16	1.3557	/
top	8.65	1.2961	/	8.65	1.2951	/
results bottom and top layer						
bottom	29.21	1.3525	/	29.21	1.3501	/
top	8.98	1.2970	/	8.98	1.2951	/

	670 nm			785 nm		
evaluation with lower RI for top layer than from iteration (RI < n_t^0)						
splitting the film + iteration + manually choosing a lower RI for the top layer						
bottom	29.16	1.4038	/	29.16	1.4018	/
top	8.65	1.1500	/	8.65	1.1629	/
results bottom and top layer						
bottom	/	/	/	/	/	/
top	/	/	/	/	/	/

[a] values for Cr and Au remain constant during the analysis.

Table 3. Influence of starting value for *RLT* on the outcome of the multilayer analysis at the example of a cellulose thin film spin coated from CHCl$_3$.

evaluation	670 nm			785 nm		
whole film	d [nm]	RI	kappa	d [nm]	RI	kappa
Cr	5.16	0.7547	6.8748	5.50	0.7312	8.9008
Au	54.04	0.0451	2.2156	55.88	0.0333	2.5363
Cellulose	35.10	1.3680	/	35.10	1.3655	/
splitting of the cellulose film with *RLT*/2 = 5 nm						
Cr	5.16	0.7547	6.8748	5.50	0.7312	8.9008
Au	54.04	0.0451	2.2156	55.88	0.0333	2.5363
bottom	30.10	1.3760	/	30.10	1.3740	/
top	5.00	1.3112	/	5.00	1.3102	/
results for top and bottom layer						
bottom	30.53	1.3709	/	30.53	1.3683	/
top	4.57	1.3450	/	4.57	1.3427	/